Analogue Gravity in Nonlocal Fluids of Light

David Emanuel Frank Vocke

Dipl. Phys.

Submitted for the degree of Doctor of Philosophy

Heriot Watt University, Edinburgh

Institute of Physics and Quantum Sciences

May 5, 2017

Scientific Supervisor:	Prof. Dr. Daniele Faccio
Submitted by:	Dipl. Phys. David E.F. Vocke
Date:	May 5, 2017

For my family

Abstract

Analogue gravity designates the study of curved spacetime in a laboratory environment and allows to test concepts of General Relativity. This analogy is established via a conformal identity between the flow of curved spacetime and inhomogeneous flows in hydrodynamics, which predicts that small waves on a fluid behave exactly as scalar fields in a curved spacetime metric. Atomic quantum fluids such as Bose-Einstein Condensates (BEC) are a widespread workbench for studying artificial black holes and many-body physics but face considerably large experimental challenges. In recent years, quantum fluids of light became a promising alternative at less technical expense, where the many-body dynamics in a laser beam are established via photon-photon interactions mediated through an optical nonlinearity. Whereas recent works considered strongly confined laser fields in microcavities, this work presents a photon fluid in a propagating geometry, i.e. a paraxially propagating laser beam in a bulk nonlinear medium. In this scenario, the propagating direction maps onto a time coordinate and the photon fluid is established in the transverse beam profile. The thermal nonlinearity is excited through heating of the absorbed laser power that introduces a nonlocal response of the medium and adds another level of complexity.

It is experimentally shown that the dynamics of small amplitude excitations are governed by the Bogoliubov dispersion relation and allows to observe superfluidity at sufficiently large wavelengths. This is confirmed by the onset of persistent currents and the nucleation of quantized vortices in sub- and supercritical flows around an extended obstacle, which is a direct observation of superfluidity in a room-temperature system. The superfluid regime is a requirement for building analogue spacetime metrics and is thus of paramount importance. The spacetime of a rotating black and white whole was then created by shaping the topology of the spatial phase using diffractive phase masks. The experimental measurements of the inhomogeneous flows revealed, for the first time conclusive evidence of a (2+1) dimensional acoustic horizon and ergosphere. Such a system promises to study Penrose superradiance, where first experimental and numerical results for its observation are presented.

Finally, nonlinear wave dynamics such as self-steepening and shock formation are studied where the dynamics can be interpreted in terms of a self-induced spacetime. Furthermore, the dynamics of a sea of incoherent waves is studied with respect to the long-range interactions provided by the nonlocality, where a novel transition from individual dispersive shock waves towards a collective giant shock wave is observed.

Acknowledgements

I am extremely grateful to my family, friends and colleagues who made the last years such a positive and enlightening experience for me. All of you played an important part in making this PhD, which was undoubtedly hard work, very enjoyable for me.

Foremost, I'd like to thank my supervisor, Prof. Daniele Faccio, who gave me the opportunity to work in his research group and for creating an environment that allows to perform research at the highest level. Despite the vast amount of other responsibilities, he always had an open door and time to discuss science and to encourage new ideas. I have learnt a lot from him during the past years and I am very grateful to have been his student.

A special thanks goes to Thomas Roger, the lab magician, for all the help inside and outside the laboratory. Thank you for being a great colleague and valued friend.

Furthermore, I'd like to thank Calum Maitland and Kali Wilson, for numerical simulations as well as useful discussions on photon fluids, Angus Prain for his insights in General Relativity and all the past and present members of the Extreme Light Group who I was lucky to work with. Not forgotten are my collaborators and colleagues outside of Heriot Watt: Francesco Marino, Ewan M. Wright, Iacopo Carusotto, Gang Xu, Antonio Picozzi and Quentin Glorieux.

My Dear Magdalena, there would be so much to be grateful for, but foremost for all your love and support over the past years. I am very lucky to have spent this adventure with you.

At last, I dedicate this work to my family, Bruni, Frank, Daniel and Oma Margret who were of immeasureble support during all the years since I started physics. Thank you so much!

List of Publications

Journal papers

- D. Vocke, T. Roger, F. Marino, E. M. Wright, I. Carusotto, M. Clerici, and D. Faccio. "Experimental characterization of nonlocal photon fluids". Optica, 2(5):484, 2015.

- D. Vocke, K. Wilson, F. Marino, I. Carusotto, E. M. Wright, T. Roger, B. P. Anderson, P. Öhberg, and D. Faccio. "Role of geometry in the superfluid flow of nonlocal photon fluids". Physical Review A 94(1), 2016

- D. Vocke, C. Maitland, A. Prain, F. Marino and D. Faccio, "Two dimensional acoustic horizon and ergosphere in a nonlocal photon superfluid", to be published 2017.

- G. Xu, D. Vocke, D. Faccio, J. Garnier, T. Roger, S. Trillo and A. Picozzi. "From coherent shocklets to giant collective incoherent shock waves in nonlocal turbulent flows". Nature Communications, 6:8131, 2015.

- T. Roger, C. Maitland, K. Wilson, N. Westerberg, D. Vocke, E. M. Wright and D. Faccio. "Optical analogues of the Newton-Schrödinger equation and boson star evolution. Nature Communications, 7:13492, 2016

- F. Marino, C. Maitland, D. Vocke, A. Ortolan and D. Faccio. "Emergent geometries and nonlinear-wave dynamics in photon fluids". Scientific reports, 6:23282, 2016.

Conference papers

- D. Vocke, T. Roger, F. Marino, E. M. Wright, and D. Faccio, "Dispersion relation of a two-dimensional photon fluid" , Photon '14, London 2014

- D. Vocke, K. Wilson, F. Marino, E. M. Wright, I. Carusotto, M. Clerici, and D. Faccio. "Experimental characterization of nonlocal photon fluids". CLEO Europe, Munich 2015

- D. Vocke, K. Wilson, F. Marino, I. Carusotto, E. M. Wright, T. Roger, B. P. Anderson, P. Öhberg, and D. Faccio. "Superfluid flow and instability in room temperature, nonlocal photon fluids", Frontiers of Quantum Optics, Bad Honnef 2016

- D. Vocke, K. Wilson, F. Marino, I. Carusotto, E. M. Wright, T. Roger, B. P. Anderson, P. Öhberg, and D. Faccio, "Nonlocal fluids made of light", SU2P Edinburgh 2016
- D. Vocke, K. Wilson, F. Marino, I. Carusotto, E. M. Wright, T. Roger, B. P. Anderson, P. Öhberg, and D. Faccio. "Superfluid flow and vortex nucleation in room temperature, nonlocal photon fluids", CLEO North America, San Jose 2016
- D. Vocke, "Nonlocal fluids of light" (Invited) , Fluids of Light workshop, Edinburgh 2016

Awards

- 1st year postgraduate research prize in recognition of outstanding research performance, Heriot-Watt University, Edinburgh, 2014
- 2nd year postgraduate research prize in recognition of outstanding research performance, Heriot-Watt University, Edinburgh, 2015

ACADEMIC REGISTRY
Research Thesis Submission

Name*:*			
School/PGI:			
Version: *(i.e. First, Resubmission, Final)*		Degree Sought (Award **and** Subject area)	

Declaration

In accordance with the appropriate regulations I hereby submit my thesis and I declare that:

1) the thesis embodies the results of my own work and has been composed by myself
2) where appropriate, I have made acknowledgement of the work of others and have made reference to work carried out in collaboration with other persons
3) the thesis is the correct version of the thesis for submission and is the same version as any electronic versions submitted*.
4) my thesis for the award referred to, deposited in the Heriot-Watt University Library, should be made available for loan or photocopying and be available via the Institutional Repository, subject to such conditions as the Librarian may require
5) I understand that as a student of the University I am required to abide by the Regulations of the University and to conform to its discipline.

* *Please note that it is the responsibility of the candidate to ensure that the correct version of the thesis is submitted.*

Signature of Candidate*:*		Date:	

Submission

Submitted By *(name in capitals):*	
Signature of Individual Submitting:	
Date Submitted:	

For Completion in the Student Service Centre (SSC)

Received in the SSC by *(name in capitals):*			
Method of Submission *(Handed in to SSC; posted through internal/external mail):*			
*E-thesis Submitted (**mandatory for final theses)***			
Signature:		Date:	

Please note this form should bound into the submitted thesis.

Updated February 2008, November 2008, February 2009, January 2011

Contents

Chapter 1

Fluids of light - An introduction

1.1 Motivation

A fluid made out of light is at first a strange thing to imagine. From daily experience, everybody is familiar how fluids look like and how they behave under external influences such as wind, gravity or temperature. So how does a "light" fluid look like?
On large scales, fluids such as water appear as a homogeneous flowing medium, whose properties are different from other forms of matter such as gases or solids. The physical definition of a solid, gas or liquid may be characterised via macroscopic properties of that matter such as density, pressure or temperature and depending on these a lump of matter takes the corresponding aggregate state. Today we know that the properties of any matter arise from the interactions of the microscopic constituent particles, an idea that dates back to greek philosophers over 2500 years ago. The macroscopic properties of a fluid are therefore directly linked to how these particles interact. In that perspective, the question of how a fluid looks like and how it behaves depends on the relevant interactions of its building blocks. With this in mind, the terminology of fluids applies to a very general system, whose appearances may differ from everyday experience. An example are traffic jams on highways, where the overall density of constituent particles, the vehicles is large enough, such that a coupling between neighbouring vehicles becomes relevant. If one vehicle changes its speed, it induces a density variation that the others have to react to in order to avoid collision. This density variation will propagate along the highway as a "pressure" wave.
In the case of light, the microscopic particles that build a ray of light, the photons, are described by the theory of quantum mechanics as massless bosons. As a consequence, photons do not interact in vacuum and will therefore not be able to create a state that may be described as a gas or fluid. If the photons build up a laser beam that is propagating inside a transparent material, this situation changes. Depending on the material and the photon density (i.e. Laser intensity), the photons can change the refractive index of the material, that will have a back-reaction on the photons itself. In other words, photons do interact in such materials and under specific conditions, such a laser beam is a fluid of interacting particles.
Interestingly, these so called fluids of light, or photon fluids have the properties of quantum fluids, a macroscopic manifestation of quantum mechanics where the dynamics of the whole fluid is governed by a single wave function. These have sparked a huge interest in the past two decades since the first realisation of an atomic Bose-Einstein Condensate, where the quantum degeneracy of a cloud of ultra-cold atoms leads to a macroscopic occupation of the ground state. The situation is becoming even more interesting in the presence of interactions that lead to spectacular effects such as su-

perfluidity or superconductivity. In general, the rich physics of many-body systems has attracted a lot of theoretical and experimental interest in various different fields from ultra-cold atoms over electrons in semiconductors to quark-gluon plasma in particle colliders. Nowadays, quantum fluids and especially atomic BECs are a platform to study nonlinear dynamics, such as generation and interaction of quantised vortices, solitons or shock waves. On the other hand, they are used for quantum simulators, where the high controllability allows to build 'artificial solids' that allow to model many-body systems, which are impossible to solve with current computational techniques. They are also promising candidates for applications that require superb interferometric accuracy, i.e. detection of gravitational waves. In the past decade, BECs became an established workbench for analogue gravity studies that are able to create artificial scenarios of curved spacetimes i.e. an experiment that simulates waves in the vicinity around a black hole. These display an experimental testbed for concepts of general relativity.
Nonetheless, the realisation of a BEC took almost 70 years after it was first predicted by Satyendranath Bose and Albert Einstein in the early 1920s, and shows how difficult it is to control a gas of particles such that they form a condensate. Even today it requires extensive experimental effort to trap and cool a cloud of atoms down to nano-Kelvin and therefore the community is always in search of new quantum fluids that require less technical and financial resources. Quantum fluids of light provide easy experimental access and wide tunability of parameters and are therefore promising alternatives. Over the recent years, a variety of different systems has reemerged that are based on light which is trapped in a cavity to enhance the light-matter interaction. The most spectacular theoretical and experimental studies have shown Bose-Einstein condensation and superfluidity of photons. In this thesis, an even simpler approach to a photon fluid is presented, where the transverse plane of a paraxially propagating laser beam in a thermal nonlinear medium is shown to exhibit characteristics of a quantum fluid. In this system, the photon-photon interactions can be tuned in magnitude and in range, which allows to control the macroscopic properties of this fluid very easily while an overall flow can be designed by the topology of the optical phase of the laser. This versatility allows to precisely build (2+1) dimensional fluid geometries that can be used to study analogue gravity of i.e. rotating black holes. For this reason, a thorough investigation of the dynamics of elementary excitations is carried out to study the photon fluid dispersion relation and aspects of superfluidity. As will be shown, when the amplitudes of such excitations are non-pertubative, the dynamics allow to study self-steepening and shock waves. Furthermore, the tunability of long range interactions can be used to investigate self-organisation processes of turbulent wave systems that draw links to dynamics of galaxies. Future directions show that the analogies are even

richer. The self-induced blow up of a narrow laser spot mimics certain facets of an expanding universe in cosmological models. Additionally, by changing from repulsive to attractive interactions the description of a fluid breaks down, but the dynamics are now ruled by the Newton-Schrödinger equation that enables to simulate self-gravitating wave functions.

1.2 A brief history

The concept of a photon fluid applies to a variety of systems exhibiting a light-matter coupling that eventually leads to a collective behaviour of a many photon system in the form of a quantum fluid. The photon-photon interactions are induced by the optical nonlinearity of the system and may therefore differ among the various implementations. Depending on the specific problem, the common approach is to reformulate the equations that govern the temporal evolution of the optical field, onto a generalised Gross-Pitaevskii equation that describes the dynamics of a quantum fluid. In optics, this identity is met by the Nonlinear Schrödinger Equation (NLSE) that describes the paraxially propagating laser field in a nonlinear optical medium. In the case of a defocusing nonlinearity, the local light intensity maps into a fluid density and the gradient of the phase into a fluid flow. The first branding of a coherent light field as a photon fluid dates back to the early nineties, where the evolution of the field in a laser cavity was reformulated into a Ginzburg-Landau equation and demonstrated the correspondence to the dynamics of a quantised fluid [1,2]. Here, the interactions are mediated via the nonlinear refractive index of the gain medium. In the following decade, a growing interest was devoted to the hydrodynamical aspects of the transverse field dynamics in cavities. In particular, the observation of phase singularities was soon interpreted as quantised vortices [3,4], a hallmark signature of quantum fluids.

The strong links to Bose-Einstein Condensates raised questions in the community regarding differences between laser operation and condensation. Where a BEC results from thermal equilibrium, the driven-dissipative laser operation follows from a dynamical balance between pumping and dissipation. Experimentally, this was recognized by a growing interest in optical semiconductor cavities, where a strong coupling between excitons in the bulk material and the photons lead to a mixed quasiparticle, the exciton-polariton. The optical nonlinearity arises here through the strong interactions between the excitons. The small mass of exciton-polaritons promised quantum degeneracy and thus condensation at higher temperatures compared to atoms. Pioneering studies reported BECs of polaritons [5–7], where the thermalisation occurred via polariton-polariton collisions. In another system, a photon BEC was observed where a cavity

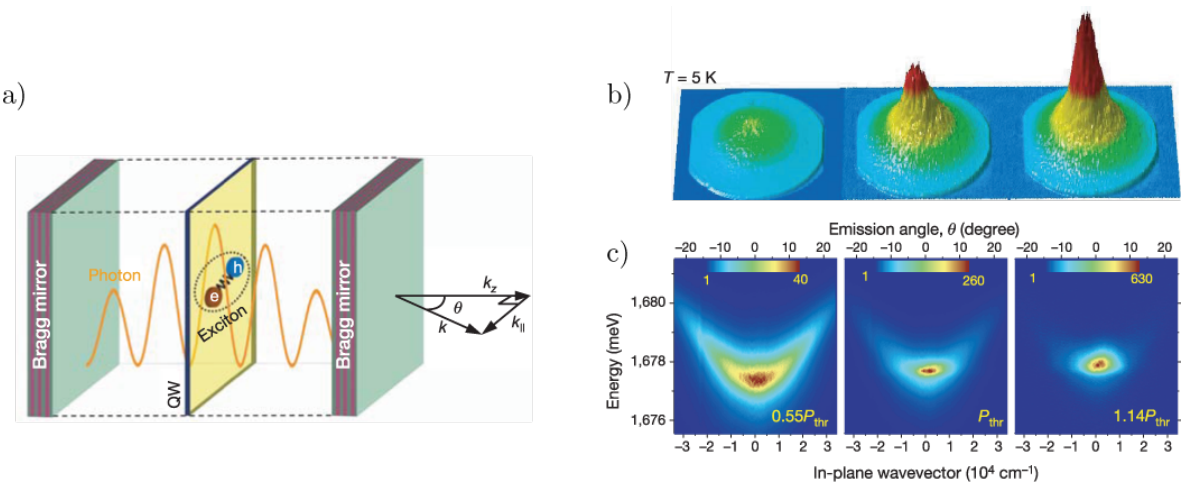

Figure 1.1: Photon fluid in a semiconductor micro cavity. a) The photon mode is strongly coupled to the excitons in the quantum well (QW) giving rise to a photon-photon interaction. The photon fluid plane is in the transverse plane, i.e. a mode with frequency ω and in-plane vector k_{II} may be excited by a laser beam with incident angle θ b) and c) Farfield spectrum showing the Bose-Einstein condensation of an exciton-polariton condensate for increasing intensity (polariton density). Taken from Kasprzak et al. [5].

filled with fluorescent dye allowed photon thermalization [8]. Like the exciton-polariton system, the dye-microcavities require continuous pumping due to dissipation and losses but possess in contrast only weak light-matter coupling [9].

However, exciton-polariton systems are off-resonantly pumped, so that the condensate forms after relaxation processes of injected hot electron-hole pairs [10]. When coherently pumped, it was shown that the field may be described by a generalized Gross-Pitaevskii formalism without dealing with complex relaxation mechanisms [11]. Consequently, the hydrodynamical aspects of these photon fluids gained a lot of interest due to easy experimental access to many-body physics and theoretical studies revealed that the dynamics of elementary excitations on top of the photon fluid follow the Bogoliubov dispersion relation [12]. The spatial confinement of the cavity provides an effective mass for the photons while the third order nonlinearity of the system gives rise to interactions. As a result, the low momentum excitations have a linear dispersion and can be described as phonons of the photon fluid. In the following, experimental studies on the superfluid aspects of the photon fluids reported the dissipationless flow around a defect, that was confirmed by an interpretation in terms of the Landau criterion for superfluids [13, 14]. As the flow was increased beyond the speed of sound, the breakdown of superfluidity was observed by the characteristic nucleation of quantised vortex and anti-vortex pairs [15] and furthermore the creation of dark solitons [16]. The superfluid

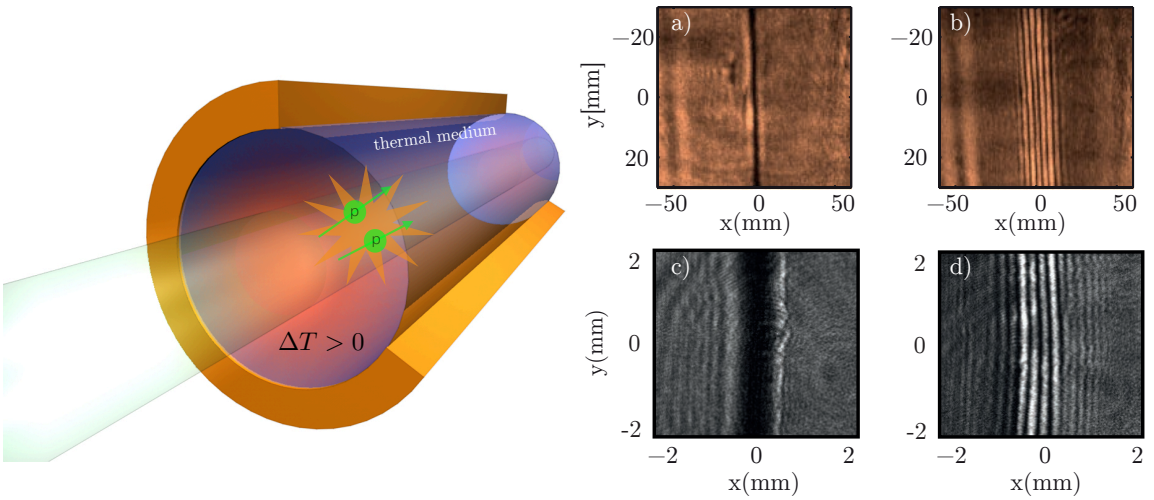

Figure 1.2: Photon fluids in a thermal bulk medium. left panel: The effective photon-photon interaction is mediated via a thermally induced change of the refractive index. The fluid plane is in the transverse plane to the propagation direction. right panel: a) Dark beam immersed in a bright background creates a dark soliton when nonlinear self-defocusing balances diffraction and gradient catastrophe b) when nonlinearity exceeds diffraction (Nd-Vanadate laser in methanol+rhodamine B, taken from Conti et al. [23]). c) and d) Same effects observed in a methanol/graphene solution from the Heriot-Watt Experiment.

character of these systems allows to build analogue gravity models, where the linear dispersion of the photon fluid mimics the dispersionless vacuum. In this situation, it is possible to map the equation of motion of these waves onto an effective Klein-Gordon equation, describing scalar fields in a curved spacetime [17]. Recently, semiconductor exciton-polariton condensates have been proposed to study Hawking radiation from an acoustic horizon in an inhomogeneous flow in the photon fluid [18] and first experimental realisations of such a flow have been reported [19].

Next to driven-dissipative systems, an alternative approach to photon fluids involves a cavityless system, where the transverse profile of the laser beam that is propagating through a bulk nonlinear material, is described as a fluid where the longitudinal propagation axis is replaced by the time coordinate. These systems are commonly referred to as *photon fluids in a propagating geometry*. The photon-photon interactions are also mediated by a third order nonlinearity of the bulk material where photo-refractive crystals and thermal nonlinear liquids are a commonly used platform. Theoretical interest in the hydrodynamic properties of these systems was stimulated by the observation of quantised vortices in laser beams travelling through a cell filled with a slightly absorbing liquid [20–22]. Especially strong attention was revived towards solitonic structures. A soliton forms when dispersive effects are counterbalanced by the self-induced change

of the properties of the underlying medium, and appear in optics as self-trapped beams in the spatial (or pulses in the temporal) domain. In general, solitons appear in various fields of physics, such as water or atmosphere, plasmas, nonlinear optics, molecular chains or BECs and are of great interest due to their particle like features. Although self-trapping of optical beams was known since the early 1960s, most research on solitons in optics was devoted to 1D systems, i.e. optical pulses in fibres, where solitons may be described as solutions of an integrable 1D NLSE. The prediction and observation of 2D solitons in saturable nonlinear media [22, 24, 25] drew the attention towards higher dimensional systems, such as beams in a propagating geometry, that showed interesting new phenomena [26–30]. In photon fluids with defocusing nonlinear media, a spatial soliton is manifested by self trapping of dark beams or stripes, i.e. a region of zero intensity immersed in a high intensity background, where the diffraction is balanced by the self-defocusing (that corresponds to an effective self-focusing of the dark beam). Whereas bright solitons may form due to instabilities of plane waves in focusing media, dark solitons are generally different in the sense that they need a phase singularity or phase jump to be created in defocusing media [31].

The rich physics of 2D soliton dynamics was mainly studied in thermal media and photofrefractive crystals. Both systems exhibit a nonlocal nonlinearity, that is found in diffusive systems where the material response is not only dependent on the local intensity but also on the surrounding intensities. This induces a long range interaction that gives rise to new phenomena, such as attractive soliton-soliton interactions and the formation of bound states [32–34]. The build up of such a nonlinearity is non-instantaneous, i.e. the charge carriers in photofrefractive crystals need a finite time to build up the space-charge field that is required for the electro-optic effect and the same is true for thermal media, where the heating of the absorbed laser power induces the nonlinearity via the thermo-optic coefficient. Such media support incoherent solitons, i.e. self-trapping of beams that are both temporally and spatially incoherent [35, 36], which is understood by an averaging effect in the temporal and spatial domain of the non-instantaneous nonlocal nonlinearity.

Besides solitons, a deeper hydrodynamical viewpoint of beams in a propagating geometry was recognized in studies on the transverse patterns of strongly self-defocusing beams. These can be interpreted as dispersive shock waves, a fundamentally different type of shock waves compared to classical fluids, that in the absence of viscosity are regularized by dispersion rather than dissipation [37]. These were also found in BECs a few years earlier [38, 39], and gave a first experimental observation of superfluid effects in these kind of photon fluids. Dispersive shock waves are characterised by an oscillatory shock front that is understood as a spatial self-phase modulation resulting

from steep gradients of the transverse intensity profiles. In the nonlocal case, these shock waves appear without the characterstic oscillations due to the averaging effect of the nonlocal nonlinearity, but can be identified via spatial phase chirp singularities [40, 41]. These studies mainly used a photon fluid language in the sense that the dynamics were described in terms of the hydrodynamical analogue of the NLSE. In that perspective, solitonic structures as well as shock waves are phenomena that are described by nonlinear equations of motion in the transverse plane of the laser beam. Their respective amplitudes are large enough so that they are locally changing the properties of the background fluid. Few studies considered the linear aspects of the hydrodynamics, i.e. where small amplitude excitations can be treated as pertubations on a strong background fluid. Following the prediction of superfluidity for classical fluctuations in this system [12], it was shown through a wave turbulence mechanism, that a sea of random waves can undergo condensation into a coherent state, formally identical to Bose-Einstein condensation, but for classical waves [42]. Only recently, the dynamics of small amplitude excitations have been considered for studies of many-body physics [43–45], while very few experimental studies in bulk nonlinear media have been reported on the dynamical aspects of coherent linear photon fluid excitations. A quasi 1D analogue gravity model using the optical analogue of a Laval nozzle has been proposed [46, 47], but a fundamental investigation of the linear wave dynamics in these systems is still missing.

This thesis presents experimental studies on linear and nonlinear wave dynamics in a propagating geometry photon fluid with a thermal nonlinearity, and shows the applicability for analogue gravity studies.

Chapter 2

Thermally induced optical nonlinearity

The experiments presented throughout this thesis are conducted in materials that require large dimensions and relatively strong nonlinearities. An obvious choice are therefore liquids and solid materials that have strong thermal nonlinearities as these provide a large propagation speed of waves on top of the photon fluid and long dimensions that allow longer temporal evolution. This chapter presents techniques and results that characterise the optical nonlinear properties of these media.

2.1 Introduction

In linear optics, the interaction between an electromagnetic wave and a material is defined by the electronic structure of the medium and the frequency and polarisation of the electromagnetic field. The optical properties of the material are not altered by the presence of the light field as long as the electric field is weak enough to only induce a linear material response, i.e. the induced electric polarisation in a material is a linear function of the applied electric field. This linearity is no longer true for strong electric fields that lead to phenomena where the optical properties are modified by the presence of strong light fields. For instance, the refractive index of many materials depends on the intensity of the optical field and can be described by

$$n = n_0 + n_2 I \tag{2.1.1}$$

with the linear refractive index n_0 at room temperature and I is the time-averaged intensity of the optical field [48]. The nonlinear refractive index n_2 is a parameter that defines the strength at which the refractive index changes with optical intensity and depends on the nonlinear mechanism that is dominant for the used light field properties. These mechanisms can be of various physical nature such as electronic polarization, molecular orientation [49], saturated absorption [50] or thermal effects. The strength and temporal responses of those nonlinearities vary over orders of magnitudes, i.e from femtosecond response times for electronic polarization to milisecond response times for thermal effects [48]. On the other hand, the nonlinear refractive index for thermal effects is usually ten orders of magnitude larger than for Kerr nonlinearities and is the dominant effect for continuous wave (CW) lasers. The thermal effect arises due to a change of temperature in the material that is caused by the absorption of laser light that transfers energy from the absorbed laser power into heat, that will change the refractive index of the material through the thermo-optic coefficient $\beta = \frac{\partial n}{\partial T}$:

$$n(T) = n_0 + \frac{\partial n}{\partial T}\Delta T \tag{2.1.2}$$

β can be positive or negative and for most solids and liquids is of the order of $10^{-5} - 10^{-4} K^{-1}$. Laser beams with a gaussian profile that are propagating through such a material will imprint a spatial refractive index profile that will act as a lens and hence back react on the beam. This is called self-lensing [51]. Materials with positive coefficients possess a self-focusing, whereas negative coefficient materials possess a self-defocusing nonlinearity.

Furthermore, the laser induced heat in the material will result in temperature gra-

dients and eventually lead to heat diffusion currents inside the medium. This leads to a *nonlocal* nonlinearity, i.e. the refractive index $n(T)$ at any point in space is not only dependent on the local intensity, but also on the surrounding intensities [52, 53]. The physical processes that can lead to nonlocal nonlinearities are not limited to heat diffusion. Any kind of transport i.e. atomic diffusion in gases [24] and diffusion of charge carriers in photorefractive media [54] will lead to nonlocality. Also orientational nonlinearity of liquid crystals [55] and dipole-dipole interactions in Bose-Einstein condensates [56] are known to cause nonlocal interactions. In principle, nonlocality tends to average out the nonlinear effects of localized excitations, i.e. it introduces an additional length scale, below the nonlinearity is effectively suppressed [57]. Nonetheless, nonlinear phenomena are still observed in highly nonlocal systems where they have shown to support solitons [24] and furthermore it was shown that nonlocality prevents collapse and stabilises solitons also in (2+1)-dimensions [58, 59]. On another perspective, nonlocality in nonlinear optics adds a long range interaction between excitations as can be seen at interacting solitons where nonlocality changes the action from repulsive to attractive, depending on their initial distance [34, 60]. These long range interactions have also been found to play a crucial role in the formation of incoherent solitons through self-organisation in turbulent flows [61] and waveguiding in focusing nonlinear media [62, 63].

2.2 Nonlocal response function

Thermal nonlinearities are caused by heat from absorbed laser power that will lead to heat diffusion inside the material. This heat transport affects the nonlinear refractive index profile $\Delta n(x, y) \propto \Delta T(x, y)$ (Eq. (2.1.2)) and consequently does not follow the spatial beam profile (i.e. $\Delta n(x, y) \propto I(x, y)$). However, the relation between Δn and I can be calculated by solving the heat transport equation.

Assuming a sufficiently low absorption, so that the heat flow along the propagation direction z is negligible ($\nabla_\perp T \gg \nabla_z T$), allows to reduce the problem to the 2D heat transport equation:

$$(\rho_0 C)\frac{\partial \Delta T}{\partial t} - \kappa \nabla_\perp^2(\Delta T) = \alpha I \tag{2.2.1}$$

Here $(\rho_0 C)$ refers to the heat capacity per unit volume, κ is the thermal conductivity and α the linear absorption coefficient. In the low absorption regime, the change in intensity along z is assumed to be negligible at all times resulting in a constant source term αI, which is justified as long as thermal lensing effects are negligible. This equation can be solved as a boundary value problem, and hence with Eq. (2.1.2) the change in

refractive index at each point in space can be found. At steady state, i.e. $\partial\Delta T/\partial t = 0$, Eq. (2.2.1) reduces to

$$\nabla_\perp^2(\Delta T(r_\perp)) = -\frac{\alpha}{\kappa} I(r_\perp) \tag{2.2.2}$$

and with $\Delta n = \beta \Delta T$ to

$$\nabla_\perp^2(\Delta n(r_\perp)) = -\frac{\alpha\beta}{\kappa} I(r_\perp) \tag{2.2.3}$$

which is the two dimensional poisson equation with the formal solution

$$\Delta n(r_\perp) = -\frac{\alpha\beta}{\kappa} \int dr_\perp'^2 G(r_\perp, r_\perp') I(r_\perp') \tag{2.2.4}$$

where G is the Green's function for Eq. (2.2.2) obeying

$$\nabla_\perp^2 G(r_\perp, r_\perp') = \delta(r_\perp - r_\perp') \tag{2.2.5}$$

Finally, with $R(r_\perp, r_\perp') = -\frac{\alpha\beta}{\kappa\gamma} G(r_\perp, r_\perp')$ the thermal change of refractive index can be written as

$$\Delta n(r_\perp) = \gamma \int d^2 r_\perp' R(r_\perp, r_\perp') I(r_\perp') \tag{2.2.6}$$

where R is the so called nonlocal response function, that is to within a constant the Green's function of the heat transport equation and describes the spatial spreading of the nonlinear refractive index due to heat diffusion [64, 65]. The response function R obeys the conditions:

$$\nabla_\perp^2 R(r_\perp, r_\perp') = -\frac{\alpha\beta}{\kappa\gamma} \delta(r_\perp - r_\perp') \tag{2.2.7}$$

$$\int_{-\infty}^{+\infty} R(r_\perp) d^2 r = 1 \tag{2.2.8}$$

Therefore the shape of R is only dependent on the geometry of the sample and for given boundary conditions, these equations can be solved numerically to find an expression for R.

In the literature, the shape of the nonlocal response function is often approximated by an exponential decay of the form $R(r) \propto e^{-|r|/\sigma}$ [47] or gaussian function $R(r) \propto e^{-r^2/\sigma^2}$ [66]. This is valid as a first order approximation for diffusion like equations such as Eq. (2.2.2), however studies of the shape on the effects of modulational stabilities in defocusing media have shown that the modulational stability is sensitive to the shape of the nonlocal response [64]. Moreover, it is known that a nonlocal interaction leads to a modification of the dispersion relation of elementary excitations in BECs [67], giving rise to the existence of a roton minimum. Hence, the shape may have an influence on

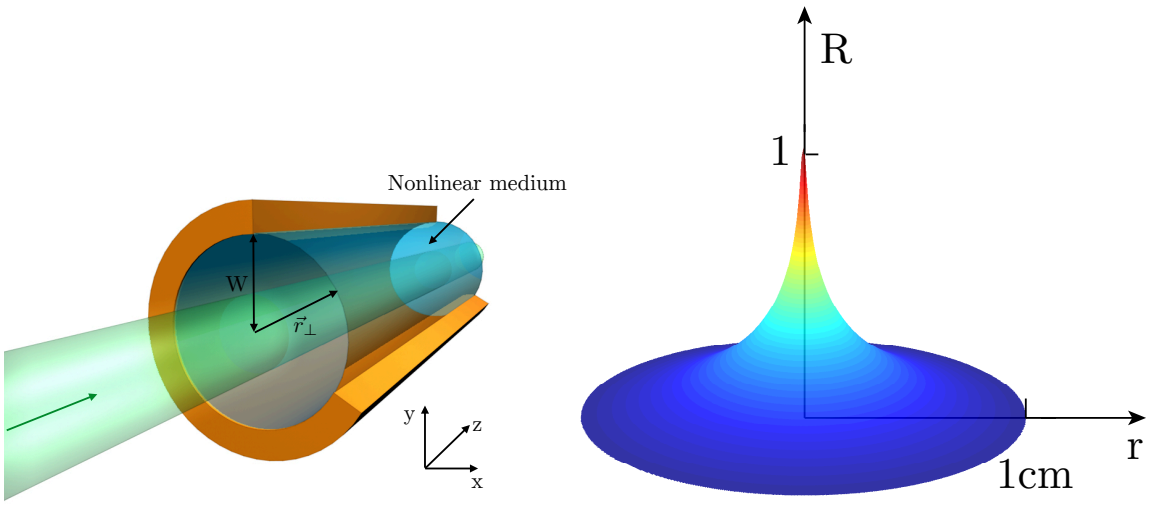

Figure 2.1: (a) Schematic of a beam propagating through the thermal nonlinear medium. (b) Numerical solution of Eq. (2.2.2) for the response function R using a gaussian beam with $w_x = w_y = 120\mu m$ and boundary dimensions $W = 1$ cm. The used material parameters are given in Table 2.1.

the excitation spectrum in the photon fluid with a defocusing nonlinearity (see Chapter 3). It is therefore important to derive an exact description of the nonlocal response in a cylindrical sample as shown in Fig. 2.1.

For boundaries at infinity in the transverse dimensions, the Fourier transform of Eq. (2.2.7) yields

$$\hat{R}(K) = \left(\frac{\alpha\beta}{\kappa\gamma}\right)\frac{1}{K^2} \tag{2.2.9}$$

$$R(r_\perp - r'_\perp) = -\left(\frac{\alpha\beta}{\kappa\gamma}\right)\frac{1}{2\pi}\ln(|r_\perp - r'_\perp|) \tag{2.2.10}$$

where $K = \sqrt{K_x^2 + K_y^2}$ denotes the transverse spatial momentum. However, Eq. (2.2.9) in real space and 2D is a logarithmic function which is very different from what would be expected from heat diffusion. That shows that in two dimensions boundaries have to be incorporated, in order to find a decaying function.

In a realistic scenario, the boundaries are located at a finite transverse distance W from the beam location and under the assumption that the width of the beam $w_{x,y} \ll W$, the system is shift invariant in $r_\perp = (x, y)$. We can then numerically find R by using a narrow gaussian beam $I(r_\perp) = I_0 e^{-2(x^2/w_x^2 + y^2/w_y^2)}$ to approximate the delta function and then use the pdetool in Matlab to solve Eq. (2.2.2) assuming that the temperature change at the boundaries is zero ($\Delta n(r_\perp = W) = 0$) with $W = 1$ cm. (see Fig. 2.1). This reveals a more realistic result than Eq. (2.2.10) predicted and provides a first estimation of the spatial extent of nonlocality for the given boundary conditions. The

width of the numerical solution can be defined by the FWHM, which is approximately $\sigma \approx 300$ μm and comparable to what was found in earlier studies [53]. Although, if σ is to be the determining parameter whether the nonlinear refractive index at a given point $\Delta n(x, y)$ is negligibly affected by a nearby intensity at a larger distance, then the slow decay and large spatial extent of R immediately shows that this is a poor definition. Therefore, an analytical solution with a physically relevant definition of the nonlocal length is necessary to accurately describe the thermal nonlinearity in the system.

2.3 Distributed loss model

The result of the response function for infinite space sample has shown that boundaries have to be included in a two dimensional modelling of the heat diffusion given by Eq. (2.2.1). Another way of including the effect of the boundaries is to introduce a loss term into the heat equation accounting for heat loss over an area proportional to the nonlocal length σ. This model will be termed in the following as *Distributed loss model* (DLM) and has been used to describe the transition from infinite to finite range nonlocalities in thermal media where σ was used as a free parameter to describe the formation and patterns of dispersive shock waves [40]. With this, the steady state heat equation extends to:

$$\nabla_\perp^2(\Delta T) = -\frac{\alpha}{\kappa} I(r_\perp) - \frac{1}{\sigma^2}\Delta T \tag{2.3.1}$$

With the addition of the loss term $\propto \Delta T/\sigma^2$. Then Eq. (2.2.7) for the Response function becomes:

$$\left(\nabla_\perp^2 - \frac{1}{\sigma^2}\right) R(r_\perp, r'_\perp) = -\frac{\alpha\beta}{\kappa\gamma}\delta(r_\perp - r'_\perp). \tag{2.3.2}$$

and again by Fourier transform, the K-space Response function reads:

$$\hat{R}(K) = \left(\frac{\alpha\beta\sigma^2}{\kappa\gamma}\right)\frac{1}{1+\sigma^2K^2} \tag{2.3.3}$$

The corresponding real space Response function equation has the form of a modified Bessel function of the second kind K_0 and is the analytical solution to Eq. (2.3.1):

$$R(r_\perp - r'_\perp) = \frac{1}{2\pi\sigma^2} K_0\left(\frac{r_\perp - r'_\perp}{\sigma}\right) \tag{2.3.4}$$

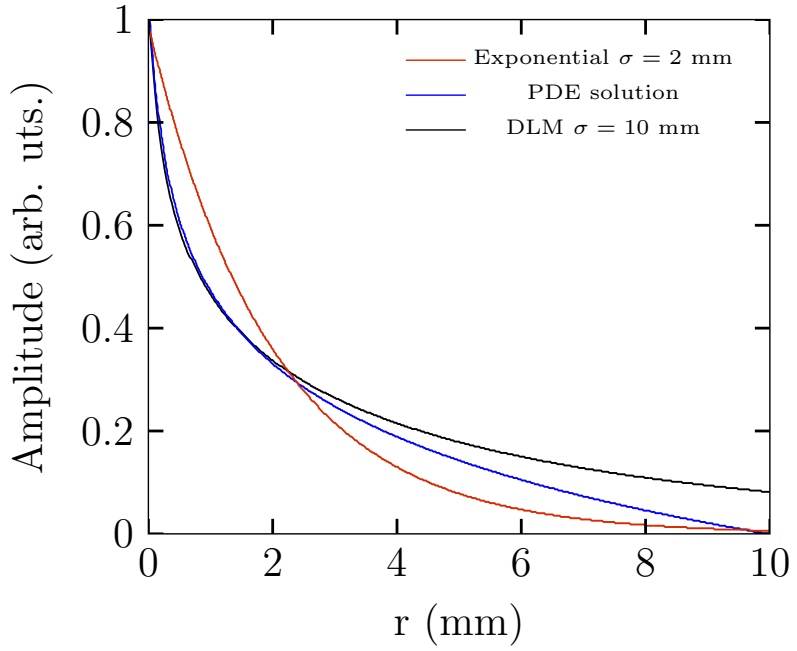

Figure 2.2: Comparison of radial profiles of the nonlocal response function $R(r_\perp)$. Numerical solution of Eq. (2.3.2) using an approximately delta like gaussian beam with $w_x = w_y = 120\mu m$ and boundary conditions W=10 mm. The analytical DLM solution has the form of a zeroth order Bessel function of the second kind (Eq . (2.3.4)) with a nonlocal length σ=10 mm which is identical to the sample radius W.

.

By comparing to the Fourier transform of Eq. (2.2.6): $\Delta\hat{n} = \gamma\hat{R}(K)\hat{I}(K)$ we can relate the model parameters and finally yield

$$\hat{R}(K) = \frac{1}{1+\sigma^2K^2} \tag{2.3.5}$$

with $\gamma = \frac{\alpha\beta\sigma^2}{\kappa}$. This is the Lorentzian response that is found for diffusion like transport mechanisms. Comparing the DLM solution Eq. (2.3.4) with the numerical solution of Eq. (2.2.7) we see that both curves are in good agreement and for the parameters chosen they slightly diverge for values greater than $r = 3$ mm (Fig. 2.2). It is also noted that the exponential decay $R \propto e^{-|x|/\sigma}$ used in earlier studies on nonlocal photon fluids [47] is valid as a first approximation with a width that is significantly smaller compared to the DLM solution. Therefore, when nonlocal length of different studies are compared, the particular form of the response function has to be taken into account. The nonlocal length obtained in the DLM model is identical to the sample dimensions $\sigma = 10$ mm and describes the response over short ranges accurately. This is confirmed by considering Eq. (2.3.1) under the approximation $\nabla^2(\Delta T) \approx -\Delta T/W^2$. This is

justified as the total temperature change over the sample radius W is on average ΔT:

$$\left(\frac{1}{\sigma^2} - \frac{1}{W^2}\right) \Delta T(r) = -\frac{\alpha}{\kappa} I(r) \tag{2.3.6}$$

Hence, for non-zero ΔT this identity holds true for any cylindrical $I(r)$ if $\sigma = W$. In conclusion, the result of the DLM model provides an analytical solution of the nonlocal response function and under cylindrical symmetry the nonlocal length is given by the radius of the boundaries.

2.4 Experimental characterisation of thermal nonlinearity

The previous section has presented the theoretical solutions of the 2D heat equation and has introduced the nonlocal response function, that is used to evaluate the transverse heat profile that is generated by a laser beam in a weakly absorptive medium. The following sections aims to experimentally quantify the thermal nonlinear properties of such a medium.

2.4.1 Experimental setup

A diode-pumped Nd:YAG continuous wave laser (Lighthouse Photonics) that operates with a frequency doubled output at $\lambda = 532$ nm with a maximum power of 7 W is used. Most photon fluid experiments require a large beam waist of a few mm up to cm so these high powers are needed to achieve intensities of a few W/cm^2. For a defocusing nonlinear medium, a dilute solution of graphene flakes in methanol is used, where the nanometer sized graphene flakes are added for absorption. Graphene's unique electronic band structure for monolayer flakes provides a strong absorption in the visible spectrum with negligible fluorescence [68] that makes it an ideal candidate to transform absorbed laser power into heat. Methanol (CH_3OH) is an optical transparent organic solvent with a strong negative thermooptic coefficient and is thus often used as a thermal nonlinear medium in combination with an absorbing additive. The nonlinear sample is a cylindrical copper cell with radius $W = 1$ cm and length $L = 13$ cm filled with the methanol/graphene solution. The input and output facets are 5 mm thick optical BK-7 windows with a standard antireflection coating for $\lambda = 350$ nm to 700 nm. The concentration of nanometric graphene flakes ($\sim$7 nm) is of the order 10^{-5} g/cm^3 (corresponding to 7×10^{14} flakes/cm^3 or ~ 0.05 ppm) in order to provide a weak absorption of around 20% along the length of the sample, which is weak enough to

ensure the slowly varying amplitude approximation.

	ρ (kg/m^3)	C_p (J/gK)	κ (W/mK)	n	$\partial n/\partial T$ (1/K)
Methanol	793	2.5	0.204	1.32	-4×10^{-4}
Water	1000	4.2	0.556	1.33	-1×10^{-4}
Lead Glass SF6	5180	0.389	0.673	1.81	1.4×10^{-5}

Table 2.1: Material properties of thermal nonlinear media. Parameters are density (ρ), specific heat capacity (C_p), thermal conductivity (κ), refractive index n and thermo-optic coefficient $\partial n/\partial T$. Data taken from [69, 70].

2.4.2 Spatial phase measurement technique

The following experiment is designed after the work from Minovich et al. [53] where the idea is to probe the thermal nonlinearity of a medium by measuring the change in optical path length $\Delta l = \Delta n \times L$ between two weak beams in a Mach-Zehnder Interferometer (Fig. 2.3). The nonlinear sample sits in one of the interferometer arms while a strong, parallel counter propagating pump beam is used to create the nonlinearity. Here, a set of beam splitters is used to split the laser beam into three components: pump, probe and reference beam. The probe and reference beam build up the interferometer, while the pump beam is separated beforehand and cross-polarized. This is necessary in order to reflect it off a polarizing beam splitter inside the interferometer. In this way, the pump beam is counter propagating to the probe beam. The probe and reference beam are orders of magnitude weaker in intensity than the pump beam so that the measured change in optical path length is solely attributed to the strong pump. The pump beam has a collimated narrow gaussian profile in order to recreate a δ-like shape to reproduce the conditions given by Eq. (2.2.6) and (2.2.7). In that case, the induced Δn profile is nearly identical to the nonlocal response function. In reality however one cannot choose a too narrow profile since the sample length has to be smaller that the Rayleigh range that guarantees a constant beam profile during propagation through the nonlinear medium. The narrow pump beam profile is created by contracting the beam with a 5:1 telescope ($f_1 = 500$ mm, $f_2 = 100$ mm) that results in a beam radius of $w = 120$ μm ($1/e^2$) with a Rayleigh range $z_R = \pi w^2 n_0/\lambda \approx 11$ cm inside the medium. The probe and reference beam are expanded with the opposite ratio ($f_3 = 50$ mm, $f_4 = 250$ mm). The change in optical path length Δl is a function of the relative phase change $\Delta\phi$ between probe and reference beam and hence, by measuring the phase of the probe

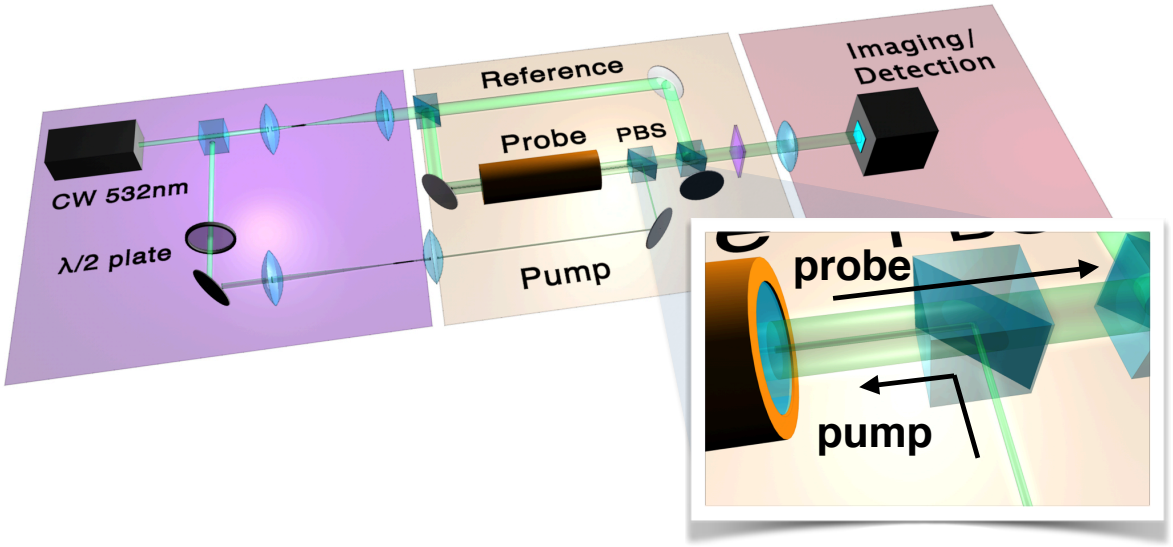

Figure 2.3: Experimental setup: A monochromatic laser beam is split into 3 components: pump, probe and reference beam. The strong pump induces a transverse heat profile that can be measured by a phase shift in the probe beam profile with respect to the reference beam. The pump is cross-polarized and counter propagating through the nonlinear sample with respect to the other beams. The output facet is imaged by a 4-f telescope onto the camera.

beam one is able to probe the nonlinearity $\Delta n(x, y)$:

$$\Delta n(x, y) = \frac{\Delta l(x, y)}{L} = \frac{\Delta \phi(x, y)}{2\pi} \frac{\lambda}{L} \tag{2.4.1}$$

The transverse phase profile $\phi(x, y)$ is measured by a technique known as Phase-shifting interferometry (PSI) [71] where the desired phase of a beam can be reconstructed by interference with a reference beam. This is done by recording the interference pattern onto a CCD, while changing the path length of the reference beam through a piezo-controlled translation stage (PZT), in order to record a set of N interferograms whose fringes are spatially equally shifted with respect to each other.
The intensity of a two beam interference pattern can be generally described as:

$$I_n(x, y) = I_0(x, y)\big(1 + V(x, y)\big[\cos\left(\phi(x, y) - \theta_n\right)\big]\big) \tag{2.4.2}$$

where I_0 is the beam intensity, V the fringe visibility and $\theta_n = \frac{2\pi}{N}(n-1)$ with $n = 1, 2, 3...., N$ an arbitrary reference phase that is varied at least over one period of the interference pattern by the PZT. Each I_n portrays one interferogram and the complete set of N interferograms is used to calculate the relative phase (see Fig. 2.4). Neglecting the coordinates and reformulate the cosine-function, each pixel in the transverse domain

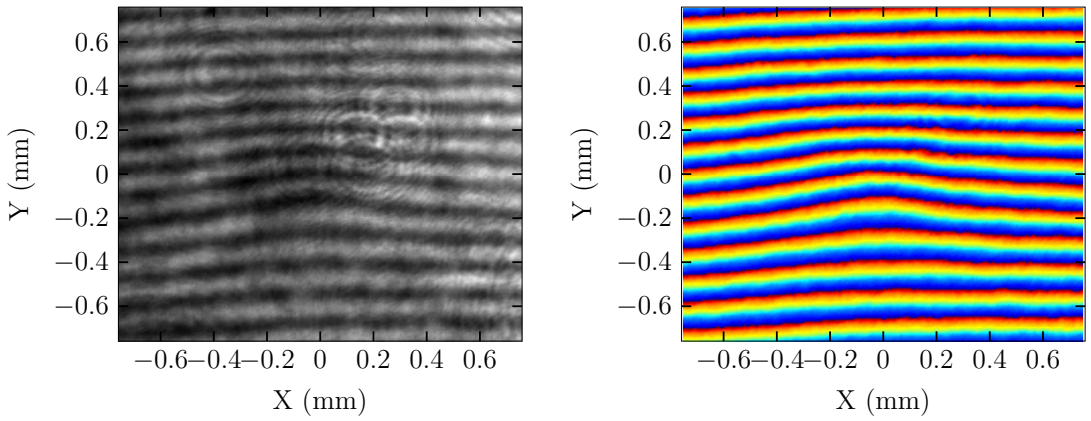

Figure 2.4: left: Example of one interferogram. The bending of the interference fringes in the centre is due to the heating of the pump beam (not visible). right: The corresponding spatial phase retrieved from Eq. (2.4.8)

can be represented as:

$$I_n = I_0(1 + V\cos\phi\cos\theta_n + V\sin\phi\sin\theta_n) \tag{2.4.3}$$

Now, by multiplying the equation by $\sin\theta_n$ and $\cos\theta_n$ and summing over n, we arrive at a set of two equations:

$$\sum_{n=1}^{N} I_n\cos\theta_n = \sum_{n=1}^{N} I_0(\cos\theta_n + V\cos\phi\cos^2\theta_n + V\sin\phi\sin\theta_n\cos\theta_n) \tag{2.4.4}$$

$$\sum_{n=1}^{N} I_n\sin\theta_n = \sum_{n=1}^{N} I_0(\sin\theta_n + V\cos\phi\sin\theta_n\cos\theta_n + V\sin\phi\sin^2\theta_n) \tag{2.4.5}$$

The first terms and the mixed terms on the right hand side are zero because of the orthogonality of the trigonometric functions. The only non-zero terms on the right hand sides are the ones with $\cos^2$ and $\sin^2$ functions. These simplify to

$$\sum_{n=1}^{N} I_n\cos\theta_n = I_0 V\frac{N}{2}\cos\phi \tag{2.4.6}$$

$$\sum_{r=1}^{N} I_n\sin\theta_n = I_0 V\frac{N}{2}\sin\phi \tag{2.4.7}$$

and finally we find a simple algorithm to process the measured I_n to calculate the phase $\phi(x, y)$:

$$\tan \phi(x, y) = \frac{\sum_{n=1}^{N} I_n(x, y) \sin \theta_n}{\sum_{n=1}^{N} I_n(x, y) \cos \theta_n} \tag{2.4.8}$$

2.4.3 Thermal nonlinearity at equilibrium

As a first approximation, the steady state heat equation with the distributed loss term predicts a nonlocal length σ that is approximately given by the radius W of the sample geometry (see Eq. (2.3.6)). The following results were measured by the technique described in the previous section, after the system has reached thermal equilibrium. This is true when the heating from the absorbed laser power and heat dissipation at the boundaries equalize. In this situation, the temperature inside the medium can be described by Eq. (2.2.2). Experimentally this is achieved by holding the laser power constant over 15 to 20 minutes before the taking any measurements. This will be confirmed by estimating the temporal heat diffusion in Section 2.4.4. The spatial phase difference $\Delta\phi(x, y)$ for two different powers is shown in Fig. 2.5. Here, the measured relative phase $\Delta\phi(x, y) = \phi(x, y) - \phi(x_0, y_0)$ is the difference between the phase at position (x,y) and at position (x_0, y_0) far away from the pump spot. In this case, this point was chosen at the boundaries of the field of view that is approximately at 8 mm distance from the pump spot. Although far away, the profile hasn't completely flattened out indicating a non-zero phase shift that will lead to a small error in phase amplitude. The corresponding cross-sections are shown in Fig. 2.6. Note that the amplitudes here are positive and normalised to one to allow to fit the spatial shape of the refractive index profile according to Eq. (2.2.6) using the DLM solution (Eq. (2.3.4)) with a single parameter σ. At low power ($P = 7.4$ mW, $I_0 \approx 32$ W/cm^2), an almost symmetric profile is observed that is well described by the solution of the DLM model with $\sigma \approx 10$ mm (blue curve).

There exists a small asymmetry along the y-axis due to convection currents that are antiparallel to the gravitational force. This effect is strong for high powers where a strong asymmetry in the heat profile is observed. At high laser powers, the heat at the pump spot induces strong temperature gradients that lead to pressure instabilities in the methanol solution and consequently results in convection currents inside the sample. This is an efficient transport mechanism that carries away the heat from the pump spot and influences the heat diffusion along the x-direction, narrowing the heat profile.

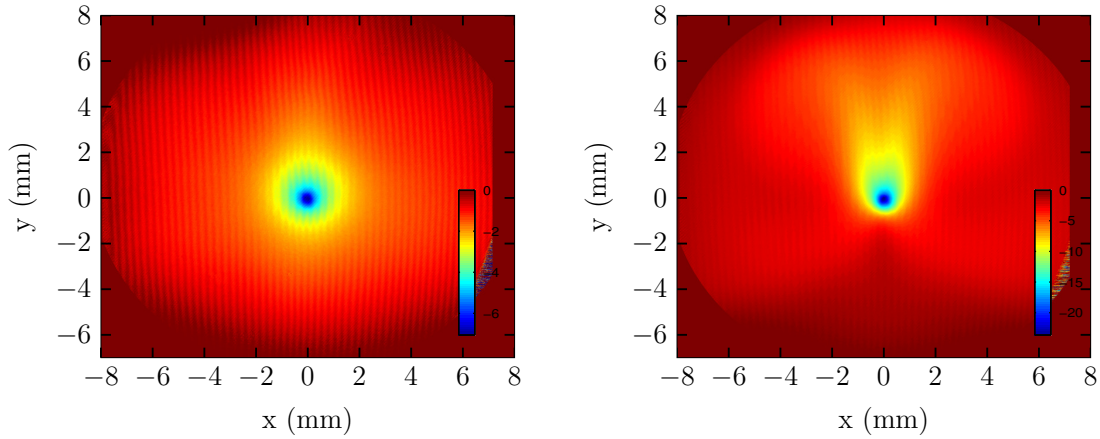

Figure 2.5: Spatial heat induced phase profile at steady state for low power (7 mW, left) and high power (38 mW, right) from a pump beam with 120 μm waist radius. High powers lead to convection currents that dominate the heat transport inside the sample leading to asymmetries in the phase profile. The colorcode shows Δn in 10^{-6} units.

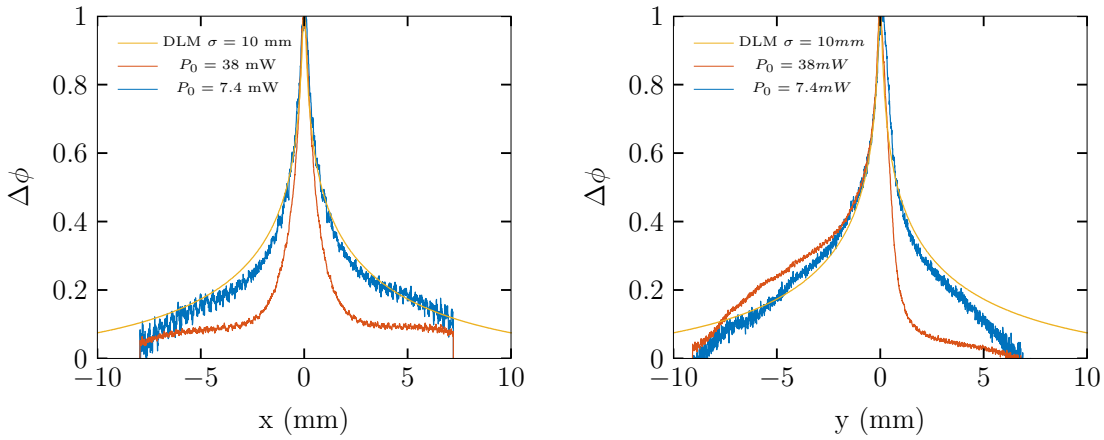

Figure 2.6: Cross-sections of phase profile shown in Fig. 2.5. The amplitude has been normalised to one in order fit the shape of the refractive index change according to Eq. (2.2.6) using the DLM solution (Eq. (2.3.4)) with a single parameter σ. At P=7 mW, the phase profile can be modelled with the DLM solution using a beam waist radius of $w = 120$ μm and nonlocal length $\sigma = 10$ mm. At P=38 mW, convection leads to asymmetric distortions in the heat profile.

2.4.4 Time dependent thermal nonlinearity

So far, the nonlocal nonlinearity has been described by the two-dimensional steady state heat equation (Eq. (2.2.2)). This is valid for weak absorption and as long as the system is in a dynamic thermal equilibrium with the environment, i.e the heating from the absorbed laser power equalises the losses at the boundaries. In this case, the

corresponding solutions for the spatial temperature profile can be accurately described by a convolution of the input beam profile with a nonlocal response function. In steady state, the nonlocal length σ is given by the smallest sample dimension which is 1 cm for the experimental samples shown here. However, for many photon fluid experiments, it is advantageous to have a control over the nonlocal length, since it determines the effective range of photon-photon interaction.

The nonlocal length is driven by heat diffusion and hence one can gain control over σ by controlling diffusion. One option is to use the build up time of diffusion currents after the laser is switched on. An estimate of the diffusion time scales can be calculated by neglecting the source term in Eq. (2.2.1):

$$(\rho_0 C)\frac{\partial \Delta T}{\partial t} = \kappa \nabla_\perp^2(\Delta T) \tag{2.4.9}$$

and approximate the temporal $\partial \Delta T/\partial t \approx \Delta T/t_d$ and spatial derivatives $\nabla_\perp^2(\Delta T) \approx \Delta T/W^2$ so that:

$$t_d \approx \frac{\rho_0 C}{\kappa} W^2 \tag{2.4.10}$$

For most liquids the heat capacity is $\rho_0 C \approx 2 \times 10^6 J/(m^3 K)$ and the thermal conductivity $\kappa \approx 0.2 W/(mK)$ and using a radius of W=10 mm, the diffusion time becomes $t_d \approx 1000$ s or 17 minutes. So for a cylindrical sample with 1 cm radius it takes approximately 17 minutes until dynamic thermal equilibrium is achieved. Setting $W \approx \sigma$ one arrives at an expression for the temporal evolution of the nonlocal length over time:

$$\sigma \approx \sqrt{\frac{\kappa}{\rho_0 C} t} \tag{2.4.11}$$

This result essentially tells us that one can achieve nonlocal lengths of a few hundred of microns by performing experiments a few seconds after the laser illuminates the sample. To study the temporal evolution, transients can be measured by setting the camera to video mode and triggering the start with a photodiode. As soon as the laser shutter opens, the camera starts recording with a set frame rate and exposure time. This procedure is repeated at least four times for each measurement, while in each step the PZT is moved by a fraction of the laser wavelength in order to shift the interference pattern (PSI technique). To calculate the nonlinear phase change $\Delta\phi(x, y, t)$, one has to subtract a reference phase (i.e. one at low power) or as in this case the phase at $t = 0$: $\Delta\phi(x, y, t) = \phi(x, y, t) - \phi(x, y, 0)$. The relative phase change is then translated into a change of refractive index according to Eq. (2.4.1).

The temporal change of refractive index over time and corresponding lineouts are shown in Fig. 2.7. Here, a total pump power of $P_0 = 7.7$ mW was used with a beam waist

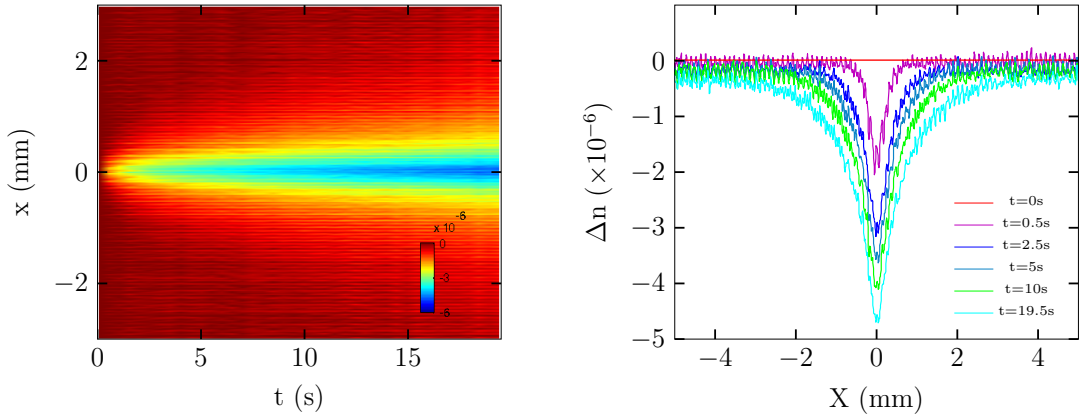

Figure 2.7: Time dependent measurement of the nonlinearity according to Eq. (2.4.1) at P=7.7 mW. left: the color code shows the relative decrease in refractive index over time due to laser induced heating of the medium. right: the lineouts taken from the left hand plot for selected times.

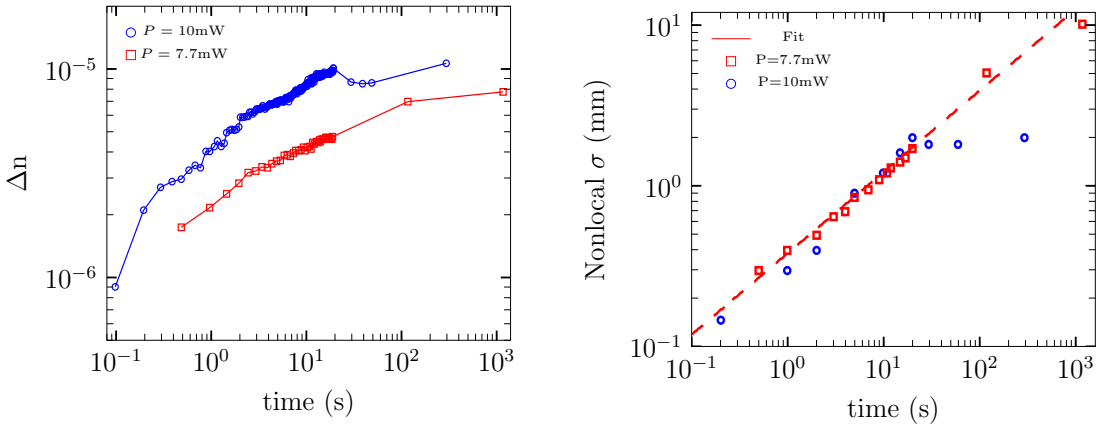

Figure 2.8: Time-dependent thermal nonlinearity in methanol/graphene for pump powers $P = 7.7$ mW (blue) and $P = 10$ mW (red) with a pump beam waist radius $w = 131$ μm. left: Peak nonlinearity $\Delta n(x = 0, t)$, right: nonlocal length $\sigma(t)$ extracted from fitting lineouts of the spatial heat profiles (see Fig. 2.7) with the DLM solution of the nonlocal response function. The fit shows $\sigma(t) = a\sqrt{t}$, with $a = 3.85 \times 10^{-4}$ $m/s^{-1/2}$ in line with the expectation value for methanol $a_M = 3.21 \times 10^{-4}$ $m/s^{-1/2}$.

radius of $w = 131$ μm. To quantify the nonlocal length, the lineouts are normalised to one and fitted with Eq. (2.2.6) using the steady state DLM response function. Although the system is not at equilibrium, this solution is used to provide a comparison to the result of the steady state heat profile at thermal equilibrium. It will be later shown that this is a valid approach. The results in Fig. 2.7 show the build up of the nonlinearity over a 20 s time frame and as can be seen after 20 s it has reached almost $\Delta n = 5 \times 10^{-6}$.

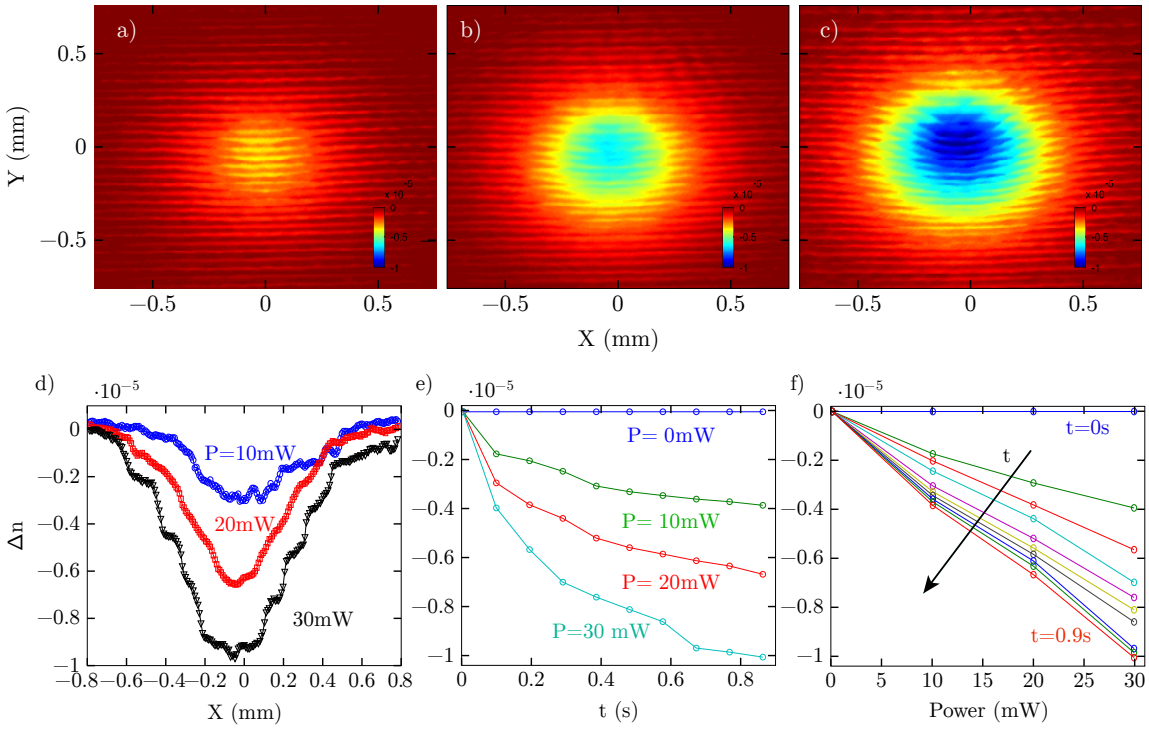

Figure 2.9: Time-dependent thermal nonlinearity in methanol/graphene for short times (< 1 s) and different pump powers with a pump beam waist radius $w = 131$ μm. (a)-(c) thermally induced refractive index profiles after 0.9 s at a) P=10 mW, b) P=20 mW and c) P=30 mW. (d) Corresponding lineouts $\Delta n(x, y = 0, t = 0.9s)$. (e)-(f) Peak nonlinear refractive index $\Delta n(x = 0, y = 0, t)$ as a function of time and power. Δn is linearly proportional to the used power in the measured time window.

The peak nonlinearity $\Delta n(x = 0, t)$ and the nonlocal length $\sigma(t)$ is plotted in Fig. 2.8 for two laser powers. At P=7.7 mW, the nonlinearity steeply increases until it starts to saturate around $\Delta n \approx 8 \times 10^{-6}$ after $t = 10^2$ s. At slightly larger power P=10 mW, the increase is abruptly capped after $t \approx 10$ s at around $\Delta n \approx 10^{-5}$. This cannot be explained by an intensity drop due to self-defocusing of the pump beam as it would lead to a much larger refractive index profile and thus to an increase in the nonlocal length. In fact, a small decrease of the nonlocal length is observed, where around $t \approx$10 s the build up is stopped and the nonlocal length saturates at $\sigma =$2 mm. This effect may be therefore attributed to the onset of convection currents inside the medium that carry away the heat and thus stop the further temperature build up. This is in line with the observation in Fig. 2.6, where the heat profile at much larger power P=38mW in the x-direction is strongly narrowed due to convection inside the sample.
Nevertheless, at $P = 7.7$ mW (red squares), the transient build up is well described by a square root function $\sigma(t) = a\sqrt{t}$, with $a = 3.85 \times 10^{-4} m/s^{-1/2}$ being a fitting parameter. Note that for material parameters of methanol $\sqrt{\kappa/(\rho_0 C)} = 3.21 \times 10^{-4} m/s^{-1/2} = 0.83a$

and the result is in good agreement with the expectation value.

Of particular interest is the millisecond time scale below one second as it provides nonlocal lengths below 500 μm which is of importance for experiments presented in Chapter 5 that use the temporal build up to tailor the nonlocality. Fig. 2.9 shows the transient build up of the nonlinearity for different laser powers up to 1 s after opening of the laser shutter. The spatial profiles of the refractive index change reveal a symmetric geometry at all powers and the respective lineouts show a linear increase of the nonlinearity with intensity. This is confirmed by Fig. 2.9e) and f), where the peak nonlinearity as a function of time and power is shown. At all times, the nonlinearity is approximately a linear function of the used power.

As mentioned earlier, the time dependent nonlocal length σ has been evaluated so far on the basis of solution of the steady state heat equation with effective boundaries for comparison at the expense of accuracy on the shape of the nonlocal response. To verify that this is a valid approach, one has to find a solution to the time dependent heat equation (Eq. (2.2.1)) and calculate the temperature profile for a given time. The time dependent solution has been reported in studies on thermal lensing assuming a weakly absorbing medium with infinite boundaries [72, 73]. For a gaussian intensity profile $I(r) = \frac{2P_0}{\pi w^2} \exp\left(-2r^2/w^2\right)$ it is given by:

$$\Delta T(r,t) = \frac{2P_0\alpha}{\pi C\rho w^2} \int_0^t \left(\frac{1}{1+2t'/t_c}\right) \exp\left(\frac{-2r^2/w^2}{1+2t'/t_c}\right) dt' \tag{2.4.12}$$

where $t_c = \frac{w^2 C\rho}{4\kappa}$ is the characteristic diffusion time and apart from a factor 4 is identical to Eq. (2.4.11). The temperature profiles are calculated for the first 20 s using the experimental parameters from above and are plotted at two selected times $t = 2$ s and $t = 20$ s in Fig. 2.11. Note that the profiles are normalised to unity to compare the spatial width. As can be seen, the shape from the solution of the temporal heat equation (green) and the one from the DLM model are almost identical confirming the experimental results and model very well.

In conclusion, the temporal build up of the thermal nonlinearity in a weakly absorbing methanol/graphene solution was measured with a time resolved phase-shifting interferometric technique. The results were compared to an analytical solution of the time dependent heat diffusion equation and are qualitatively in very good agreement. The spatial profile of the heat induced refractive index could be well recovered by the theoretical model, however a discrepancy of the magnitude of the nonlinear index of about a factor three was observed. This might be due to an intrinsically underlying assumption that the absorption in the medium is homogeneously distributed. In the experiment, the absorption is mainly due to the graphene particles that display localised regions of

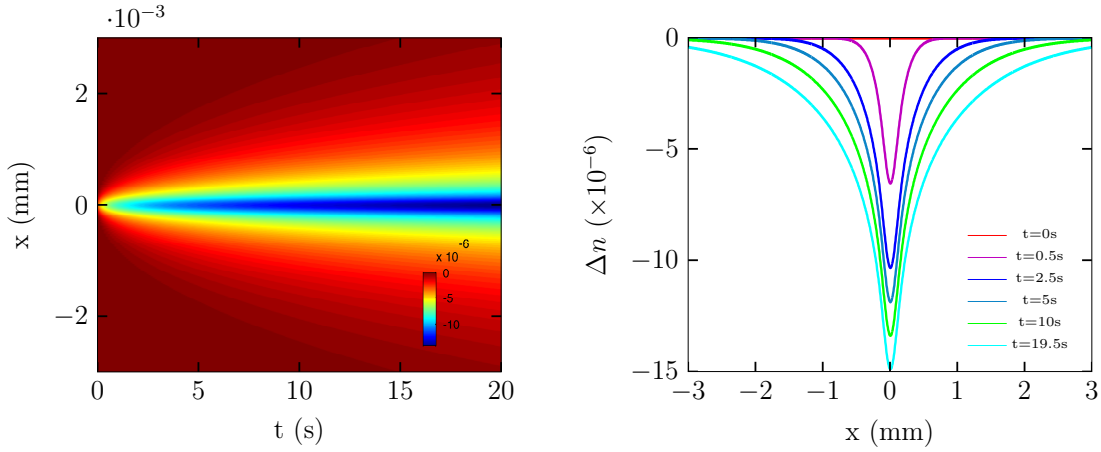

Figure 2.10: Transient build up of the thermal nonlinearity obtained by integration of the analytical solution (Eq. (2.4.12)) to the heat equation. Parameters taken from the experiment: absorption $\alpha = 0.017cm^{-1}$, beam radius $w = 131$ μm, Power P_0=7.7 mW.

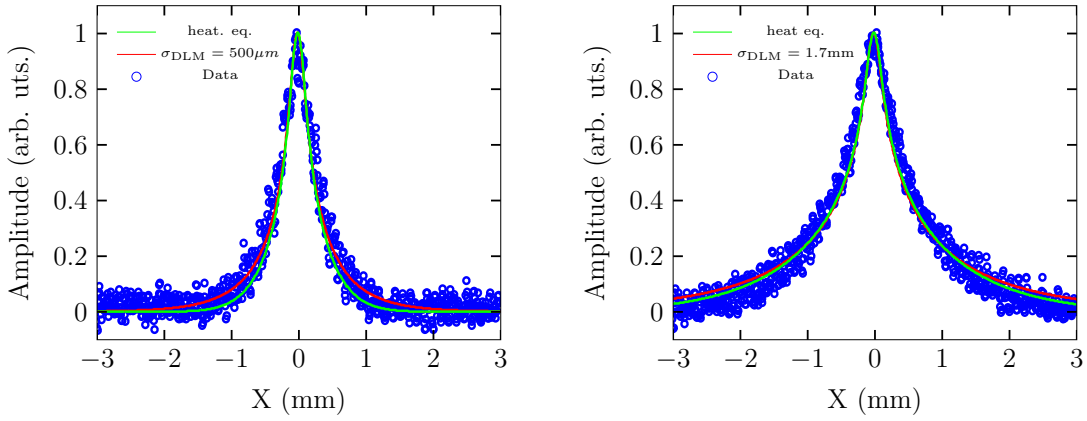

Figure 2.11: Comparison between DLM model and time dependent heat equation: The data (blue circles) shows the normalised amplitude of the measured spatial temperature profile at $t = 2$ s (left) and $t = 20$ s (right) for input power $P = 7.7$ mW. The green curve shows the temperature profile according to Eq. (2.4.12) and the red curve from Eq. (2.2.6) using the response function from the DLM model. All results were obtained using a beam waist radius of $w = 131$ μm.

high absorption in contrast to very low absorption in the pure methanol. This might lead to a less efficient heat build up in the medium that is reflected in the refractive index change and needs further investigation. With this it is possible to monitor the change in refractive index as well as the nonlocal length over time which are the defining parameters in a nonlocal thermal medium and therefore display a full characterisation of the thermal nonlinearity.

Chapter 3

Photon fluid - characterisation

This chapter presents the concepts and techniques of how waves propagate on a photon fluid. The study of elementary excitations provides crucial insights into the dynamics of many body quantum fluids and is therefore of paramount importance. It is shown by experimental techniques that these follow the Bogoliubov dispersion relation for superfluids. The wave kinematics are directly linked to the properties of the fluid itself and are therefore an elegant way of characterising the photon fluid. The results presented in here were published in "Experimental characterisation of nonlocal photon fluids", Optica (2015) [57].

3.1 The Nonlinear Schrödinger Equation

A fluid of light, or photon fluid, is a term widely used to describe a gas of photons, i.e. the many weakly interacting photons forming a laser beam in an optical nonlinear medium. This is a many body problem of weakly interacting bosons and it has been shown that the collective macroscopic dynamics are governed by a nonlinear Schrödinger equation (NLSE) [22, 24, 74].
The physical system that is described throughout this thesis considers a monochromatic CW laser beam that is propagating inside an optical nonlinear medium. Here it will be outlined how in classical nonlinear optics, the nonlinear Schrödinger equation follows from the paraxial approximation of the electromagnetic wave equation. Considering a monochromatic wave of frequency ω and neglecting the polarization degree of freedom for simplicity, the propagation of the electric field

$$\tilde{E}(\vec{r},t) = E(\vec{r})e^{i\omega t} + E^*(\vec{r})e^{-i\omega t} \tag{3.1.1}$$

in a dispersive, isotropic medium with a nonlinear polarization can be described by the nonlinear wave equation [48, 75]:

$$\nabla^2\tilde{E}(\vec{r},t) - \frac{\epsilon_r(\omega)}{c^2}\frac{\partial^2}{\partial t^2}\tilde{E}(\vec{r},t) = \frac{1}{\epsilon_0 c^2}\frac{\partial^2}{\partial t^2}P_{NL}(\vec{r},t) \tag{3.1.2}$$

with the linear dielectric permittivity ϵ_r, the vacuum dielectric permittivity ϵ_0 and the nonlinear polarization with a third-order nonlinear susceptibility $\chi^{(3)}$:

$$P_{NL}(\vec{r},t) = \epsilon_0\chi^{(3)}\tilde{E}(\vec{r},t)^3 \tag{3.1.3}$$

Introducing Eq. (3.1.1) into Eq. (3.1.2) and keeping the parts of the nonlinear polarization that will influence the propagation of the beam, i.e. neglecting the third harmonic terms, equation (3.1.2) can be reduced to the stationary equation:

$$\nabla^2 E(\vec{r}) + \frac{\omega^2}{c^2}\epsilon_r(\omega)E(\vec{r}) = -3\frac{\omega^2}{c^2}\chi^{(3)}|E(\vec{r})|^2E(\vec{r}) \tag{3.1.4}$$

This equation describes the evolution of the complex amplitude of the electric field in a nonlinear Kerr-type medium. To arrive at a useful description for a directed laser beam, only solutions are considered whose amplitudes only slowly change along the propagation (z- or k_0-) direction (*slowly varying amplitude approximation*) and where wave propagation is limited to within a small angle from the propagation direction

(*paraxial wave approximation*).

$$E(r_\perp, z) = E_0(r_\perp, z)e^{ik_0 z} \tag{3.1.5}$$

The variation of the amplitude $E_0(r_\perp, z)$ along z is negligible with respect to the optical wavelength and by reinstating Eq. (3.1.5) into Eq. (3.1.4) one can neglect the second order derivative ($\frac{\partial^2}{\partial z^2}E_0(r_\perp, z) \approx 0$) and with $k_0 = \frac{\omega}{c}\sqrt{\epsilon_r(\omega)} = \frac{\omega n_0}{c}$ one arrives at an equation for the complex electric field amplitude in the form of a nonlinear Schrödinger equation (NLSE) [48]:

$$\frac{\partial}{\partial z}E_0(r_\perp, z) = \frac{i}{2k_0}\nabla_\perp^2 E_0(r_\perp, z) + \frac{3}{2}\frac{ik_0}{n_0^2}\chi^{(3)}|E_0(r_\perp, z)|^2 E_0(r_\perp, z) \tag{3.1.6}$$

Although it was derived here in the context of nonlinear optics, this form of equation is found in many fields in physics, i.e. it is used to study small amplitude gravity waves in fluids and it is identical to the Gross-Pitaevskii equation for quantum fluids such as Bose-Einstein condensates and liquid helium. In a similar form it also appears in the Ginzburg-Landau theory for superconductors. Essentially, it describes the propagation of slowly varying wave packets in dispersive, weakly nonlinear media. In optics, it is used to describe nonlinear beam propagation in optical nonlinear media. The first term on the right hand side of Equation (3.1.6) describes the diffraction whereas the latter, nonlinear term describes the interaction of the beam with itself, i.e. depending on the sign of the $\chi^{(3)}$ it will be either an attractive or repulsive interaction.
It is convenient to write the self-interaction term in Eq. (3.1.6) in a more simpler form by introducing the nonlinear change in refractive index $\Delta n = n_2 I$ with $n_2 = \frac{4}{3n_0^2\epsilon_0 c}\chi^{(3)}$ and the intensity $I = \frac{1}{2}\epsilon_0 n_0 c|E|^2$. With this the NLSE becomes:

$$\frac{\partial}{\partial z}E_0(r_\perp, z) = \frac{i}{2k_0}\nabla_\perp^2 E_0(r_\perp, z) + \frac{ik_0\Delta n}{n_0}E_0(r_\perp, z) \tag{3.1.7}$$

The derivation shown here considers a Kerr type nonlinearity in the sense that the refractive index of the medium will depend on the square of the applied electric field. Such a nonlinearity must not necessarily arise from electronic polarization according to Eq. (3.1.3), but is also found for example for photorefractive effects, where the nonlinearity is a result of an optically induced space-charge electric field, or thermal nonlinearities that arise through heat from absorbed laser power. Especially in the case for thermal nonlinearities the resulting nonlinear response is determined by the thermal properties of the material and will often depend on heat diffusion that adds a level of complexity in evaluating the temporal and spatial shape of the nonlinear term as was

shown in the previous Chapter. In the nonlocal case, the parameter Δn in the NLSE is given by Eq. (2.2.6).

3.2 Hydrodynamical analogue

A laser beam propagating in a Kerr nonlinear medium is governed by the Nonlinear Schrödinger equation. Here, it will be shown that by reformulating the NLSE it is possible to describe the transverse beam profile as a fluid. In the paraxial approximation, we start from the electric field E_0 propagating along the z-direction described by the nonlinear Schrödinger equation (Eq. (3.1.6)):

$$\frac{\partial}{\partial z}E_0(r_\perp, z) = \frac{i}{2k_0}\nabla_\perp^2 E_0(r_\perp, z) + \frac{ik_0\Delta n}{n_0}E_0(r_\perp, z)$$

where $k_0 = 2\pi n_0/\lambda$ is the optical wave vector and $\Delta n = -n_2|E|^2$ a self-defocusing nonlinearity, that guarantees modulational stability of the beam. By using the well known Madelung transformation from quantum mechanics, one can write the electric field as:

$$E_0(r_\perp, z) = \sqrt{\rho(r_\perp, z)}e^{i\phi(r_\perp, z)} \tag{3.2.1}$$

where ρ is the fluid density and phase ϕ. Additionally, the propagation direction z is mapped into a time coordinate $t = zn_0/c$ (c: speed of light) and by splitting the NLSE into real and imaginary part one arrives at a set of hydrodynamical equations [17].

$$\partial_t\rho + \nabla(\rho v) = 0 \tag{3.2.2}$$

$$\partial_t\psi + \frac{1}{2}v^2 + \frac{c^2 n_2}{n_0^3}\rho - \frac{c^2}{2k^2 n_0^2}\frac{\nabla^2\sqrt{\rho}}{\sqrt{\rho}} = 0 \tag{3.2.3}$$

The first equation is a continuity equation that describes the mass conservation whereas the latter is the Euler equation, describing a flow $\vec{v} = c/kn_0)\nabla\phi = \nabla\psi$ of an incompressible fluid with density ρ. The repulsive interaction that leads to the bulk pressure $P = c^2 n_2\rho^2/2n_0^3$ is given by the optical nonlinearity that defines a local speed of sound:

$$c_s^2 = \frac{\partial P}{\partial\rho} = \frac{c^2 n_2\rho}{n_0^3} \tag{3.2.4}$$

The last term in Eq. (3.2.3) is the so called quantum pressure that does not have an analogy in real fluids. In quantum fluids it arises from the uncertainty principle, i.e. a local compression of the condensate or fluid leads to a decrease of the delocalisation of particles Δx. Since the uncertainty principle dictates therefore an increase in the particles momenta Δp, the quantum pressure opposes any stretching or contraction

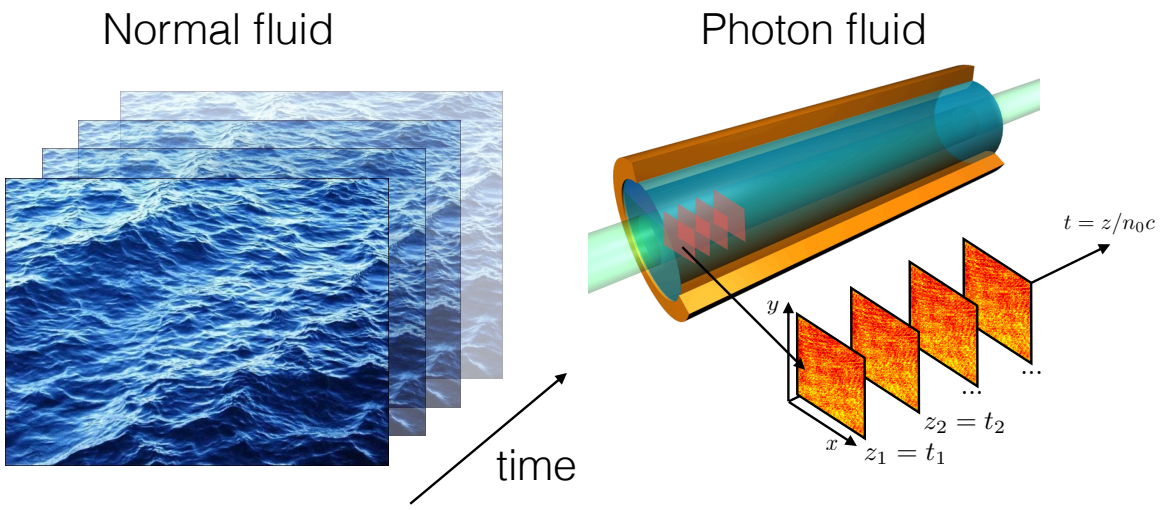

Figure 3.1: Hydrodynamical analogue: The transverse profile of a laser paraxially propagating through a nonlinear defocusing medium can be described by a set of hydrodynamic equations, describing the flow of an incompressible fluid, while the z-axis maps into a time axis. Hence, the temporal evolution of the photon fluid can be observed along the propagation of the laser beam.

of the condensate over distances of the healing length. The quantum pressure can be neglected on macroscopic length scales, i.e. when the density is only slowly changing, however, it starts dominating the dynamics in regions of rapidly changing density. It appears in optics as a result from diffraction which is due to the wave nature of light. These equations describe the transverse profile of a laser beam as a (2+1) dimensional fluid, where the the fluid density $\rho(r_\perp)$ is controlled by the laser intensity and the flow is controlled by the spatial phase gradient. This propagating geometry is therefore a simple and straight forward implementation of a photon fluid.

3.3 Bogoliubov dispersion relation

As seen in the previous section, the transverse beam profile is described by a set of hydrodynamical equations, so the fluid is realised by setting a constant intensity that excites the nonlinearity. The question is now how small perturbations on top of a constant background will propagate. This can be deduced by linearising Eq. (3.2.2) and (3.2.3) by means of first order fluctuations around a background solution i.e. $\rho = \rho_0 + \rho_1$ and $\vec{v} = \vec{v_0} + \vec{v_1}$, where $\rho_1 \ll \rho_0$ and $\vec{v}_1 \ll \vec{v}_0$. Assuming the background density is constant and background flow is zero, i.e. $\vec{v}_0 = 0$, the continuity and Euler equation

can be expressed as

$$\partial_t \rho_1 + \rho_0 \nabla_\perp \vec{v}_1 = 0 \tag{3.3.1}$$

$$\partial_t \vec{v}_1 + \vec{v}_1 \nabla_\perp \vec{v}_1 + \frac{c^2 n_2}{n_0^3} \nabla_\perp \rho_1 - \frac{c^2}{2k^2 n_0^2} \nabla_\perp \left(\frac{\nabla_\perp^2 \sqrt{\rho}}{\sqrt{\rho}} \right) = 0 \tag{3.3.2}$$

Here, the spatial derivative of Eq. (3.2.3) was taken to obtain the second equation. Now, the second term in Eq. (3.3.2) is a linear function in $\vec{v}_1$ and can be neglected. By straight forward expansion of the last term one arrives at:

$$\partial_t \vec{v}_1 + \frac{c^2 n_2}{n_0^3} \nabla_\perp \rho_1 - \frac{c^2}{2k^2 n_0^2} \nabla_\perp \left(\frac{\nabla_\perp \rho_1}{4\rho_0^2} + \frac{\nabla_\perp^2 \rho_1}{2\rho_0} \right) = 0 \tag{3.3.3}$$

The wave equation for small density pertubations can then be obtained by taking the time derivative of Eq. (3.3.1) and inserting Eq. (3.3.3), where the first term in the brackets can be neglected since it contains higher order of ρ_0 in the denominator. Finally one gets:

$$\partial_t^2 \rho_1 - \frac{c^2 n_2 \rho_0}{n_0^3} \nabla_\perp^2 \rho_1 + \frac{c^2}{4k^2 n_0^2} \nabla_\perp^4 \rho_1 = 0 \tag{3.3.4}$$

Note that this reduces to the equation of motion for sound waves with the speed of sound $c_s^2 = \frac{c^2 n_2 \rho}{n_0^3}$, when the higher order terms arising from the quantum pressure ($\propto \nabla^4 \rho_1$) are neglected. It is here explicitly derived for the density, however the same form of equations can be derived for the velocity $\vec{v}_1$ or velocity potential ψ_1. The perturbations can be treated as plane wave solutions of the form [17, 76]:

$$\rho_1 = u e^{i(\vec{K}\vec{r} - \Omega t)} + v^* e^{i(\vec{K}\vec{r} + \Omega t)} + c.c. \tag{3.3.5}$$

where u and v are complex amplitudes with a temporal frequency Ω and transverse mode K-vector $\vec{K} = (K_x, K_y)$ that satisfy the Bogoliubov dispersion relation:

$$(\Omega - \vec{v}\vec{K})^2 = \frac{c^2 n_2 \rho_0}{n_0^3} K^2 + \frac{c^2}{4k^2 n_0^2} K^4 \tag{3.3.6}$$

Using the optics terminology, note that $\Omega = \frac{c}{n_0} K_z$ is the frequency in the photon fluid time variable $t = z n_0 / c$, with K_z the longitudinal wave vector component of the perturbation. In the hydrodynamical analogue, this dispersion describes a linear relationship between frequency and wave vector $\Omega \propto K$ for small wave vectors, hence the sound modes follow a phononic dispersion and a quadratic relationship $\Omega \propto K^2$ for large wave vectors, that is characteristic for a single-particle dispersion. The small momentum excitations can be understood as collective sound modes propagating at the speed of sound

given by Eq. (3.2.4). The linear dispersion of collective excitations is a characteristic of superfluidity, as it defines a critical Landau velocity (see Chapter 4). The excitations with large momenta are understood as excited particles, propagating at high speed undisturbed through the fluid. Both are separated by a characteristic length scale, the so-called healing length ξ, that is fixed by the balance between the interaction energy and quantum pressure, or in optics terminology, between the nonlinear interaction and linear diffraction. It is calculated by equating the two terms in Eq. (3.3.6):

$$\xi = \frac{\lambda}{2\sqrt{n_0 n_2 \rho_0}} \tag{3.3.7}$$

The term healing length arises from the BEC literature where it defines the minimum distance over which the order parameter Ψ heals from 0 to the constant density of the condensate. For example, the typical size of quantized vortices are given by the healing length.

It needs to be stressed that Eq. (3.3.6) can be derived by linearising the NLSE without the "detour" through the hydrodynamic equations [12, 43]. In this case the notation for the density changes to $\rho_0 = |E_0|^2$. Both notations are identical, but $|E_0|^2$ will be used since it appears later as an experimental parameter. However, it is the Euler equations (Eq. (3.2.2) and (3.2.3)) where the hydrodynamics analogy becomes visible, that further provide a useful link to gravitational analogues [17, 77].

So far, a local nonlinearity $\Delta n = -n_2|E|^2$ was used and therefore the interactions involved are local, or short ranged. In this case, the dispersion derived above for small amplitude excitations is identical to those found in dilute non-polar BECs. When dealing with thermal nonlinear media, the nonlinearity becomes highly nonlocal that effectively leads to long range interactions and as will be shown next, this strongly affects the dispersion relation. Considering the NLSE with a nonlocal nonlinearity of the form $\Delta n(r_\perp) = \gamma \int d^2 r'_\perp R(r_\perp, r'_\perp) I(r'_\perp)$, a straight forward extension of the Bogoliubov theory leads to a modified dispersion of the form [47, 67]:

$$(\Omega - \vec{v}\vec{K})^2 = \frac{c^2 n_2 |E_0|^2}{n_0^3} \hat{R}(K, n_0\Omega/c) K^2 + \frac{c^2}{4k^2 n_0^2} K^4 \tag{3.3.8}$$

where $\hat{R}$ is the Fourier transform of the nonlocal response function. The dependence on the rescaled frequency $K_z = n_0\Omega/c$ is negligible since in the paraxial approximation $K \gg K_z$ and the main contribution of the nonlocal response is along the transverse dimensions. Therefore, in the example of a thermal nonlinearity described in the limits of the DLM model, the response function can be simplified to $\hat{R}(K, 0) = 1/(1 + \sigma^2 K^2)$. This is the Lorentzian response function in the two-dimensional K-space with the non-

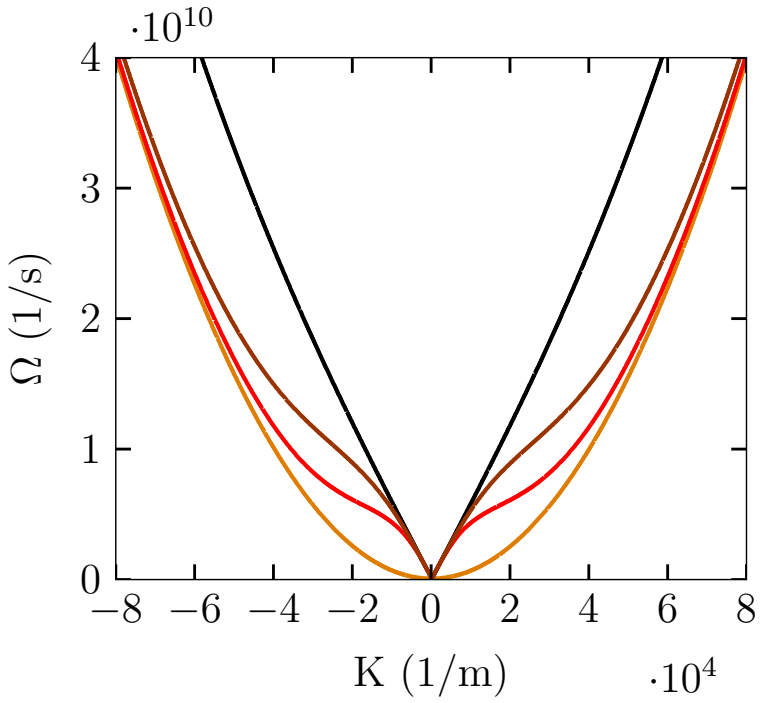

Figure 3.2: Bogoliubov dispersion relation according to Eq. (3.3.8). (black) Local nonlinearity $\Delta n = 10^{-5}$, $\sigma = 0$; (brown) Nonlocal nonlinearity $\Delta n = 10^{-5}$, $\sigma = 50$ μm; (red) Nonlocal nonlinearity $\Delta n = 10^{-5}$, $\sigma = 100$ μm; (orange) linear dispersion $\Delta n = 0$.

local length σ. The interaction term in the nonlocal dispersion is therefore altered in presence of a non zero nonlocal length in a way that it effectively reduces the nonlinear interactions for excitation with wavelengths much larger than σ (Fig. 3.2). This has striking consequences since the nonlocal length is usually bigger than the healing length ($\sigma > \xi$), hence σ determines the length scale whether an excitation propagates as particle or wave. In an experiment, it is therefore necessary that the transverse wavelengths are larger $\Lambda > \xi, \sigma$ to ensure superfluidity.

3.4 Dispersion measurement

3.4.1 Oceanographic technique

The experimental technique presented here was inspired from studies on ocean wave dispersion [78, 79]. The central idea in these oceanographic studies is to capture a time series of airborne images of the ocean surface and collect the amplitudes of random surface waves over time and space. By analysing the Fourier spectrum over space and time one can gather information about the population of the frequency spectrum $\Omega(K)$.

The same algorithm can be applied to the photon fluid, where random spatial amplitude fluctuations on the laser beam are used as the analogue of surface waves in the ocean, where intensity fluctuations translate into sound waves in the photon fluid analogy. The spatial random wave pattern appears naturally on the beam profile, unless one invests a lot effort to filter it out, and is used in the experiment. The time series can be captured by imaging the beam profile and scanning the imaging plane in defined increments along the z-direction. Since $t = zn_0/c$ each image captured at a position z_0 corresponds to a time t_0 (Fig. 3.1). The speed of sound is a function of the laser intensity and therefore it is desirable to have a top-hat like spatial beam profile that would guarantee that the tranverse beam intensity does not vary significantly over distances compared to those waves propagate inside the photon fluid. In the experiment, the gaussian beam profile is expanded by a 7-fold telescope to a beam waist diameter of around $w \approx 16$ mm and selected the central, high intensity region with an aperture. This results in an approximated top hat like profile with appropriate constant intensity across the beam without the need of complicated beam shaping techniques. This beam is then launched into the sample filled with nonlinear methanol/graphene solution (abs. $\alpha \approx 0.017\ cm^{-1}$), where its transverse beam profile can be imaged by a camera/lens system. The camera and imaging lens ($f = 75$ mm) are mounted at a fixed image distance on a computer controlled translation stage, that allows to scan the object plane along z with uniform scaling of the transverse directions (Fig. 3.4). By this technique, a set of up to 60 images along the z-direction is captured and stored in a 3D $I(x, y, z)$ dataset. The dispersion is then calculated via the Fourier transform of the measured intensity profile $I(x, 0, z)$. The intensity-to-noise ratio was enhanced by averaging over 200 lineouts along the y-direction. The measured dispersions of the photon fluid are shown in Fig. 3.4 b)-d).

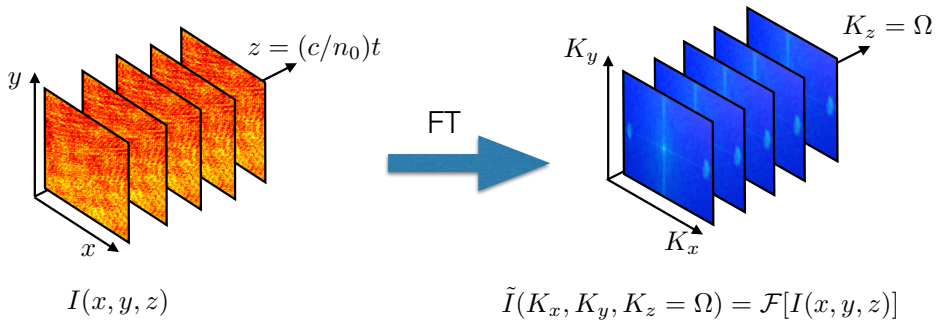

Figure 3.3: Oceanographic technique: transverse laser intensity is measured as a function of all spatial coordinates $I(x, y, z)$. The dispersion is calculated by a 2D Fourier transform of the signal $I(x, 0, z)$.

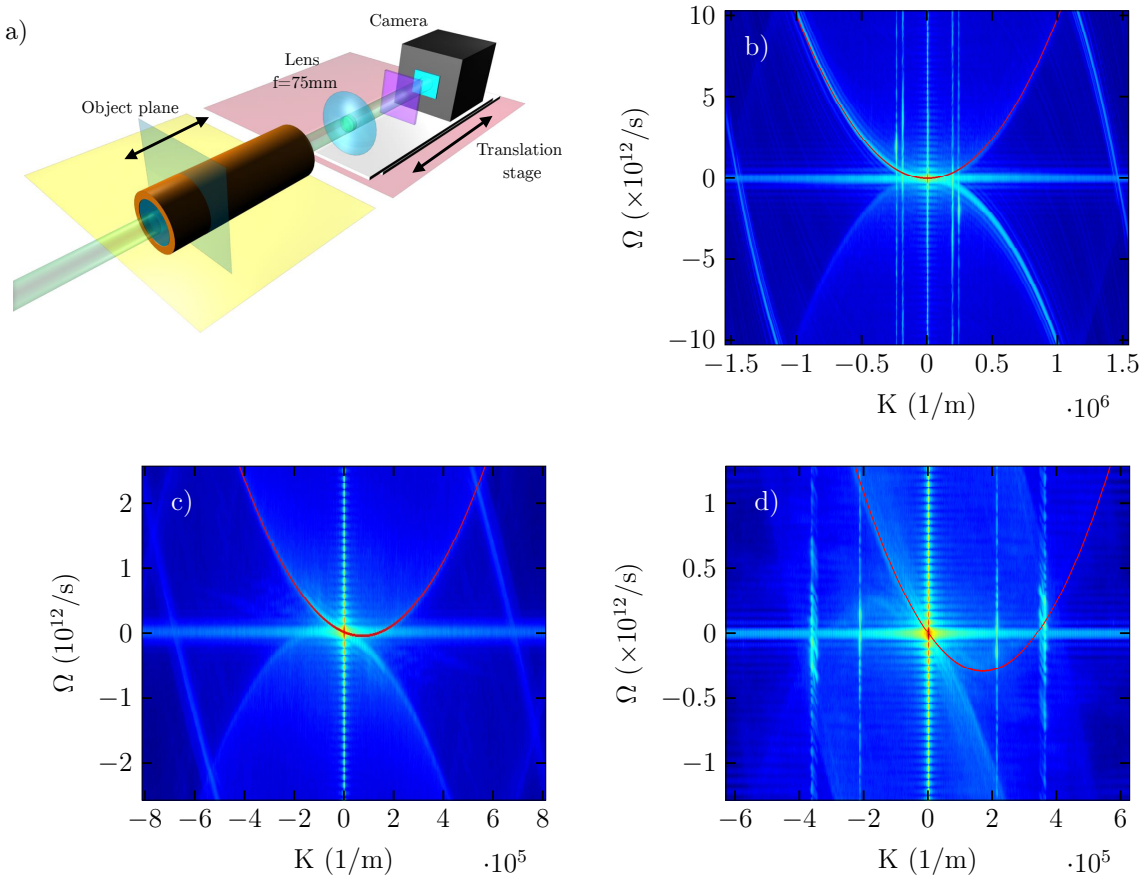

Figure 3.4: a) Experimental setup: Spatial beam profile is imaged at various z-positions. The camera and lens are sitting at a fixed distance on a linear translation stage. b)-d) Measured photon fluid dispersion for different scanning distances b) 1.5 cm c) 5 cm d) 12 cm. The effective flow is controlled by an angle between the optical axis of the laser beam and the imaging axis of the camera/lens: b) $v = 0$ m/s c) $v = 1.3 \times 10^6$ m/s d) $v = 3.0 \times 10^6$ m/s.

The contour plots show the logarithmic amplitude of the spatiotemporal frequency spectrum of random noise on the photon fluid. All the spectra show some folding, that is due to the discrete sampling of the intensity signal by the finite pixelation of the CCD sensor. Figure 3.4 b) shows data taken from 60 images along a scanning distance of 1.5 cm with an increment separation $\Delta z = 250$ μm and an intensity of $I \approx 2$ W/cm^2. The measured dispersion $\Omega(K)$ reveals a parabolic behaviour expected from the Bogoliubov dispersion relation for large K-vectors given by Eq. (3.3.6). The intensity used here yields a nonlinearity of $\Delta n \approx 10^{-6}$ resulting in a healing length $\xi \approx 230$ μm. Translated into K-space, the critical K-value below a phononic linear dispersion is expected is around $K_C = 2\pi/\xi \approx 0.3 \times 10^5$ m^{-1}. The resolution in K or Ω, is given by $\Delta K = 2\pi/\Delta x_{max} \approx 10^2$ m^{-1} and $\Delta\Omega = 2\pi/\Delta z_{max} \approx 4 \times 10^{-10}$ s^{-1} where Δx_{max} is

the size of the sensor format of the camera and Δz_{max} is the overall scanning distance. Comparing with Fig. 3.2, a sufficient resolution in K-space is given, but the resolution in Ω is the limiting parameter in observing a linear dispersion. For this reason, to enlarge the resolution in Ω the data was measured over longer distances $\Delta z_{max} = 5$ cm and 12 cm with an increment of 1 mm. However, the result of all measurements is a parabolic dispersion, where the experimental accuracy and resolution does not allow to distinguish between a purely parabolic (linear beam propagation) and Bogoliubov dispersion (nonlinear beam propagation). This would require a much longer beam propagation over several meters or stronger nonlinearity, however the results clearly indicate that the limiting length scale in a nonlocal medium is indeed the nonlocal length $\sigma \approx 10$ mm leading to $K_C \approx 10^3\ m^{-1}$.

Furthermore, by tilting the imaging axis of the camera lens system with respect to the beam axis, one can introduce a linear phase gradient along the tilt direction. According to the hydrodynamical equations, this yields to a non-zero background flow in the photon fluid. This is verified by a tilted dispersion in Fig. 3.4 c) and d) where the flow v can be calculated by fitting the data to Eq. (3.3.6) with $\Delta n = 0$ and c) $v = 1.3 \times 10^6$ m/s and d) $v = 3.0 \times 10^6$ m/s.

The oceanographic technique has been successfully transferred to the photon fluid as it shows that small amplitude excitations follow a parabolic dispersion that is identical to the Bogoliubov dispersion in the case $\Delta n = 0$. As discussed, it has however experimental limitations with respect to resolution that can only be overcome by very long propagation inside the nonlinear medium. Since the nonlinearity is feeded by absorption of the laser beam, there exists an upper limit for the nonlinear propagation length before the intensity significantly changes along propagation. This is problematic as the intensity maps into a fluid density that would then significantly change over time. Another technical problem with this technique that it requires to image photon fluid planes inside a nonlinear medium and in the case of strong nonlinearity this can no longer be considered as linear imaging because of possible deformations of various image planes [65]. However, an object was imaged through the nonlinear medium in order to experimentally verify that the distortions are only significant in the presence of high intensity contrast, i.e. the sharp edge of a knife edge (Fig. 3.5). It is therefore expected, that the weak oscillations on top of the more intense background beam do not significantly distort the images and therefore the measured dispersions are indeed correct. This is further corroborated by the excellent theoretical fit of Eq. (3.3.6).

Nonetheless, a precise estimate of the low frequency dispersion has to be assessed by a technique that is not bound to the resolution limits or imaging inside the nonlinear medium. Such a technique is presented in the next section.

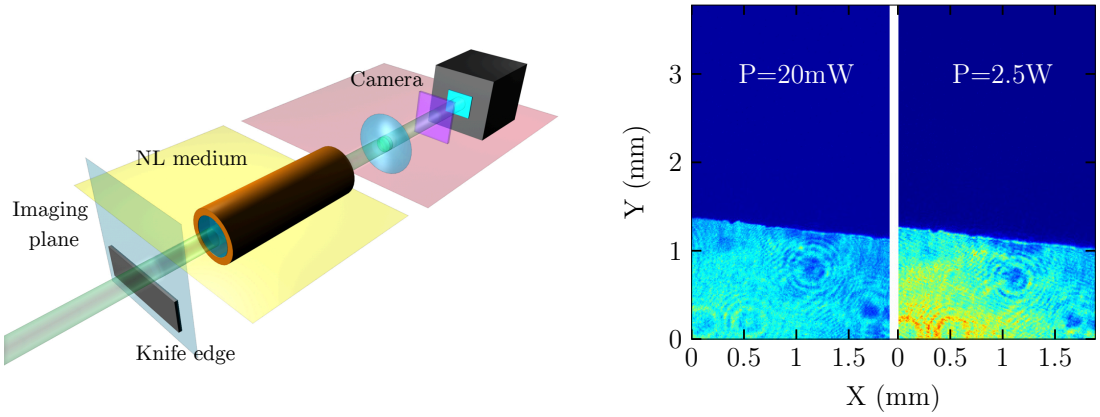

Figure 3.5: Imaging through a nonlinear medium. A knife edge blocking part of the beam is imaged through the medium at low power (P=20 mW, linear imaging) and high power (P=2.5 W, nonlinear imaging).

3.4.2 Pump and probe technique

This following technique varies from the oceanographic technique as in seeding defined wavelengths rather than using random noise on the beam [43]. The key idea is to measure the wave phase velocity by comparing the initial and final location of such a wave after it has propagated for a given distance. To experimentally seed a wave, the beam is sent through a Mach-Zehnder-Interferometer as to create a weak probe beam that is recombined with a strong pump. In this configuration, the strong pump is used to create the strong background field required to set the photon fluid properties and the weak probe is used to create a small intensity modulation on top of the strong pump through linear interference. A theoretical study of this configuration was discussed in [43].

The intensity of the probe beam is controlled by a combination of $\lambda/2$-plate and polarizing beamsplitter to avoid absorptive elements that may lead to unwanted heating. By controlling intensity and angle between pump and probe one is able to easily control the desired modulation depth ($\approx 5\%$) and wavelength. Both beams are then loosely focused onto the sample input using a set of cylindrical lenses ($f_1 = 200$ mm and $f_2 = 50$ mm) to create an elliptical beam with a narrow minor axis waist radius $w_y = 180$ μm and a wide major radius with $w_x = 0.7$ cm (values corresond to the radii where the intensity has dropped to $1/e^2$ of the peak intensity). The respective angles of the beams were aligned such that the interference fringes are parallel to the y-axis so that the K-vector of the phonon waves are aligned along the x-axis. Then, the K vector of the excitation is given by the geometric relation $K = k_0 \sin(\phi_{pr})$, where ϕ_{pr} is the angle of the probe beam with respect to the pump. A similar configuration was used before in studies

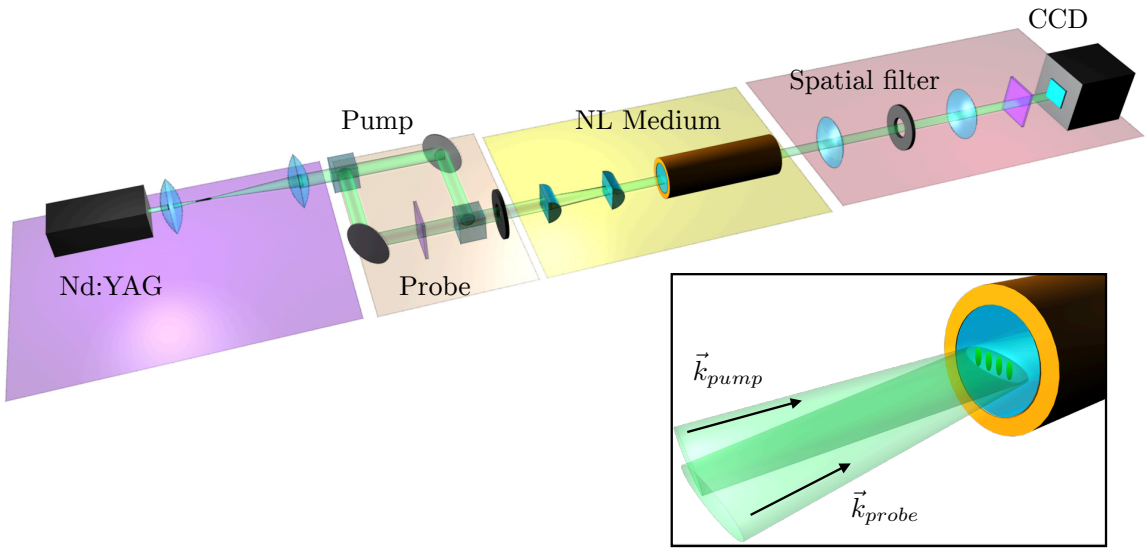

Figure 3.6: Pump and probe technique: A weak intensity modulation is created by an interference pattern between a strong pump and a weak probe beam. Both beams have a highly elliptical intensity envelope due to a loosely focusing by a set of cylindrical lenses. The spatial filter is an iris in the focal plane of the imagine telescope after the sample to block the phase conjugated beam at the output. Finally, the shift of the interference pattern is imaged by a 4-f telescope onto a CCD.

on periodic soliton formations [80, 81], however the intensity modulation contrast used here is very low compared to earlier works. The elliptical beam configuration was used to achieve higher intensities while working with a large beam profile as this is necessary to fit in the relatively large phonon wavelengths of the order of a few mm that are required to access the low frequencies in the Bogoliubov dispersion. After the beam has propagated through the sample, the output facet is imaged onto a CCD camera and a shift ΔS in the interference pattern can be measured as a function of the laser intensity (Fig. 3.7). This is understood as the weak intensity modulation through the linear interference is set as the initial condition of an excitation in the photon fluid as soon as the beams enter the nonlinear medium. In the Bogoliubov theory, this initial condition is translated into eigenstates of the photon fluid and becomes a superposition of Bogoliubov modes with opposite momenta $\pm K$ (see (Eq. (3.3.5)) [43, 82]. As the beam propagates through the nonlinear sample, the initial excitation splits up into a positive and negative transverse momentum components that are propagating in opposite directions at the phase velocities given by the dispersion relation at $\pm K$.
For excitations with $K < K_C$, this is the speed of sound determined by the nonlinearity in the system. Assuming a nonlinearity $\Delta n = 10^{-6}$, the speed of sound can be estimated to $c_s \approx 2 \times 10^5$ m/s. Given the effective propagation time in a 13 cm long sample

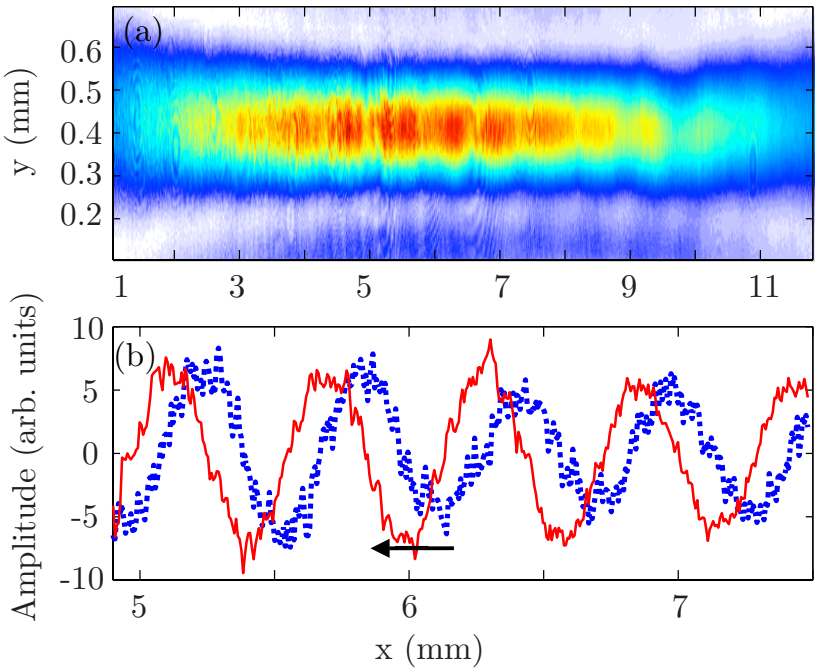

Figure 3.7: a) Beam profile at the sample output facet. The modulation is due to the low contrast barely visible. b) Example of a background subtracted lineout taken from a) for low power (P≈0, dotted blue line) and high power (P=28 mW, solid red line) showing a shift ΔS relative to the low power case [57]).

is around $t = zn_0/c \approx 0.5$ ns, the excitations propagate only around $\Delta S = c_s t = 100$ μm. This shows clearly, that if the low frequency excitations with opposite momenta have wavelengths of a few hundred of μm, they will never completely separate and are thus always superimposed in the experiment.

In optical terms, the Bogoliubov splitting can be understood as a third order nonlinear mixing process, where the pump and probe generate an idler beam that propagates at the conjugate angle $-\phi_{pr}$. Note that this process is not phase matched and therefore the idler is only generated by the sudden change in nonlinearity when the beam enters the nonlinear medium (see Section 3.5). Since the probe and the idler beam are superimposed, a spatial filter in the focus of the imaging optics is used, to filter out the $-K = k_0 \sin(-\phi_{pr})$ component in the farfield and image only the positive component on the camera. The phase velocities of the excitations are given by $v_{ph} = \Omega/K$ with $\Omega(\Delta n)$ defined by (Eq. (3.3.6)) and are thus dependent on the nonlinearity set by the pump beam. By changing the nonlinearity through the pump power one can therefore control the phase velocity and as a consequence, a shift of the interference pattern can be measured according $\Delta S(\Delta n) = v_{ph}(\Delta n)t$ with $t = zn/c$ for various laser powers.

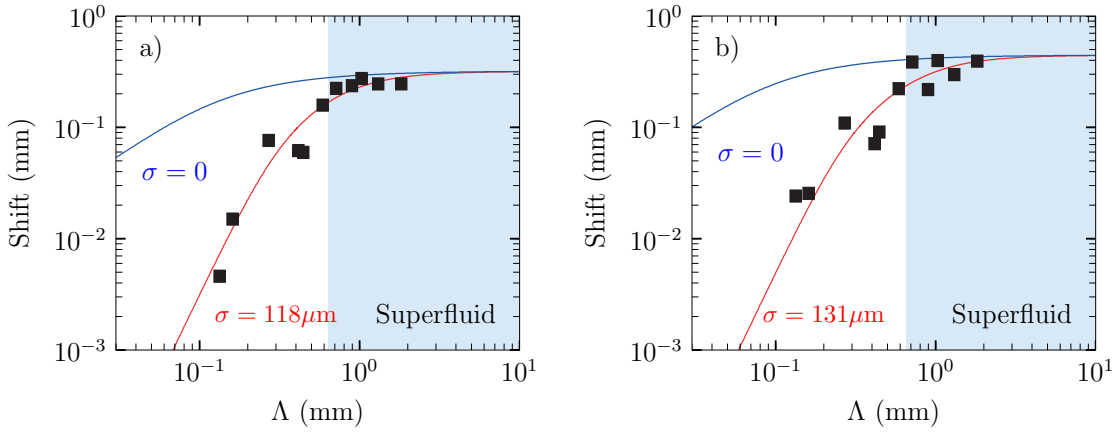

Figure 3.8: Shifts measured for various wavelengths Λ at a) P=28 mW and b) P=45 mW. The predicted shifts according to Eq. (3.4.1) are shown with the red solid lines. The blue lines show the predicted shifts for a local nonlinearity a) $\Delta n = (0.7 \pm 0.1) \times 10^{-5}$ and b) $\Delta n = (1.4 \pm 0.1) \times 10^{-5}$ with $\sigma = 0$. The corresponding healing lengths are a) $\xi \approx 86$ μm and b) $\xi \approx 62$ μm. The shaded blue area covers the region where a saturation of the phase velocity is observed. The healing length

Using Eq. (3.3.6), one obtains an expression for the shift $\Delta S(\Delta n, K)$:

$$\Delta S(\Delta n, K) = \frac{K}{2k_0}\left[\sqrt{1 + \frac{|\Delta n|}{n_0}\hat{R}(K)\left(\frac{2k_0}{K}\right)^2} - 1\right] z \tag{3.4.1}$$

that allows to estimate the nonlinearity Δn and the nonlocal length σ of the system by measuring the shifts for several wavelengths Λ. This is shown in Fig. 3.8 for wavelengths between $\Lambda \approx 100$ μm -1.5 mm at fixed laser powers a) P=28 mW and b) P=45 mW. The data is in very good agreement with the theoretical predictions given by Eq. (3.4.1) with a nonlocal response $\hat{R}(K) = 1/(1 + \sigma^2 K^2)$ and a) $\Delta n = (0.7 \pm 0.1) \times 10^{-5}$ and b) $\Delta n = (1.4 \pm 0.1) \times 10^{-5}$. In both cases, the estimate for the nonlocal length is around $\sigma \approx 125$ μm. For comparison with a purely local nonlinearity $\sigma = 0$, the expected shifts were plotted and show clearly that the behaviour for small wavelengths is very different from the nonlocal case. In the local case, a Taylor series expansion reveals that the shifts go to zero with a $1/K$ dependence where in contrast to the nonlocal case, they tend to zero as $1/K^3$ because the nonlocal response adds an extra decay of $1/K^2$. In the $K \to 0$ ($\Lambda \to \infty$) limit, the local and nonlocal shifts both go towards $\sqrt{\Delta n/n_0}$. Overall, the measured data cannot be fitted with any value Δn by considering a purely local nonlinearity.

The remarkable feature is that even in the nonlocal case the data shows clearly that the shifts become wavelength independent for $\Lambda > 500$ μm (shaded blue area), where

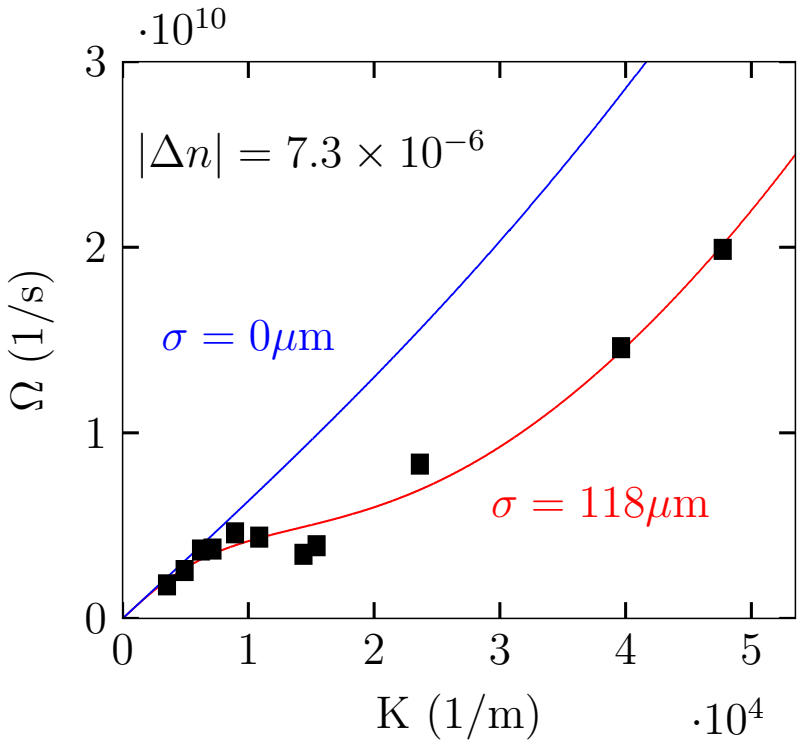

Figure 3.9: Nonlocal Bogoliubov dispersion. The measured data shows excellent agreement with the predicted dispersion given by Eq. (3.3.6) with $\sigma = 118$ μm and $|\Delta n| = 7.3 \times 10^{-6}$ for P=28 mW.

the waves are considered as collective phononic excitations. This saturation is evidence of a constant phase velocity or in other words of a linear dispersion relation. Using $\Delta S = v_{ph}t = \Omega t/K$ the measured shifts can be translated into temporal frequencies and show good agreement with the nonlocal Bogoliubov dispersion (Fig. 3.9). It is the linear dispersion that leads to a minimum non-zero propagation speed for excitations $c_s = \lim_{K\to 0}(\Omega/K)$, hence there exists a critical speed below no waves at any given frequency can propagate. A striking consequence is that energy transfer into the fluid in the form of excitations, i.e. through scattering from an object, is suppressed and therefore a frictionless flow characteristic for superfluids is expected.

3.5 Discussion and Conclusion

The techniques and experiments presented in Chapter 3 were aimed at realizing a photon fluid in a propagating geometry with a nonlocal thermal nonlinearity. The main focus was laid on developing ideas and techniques to measure the dynamics of small amplitude excitations on top of a strong background fluid. As such, the dispersion relation lies at the centre of understanding the rich physics of fluid dynamics and therefore a technique from oceanography was adapted to investigate the dispersion of a nonlocal photon fluid. Using the random noise on the laser beam, the result confirmed the parabolic dispersion for excitations with large momenta and highlighted the influence of the phase gradient resulting in a hydrodynamic flow. As this technique involves Fourier transforms in the spatial and temporal domain, the resolution of the measured spectra is limited by the finite sample dimensions which was found to be too small to resolve the low momenta spectrum. Different sample lengths were tested (1.5-12 cm) but to gain sufficient resolution, propagation lengths of a 100 cm or more would have been needed, but are disadvantageous due to their increased absorption. Furthermore, the technique involved imaging through a nonlinear medium which is technically problematic as it is known that the nonlinearity distorts the image planes. This led to a different experiment that involved a pump probe scheme which overcomes both problems.
By measuring the phase velocity of seeded excitations, it was shown that the low momenta dispersion follows the Bogoliubov dispersion relation for superfluids. It was verified that the nonlocality alters the dispersion for large momenta and in the presence of strong nonlocality always dominates the healing length, which is the defining length scale for quantum fluids with local interactions. Most importantly, it was shown that there exists a linear dispersion even in highly nonlocal media and that allows to observe superfluidity under specific conditions. Using a lorentzian K-space response, one is able to fit the experimental data with a modified nonlocal dispersion relation to estimate the nonlocal length $\sigma \approx 125$ μm and the nonlinearity to $\Delta n = (0.7 \pm 0.1) \times 10^{-5}$ at $P = 28$ mW and $\Delta n = (1.4 \pm 0.1) \times 10^{-5}$ at $P = 45$ mW. Comparing the nonlocal length found here with the result from Section 2.4.3, one finds that the nonlocal length is two orders of magnitude smaller which is a significant difference. Both experiments were conducted with the same sample and nonlinear medium at thermal equilibrium and since σ is a function of material properties and boundary conditions they should yield the same value. However the experiments conducted in Section 2.4.3 were performed with a spatially symmetric gaussian beam profile whereas the pump and probe experiment presented in this chapter involved a highly elliptical beam profile. The significant difference can be explained by the difference of beam waist radii which introduces a new

way of controlling the degree of nonlocality. This is in itself a surprising and important result and is investigated and used in the next Chapter, where a highly elliptical beam is used to create a superfluid flow around an extended obstacle.

The superfluid characteristics of the photon fluid are also reflected in the earlier mentioned "Bogoliubov splitting". In the experiment it is manifested by the appearance of a weak beam that is propagating at the conjugate angle of the probe beam (Also see Fig. 6.3). In the photon fluid, this corresponds to a wave with positive and negative transverse momenta $\pm K_x$. This is a consequence of the intrinsic modes of a superfluid, which are a superposition of positive and negative frequency components (Eq. (3.3.5)) that arises via the nonlinear coupling of the particles in the Bogoliubov theory [43, 76]. In particular, the dynamics of the here discussed superfluid are ruled by the NLSE, where such a mode coupling appears in an additional term $\propto E_0^2\epsilon^*$ when the total field ansatz $E = E_0 + \epsilon + c.c.$ is chosen for linearisation. The linearised NLSE for the real part then reads:

$$\frac{\partial \epsilon}{\partial z} = \frac{i}{2k}\nabla_\perp \epsilon + \frac{ikn_2}{n_0}\left[E_0^2\epsilon^* + 2|E_0^2|\epsilon\right] \tag{3.5.1}$$

In nonlinear optics, this term corresponds to a four-wave mixing term that couples the pump, the probe and the idler amplitudes. In a phase matched condition, this would lead to energy transfer between the beams but in the non-phase matched scenario this term is essentially switched off due to dephasing of the beams. In the experiment all beams have the same frequency and propagate at different angles such that they never satisfy phase matching conditions. Therefore, the generation of the idler in the experiment is due to the sudden change in nonlinearity as the beams enter the nonlinear medium and is suppressed shortly thereafter. A back reaction from the idler back to the two other beams (i.e. pump depletion) can be safely neglected due to its weak intensity (usually less than 1%). Therefore, the photon fluid waves are always superimposed but only coupled at $t = n_0 z/c \approx 0$, and one can therefore filter out the wave component with negative $-K_x$ after the sample ($t \gg 0$) without affecting the dynamics of the wave with positive momentum $+K_x$ and vice versa. Note that the last term in the NLSE mediates the photon-photon interaction and is responsible for the superfluid dynamics and does not require phase matching. Thus the requirements to establish superfluidity in the sense that the excitations follow the Bogoliubov dispersion, are always present during the propagation of the beam through the entire nonlinear medium.

The shifts of the small amplitude waves were analysed in the language of photon fluids where they are interpreted as a change of propagation speed in fixed time window. In the language of nonlinear optics, this effect is explained in terms of a phase modulation between the two beams $E_1(\omega_1, \vec{k}_1)$ and $E_2(\omega_2, \vec{k}_2)$, propagating in a nonlinear medium

at a small angle. The resulting interference pattern depends on the angle and the relative phase between the beams. If the latter is changed due to a nonlinear process, a lateral shift of the interference pattern is observed. The general form of the third-order nonlinear polarization amplitude reads:

$$P^{(3)}(t) = \epsilon_0 \chi^{(3)} E(t)^3 \tag{3.5.2}$$

with the total electric field amplitude $E(t) = E_1 e^{-i(\omega_1 t + \vec{k}_1 \vec{r})} + E_2 e^{-i(\omega_2 t + \vec{k}_2 \vec{r})} + c.c.$ The resulting full expression can be written in the common notation $P^{(3)}(t) = \sum_n P(\omega_n) e^{i\omega_m t}$ and consists of 64 terms, but only the self-action (SA) and cross-action (XA) terms at positive frequencies are considered here. These are responsible for a nonlinearly induced phase shift and by assuming that the probe beam is much weaker than the pump, i.e. $E_2 \ll E_1$, the relative phase is only significantly changed by the self-phase modulation (SPM) of the pump beam E_1 and the cross-phase modulation (XPM) of E_2 by E_1:

$$\begin{aligned} P_{SA}(\omega_1, \vec{k}_1) &= \epsilon_0 \chi^{(3)} (E_1 E_1^* E_1 + E_1^* E_1 E_1 + E_1 E_1 E_1^*) && (3.5.3) \\ P_{XA}(\omega_2, \vec{k}_2) &= \epsilon_0 \chi^{(3)} (E_1 E_1^* E_2 + E_1^* E_1 E_2 + E_1 E_2 E_1^* \\ &+ E_1^* E_2 E_1 + E_2 E_1 E_1^* + E_2 E_1^* E_1) && (3.5.4) \end{aligned}$$

In general, there are three self-action term and six cross action terms. Hence in the case $E_1 \gg E_2$ the change of refractive index experienced by the weak probe is twice the self-induced refractive index change from the pump on itself. This leads to an increasing relative phase shift between both beams during propagation that results in a shift of the interference pattern between sample input and output. This can be understood as a change of the wavevector magnitudes in the nonlinear case $k_1' = \frac{2\pi}{\lambda}(n_0 + \gamma |E_1|^2)$ and $k_2' = \frac{2\pi}{\lambda}(n_0 + 2\gamma |E_1|^2)$ (Fig. 3.10). Note that in the defocusing case ($\gamma < 0$), the magnitude of the k-vectors decrease.

Each of these terms $P(\omega_i = \omega_j + \omega_k + \omega_l, \vec{k}_i = \vec{k}_j + \vec{k}_k + \vec{k}_l)$ with $\omega_{j,k,l} = \pm\omega_{1,2}$ and $\vec{k}_{j,k,l} = \pm\vec{k}_{1,2}$ describes a nonlinear process, where a nonlinear refractive index grating is created by the jth and kth wave, and from which the lth wave is scattered [81]. Note that this grating is oscillating with $\omega_{gr} = \omega_j + \omega_k$ and has a wave vector $\vec{k}_{gr} = \vec{k}_j + \vec{k}_k$. Now in the special case of a thermal nonlinearity which has a slow response compared to the laser frequency ω, only terms in the above equations that create a stationary refractive index grating ($\omega_{gr} = 0$) will be effective. Here, in the degenerate case where $\omega_1 = \omega_2$, the third term in the self-action polarisation is nonzero ($\omega_{gr} = 2\omega_1$) and so is the third and fifth term in the cross-action polarisation ($\omega_{gr} = \omega_1 + \omega_2 = 2\omega_1$). In the degenerate situation, there are still two self action and four cross-action terms left and

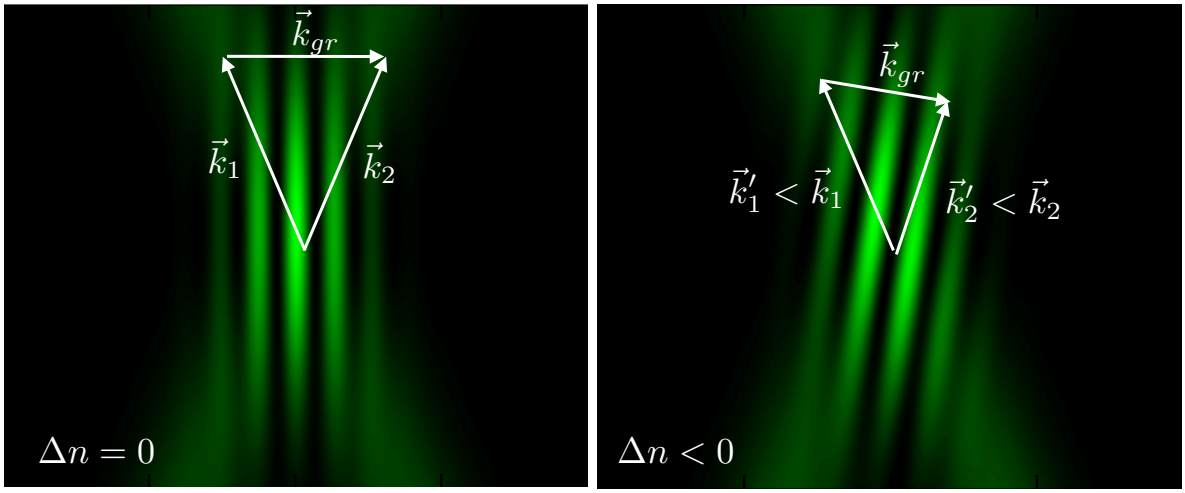

Figure 3.10: Qualitative explanation of the wavelength shifts as a result of cross-phase modulation. a) linear scenario ($\Delta n = 0$). Two beams are propagating at an angle from bottom to top and create an interference pattern that is parallel to the vertical axis. b) nonlinear scenario ($E_1 \gg E_2, \Delta n < 0$). The magnitudes of the k-vectors change such that $|\vec{k'}_2| < |\vec{k'}_1|$ and thus the interference pattern is tilted. Angles and magnitudes are exagerrated for clarity.

hence the cross-phase modulation is still twice the self-phase modulation.
It is interesting to note that the fourth and the sixth terms in the cross-action polarisation are creating a stationary index grating that depends on the relative angles between both beams and has exactly the same spatial modulation as the interference pattern. Therefore, if the system is highly nonlocal in the sense that the nonlocal length is much larger than the wavelength of the refractive index grating, these terms will be effectively damped. As a consequence, the XPM is equal the SPM and a shift in the interference pattern is suppressed. This is reflected in the dispersion measurement, where the shifts of the long waves are pushed towards zero in Fig. 3.8 and their respective frequency Ω towards the linear dispersion in Fig. 3.9.

Chapter 4

Superfluidity

The previous chapter showed that excitations in the photon fluid obey the Bogoliubov dispersion relation that is also found for quantum fluids such as He^3 or Bose-Einstein condensates. Therefore it is expected that there exists a condition where the fluid becomes superfluid, a state in which the fluid is described by an order parameter, a macroscopic wave function that leads to frictionless flow in subcritical and nucleation of quantized vortices in supercritical flows. This chapter presents the observation of these phenomena in the photon fluid at room temperature and the results were published in "The role of geometry in the superfluid flow of nonlocal fluids", PRA (2016) [83].

4.1 Introduction

Superfluidity is without doubt one of the most fascinating manifestations of quantum physics at the macroscopic level and describes a state of a fluid in which it loses any friction and establishes a dissipationless flow. This peculiar fluid state was first observed in liquid Helium in the early 20th century and until now has attracted countless experimental and theoretical studies that laid the foundation of todays understanding of quantum liquids. Similar to Bose-Einstein condensates, it manifests itself when cooling bosonic particles below a critical temperature where they undergo a phase transition from normal to superfluid. This phase transition cannot be explained by classical theories, but is a consequence of quantum degeneracy that leads to the collective behaviour. At low temperatures, the de-Broglie wavelength of the atoms is of the order of the inter-atomic spacing and this delocalization allows to describe the gas or fluid as a macroscopic wave function, the order parameter. When weak interactions are introduced, then the evolution of the order parameter is governed by an equation that was derived by Gross and Pitaevskii and has the form of a Nonlinear Schrödinger Equation [84, 85]. Quantum fluids of light that are described by the same equation, where the electric field of a monochromatic beam plays the role of the order parameter and the optical nonlinearity mediates the interaction. Photon fluids share therefore a strong resemblance to Bose Einstein condensates or superfluid helium. The possibility of superfluidity in photon fluids was proposed by Chiao et. al. [12] and experimental realisations were presented in exciton-polariton condensates few years later [13,14]. These driven-dissipative systems work at cryostatic temperatures where the light particles in the semiconductor microcavity are described by strongly interacting exciton-polaritons. Besides exciton-polariton condensates, photon condensates have been observed in optical micro cavities filled with fluorescent dye [8, 9] while superfluid shock waves and condensation of classical waves have been observed in defocusing bulk nonlinear media using photo refractive crystals [37, 42].

In all these systems, superfluid flow is usually observed in the scattering of a flow around an obstacle. In a normal fluid, the kinetic energy of the fluid is dissipated in the form of waves that are scattered from the obstacle. In a superfluid however, there exists a critical flow speed below such waves are not allowed to be excited, and consequently the fluid passes the obstacle undisturbed. At the breakdown of superfluidity, i.e. at flows speeds close to the critical flow, the onset of turbulence in the form of quantised vortex nucleation is commonly considered to be a hallmark signature of such superfluids. These vortices are topological defects in the form of a phase singularity with quantized circulation and are a well known feature of solutions to the NLSE. Chapter 3 presented

the phononic, linear dispersion for long wavelength photon fluid excitations as a first signature of superfluidity, but the vortex shedding in the superfluid flow in the wake of an obstacle has so far not been shown photon fluids in a propagating geometry.
The physics of quantized vortices is of profound interest since the realisation and discovery of superfluids like ^{4}He and BECs, and today dynamical aspects are thoroughly investigated in quantum turbulence [86]. Vortices have the dimensions of the healing length and are thus hard to optically visualize in liquid ^{4}He, where they are of the order of a few Angströms. In comparison, due to their lower density, dilute atomic gas BECs have healing lengths of the order of microns while photon fluids can reach tens to hundreds of microns. Furthermore, the spatial phase interferometry in optics allows easy access to phase information and thus straight forward localisation and characterisation of winding numbers of vortices. This makes photon fluids a promising toolbox for studying vortex formation and superfluid dynamics.
However, the nature of the nonlinearity plays a fundamental role regarding photon superfluids. Most studies and experiments so far were conducted in systems with quasi local nonlinearities, but only few of them considered highly nonlocal nonlinearities found in thermal media. In fact, a superfluid scattering experiment as discussed earlier has not been reported for a nonlocal photon fluid. A nonlocal nonlinearity introduces effective long range interactions that will lead to earlier breakdown of superfluidity in terms of wavelengths and critical flow speeds. More importantly, the results found for the nonlocality in Chapter 2 and 3 are contradicting, i.e from theoretical and also experimental findings the nonlocal length is determined by the sample dimensions ($\sigma \approx$10 mm) which is two orders of magnitude larger than the nonlocality found in the dispersion relation measurements. There, superfluid wave propagation could be identified for waves much shorter than the nonlocal length (10 mm) and this significant difference hints that the understanding of nonlocal effects on superfluidity is still incomplete. Therefore, the stability and breakdown of superfluidity in the presence of nonlocality is of profound interest and also ties links to dipolar BECs, where the nonlocality gives rise to a roton/maxon spectrum [87]. Therefore nonlocal photon fluids provide a useful platform for deeper understanding of nonlocal superfluids in general.

4.2 Landau criterion

A frictionless flow of a fluid around a barrier or obstacle is only possible if no kinetic energy from the flow is transferred into heat or excitations in the fluid. In particular, considering a superfluid flow along the positive x-direction with a non-zero flow velocity relative to an obstacle at rest, quasi-particles in the fluid can be excited under energy and momentum conservation. Supposing that the interaction between the obstacle and the flow is such that it can only create elementary excitations in the fluid and not change the overall flow. In the co-moving frame, the obstacle changes velocity from v_i to v_f, therefore the energy of such an excitation is:

$$\epsilon(p) < \frac{m}{2}(v_i^2 - v_f^2) = p^2/2m \tag{4.2.1}$$

The momentum is conserved, thus using $m\vec{v_i} = \vec{p} + m\vec{v_f}$ one gets:

$$\epsilon(p) < \vec{p}\vec{v_i} - \frac{p^2}{2m} \tag{4.2.2}$$

Since the last term is always positive, the condition reduces to:

$$\epsilon(p) < |\vec{p}||\vec{v_i}| \tag{4.2.3}$$

For a quadratic dispersion $\epsilon \propto p^2$, this is satisfied for arbitrary small flow speeds v_i, hence excitations can be created by the obstacle at all velocities. However, if the dispersion is linear, i.e. $\epsilon(p) = cp$, excitations can only be created if $v_i > c$. This is the Landau criterion for superfluids that states that below a critical flow velocity it is not possible to excite waves by means of a scattering from a boundary or obstacle and therefore frictionless, superfluid flow is established. In general, the critical speed is therefore defined and evaluated via $v_c = \min_p \epsilon(p)/p = \min_K(\Omega/K)$.
The energy spectrum $\epsilon = \hbar\Omega$ of elementary excitations in a superfluid is given by the Bogoliubov dispersion relation, that for nonlocal photon fluids takes the form (Eq. (3.3.8)):

$$\epsilon^2 = \hbar^2(\Omega - \vec{v}\vec{K})^2 = \hbar^2 \frac{c^2 n_2 |E_0|^2}{n_0^3} \hat{R}(K, n_0\Omega/c)K^2 + \hbar^2 \frac{c^2}{4k^2 n_0^2} K^4$$

with the nonlocal response function $\hat{R}$. Considering a local medium, i.e. $\hat{R} = 1$, this dispersion is linear for waves with momenta smaller that the inverse healing length ($K < 1/\xi$) and their propagation speed is given by the speed of sound $c_s = \lim_{K\to 0} v_{ph}(K) = \lim_{K\to 0}(\Omega/K)$. In this case, the critical Landau speed $v_c = \min_K v_{ph}(K)$ is given by the

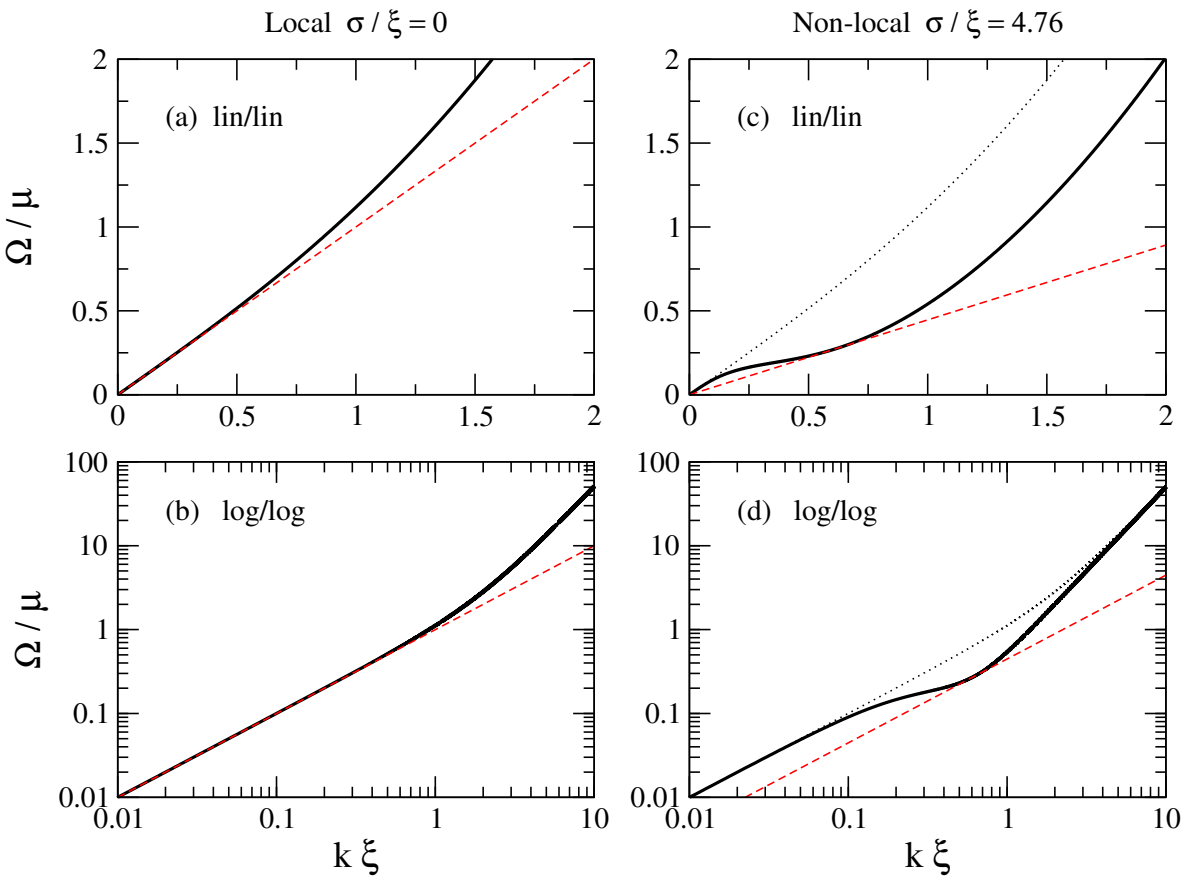

Figure 4.1: Bogoliubov dispersion relation in the lab frame. The dispersion a) and b) for a local ($\sigma = 0$) and c) and d) for a nonlocal fluid (σ/ξ=4.76, experimental parameters) in linear and logarithmic scaling. The red dashed line is the straight line found for $\Omega = v_c K$ with the critical speed v_c [83].

sound speed. As this is a function of the nonlinearity, the critical velocity will depend on the intensity in the experiment. However, as discussed in the previous Chapter the nonlocality alters the dispersion relation and has therefore also an effect on the critical Landau velocity. For further discussion, using the parameters $m = k_0 n_0 \hbar/c$ and $g = ck_0\hbar/n_0^2$ and $\rho = n_2|E_0|^2$ the phase velocity $v_{ph} = \Omega/K$ can written in the convenient form:

$$v_{ph}(K) = \left(\frac{g\rho/m}{1+\sigma^2 K^2} + \frac{\hbar^2 K^2}{4m^2}\right)^{1/2} \tag{4.2.4}$$

The critical velocity is the local minimum with respect to K and depends on the relative value between the nonlocal length σ and healing length ξ and thus two regimes can be identified:

1.) For a local medium and weak nonlocalities i.e. $\sigma < \xi/2$, the minimum of $v(K)$

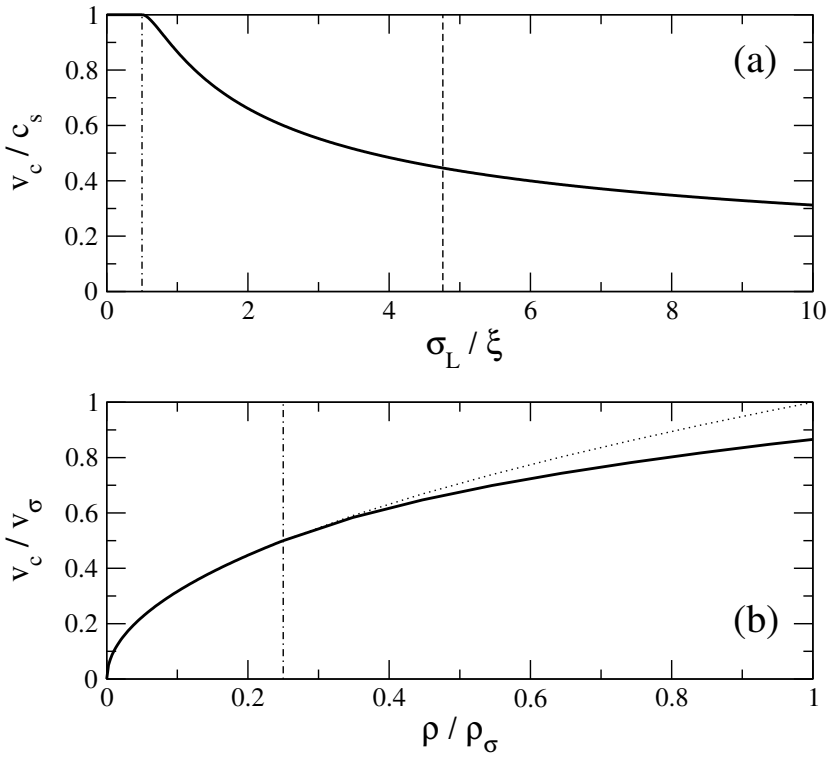

Figure 4.2: Critical velocity v_c as a function of nonlocal length σ (a) and fluid density ρ (b). Here, $\rho_\sigma = \hbar^2/mg\sigma^2$ and $v_\sigma = \hbar/m\sigma$. The vertical dot-dashed line identify the two regimes $\sigma > \xi/2$ and $\sigma < \xi/2$. The conditions met in the experiment are identified by the dashed line. The dotted line in b) plots the $\sqrt{\rho}$ behaviour for comparison.

is given at K=0 and is identical to the speed of sound c_s (see Fig. 4.1a) and b)

$$v_c = \min_K v_{ph}(K) = \sqrt{\frac{g\rho}{m}} = c_s \tag{4.2.5}$$

2.) In the case of strong nonlocalities, i.e. $\sigma > \xi/2$ (see Fig. 4.1c) and d), the local minimum of $v(K)$ is attained at $K_c = \sqrt{\frac{1}{\sigma}\left(\frac{2}{\xi} - \frac{1}{\sigma}\right)}$ with a lower value:

$$v_c = \sqrt{\frac{\hbar^2}{m^2\sigma}\left(\frac{1}{\sigma} - \frac{1}{4\sigma}\right)} \tag{4.2.6}$$

Fig. 4.2 shows the critical velocity as a function of fluid density and nonlocal length. For values up to $\sigma = \xi/2$, the critical velocity is identical to the speed of sound and slowly decays afterwards. The density dependence of v_c shows the familiar $\sqrt{\rho}$ for quasi local photon fluids and then decays slower proportional to $\rho^{1/4}$ as expected since $1/\xi \propto \sqrt{\rho}$. For the experimental parameters $\Delta n = 7.6 \times 10^{-6}$ and $\sigma = 110$ μm, the ratio $\sigma\xi \approx 4.76$, which results in a reduction of the critical speed by almost a factor 2.

Summarising, the critical Landau speed is reduced in the presence of nonlocality if the nonlocal length is larger than half the healing length. The usual nonlinearities and nonlocal lengths present in the 2D photon fluids using methanol/graphene solutions were measured in Chapter 2 for thermal equilibrium and transient conditions. There, the nonlocal length σ at thermal equilibrium is about 10 mm which exceeds $\xi \approx 70$ μm (assuming $\Delta n = 10^{-5}$) by a factor of 14 and consequently reduces the critical velocity significantly. It is therefore necessary to find conditions under which the nonlocality can be reduced and establish superfluidity, as presented in the following section.

4.3 The role of geometry

The nonlocal nature of the thermal nonlinearity plays a significant role in many phenomena regarding photon (super-) fluids. In Chapter 2 it was shown that it can be well modelled via the 2D heat equation and numerical as well as analytical solutions were found to correctly predict experimental measurements of the thermally induced refractive index change. In thermal equilibrium, the nonlocal length was found to be determined by the radius of the sample geometry (Eq. (2.3.6)) which was 10 mm. This result is contradicting to the value of σ found in the dispersion relation measurements (Chapter 3), where $\sigma \approx 120 - 130$ μm at thermal equilibrium. This is somewhat surprising since the same sample geometries as well as same graphene concentrations were used. Furthermore, the nonlocal length is independent on the laser power as long as convective effects can be neglected. Although convection was observed at higher powers, it cannot explain the two orders of magnitude difference in nonlocal length in both experiments. However, different beam geometries were used, a quasi 1D highly elliptical beam profile in the dispersion relation measurements and a gaussian profile in the thermal nonlinearity setup, thus the discrepancy has so far not been analyzed with respect to the beam geometries.

In order to understand how the beam or fluid geometry influences the nonlocal length, the two dimensional heat equation with the distributed loss term is considered (DLM model):

$$\nabla_\perp^2(\Delta T) = -\frac{\alpha}{\kappa} I(r_\perp) - \frac{1}{\sigma^2}\Delta T$$

The analytical solution provides the nonlocal response function in K-space as the Lorentzian function $\hat{R}(K_x, K_y) = 1/(1 + \sigma^2 K_x^2 + \sigma^2 K_y^2)$, while its Fourier transform is a zero-order Bessel-K function in real space. As discussed previously, when using a gaussian beam with radii $w_x = w_y \approx W$ (W: medium radius), the nonlocal length is approximately given by the medium dimensions, i.e. W and thus superfluid flow would

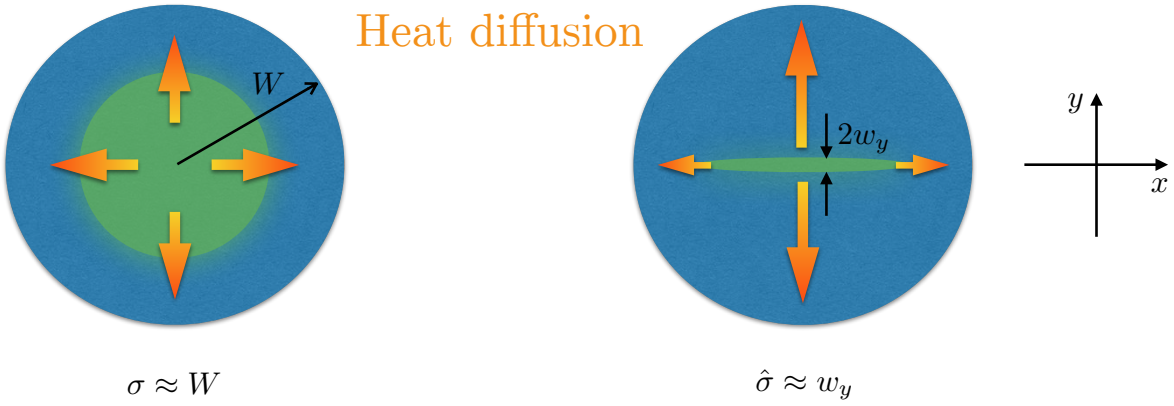

Figure 4.3: Sketch of heat diffusion in the x-y-plane (orange arrows). Highly asymmetric beam geometries lead to an enhanced heat flow along the minor beam axis and effectively reduces nonlocality along the major beam axis.

require wavelengths much larger than the medium itself and is experimentally unrealistic. The more interesting situation occurs with a beam profile that is highly elliptical i.e. $w_y \ll w_x$, that can be achieved by loosely focusing with cylindrical lenses. The focusing leads to a temperature distribution inside the sample with a width that scales according to w_y along the y-axis and thus the spatial derivative along y can be approximated $\partial^2(\Delta T)/\partial y^2 \approx -\Delta T/w_y^2$. In other words, the heat diffusion occurs mainly along the y-axis due to the higher temperature gradients, effectively reducing heat transport along the x-axis. Using this approximation, the 2D heat equation reduces to an effectively 1D equation with an additional loss term proportional to $1/w_y^2$:

$$\frac{\partial^2}{\partial x^2}(\Delta T) = -\frac{\alpha}{\kappa} I(r_\perp) - \left(\frac{1}{\sigma^2} + \frac{1}{w_y^2}\right)\Delta T \tag{4.3.1}$$

$$\frac{\partial^2}{\partial x^2}(\Delta T) = -\frac{\alpha}{\kappa} I(r_\perp) - \frac{1}{\hat{\sigma}^2}\Delta T \tag{4.3.2}$$

and results in the effective nonlocal length $\hat{\sigma} = w_y\sigma/\sqrt{w_y^2+\sigma^2}$ and corresponding response function $\hat{R}_{1D} = 1/(1+\hat{\sigma}^2 K_x^2)$. Note that if $w_y \ll \sigma$, the effective 1D nonlocal length acting along the x-direction is approximately given by the minor beam radius $\hat{\sigma} \approx w_y$. Therefore, in a highly elliptical beam geometry it is possible to effectively reduce the nonlocality along the major axis and establish superfluidity for realistic experimental scenarios, i.e. for wavelengths much smaller than the fluid itself.
A different perspective on the tailoring of the nonlocal response by the beam geometry can be gained by considering the largest possible wavelengths that can be supported along the minor beam axis, $\Lambda_y < w_y$ or $K_y > 1/w_y$. To obtain the response function in K-space, the full 2D heat equation is numerically solved for parameters sim-

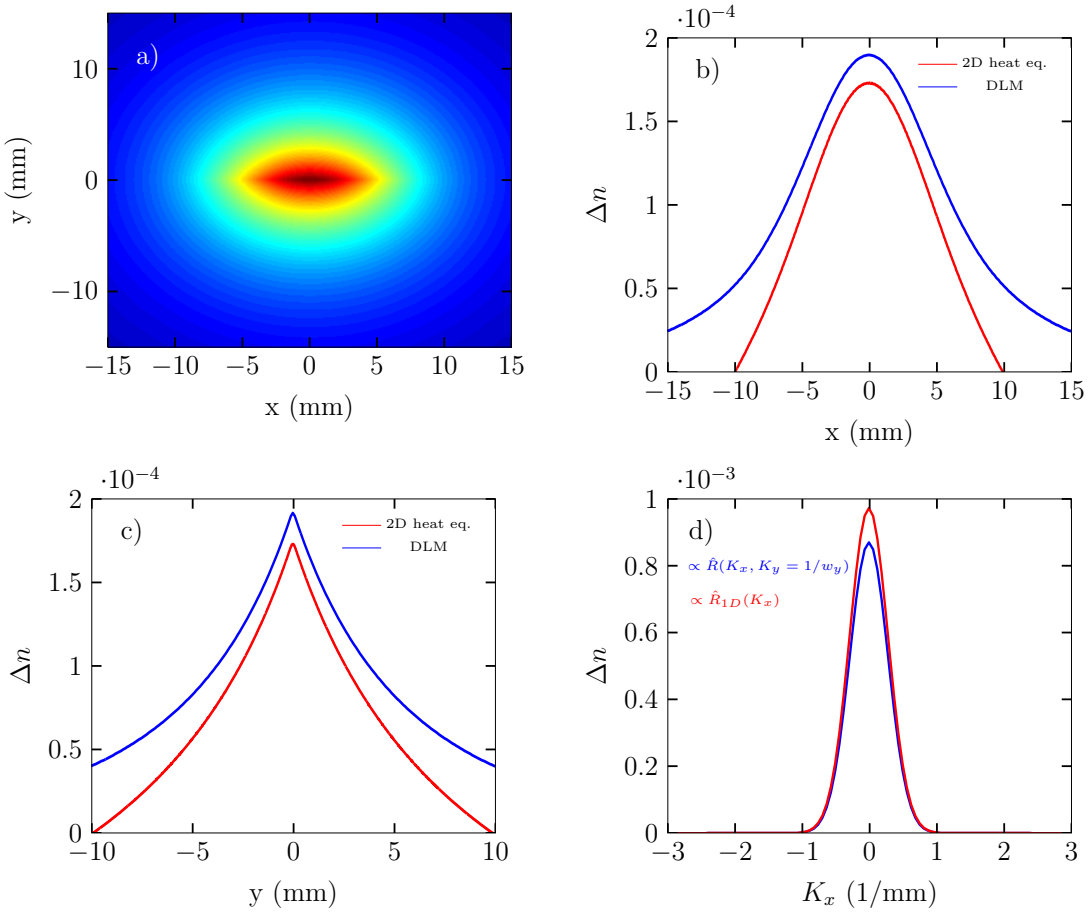

Figure 4.4: a)-c) Numerical solution of the 2D heat equation, showing the spatial nonlinear response $\Delta n(x, y)$ for an highly elliptical beam profile in comparison with the analytical solution of the DLM model. (Parameters are inspired by the experiment: $w_x = 7$ mm, $w_y = 120$ μm, $\alpha = 0.035$ cm^{-1}, $I_0 = 7$ W/cm^2, $W = 1$ cm). d) K-space: Comparison between the 2D nonlinear response $\Delta\hat{n}(K_x, K_y) = \gamma\hat{R}(K_x, K_y)\hat{I}(K_x, K_y)$ in the limit $K_y = 1/w_y$ (blue) and the effective 1D nonlinear response $\Delta\hat{n}(K_x) = \gamma\hat{I}(K_x, K_y = 0)/(1 + \hat{\sigma}^2 K_x^2)$ (red).

ilar to the experiments in Chapter 3. Using a highly elliptical beam geometry with $w_x = 7$ mm, $w_y = 120$ μm and Intensity $I_0 = 7$ W/cm^2, the steady state temperature profile and hence the spatial distribution of $\Delta n(x, y)$ is compared to the analytical solution of the DLM model using Eq. (2.2.6) and (2.3.5) and the results are shown in Fig. 4.4 a)-c). Both solutions are in very good agreement and allow to calculate $\Delta\hat{n}(K_x, K_y) = \gamma\hat{R}(K_x, K_y)\hat{I}(K_x, K_y)$ by means of a 2D Fourier transform as a valid description of the K-space nonlinear response. Now, only waves with wave vectors $K_y > 1/w_y$ are supported by the fluid geometry, so the effective nonlinear response $\Delta\hat{n}(K_x, K_y)$ is approximated in the limit $K_y > 1/w_y$. It was found that either integrating over all $K_y > 1/w_y$ or simply taking $K_y = 1/w_y$ yields almost identical results.

For the latter case, the nonlinear response $\Delta\hat{n}(K_x, K_y = 1/w_y)$ is shown in Fig. 4.4d) in comparison to the nonlinearity obtained via the previously introduced effective response function $\hat{R}_{1D}$: $\Delta\hat{n}(K_x) = \gamma\hat{I}(K_x, K_y = 0)/(1 + \hat{\sigma}^2 K_x^2)$. The almost identical results confirm that the nonlocal response function can indeed be described as an effectively 1D response function with a nonlocal length with approximately the minor beam radius. The different results for the nonlocal length found from the dispersion relation measurement in Chapter 3 and those from Chapter 2 can be explained as due to the different beam geometries. It has to be emphasized that the physical nonlocal length of the whole system is always determined by the boundary conditions, regardless of the beam size or geometry. The photon fluid dynamics however, are determined by the effective nonlocal length of the order of the smallest beam dimension. Therefore, tailoring the beam geometry allows to tune the effective nonlocality and establish superfluid dynamics over a wide range of wavelengths that would be otherwise impossible. In conclusion, the fundamental nonlinear properties of the thermal nonlinear medium have been characterised that are crucial in interpreting the dynamics in the photon fluid that lay the foundation of the understanding of superfluidity in these systems.

4.4 Superfluid flow and vortex nucleation

So far, it was shown that the propagation of small amplitude waves in a nonlocal photon fluid follow the Bogoliubov dispersion relation and in particular in the long wavelength limit the linear relationship $\Omega = c_s K$ confirms signatures of superfluidity. These results were obtained in a quasi 1D photon fluid using a highly elliptical beam profile that, as was previously shown, allows to reduce the effective nonlocal length by roughly two orders of magnitude. However, a direct observation of superfluid phenomena such as frictionless flow or vortex shedding has not been presented yet. So following the idea of superfluid scattering experiments [14, 43], the superfluid flow around an extended obstacle and onset of its breakdown was studied.

The idea is to create a flow in the photon fluid around an ideally small, rigid obstacle and investigate the dynamics for different Mach numbers M, in fluid dynamics defined as the ratio of the relative flow velocity to the obstacle and the speed of sound, $M = v_f/c_s$. The experimental layout is shown in Fig. 4.5 where the beam is loosely focused by a set of cylindrical lenses (f_1=200 mm, f_2=50 mm) to yield beam radii $w_x \approx 1$ cm and $w_y \approx 210$ μm. This beam is launched through an 18 cm long sample filled with a methanol/graphene solution with an absorption coefficient $\alpha = 0.035$ cm^{-1} to ensure optimum thermal nonlinearity. This is necessary as higher nonlinearity yields faster dynamics that are crucial regarding the limited temporal evolution in the photon fluid

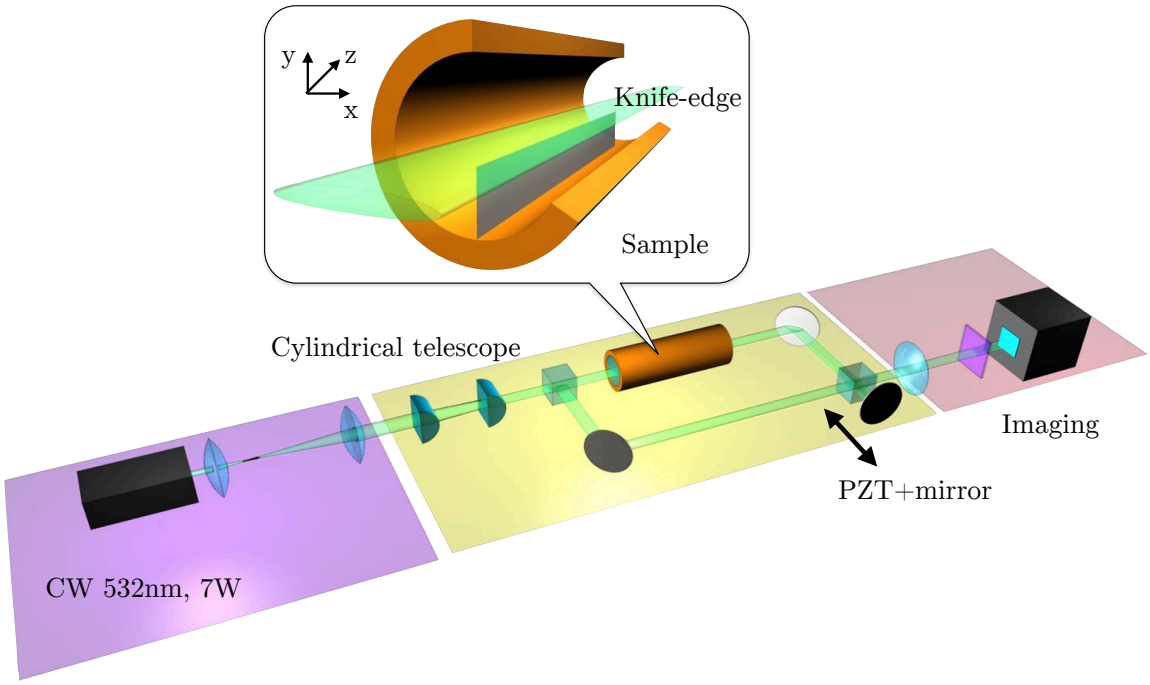

Figure 4.5: Experimental setup. A 532-nm CW-laser beam with an highly elliptical spatial beam profile is launched into a sample (2×18 cm) filled with a methanol-graphene solution. A knife blade is installed inside the sample and slightly tilted with respect to the propagation direction at an angle θ that determines the flow of the photon fluid. A plane wave reference beam is used to measure the spatial phase profile of the pump beam with spatial phase interferometry.

determined by the sample length. The graphene concentration is chosen to maximise the nonlinearity and hence the dynamics in order to observe superfluidity and vortex nucleation. The obstacle consists of an aluminium knife blade installed in the medium along the beam path such that the beam propagates at a small angle θ with respect to the knife blade, introducing a flow $v_f = (c/n_0)\sin(\theta)$ along the x-axis. Finally, the sample is placed in one arm of a Mach-Zehnder interferometer so as to probe the output beam profile with a plane wave reference beam. At the second beam splitter, a mirror on a piezo-controlled delay stage is introduced to retrieve the relative phase of the pump beam by means of the spatial phase interferometry described in Section 2.4.2. The output of the sample is finally imaged with a 4× magnification onto a CCD camera.

To get an estimate of the nonlinearity, the value obtained from the best fit of the dis-

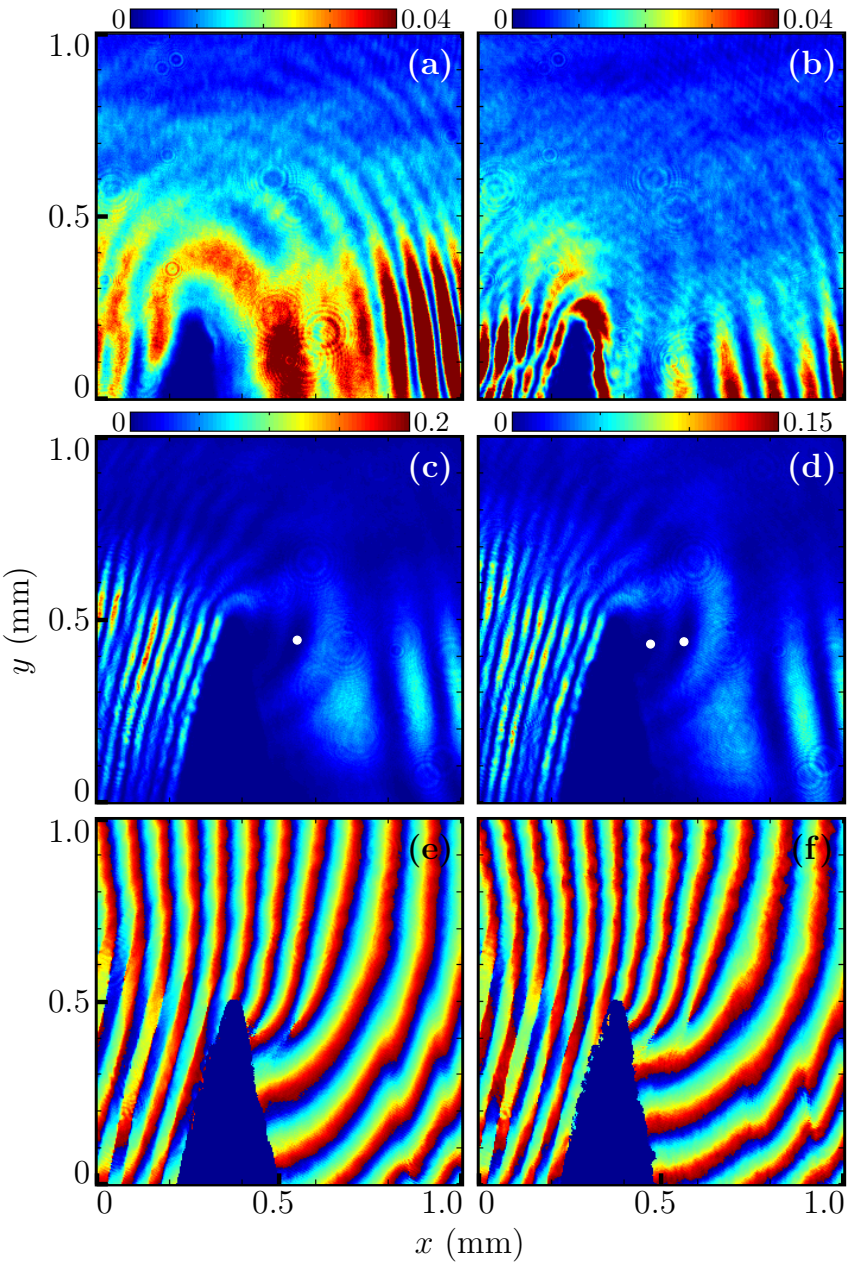

Figure 4.6: Experimental measurements of the nearfield beam profile at the sample output $I(x, y)/I_0$, normalized by input beam intensity I_0. (a) and (b) $I(x, y)/I_0$ is capped at 0.04 to emphasize waves scattered from the obstacle into the upper right-hand region of each panel. (a) $v_f \sim 6 \times 10^5$ m/s and $I_0 = 0.2$ W/cm^2 (linear propagation, i.e. non-superfluid regime). (b) $v_f \sim 6 \times 10^5$ m/s and $I_0 = 3.8$ W/cm^2 (nonlinear propagation, i.e. superfluid regime with $v_f/c_s \sim 0.5$). (c) and (d) show superfluid instability at higher flow speed, $v_f \sim 1.3 \times 10^6$ m/s: (c) $I_0 = 4.0$ W/cm^2 i.e. $\Delta n = 3.0 \times 10^{-5}$ and $v_f/c_s \sim 1.2$ and (d) $I_0 = 6.8$ W/cm^2 i.e. $\Delta n = 5.2 \times 10^{-5}$ and $v_f/c_s \sim 0.9$. White circles indicate the position of the vortex singularities obtained from the corresponding phase diagrams shown in (e) and (f), respectively [83].

persion relation is $|\Delta n| = |n_2| I_0 = 7.3 \times 10^{-6}$ is used (see Fig. 3.9). Note that $|\Delta n|$ does not correspond to a physical parameter in the system since the nonlinearity is nonlocal (the physical nonlinearity at a point (x,y) at given intensity is evaluated according to Eq. (2.2.6)), but is understood to be the determining parameter of the dynamics in the hydrodynamic limit ($\Lambda > 1/\sigma, 1/\xi$). Considering a slightly higher absorption than in Chapter 3 (the ratio of the total absorbed power is ~ 1.5) the nonlinearity in this experiment is estimated to be $|n_2| \approx 7.8 \times 10^{-6}$ cm^2/W. Therefore, intensities of $I_0 = 4 - 7$ W/cm^2 were used to gain sound speeds of about $c_s = 1 - 1.4 \times 10^6$ m/s and thus superfluid behaviour is expected for comparable smaller flow speeds. However, the previously discussed critical Landau velocity is only applicable for obstacles of the order of the healing length ($\sim 30 - 40$ μm), while the knife blade certainly exceeds these dimensions. It was reported that in the vicinity of such extended obstacles, the local flow velocity becomes supercritical even in the case of a subcritical flow $v_f < c_s$ far away from the obstacle [88]. This is understood by the local bending of streamlines around the extended obstacle which is modifying the local flow speed. Therefore, in addition to the reducing effect of the nonlocality on the critical flow speed, a breakdown of superfluidity is expected at values lower than the speed of sound.

The detailed dynamics of a flow along the positive x-direction around the obstacle is shown in Fig. 4.6. The nearfield images present a magnified section of the whole field of view, where the obstacle is visible as a dark triangular shadow in the lower part of the image. At low speeds $v_f \sim 6 \times 10^5$ m/s and low intensity $I_0 = 0.2$ W/cm^2 (Fig. 4.6a), the fluid is in the non-superfluid regime and waves are being scattered radially from the tip. This is basically a similar phenomenon one would observe in a flowing water stream hitting a barrier. As the intensity is increased, the fluid enters the superfluid regime, i.e. $v_f/c_s \sim 0.5$, and the radially scattered waves in the top right corner are highly suppressed (Fig. 4.6b)). This is a consequence of the onset of superfluid, dissipationless flow. Note that this does not display a fully frictionless flow yet, since the system has not had time to be in equilibrium, i.e. as the beam enters the nonlinear medium, the photon superfluid is suddenly switched on and evolves for a given, limited time. In that time, the waves that have been scattered in the non-superfluid state have not propagated much farther. As the flow is increased ($v_f \sim 1.3 \times 10^6$ m/s), the breakdown of superfludity is observed as the nucleation of quantised vortices in the downstream region of the obstacle. In the linear i.e. non-superfluid regime, a shadow of the obstacle is observed in the downstream region, but in the nonlinear i.e. superfluid regime, the light intensity flows around the rigid obstacle and fills in the dark region just as in a fluid. Clearly visible, a series of vortices that appear as dark spots in the intensity profiles, are nucleated in the vicinity of the tip (Fig. 4.6c) and d)). The correspond-

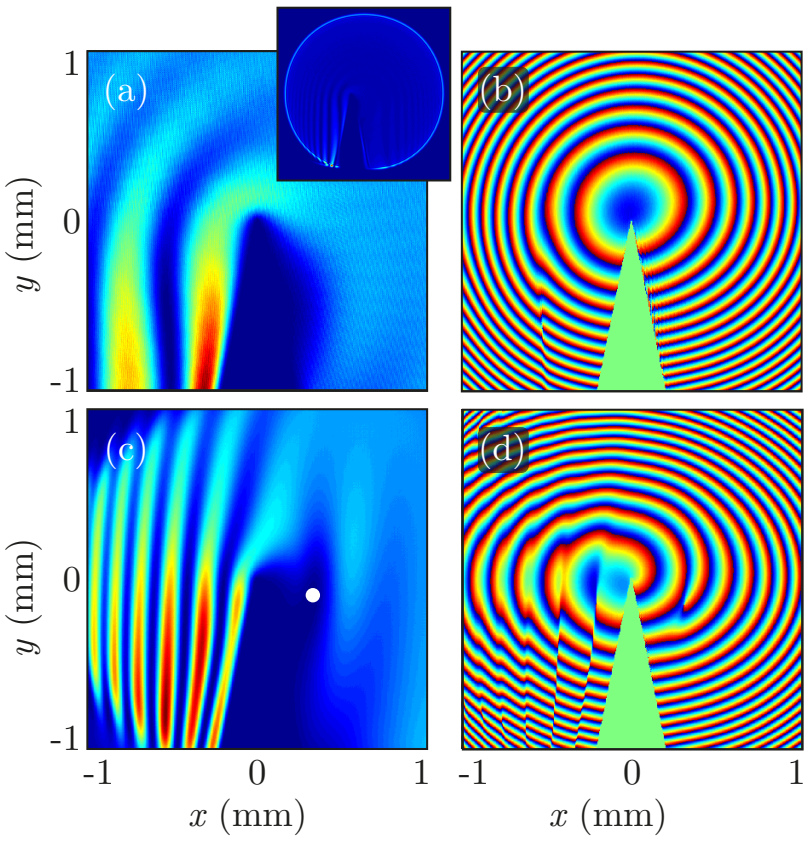

Figure 4.7: Numerical simulations. Circular input pump beam with 1 mm ($1/e^2$) beam radius: (a) zoomed in intensity profile at the output of the nonlinear medium. The full beam profile is shown in the inset. (b) phase profile for the circular beam (wrapped between $-\pi$ and $+\pi$. Elliptical input pump beam ($w_x = 1$ mm, $w_y = 0.15$ mm): (c) intensity profile with a white circle indicating the position of a vortex nucleated from the obstacle, and corresponding phase profile (d). All simulations are performed under identical conditions, aside from the input beam profile. Simulation parameters are: $I_0 = 2.65$ W/cm^2, propagation length $L = 18$ cm, fluid flow speed $v_f = 1.0 \times 10^6$ m/s, and nonlocal interaction length $\sigma = 1$ cm. Taken from Vocke et al. [83].

ing phase profiles confirm the quantisation of the vorticity around a phase singularity. Furthermore, the drag forces from the obstacle exerted on the fluid are visualised by the bending of the phase pattern around the obstacle. The flow is proportional to the phase gradient, hence the drag force is reflected in the change of flow direction behind the obstacle (Fig. 4.6e) and f). At higher intensities, more vortices are shed although v_f/c_s is decreasing at the same time. However, higher sound speeds also lead to faster dynamics in a certain limit (i.e. waves travel at a higher speed) and thus increasing the nonlinearity has similar effects as increasing the temporal evolution of the system. Therefore, the two vortices at higher intensity in f) are due to the faster sound speed.

At even higher flow speeds, the transition from vortex nucleation to the emission of

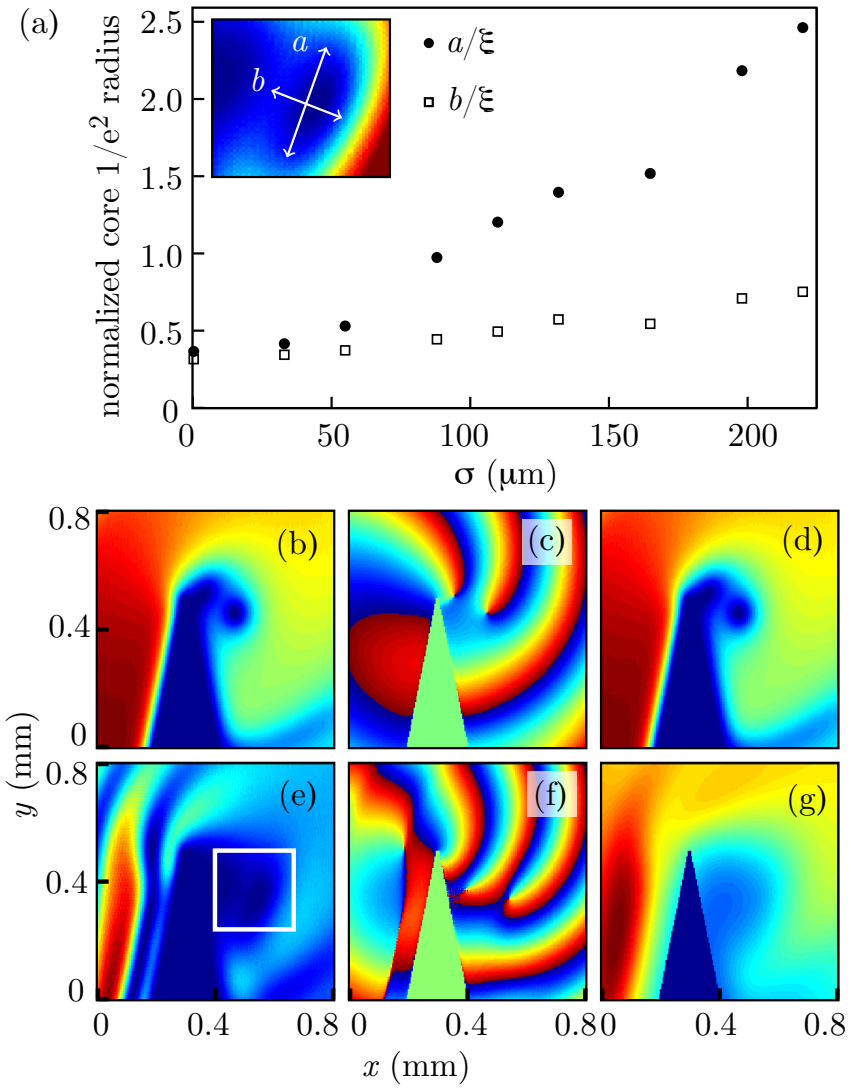

Figure 4.8: Numerical results: (a) Plot of vortex core $1/e^2$ radii, a and b, normalized to the local healing length ξ, versus σ. The inset, corresponding to the white region in (e), shows a vortex core with labeled major axis a and minor axis b. (b) normalized beam intensity, $I(x,y)/I_0$, (c) phase $\phi(x,y)$ and (d) nonlinear potential, $\Delta n(x,y)/\Delta n$, for a purely local superfluid after 20 cm of propagation, with $v_f/c_s = 0.56$, $\Delta n = -1.2\times10^{-5}$, and $1/e^2$ beam radii $w_\mathrm{x} = w_\mathrm{y} = 1$ mm. (e), (f) and (g) show the corresponding profiles for a nonlocal superfluid with $\sigma = 110$ μm, and $\Delta n = -2.4\times10^{-5}$ [83].

hydrodynamic dark soliton was recently reported for exciton-polariton fluids [16] and is in principle also observable in this system. However, these are created by strong velocity gradients in the vicinity of extended obstacles that eventually lead to density variations of the order of the healing length, that may be suppressed in the presence of nonlocality. This is still to be confirmed and is subject for future investigations.

For more insight into the vortex shedding process and the impact of nonlocality, numer-

ical simulations based on a split-step method to numerically integrate the full NLSE were performed with parameters close to the experiment. A Lorentzian shaped nonlocal response function $\hat{R}$ with a nonlocal length $\sigma = 1$ cm was used to describe the nonlinear response. As in the experiment, a triangular shaped obstacle with the same dimensions is immersed in the transverse beam profile. First, the influence of the beam geometry was tested by simulating the scattering experiment with a round and an elliptical beam at a constant intensity $I_0 = 2.65$ W/cm^2. Fig. 4.7a) and b) show the nearfield and corresponding phase in the case of a round beam where no particular features of vortex nucleation is observed. In the case of an elliptical beam with a minor axis of $w_y = 150$ μm (Fig. 4.7c) and d)), a vortex is spawned in the downstream region of the obstacle matching the results of the experiment and thus confirms the superfluid state of the fluid. This result corroborates the theoretical prediction of a purely geometric interpretation of the geometry induced reduction of nonlocality. Furthermore, the vortices in the experiment as well as in the simulation have an elliptical shape. The vortex dimension is usually given by the healing length that is determined by the strength of the kinetic and potential energy in the NLSE. Therefore, local variations in the density caused by the smoothing of the nonlocality in the presence of an extended obstacle can explain such elliptic shapes. Fig. 4.8a) shows the vortex core radii $1/e^2$ a, b as a function of nonlocality. The radii are normalised to the local healing length in order to account for local density variations in the fluid. Due to the impact of nonlocality in the vortex nucleation, a constant ratio of intensity and flow speed $v_f/c_s \sim 0.56$ is chosen for each σ so that one vortex core is clearly observed. The results reveal that in a purely local medium, i.e. $\sigma = 0$ μm, the ratio of the beam radii $a/b \sim 1$ and the cores are of circular shape, whereas with increasing nonlocality, the vortex cores develop a more and more elliptical shape. The effect of nonlocality on the intensity, phase and effective nonlinear potential energy $\Delta n(x, y)/\Delta n$ is shown in Fig. 4.8b)-g). In the purely local case, the potential energy as well as the vortex core are of circular shape. In the nonlocal case ($\sigma = 110$ μm), the elliptical vortex core is reflected in the corresponding potential energy profile. This asymmetry in the potential is a result of the nonlocal smearing of the overall fluid density. In particular, the spatial extent of the knife blade is much larger in the nonlocal case resulting in an elongated potential valley along the y-axis. The deformation of the vortex cores is therefore a consequence of the obstacle shape in addition to a nonlocal nonlinearity.

4.5 Conclusion

The physical nonlocal length in thermal nonlinear media is given by the dimension of the system boundaries and it is therefore impossible to study perturbative photon fluid dynamics that require transverse dimensions much larger than the range of nonlocality. Furthermore, large nonlocal lengths effectively suppress the photon-photon interactions and therefore drastically alter the linear dispersion relation that is necessary to observe superfluidity. As a consequence, a superfluid state of light is experimentally unrealistic in a medium with strong nonlocality. However, it was shown that by using highly asymmetric fluid geometries, the effective nonlocal length that governs the dynamics in the system can be reduced by several orders of magnitude and re-establish conditions under which superfluidity is observed. This conclusion is reached by quantitatively modelling the heat flow by means of a distributed loss model and is confirmed experimentally as well as numerically. The beam geometry was chosen such that the degree of nonlocality was reduced by two orders of magnitude, and superfluid phenomena were observed for different flow velocities. The hallmark signature, the nucleation of quantised vortices confirms the onset of superfluid turbulence and is distinguished from hydrodynamic turbulence in a normal fluid.

Although the detailed analysis following the thermal modelling of the current underlying system was necessary to quantitatively explain the physical mechanisms responsible for tailoring the nonlocality, it must be emphasised that the general conclusions apply to any form of nonlocality. As was outlined, a general perspective can be gained by considering geometric parameters of the system to justify a reduction in the effective nonlocal length. This also finds confirmation in the numerical simulations with balanced beam dimensions, where no vortex shedding or dissipationless flow could be observed. Therefore, thermal photon fluids bear a strong resemblance to dipolar BECs, that show nonlocal effects due to long range dipole-dipole interactions [89]. Furthermore, the nonlocal interaction with an extended obstacle affects the shape of the vortex cores, that were found to be of elliptical shape. This effect can be understood as a smoothing of the local effective nonlinear potential in the vicinity of the obstacle that is translated into an anisotropic healing length determining the core shapes.

Summarising, the superfluid condition in this photon fluid is vital for studies regarding analogue gravity experiments since the linearity of the low-momentum dispersion relation allows to build a valid analogy towards spacetime metrics. In that sense, a constant speed of sound corresponds to the constant light speed in vacuum that guarantees local Lorentz invariance [17].

Chapter 5

Analogue Gravity

It is known that elementary excitations in an inhomogeneous flow behave analogous to scalar fields in curved spacetime. This Chapter presents the experimental realisation of a two-dimensional rotating spacetime in a photon fluid that resembles a Kerr black hole. The measurement of the flow and sound speed allows to identify an acoustic event horizon and ergosphere in (2+1) dimensions that opens the door to study Penrose superradiance.

5.1 Introduction

5.1.1 Black holes in a nutshell

General relativity is the best theory we have describing gravity and its most important prediction is the curvature of spacetime through massive objects. The shape of spacetime itself is described by a metric which defines an infinitesimal physical distance in space and time, in a given set of coordinates. In the presence of massive objects, the metric is distorted in such a way that test bodies move along non-trivial 'curved' trajectories, what is commonly known as *gravity*. For bigger masses, the curvature or distortion and hence their gravitational field becomes stronger. By far one of the most exciting consequences are black holes, which are defined by a region of spacetime where nothing, not even light, can escape from. In more detail, being a solution of the Einstein equations, the curvature of spacetime of a spherically symmetric massive object is described by the *Schwarzschild* metric in the Schwarzschild coordinates (t,r,θ,ϕ):

$$ds^2 = \left(1 - \frac{r_s}{r}\right) c^2 dt_s^2 - \left(1 - \frac{r_s}{r}\right)^{-1} dr^2 - r^2 d\Omega^2 \tag{5.1.1}$$

Where $r_s = 2GM/c$ is the Schwarzschild radius, dt_s the Schwarzschild time and $d\Omega^2 = d\theta^2 + sin^2\theta d\phi^2$ the angular line element. This metric describes, for example, the spacetime in the vicinity of a massive stellar object with mass M. Equation (5.1.1) bears a singularity which becomes relevant if the entire mass M is confined in a volume with radius R smaller than the Schwarzschild radius r_s [90]. The apparent singularity at the point $r = r_s$ defines a boundary in spacetime, called the *event horizon* but it is important to note that there is no physical singularity at $r = r_s$, being merely a singularity of the Schwarzschild coordinate system. Beyond this boundary, the gravitational curvature is so strong, that nothing can escape and therefore, such objects are called *black holes*.

In 1974, Stephen Hawking showed that black holes are not entirely black by predicting a thermal radiation emitted from the event horizon [91]. This effect arises from quantum mechanics which shows that the vacuum is not entirely empty, but is a teeming soup of virtual particles in constant flux that possesses a non-zero energy content. Fluctuations of this ground state create virtual matter/antimatter particles, which annihilate again shortly after being created [92]. He proposed that these pairs, excited from the vacuum state, could be separated in the vicinity of an event horizon. One particle could be sucked into the black hole while the other could escape and become a real entity of spacetime. His results followed a thermodynamical treatment of black holes by Bekenstein [93] and he derived an expression for the temperature of a black hole,

being dependent of the gravitational field strength κ at the event horizon.

$$T = \frac{\hbar\kappa}{2\pi k_b c} = \frac{\hbar c^3}{8\pi k_b GM} \tag{5.1.2}$$

Thus, the emitted radiation has a thermal spectrum of a black-body with temperature T. This tells us that the temperature of a solar mass black hole would be of the order of $10^{-9}K$, thus emitting a very cold radiation compared to the cosmic microwave background ($T_{CMB} = 2.73K$) which makes this theory experimentally nearly untestable. However, there has been extensive research in analogue systems that show possible experimental verifications on such problems in black hole physics [94, 95].

5.1.2 Black holes in the laboratory

It was Unruh in 1981, who proposed that sound waves in a flowing medium like water, are propagating in the same way than scalar fields do in a gravitational field. He showed that the dynamical equations of motion from fluid dynamics can be cast into that of a scalar field propagating in the modified geometry of a gravitational field [94]. Simply speaking, the curvature of spacetime from a massive object can be mimicked by an inhomogeneous flow of a classical fluid in which waves can propagate. A horizon exists at a surface whenever the wave propagation speed exceeds the local flow speed orthogonal to that surface. This similarity leads to a useful analogy where parts of general relativity can be identified with parts of non-relativistic fluid mechanics.
The main driver for the interest in analogue models was certainly the prospect to observe Hawking like emission from an analogue black hole since Hawking radiation is a kinematic effect that is well covered with the ingredients that come with most analogue systems. Simply speaking, these involve some quantum fields that live on a classical background creating an effective spacetime. If the spacetime is such that there exist a horizon for the quantum field propagation, then a thermally distributed emission of particles is expected to appear [91, 96]. After Hawkings discovery of black hole evaporation, it was soon realised that the derivation of a thermal emission relied on the existence of ultra high frequencies at the horizon with wavelengths shorter than the Planck scale. In a nutshell, the thermal spectrum for an observer at infinity is infinitely blue-shifted at the black hole horizon if back propagated in time, and the corresponding high energies would rely on physics that are currently unknown, i.e. possibly requiring a full quantum theory of gravity. This so called *Trans-Planckian* (TP) problem unveils the limits of Einstein gravity and quantum field theory and hints that a combined quantum theory of gravity is needed to tackle the problem [97].

For this reason, a major interest was laid on analogue models where the underlying structure is well understood, i.e. the fluid wave equation beyond the long-wavelength limit are known and can therefore be used to shed more insight into the Hawking process. For shallow water waves the long wavelength limit is given by the water depth, for quantum fluids such as BECs or photon fluids, the long wavelength limit is defined by the healing length which is the sort of analogue to the Planck scale in quantum gravity. Beyond this scale, the wave dispersion relation is not linear anymore and the equation of motion can no longer be described by a second order wave equation in an effective spacetime metric. Since the underlying physics beyond the "analogue Planck scale" is well understood for most analogue models, one can use the full wave equations (with higher order derivatives) to study analogue Hawking radiation. The resulting dispersion introduces a natural cut-off that prevents infinite blue shifting and hence ultrahigh frequencies that circumvents the TP problem. The existence of Hawking radiation in the presence of a high frequency cut-off was studied theoretically in the early nineties [97,98] and led to the idea of using dispersive gravity waves in trans-sonic flows as experimental testbed [99].

An important question regarding the analogy has to be asked of how important the quantum fluctuations in the considered systems are. Classical fluids yield a Hawking temperature of the order of nK which is too small to provide a measurable contribution over thermal fluctuations. Although being far from being considered as a quantum system, fluids have been used to study classical scattering between positive and negative norm modes in trans-sonic flows [100], which is known as the *stimulated* Hawking process. Instead of using random fluctuations that naturally live in the system, a defined ingoing frequency is excited that scatters off a horizon and non-zero scattering amplitudes of positive and negative norm modes can be measured. The results indeed supported the viewpoint that the thermal nature of the black hole emission does not rely on Planck scale physics. That shows that even classical analogue gravity systems are a useful tool to study black hole evaporation.

The measurement of the analogue *spontaneous* Hawking effect, i.e. the emission of quanta from a vacuum state requires analogue systems with measurable quantum fluctuations. With the rapid development of atom traps, ultra-cold dilute Bose Einstein condensates became a promising candidate since they operate at temperatures in the nano-Kelvin scale [101–103]. In fact the measurement of analogue Hawking radiation in a BEC has been recently reported and is currently heavily debated in the community [104].

5.1.3 Black holes with a twist

Today, there exist a plethora of quantum analogue systems, from BECs in condensed matter systems [18,19] (semiconductor exciton polariton condensates) to nonlinear optics in fibres [105] and silica glass [106]. Whereas most of these systems display a geometry involving one spatial and one temporal dimension (so called (1+1)D), quantum fluids of light in a propagating geometry have been proposed to realise a (2+1)D geometry [17,77]. This allows to create 2D spacetime geometries and hence the realisation of rotational flow next to radial flow. This would lead to an experimental testbed for rotating (Kerr-like) black holes, that are surrounded by a region that drags the spacetime fabric along the rotation. Like in a draining bathtub, the angular velocity increases towards the rotation axis up to a point where the total velocity equates the speed of light, the stationary limit beyond nothing can stay at rest for an observer at infinity. This creates the so-called ergo region that is defined by two surfaces the outer limit of which is the stationary limit described above, whereas the inner one is the event horizon, i.e. where nothing can escape to infinity. The ergoregion is located outside the event horizon in the plane of rotation and, as was proposed by Penrose, could be used to extract rotational energy from a black hole.
His idea follows a Gedankenexperiment, where a particle with energy E is dropped into the ergoregion where it is scattered and if escaping to infinity, carries away additional energy. It is understood by analyzing the energy of a test particle on a trajectory through the ergo region. In General Relativity, the energy is defined as the scalar product between the particle 4-momentum and a vector-field, the so called time-like *Killing* vector field, that describes time translation symmetry in General Relativity. For example, the scalar product with the time-like Killing vector field $V = (1, 0, 0, 0)$ describes the time-translation symmetry and hence energy conservation. With the Killing vector and 4-momentum $p = (p^0, p^1, p^2, p^3)$ the energy is thus given by:

$$\begin{aligned} V \cdot p &= g_{\mu\nu} V^\mu p^\nu && (5.1.3)\\ &= g_{0\nu} p^\nu && (5.1.4)\\ &= g_{00} p^0 + \sum_{i=1}^{3} g_{0i} p^i && (5.1.5) \end{aligned}$$

Here, $g_{\mu\nu}$ is the spacetime metric. For example, in flat Minkowski spacetime (i.e. $r \to \infty$), the off-diagonal components of $g_{\mu\nu}$ vanish and the sum in Eq. (5.1.5) is identical to zero and the energy is given by p^0. Now for the Kerr metric, some of these off-diagonal elements do not vanish and as it turns out, depending on the trajectory of the particle, may lead to an energy that is negative as measured from infinity. Specifically, Penrose

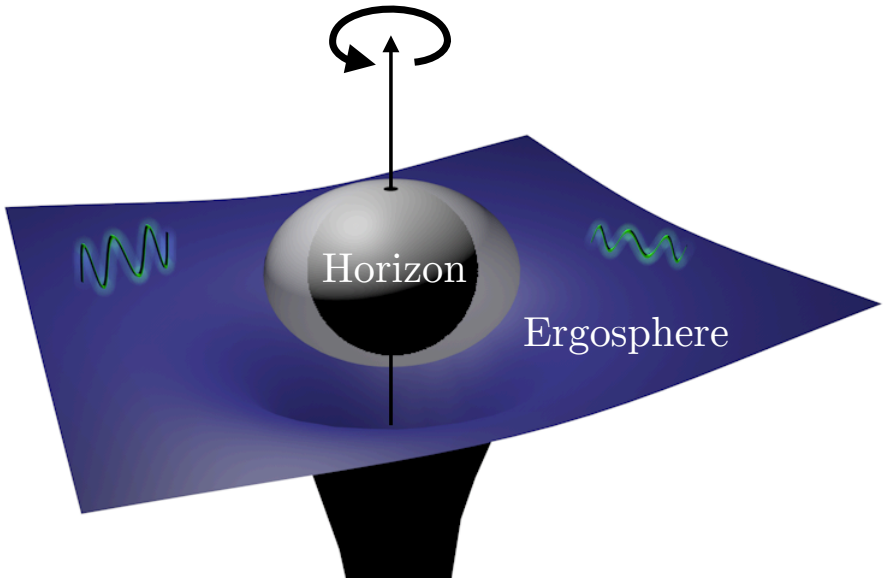

Figure 5.1: Superradiant scattering from a rotating black hole.

considered a scattering process where the particle decays into two components inside the ergoregion where one has negative energy, i.e $-E_1$ and will be swallowed by the event horizon. The other part escapes to infinity, but due to energy conservation, now carries more energy than the total incident energy $E_2 > E$, where the excess is provided by the angular momentum and mass of the Black hole [107]. The extracted energy E_1 and extracted angular momentum J_1 satisfy the very general relation:

$$E_1 - aJ_1 > 0 \tag{5.1.6}$$

where a is the specific angular momentum of the black hole and J the angular momentum of the particle. Therefore, if the infalling particle has negative energy, the gain $-E_1$ is limited by the angular momentum $-J_1$. It was noted by Zeldovich, that this so called *Penrose process* has an analogue for electromagnetic waves scattered from a rotating cylinder. He calculated for such a cylinder with frequency Ω made of absorbing material, that incident electromagnetic modes with frequencies ω impinging on it would amplify if

$$\omega - m\Omega < 0 \tag{5.1.7}$$

is satisfied, where m is to the axis of rotation according azimuthal quantum number [108]. It was later realised that this superradiant scattering is a rather general physical process [109], while rotational superradiance is one phenomenon belonging to a wider class of processes that allow stimulated and spontaneous emission of energy. These include the superluminal motion of objects that allow energy dissipation in a

transparent medium, such as the anomalous Doppler effect or the Vavilov-Cerenkov effect. From a thermodynamic viewpoint, the effect can be understood by the second law of thermodynamics that demands the change of entropy must not decrease. Considering a superluminal moving object at velocity $\vec{v}$ in a transparent medium with incident radiation. It can be shown that in the presence of dissipation, this condition is met if

$$\frac{\partial S}{\partial t} \propto (\omega - \vec{v}\vec{K})a(\omega) > 0 \tag{5.1.8}$$

holds true [109]. Here K is the objects momentum and $a(\omega)$ denotes the frequency dependent absorption coefficient that must become negative if $w < \vec{v}\vec{K}$. This example presents the effect for inertial motion, but the same argument can be found for rotational motion where $\vec{v}\vec{K}$ is replaced by $m\Omega$. It is therefore thermodynamically favourable for such a system to emit radiation.

In practical terms, superradiance is a classical scattering mechanism in which the total reflected amplitude of a wave is larger than the total incoming amplitude for a specific range of frequencies, depending on the energy of the scattering potential [110]. In the specific case of black hole superradiance, the radial part $u(r)$ of the scalar field in the Klein-Gordon equation is cast by means of a coordinate transformation into a very simple form [111]:

$$\frac{d^2u}{dr^{*2}} + V_{\omega,m}(r^*)u = 0 \tag{5.1.9}$$

r^* is the so-called tortoise coordinate, that goes to $-\infty$ at the event horizon and describes the radial coordinate r at $+\infty$. The effective potential $V_{\omega,m}$ has a complicated expression, but it possesses the asymptotic values

$$V_{\omega,m}(r^*) \to \begin{cases} (\omega - m\Omega_H)^2, & r^* \to -\infty \\ \omega^2 & r^* \to +\infty \end{cases} \tag{5.1.10}$$

with the angular velocity Ω_H at the horizon. With this, it was shown that Eq. (5.1.9) allows superradiant solutions for incident waves that satisfy $\omega < m\Omega_H$ [112]. The effect relies on two factors: First, the system must provide a region where a superluminal motion of an object or a wave is possible. In a rotating black hole, this is true inside the ergo region, where the spacetime itself is dragged along the rotation in a superluminal fashion. Second, the system needs some sort of dissipation, i.e for a black hole it is given by the presence of an event horizon. If there wasn't dissipation or absorption, the negative energy wave can escape to infinity and the total energy remains the same.

Summarising, in analogue models it is known that in the hydrodynamic limit, the equation of motion for elementary excitations is given by an analogue Klein-Gordon

equation. Therefore, superradiant scattering has been studied in theory for classical fluids [113–115] as well as for BECs [116, 117] and was recently proposed for photon fluids, but has not been experimentally observed yet. The advantage of the photon fluid over other analogue systems is the rather easy implementation. A rotational flow in the photon fluid can be imprinted with the use of a Laguerre-Gaussian phase in the pump beam that translates into a vortex like flow geometry. As described in Chapter 3, by measuring the intensity and phase of such a beam it is possible to identify an event horizon and ergo region and study scattering phenomena from rotating spacetimes. In the following sections, a detailed experimental approach is presented to create a rotating black hole in a photon fluid with thermal nonlinearity.

5.2 Acoustic spacetimes

A simple representation of an analogue system are sound waves in an inhomogeneous moving fluid. Like in a river, the flow will drag the waves downstream, but they are able to move upstream as long as the flow is smaller than the sound speed (Fig. 5.2). However, if the flow becomes supersonic, the waves are not able to propagate upstream anymore and are swept away downstream. The waves will therefore never reach an observer standing upstream, which is a handwaving description of an acoustic horizon that creates a region where sound cannot escape from and is known as a so-called "dumb hole" .

Considering a wave propagating at the sound speed c_s in a flowing medium at velocity $\vec{v} = (\text{-v}, 0)$, the metric can be derived in its most simple form by purely geometric assumptions [96]. Introducing (2+1) spacetime coordinates $x^\mu = (t, x, y)$, the observer at rest (lab frame) observes the sound mode propagate according to $dx' = dx - vdt$, hence the line element ds^2 in (2+1)D is given by :

$$\begin{aligned} ds^2 &= -c_s^2 dt^2 + (dx - vdt)^2 + dy^2 && (5.2.1)\\ &= -(c_s^2 - v^2)dt^2 - 2vdxdt + dx^2 + dy^2 && (5.2.2) \end{aligned}$$

This can be written in the well known form

$$ds^2 = g_{\mu\nu} dx^\mu dx^\nu \tag{5.2.3}$$

with the metric tensor:

$$g_{\mu\nu} = \begin{pmatrix} -(c_s^2 - v^2) & -v & 0 \\ -v & 1 & 0 \\ 0 & 0 & 1 \end{pmatrix} \tag{5.2.4}$$

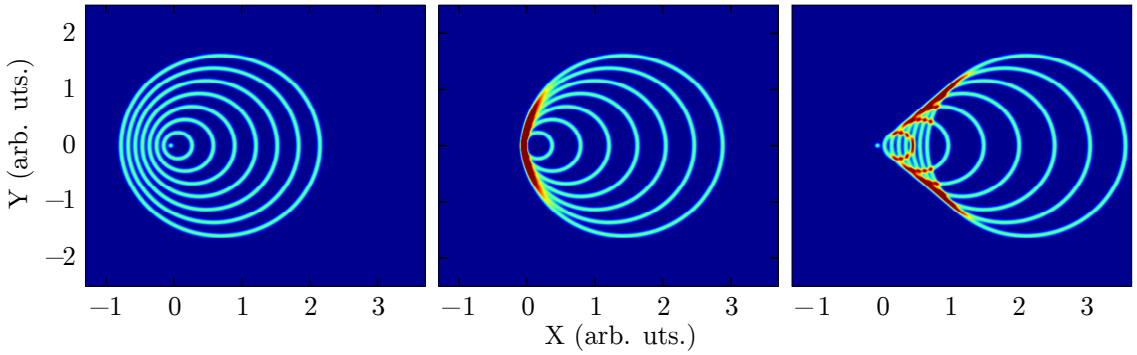

Figure 5.2: A sound pulse in a flowing medium: a) subsonic $v < c$, waves are able to propagate upstream b) sonic $v = c$, waves are blocked at a sonic horizon and creates shock fronts c) supersonic $v > c$, waves are swept downstream into the Mach cone.

Here, dx and dt measure the infinitesimal distance and time in the lab frame and Eq. (5.2.2) - (5.2.4) describe an effective spacetime for waves in a homogeneous, stationary flow v. One can find the sound cone, which are curves $x^\mu(s)$ traversed by sound waves, by solving $ds^2 = g_{\mu\nu}dx^\mu dx^\nu = 0$ and the solutions are plotted for various flow speeds in Fig. 5.2.

Now, let's assume a non homogeneous flow in two dimensions, i.e the flow becomes a function of space $v = v(r)$. In this case, it is convenient to use spherical coordinates $(t, x, y) = (t, r\cos\theta, r\sin\theta)$ and hence Eq. (5.2.2) reads

$$ds^2 = -c_s^2 dt^2 + (dr - v(r)dt)^2 + r^2 d\theta \tag{5.2.5}$$

which in the case $v(r) = c_s\sqrt{r_s/r}$ has the form of the Schwarzschild metric [118–120] in Painleve-Gullstrand coordinates and describes the spacetime around a black hole. This representation highlights, that the curvature of spacetime appears as an additional flow term in the metric and in essence, this is the important analogy that laboratory experiments are using to study analogue black holes.

The equation of motion for sound waves in the photon fluid are identical to those in an inviscid, barotropic fluid as long as the quantum pressure is negligible. In this case, the kinematics are governed by a linear dispersion that guarantees a fixed sound speed for modes larger than the healing length. This is important in the relativistic analogy since it allows to describe the kinematics with a wave equation on a curved spacetime metric. Again, using linearised fluctuations of the density ρ_1 and velocity potential Ψ_1 around a stationary background and the continuity and euler equation (Eq. (3.2.2))

and (3.2.3)) one obtains:

$$\frac{\partial}{\partial t}\rho_1 + \nabla(\rho_0\Psi_1 + \rho_1\vec{v}) = 0 \tag{5.2.6}$$

$$\frac{\partial}{\partial t}\Psi_1 + \nabla\Psi_1\vec{v} = \frac{c^2}{4k^2n_0^2}\left[\nabla\left(\frac{\nabla\rho_1}{\rho_0}\right) - \frac{\rho_1}{\rho_0}\nabla\left(\frac{\nabla\rho_0}{\rho_0}\right)\right] - \frac{c^2n_2}{n_0^3}\rho_1 \tag{5.2.7}$$

Neglecting the term in the square brackets on the right hand side of Eq. (5.2.7) (quantum pressure) and substituting into Eq. (5.2.6) one arrives at a single second order equation for the velocity potential [17]:

$$-\frac{\partial}{\partial t}\left[\frac{\rho_0}{c_s^2}\left(\frac{\partial}{\partial t}\Psi_1 + \vec{v}\,\nabla\Psi_1\right)\right] + \nabla\left[\rho_0\nabla\Psi_1 - \frac{\rho_0\vec{v}}{c_s^2}\left(\frac{\partial}{\partial t}\Psi_1 + \vec{v}\,\nabla\Psi_1\right)\right] = 0 \tag{5.2.8}$$

with the sound speed $c_s^2 = c^2n_2\rho_0/n_0^3$. This can be written in a more compact form and is identical to a wave equation for a massless scalar field Ψ_1

$$\Delta\Psi_1 = \frac{1}{\sqrt{-g}}\partial_\mu\left(\sqrt{-g}g^{\mu\nu}\partial_\nu\Psi_1\right) = 0 \tag{5.2.9}$$

which is propagating in a (2+1) dimensional curved spacetime given by the metric

$$g_{\mu\nu} = \left(\frac{\rho_0}{c_s}\right)^2\begin{pmatrix} -(c_s^2 - v^2) & -v_r & -v_\theta \\ -v_r & 1 & 0 \\ -v_\theta & 0 & 1 \end{pmatrix} \tag{5.2.10}$$

with $g = \det(g_{\mu\nu})$. Here, v_r and v_θ are the radial and azimuthal velocity components and obey $v^2 = v_r^2 + v_\theta^2$. This metric is, apart from a scaling factor, identical to the one derived for waves on a flowing fluid (Eq. (5.2.4)) under purely geometric assumptions and shows that photon fluid sound modes in an inhomogneous flow can be treated as waves in a curved spacetime. Although derived in the context of a photon fluid [17], this form of metric has been also found earlier for BECs [102, 121] and classical fluids [94, 122]. It should be highlighted that only the phonons in the hydrodynamic analogy, i.e excitations in the photon fluid in the large wavelength limit, are coupled to the above derived acoustic metric. The photons of the laser beam are still coupled to the physical spacetime metric which is the flat Minkowski spacetime. Moreover, the acoustic metric describes a (2+1) dimensional spacetime that is shaped by the flow geometry and can only reproduce a subset of the (3+1) geometry in general relativity, where the curvature is related to the energy and mass distribution via the Einstein equations. Therefore, analogue systems are only useful to study *kinematical* problems of general relativity, i.e. trajectories of waves or particles defined by position, speed

and acceleration, but not *dynamical* problems that involve forces.

5.3 Acoustic horizons and ergoregions in a (2+1)D photon fluid

An acoustic spacetime in a photon fluid that recreates that of a black hole can be realised by spatially shaping the intensity and phase profile of the laser beam. As was described in Chapter 3, these are the two parameters that can be experimentally tweaked to control the speed of sound c_s and the flow v of the photon fluid. Both can be functions of spatial coordinates and therefore there exist two ways of building a horizon. The first is to keep the flow fixed in all spatial dimensions and modulate the sound speed, or the opposite where the sound speed is held constant with a spatially varying flow [122]. In this work, both quantities are controlled to create an acoustic horizon.

The fluid density and hence sound velocity is given by the optical field intensity $I(r)$ and a current flow can be induced by a phase gradient $\nabla\phi$ of the optical field. To create a spacetime flow analogous to a Schwarzschild black hole in Painlève-Gullstrand coordinates (i.e. $v(r) \propto -1/\sqrt{r}$), the field is chosen in cylindrical coordinates (r, θ):

$$E(r) = \sqrt{I(r)}e^{-i(2\pi\sqrt{r/r_0}-m\theta)} \tag{5.3.1}$$

where $I(r)$ is the gaussian intensity envelope, r_0 is the scaling factor defining the radial phase curvature and m denotes the OAM integer. In the case $m = 0$, the phase gradient has only radial components leading to a current flow directed towards the centre with velocity $v_r(r) = -c\pi/(kn_0\sqrt{r_0 r})$. When $m \neq 0$, the OAM adds a helical phase that creates an optical vortex with an azimuthal phase gradient, that in addition to the radial phase, creates a flow that has radial and azimuthal components that forms the spacetime of a rotating Kerr black hole. This vortex structure, which finds it hydrodynamic analogue in a "draining bathtub", curls the spacetime fabric around its center and if the rotation is strong enough, creates an *ergosphere*. This is a region outside the event horizon, where the total current flow, $v_{flow} = \sqrt{v_r^2 + v_\theta^2}$, overcomes the local sound speed and nothing can stay at rest in the reference frame of an external observer. Examples of such a beam geometry with a field given by Eq. (5.3.1), recreating a non-rotating and a rotating black hole are shown in Fig. 5.3. The intensity $|E(r)|^2$ and phase $\phi(r) = 2\pi\sqrt{r/r_0} - m\theta$ are calculated using realistic parameters that are later used in the experiment. The intensity and phase has to be chosen such that there exists

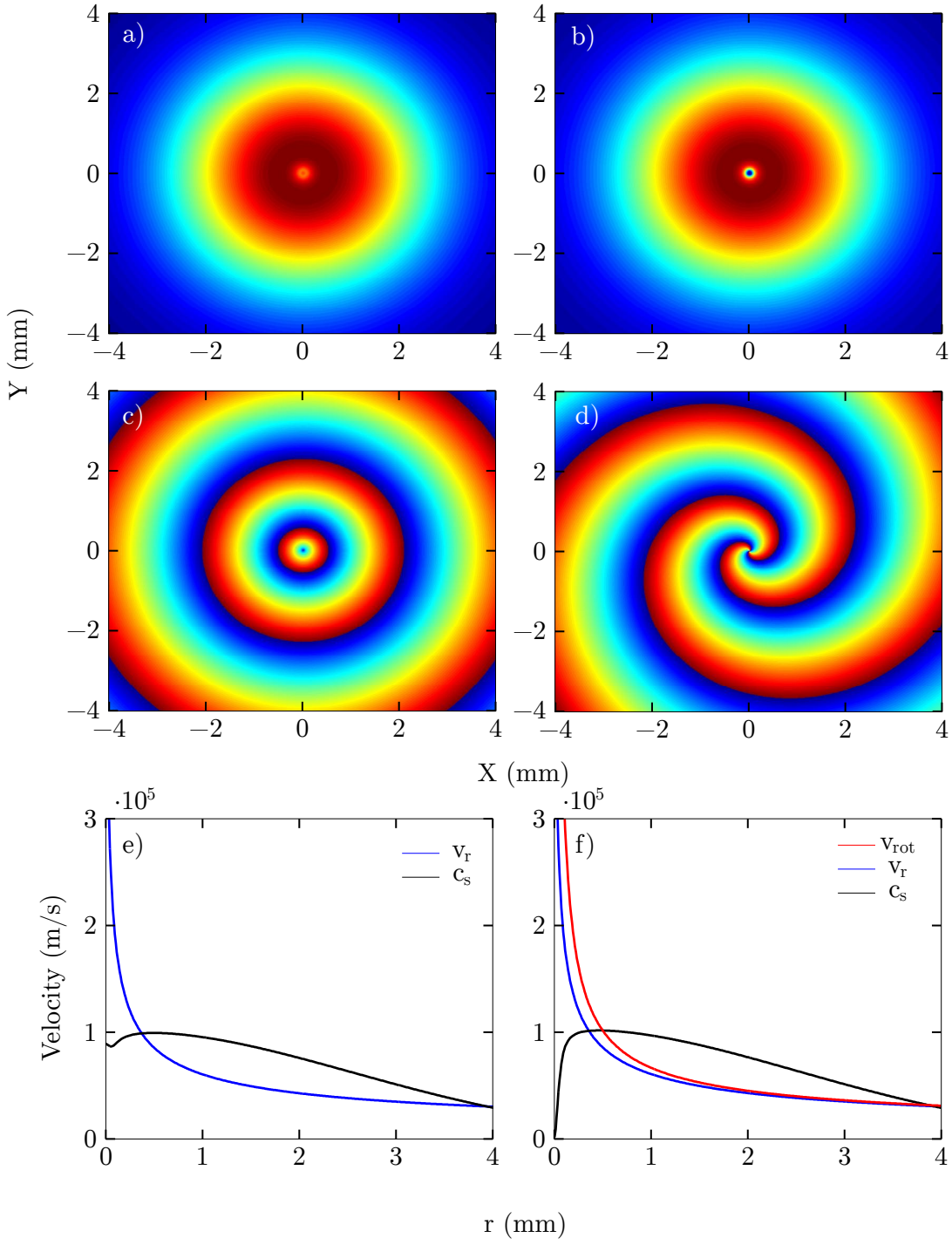

Figure 5.3: Calculations of transverse intensity $I(r)$ (top row) and phase profiles $\Phi(r)$ (middle row) of a laser beam with a field according to Eq. (5.3.1) for a static black hole (m=0) and a rotating black hole (m=2). The color code for the phase runs from 0 (blue) to 2π (red). The resulting flow velocity and speed of sound (bottom row) are calculated using parameters similar to the experiment: Power $P = 140$ mW, nonlinear $n_2(t = 200\text{ ms}) = 4.4 \times 10^{-7}$ cm^2/W, beam radius $w_{1/e^2} = 5$ mm, $r_0 = 0.5$ mm, $m = 2$.

an intersection of sound and flow velocity close to the beam centre. The beam has a phase singularity at $r = 0$ and consequently its intensity drops to zero, changing the local sound speed.

Experimentally, such fields can be realised by using a flat intensity profile of a broad gaussian beam that is sent onto a diffractive optical element i.e. Spatial light modulator (SLM) or phase mask, to imprint the desired phase. These elements are essentially diffraction gratings that are designed such that the first orders are carrying the desired spatial phase profile. A SLM consists of a matrix of addressable liquid crystal pixels, that are individually controlled via a voltage drop and capable of changing the refractive index for the incoming light. This allows to induce a spatially dependent phase retardation for individual parts of the laser profile hitting the SLM. Phase masks are diffraction gratings where the spatial design of the periodic structure is such that the interference in the first diffracted order leads to a beam with the desired spatial phase profile. These can be made from a thin chrome layer on a glass substrate, i.e. a periodic array of opaque and transparent structures or by a periodic relief on an etched glass substrate. Phase masks are very robust against high laser powers and provide a large format that is beneficial when using large beam diameters that are needed for such an experiment. Undoubtedly, SLMs provide high flexibility in quickly changing the phase without changing any optical elements and are therefore a versatile tool, but great care has to be taken to not damage them while working at high powers. So far, phase masks are used in the experiments presented here but also SLMs will be tested in the future. The experimental setup is shown in Fig. 5.4. A strong CW pump beam is sent through a diffractive phase mask, where the +1 or -1 order can be selected by a spatial filter in the focus of a 4f telescope. The sign of the orders determines the sign of the phase, i.e. the +1 leads to a phase $+\Phi(r)$ and -1 to $-\Phi(r)$. With that it is possible to create black hole metrics $v(r) \propto -1/\sqrt{r}$ and white hole metrics $v(r) \propto +1/\sqrt{r}$. The beam is imaged a few cm after the phase mask onto the sample input facet by a 4f imaging telescope. This is necessary since the curved phase fronts near the centre of the beam will overlap with further propagation, before they would reach the sample input. The beam then propagates through the nonlinear sample filled with a 25% absorptive methanol graphene solution where the near- and farfield at the sample output is imaged by a CCD camera/4f imaging system. The nearfield is used to measure the speed of sound whereas the farfield is used to measure flow velocity. All measurements were performed in a time resolved manner described in Chapter 2, i.e. the near- and farfield signals were recorded after a predefined delay from the opening of the laser shutter. This is necessary in order to control the nonlocal length and hence retain superfluidity for excitations with long wavelengths (see "Measurement of the speed of sound").

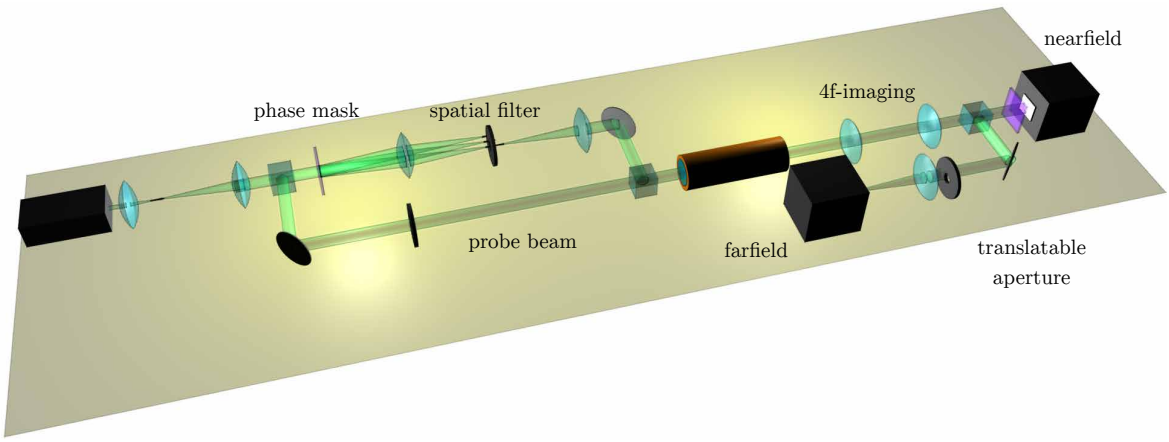

Figure 5.4: Setup: 532 nm CW beam with a waist diameter of $w \approx 7$ mm is launched onto a phase mask imprinting a spatial phase according Eq. (5.3.1) with parameters $r_0 = 0.5$ mm, $m = 2$. The beam is then sent through the nonlinear sample filled with a dilute methanol/graphene solution (25% abs.) and finally imaged by a 4f telescope onto a CCD camera to measure the nearfield (speed of sound measurement), and onto a translatable aperture to measure the spatially resolved farfield (flow speed measurement).

5.3.1 Measurement of the flow velocity

The flow is proportional to the gradient of the spatial phase $\vec{v}(r) = (c/n_0 k_0)\nabla\Phi(r)$. The phase can in general be expressed as (with $\vec{r} = (x, y)$)

$$\Phi(\vec{r}) = \vec{k}_\perp \vec{r} - \omega t \tag{5.3.2}$$

and hence the flow is proportional to the transverse k-vector $\vec{k}_\perp = (K_x(\vec{r}), K_y(\vec{r}))$.

$$\begin{pmatrix} v_x(\vec{r}) \\ v_y(\vec{r}) \end{pmatrix} = \frac{c}{n_0 k_0}\nabla\Phi(\vec{r}) = \frac{c}{n_0 k_0}\begin{pmatrix} K_x(\vec{r}) \\ K_y(\vec{r}) \end{pmatrix} \tag{5.3.3}$$

The components $K_{x,y}$ can be measured by spatially isolating parts of the transverse beam profile with a small aperture and measure the angle $\phi_{x,y}$ between the propagation and z-direction in the farfield. Using the trigonometric relation $K_{x,y} = k_0 \sin\phi_{x,y}$, the flow is then given by

$$\begin{pmatrix} v_x(\vec{r}) \\ v_y(\vec{r}) \end{pmatrix} = \frac{c}{n_0}\begin{pmatrix} \sin\phi_x(x, y) \\ \sin\phi_y(x, y) \end{pmatrix} \tag{5.3.4}$$

In the experiment, a 4f-telescope is used to image the beam at the sample output onto the camera and onto a translatable aperture using a 50:50 beam splitter. The aperture has a diameter of 200 μm and can be scanned across the full beam diameter to measure the spatially resolved farfield (Fig. 5.5a). The position of the aperture is controlled by

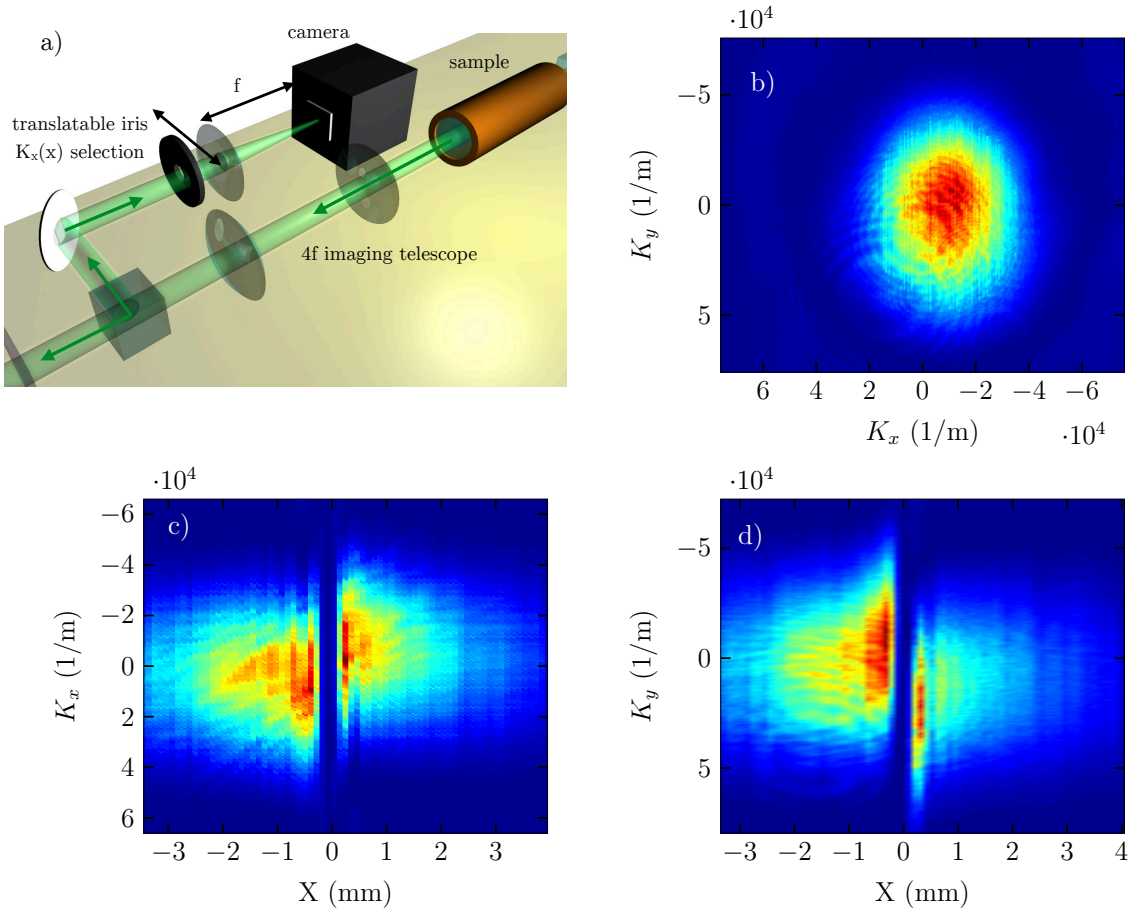

Figure 5.5: Flow measurement technique: a) The spatially resolved farfield is measured with a translatable iris ($\oslash \approx 200$ μm) that selects a small area of the beam profile whose farfield intensity distribution is recorded by a camera in the focal plane of a f=20 cm lens. The iris is scanned along x-direction across the beam profile with step increments of 0.1 mm, while the farfield image at each position is recorded. b) Example of the measured farfield intensity distribution. The gaussian envelope is fitted and the (K_x, K_y)-coordinates of the center are recorded for each step. Lineouts of the farfield b) at $K_y = 0$ (c) and $K_x = 0$ (d) for different positions across the beam profile. The dark notch at $x \approx 0$ is due to the zero intensity at the beam center (see Fig. 5.3 and Figs. 5.9, 5.10).

a computer controlled translation stage with μm precision. An example of the farfield intensity is shown in Fig. 5.5b). The farfield has an almost gaussian profile due to the small aperture diameter and is fitted with a 2D gaussian function. With this technique, the centre of the gaussian envelope is tracked along the transverse dimensions and it is possible to perform a direct measurement of the spatially resolved flow velocity. A set of up to 80 farfield images with steps of 0.1 mm is taken to measure across the full beam diameter (Fig. 5.5c) and d)).

5.3.2 Measurement of the speed of sound

Theoretically, the speed of sound is a function of the nonlinearity $\Delta n = \gamma I$ in the system that scales linearly with laser intensity. It is then valid to say that, if the nonlinear γ is known, it is sufficient to measure the intensity distribution in the nearfield to calculate the speed of sound c_s.

However, the description of an inhomogeneous flow as a curved spacetime metric only makes sense if the phase velocity of waves in the fluid is independent from their momentum. In the photon fluid, this is true for excitations with a phonon-like wave character whose wavelengths are larger than the healing and nonlocal length and consequently all the phonons travel with a constant speed of sound. In previous chapters, it was shown that photon fluids in a (1+1)D geometry are superfluid and excitations in the long wavelength limit have the character of non-dispersive phonons. This was achieved by using a highly elliptical beam profile that allowed to limit the nonlocal length to $\sigma \approx 125$ μm and access superfluidity over a broad range of wavelengths. This is no longer possible when using 2D beam geometries with few millimeter diameters that would result in too large nonlocal lengths that push the length scale for phonon wavelengths beyond the beam dimensions. It is therefore necessary to find alternative ways of reducing the nonlocality.

Since the nonlocality is essentially a measure of heat diffusion that develops over the rather slow thermal time constant of the medium, it is possible to reduce σ by using an

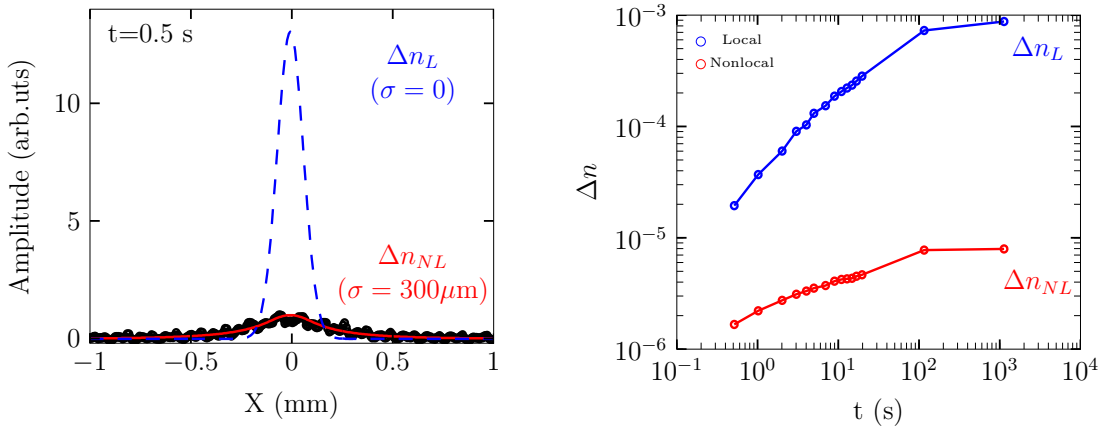

Figure 5.6: Calculating *local* Δn_L: Nonlinear nonlocal refractive index profile measured with spatial phase measurement technique (Chapter 2) with $I = 28W/cm^2$, t=0.5 s. The measured normalised signals Δn_{NL}(t=0.5 s) (black dots) are fitted with Eq. (2.2.6) with the real space response function $R(r, r', \sigma(t))$) described by Eq. (2.3.4 (red line). Afterwards, the blue dashed line is obtained by setting $\sigma = 0$ where the *local* peak nonlinearity $\Delta n_L(t)$ can be extracted for given $\sigma(t)$.

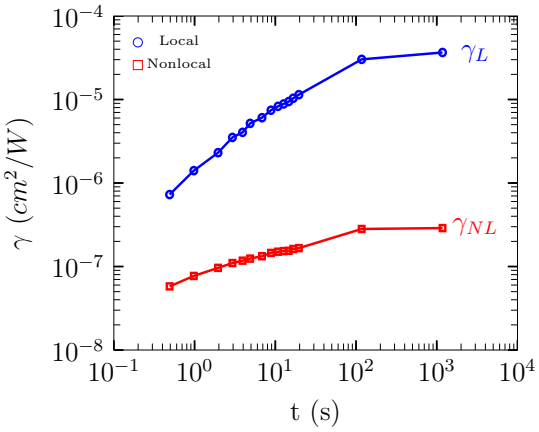

Figure 5.7: Local and nonlocal nonlinear coefficient $\gamma_{L,NL}(t) = \Delta n_{L,NL}(r=0,t)/I(r=0)$. Data obtained from Fig. 5.6 with $I(r=0) = 28$ W/cm^2.

out of thermal equilibrium condition of the system. This can be done by opening the laser shutter and capturing an image of the photon fluid after a short ms time delay. This is a valid technique since the evolution time in the photon fluid ($<$ 100ns) is much faster than the thermal diffusion time in the system ($\approx$ 10 min , see Chapter 2).
The transient build up of the thermal nonlinearity and nonlocal length was measured and described in Chapter 2. The temporal increase of the nonlinearity $\Delta n(t)$ shown in Fig. 2.8 displays the *nonlocal* $\Delta n(t)$ that is physically described by the convolution of the intensity profile and nonlocal response function. The measured peak amplitude is therefore affected and reduced by the nonlocality in the system. The speed of sound however is independent from the nonlocal length, that only defines the range of spatial frequencies that travel with c_s, but not its absolute value. Note that c_s refers to the sound speed of the phonons, which is given by the slope of the linear part of the Bogoliubov dispersion.

$$c_s = \sqrt{\frac{c^2 \Delta n_L}{n_0^3}} \tag{5.3.5}$$

It is therefore necessary to introduce the here called *local* Δn_L, that is independent from σ and the only parameter to define the speed of sound. It is calculated by fitting Eq. (2.2.6):

$$\Delta n_{NL}(r,t) = \gamma_{NL}(t) \int d^2r' R(r,r',\sigma(t)) I(r')$$

to the measured $\Delta n(r,t)$ with the real space response function $R(r,r',\sigma(t)))$ described by Eq. (2.3.4) with σ being the only fitting parameter and then set $\sigma = 0$ μm to find

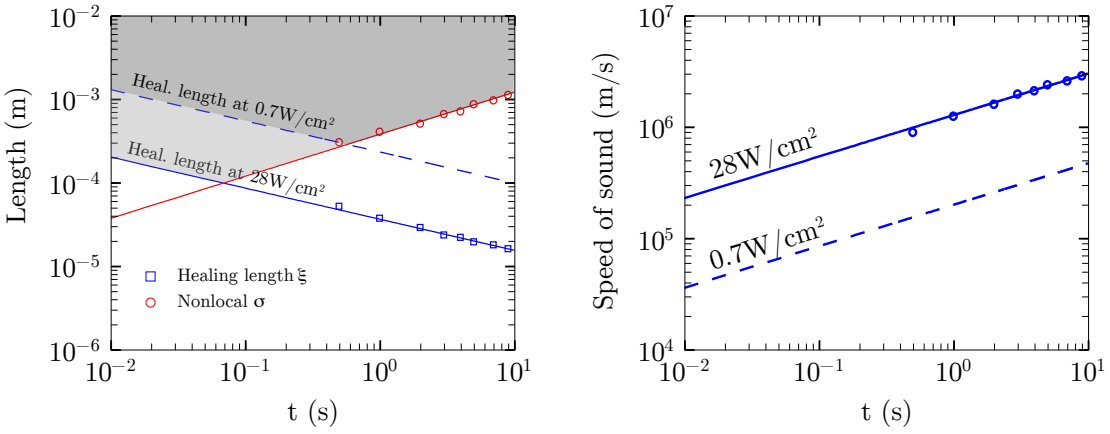

Figure 5.8: Time dependent photon fluid parameters. Data taken from results in Chapter 2 (solid line), the dashed lines are calculated by linear scaling according to the intensity ratios. Left) The grey shaded areas mark the wavelengths of excitations that travel with constant sound speed and have superfluid phonon character. Right) time dependent speed of sound.

the peak amplitude of the quasi-local nonlinearity Δn_L (see Fig. 5.6 and 5.7):

$$\Delta n_L(r,t) = \gamma_L(t) I(r) \tag{5.3.6}$$

It has to be stressed that Δn_L is not a physical quantity, but is used to describe the nonlinear amplitude and nonlocality independently from each other. In the end, it is a result of the spatial phase measurement technique used in Chapter 2, that is not capable of independently measure Δn and σ. The time dependent $\Delta n(t)$ was measured at an intensity $I = 28$ cm^2/W that was needed to induce a detectable signal. This was due to the small beam radius of the pump beam around $w = 130$ μm. As described above, the black hole experiment requires large beam radii of $w \approx 3 - 4$ mm, hence the intensity used here is much lower. Therefore, it is very useful to work out the time dependent nonlinear $\gamma(t)$ (Fig. 5.7), that will allow to measure the nonlinearity and consequently the speed of sound by simply recording the beam intensity. It was shown in Chapter 2, Fig. 2.9, that the nonlinearity scales linearly with laser power, and since the spatial beam profile is constant, with laser intensity.
A pump power of $P = 140$ mW was used with a beam waist radius of $w = 3.6$ mm that yields a peak intensity of $I = 0.7$ W/cm^2. Fig. 5.8 shows the calculated time

dependent quantities for the two intensities:

$$\begin{aligned} \text{Healing length } \xi(t) &= \lambda/(2\sqrt{n_0\gamma_L(t)I}) \\ \text{Sound speed } c_s(t) &= \sqrt{c^2\gamma_L(t)I/n_0^3} \\ \text{Nonlocal length } \sigma(t) &= 3.85\times10^{-4}m/s^{-1/2}\sqrt{t} \end{aligned}$$

The grey shaded areas mark the cut off length scales where the photon fluid excitations are phonons and travel at a constant phase velocity (speed of sound c_s). The healing length decreases over time whereas the nonlocal length increases, defining a time window between $t = 0.1 - 1$ s where the cut off length scale is minimal. In this window, at $I = 0.7$ W/cm^2 the cutoff wavelengths have a reasonable size between 300-600 μm to fit waves into the photon fluid. The speed of sound c_s has in the same window values between $c_s = 0.8 - 2\times10^5$ m/s, which is the approximate value that is needed to create an horizon with the used beam parameters (see Fig. 5.8 and Fig. 5.3).

5.3.3 2D rotating black and white holes

The speed of sound and flow velocity for a black and white hole configuration was measured according the previous sections. A pump beam with a peak power of $P = 140$ mW was used to excite the nonlinearity in the temporal build up after t=200 ms (black hole) and t=600 ms (white hole). In both cases, the beam carries a spatial phase described in Eq. (5.3.1) with parameters $r_0 = 0.5$ mm and m=2. The flow measurement was performed along the x-axis at y=0. It is then possible to easily separate the radial flow and azimuthal flow component because they point along the x- and y-direction: $v_x = v_r$, $v_y = v_\theta$. Fig. 5.9 and 5.10 show the nearfield intensity at the sample output and flow and sound velocities creating a metric of a rotating black and white hole. The intensity distribution shows a gaussian like envelope with a hole at the centre at the location of the phase singularity. The speed of sound is a scalar quantity and is plotted as a lineout at y=0 and made negative for $x > 0$ for the black hole and for $x < 0$ for the white hole for easier comparison with the vectorial flow velocity. The radial flow v_r and total flow $v_{tot} = \sqrt{v_r^2 + v_\theta^2}$ show qualitatively very good agreement with the theoretical fits and both exceed the sound speed at $x \approx \pm0.5$ mm, creating a 2D ergosphere ($v_{tot} = c_s$) and a 2D event horizon ($v_r = c_s$).
The amplitude of the radial flow decreases towards the centre inside the horizon, which is a consequence of two things: First, the finite aperture size of 200 μm leads always to a measurement of an average flow velocity, especially in the centre beam where the flow is changing very fast and even flips sign. It is therefore not surprising that the measured

values deviate from the theoretical expectation. The azimuthal OAM phase component seems to be a lot more robust against these effects, which is visible in the large flow velocities near the centre. In the white hole, both components seem to be more robust as in the black hole. This might be due to the transverse K vectors pointing outwards, avoiding overlap of phase fronts during propagation enabling a cleaner measurement of flow velocities.

The measured white hole velocities showed higher amplitudes than in the black hole case. The best fit for the radial flow was achieved for $r_0 = 0.18$ mm being less then the expected $r_0 = 0.5$ mm given by the phase mask. The reason for that is not fully understood yet, but a misalignment of the imaging optics can be ruled out since it leads to an additional phase that will depend quadratically on x, which results in an additional linear flow term that does obviously not go along the excellent fit $v(r) \propto 1/\sqrt{r_0 r}$. The higher flow also required to use a longer delay of $t = 600$ ms to achieve a higher sound speed due to the larger nonlinearity. However, the data shows very good evidence of an ergosphere and an event horizon for phonons with a wavelength larger than $\Lambda \approx 500$ μm. Summarising, the here presented results show 2D spacetime metrics recreating those of rotating black and white holes.

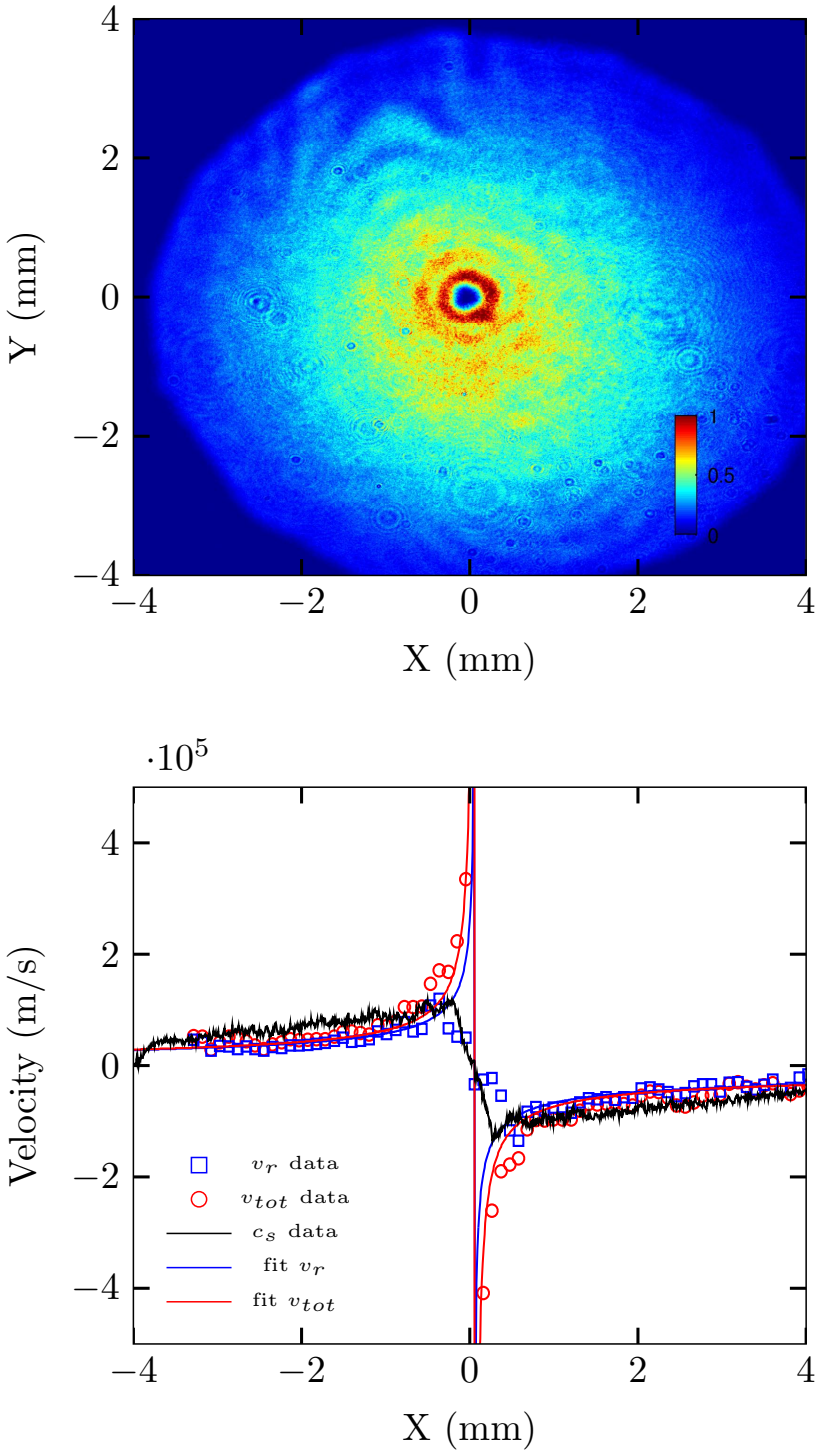

Figure 5.9: Black hole with experimental parameters $r_0 = 0.5$ mm, $m = 2$, $P = 140$ mW, $t = 200$ ms. Top: nearfield intensity distribution at the sample output. The color code shows the intensity from 0 (dark blue) to 1 W/cm^2 (dark red). Bottom: Radial and total flow velocities (red circles and blue squares) and speed of sound (black). An event horizon and ergosphere is found at $x \approx \pm 0.5$ mm.

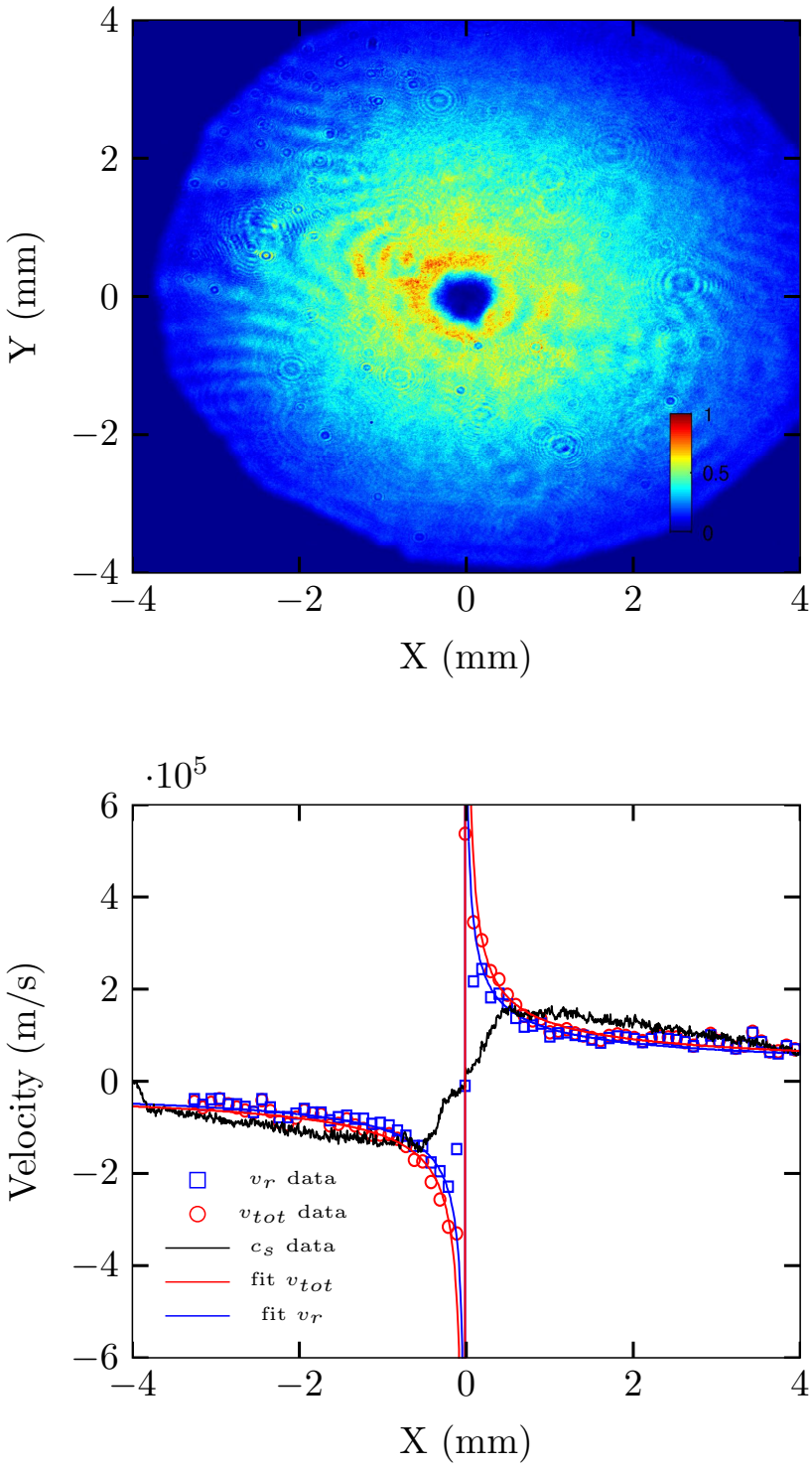

Figure 5.10: White hole with experimental parameters $r_0 = 0.5$ mm, $m = 2$, $P = 140$ mW, $t = 600$ ms. Top: nearfield intensity distribution at the sample output. The color code shows the intensity from 0 (dark blue) to 1 W/cm^2 (dark red). Bottom: Radial and total flow velocities (red circles and blue squares) and speed of sound (black). The best fit was achieved for $r_0 = 0.18$ mm. An event horizon and ergosphere is found at $x \approx \pm 0.5$ mm.

5.4 Wave scattering from rotating spacetimes

In recent years, most attention in analogue systems was drawn towards the Hawking process although other aspects of curved spacetime physics gain more and more interest with the further development of multidimensional analogue gravity systems [115, 123]. One effect is the superradiant scattering of scalar waves from a rotating (Kerr) black hole, where scalar waves approaching and entering the ergosphere are reflected, and depending on their frequencies, escape and are amplified with respect to their incoming amplitude. The wave gains energy from the rotating spacetime, leaving a slower spinning black hole behind. This process shares similarities with the Hawking effect and is therefore not directly detectable for astrophysical black holes, but is expected to be observable in analogue systems capable of creating a 2D ergosphere.
The last section has presented experimental evidence of such an ergosphere in a 2D photon fluid, with the use of an optical vortex phase that creates a rotational flow around the phase singularity. To study superradiance, a wave has to be seeded through the interference with a second weak probe beam, that then may be amplified under certain conditions. Since this effect is a purely kinematical scattering process, a standard approach is to analyze the amplitudes of the asymptotic solutions of the underlying wave equations, which was studied theoretically for photon fluids in a cavity by Marino et al. [77]. The reflection and transmission coefficients R and T of radial sound waves obey the relation

$$|R|^2 = 1 - \left(\frac{\Omega - n\Omega_H}{\Omega}\right)|T|^2 \tag{5.4.1}$$

Here, Ω is the phonon frequency, $\Omega_H = m\xi c_s/(\pi r_H^2)$ is the angular frequency at the horizon r_H, m is the topological charge of the vortex pump beam and n that of the probe beam. For frequencies $0 < \Omega < n\Omega_H$, $|R|^2$ becomes greater than 1 and thus the reflected wave component carries more energy than the incoming one. It was numerically reported that the amplification is largest for n=1 and decreases with increasing n [77] (see Fig. 5.11). As mentioned above, the amplitude components are evaluated far away from the ergosphere where the spacetime curvature is essentially flat, so one has to make sure that the waves are given enough time to travel to and back from the black hole. As this is the case for classical fluid experiments or photon fluids in a cavity, where the evolution time is the real time, quasi asymptotic amplitudes can be measured by letting the system evolve over enough time. Photon fluids in a propagating geometry do not provide such a flexibility, since the evolution time $t = zn_0/c$ is given by the nonlinear propagation distance which is limited by absorption. Given a nonlinear sample of $L = 10 - 20$ cm, the time evolution is limited to t=$40 - 80$ ns and although

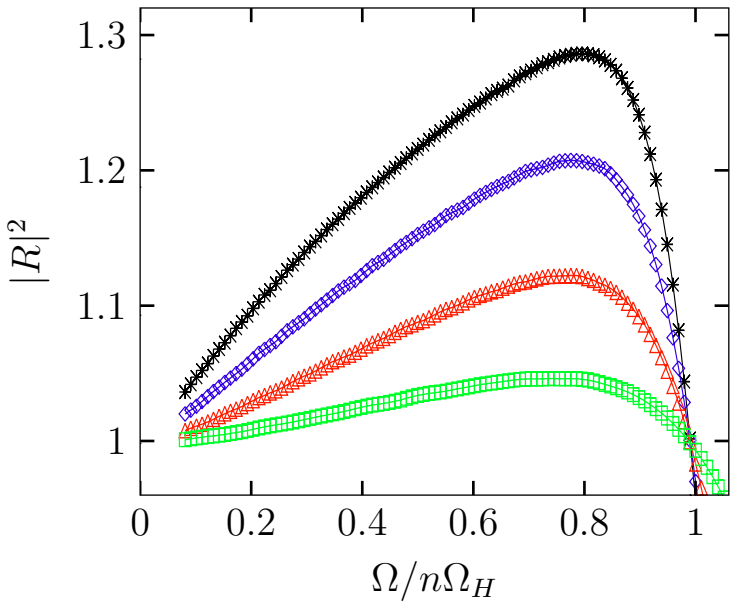

Figure 5.11: Reflection coefficients $|R|^2$ as a function of $\Omega/n\Omega_H$ for n=1 sound waves and different values of the black-hole rotation parameter: m=4 (green), m=6 (red), m=8 (blue), m=10 (black). Figure taken from Marino et al. [77].

the sound speed is of the order $c_s = 10^5$ m/s the total way that waves will propagate is at best not more than a few hundred of microns. Furthermore, to create phonons in a superfluid, wavelengths larger than the healing and nonlocal length have to be used and thus the few hundred micron propagation distance correspond only to a fraction of the wavelength.

Nevertheless, this photon fluid has several advantages over other systems since it allows to study the delicate details of the scattering process itself in a sub-nanosecond time resolution. The phase and intensity of the probe beam can be precisely controlled that allows accurate seeding of waves with defined frequencies, shape and momentum. The work presented here investigates the possibility of observing superradiant scattering in a 2D photon fluid with experimental and numerical techniques.

For the above reason, the detection of such an effect requires a precise measurement of amplitude and momentum of incoming and outgoing modes which are spatially inseperable in this system due to the short evolution time. However, scattered modes could be spectrally detected in the farfield since they possess different K-vectors as the incoming modes and are thus distinguishable from each other. In optical terms, this scattering could be understood as a specific nonlinear $\chi^{(3)}$-process, where the pump and probe beam generates a field with additional transverse momenta and possibly carrying orbital angular momentum similar to what one would expect from a four-wave mixing

process (FWM). From a theoretical perspective, it is known that the hydrodynamic description of the beam propagation as a photon fluid allows superradiant solutions of the Klein-Gordon equation. Unfortunately, the FWM terms are hidden in the continuity and euler equations that makes it difficult to study the role of FWM for superradiance. It is therefore useful to directly linearise the nonlocal NLSE (Eq.3.1.6) using the ansatz $E = E_0 + \epsilon$ (with $\epsilon \ll E_0$) and one obtains the equations for the field perturbations ϵ and ϵ^*:

$$\frac{\partial \epsilon}{\partial z} = \frac{i}{2k}\nabla_\perp^2 \epsilon + \frac{ikn_2}{n_0}\left[\left((E_0\epsilon^* + E_0^*\epsilon) \star R_\sigma\right)E_0 + (|E_0|^2 \star R_\sigma)\epsilon\right] \tag{5.4.2}$$

Here, R_σ is the nonlocal response function and the $\star$ operator denotes a convolution. In the special case of a local nonlinearity, the last two terms are identical and the equation reduces to:

$$\frac{\partial \epsilon}{\partial z} = \frac{i}{2k}\nabla_\perp^2 \epsilon + \frac{ikn_2}{n_0}\left[E_0^2\epsilon^* + 2|E_0^2|\epsilon\right] \tag{5.4.3}$$

The second term on the right hand side couples the pump field E_0 to the pertubative probe field ϵ, hence the phase and amplitude of the pump determine the evolution of the probe, whereas the last term only depends on the intensity of the pump and adds a nonlinear phase. In the following, these terms are called the four-wave mixing (FWM) and cross phase modulation (XPM) terms.

The evolution of linearised field perturbations ϵ is governed by Eq. (5.4.3), which allows solutions whose phase depends on the phase of the background field E_0. In other words, during propagation, a nonlinear mixing process could lead to a OAM transfer from the pump to the idler [124]. So by analysing the OAM content of the idler beam, one could determine the scattering amplitudes and look for superradiant features. However, so far it is not clear under which conditions and requirements a four-wave mixing process would yield gain or loss for spatial frequencies that follow Eq. (5.4.1) and shares the same features as superradiance. Nevertheless, a detailed investigation of FWM with beams carrying a phase creating a rotating curved spacetime would provide vital insights in the nonlinear processes that share similarities to Penrose superradiance. In the following, preliminary experimental and numerical results are presented.

5.4.1 Experiment

The first step is to look for such an idler generated between a pump beam and a weak plane wave probe beam. The experimental setup is the same as in the previous section with an additional probe beam that is split off by a 50:50 beamsplitter before the phase mask (see Fig. 5.4). The farfield is recorded at the sample output, where now the

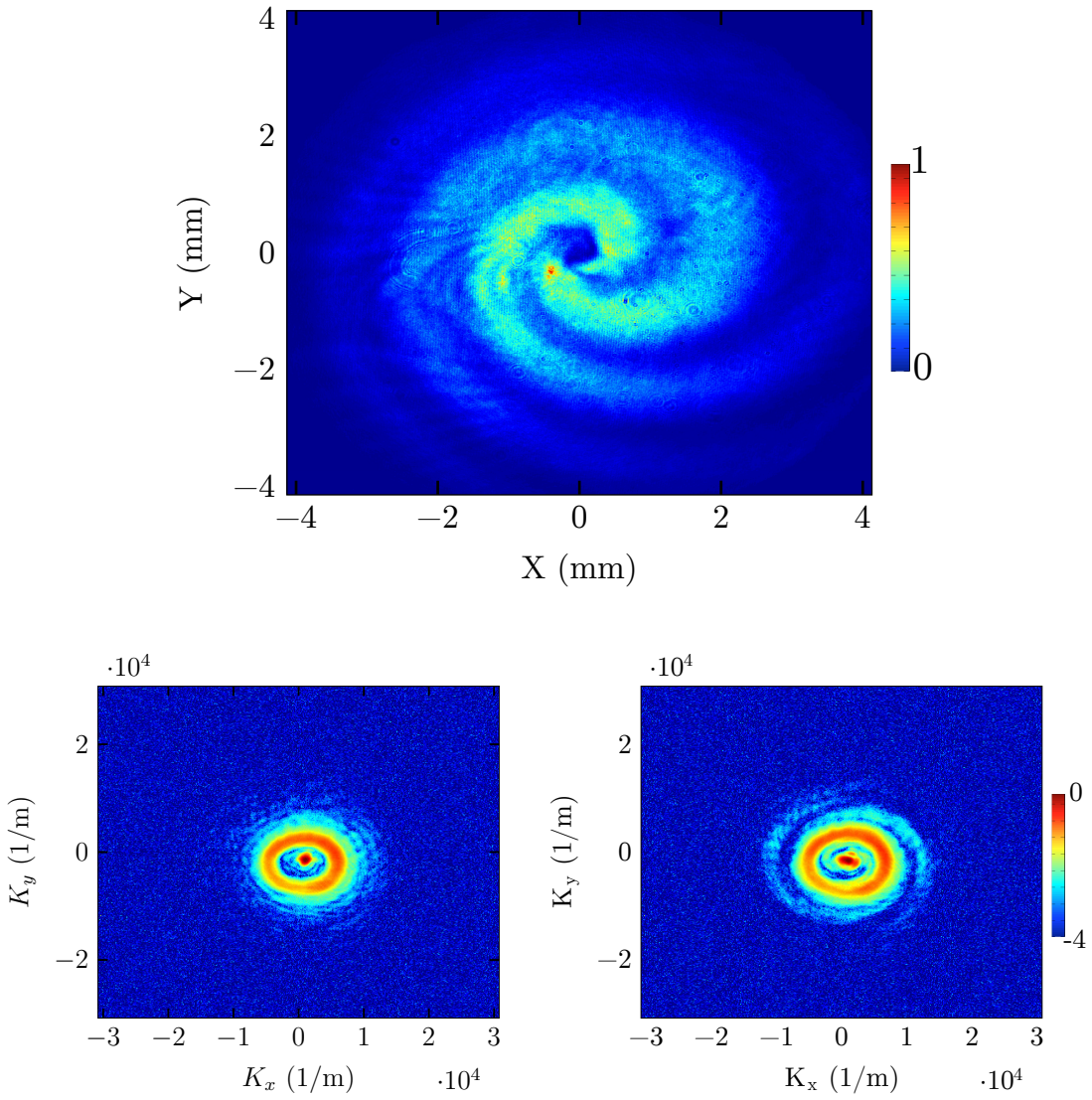

Figure 5.12: Top: Nearfield image of the pump beam with phase creating a white hole according to Eq. (5.3.1) with m=2, $r_0 = 0.5$ mm and co-propagating plane wave probe beam at $t = 300$ ms. $I_{pump}/I_{probe} \sim 10$. The color code shows the relative intensity normalised to $I = 2$ W/cm^2. Bottom: Corresponding farfield images at $t = 0$ s (left) and $t = 300$ ms (right). The pump beam appears as ring due to its radial and azimuthal phase, while the probe is a gaussian spot centered at $K = (0, 0)$ m^{-1}. After t=300 ms, additional spatial frequencies appear in the form of a spiral pattern, which is due to the linear interference of the pump (m=2) and a four-wave mixed idler beam (l=4). The color code shows the relative amplitude in $\log_{10}$-scale.

camera sits in the focal plane of a $f = 500$ mm lens. The nearfield is imaged onto the camera by a single lens, with a magnification of $M = 1.71$. Fig. 5.12a) shows an example of the interference in the nearfield with pump beam parameters $r_0 = 0.5$ mm and $m = 2$ and a weak probe beam with a flat phase that is aligned along the

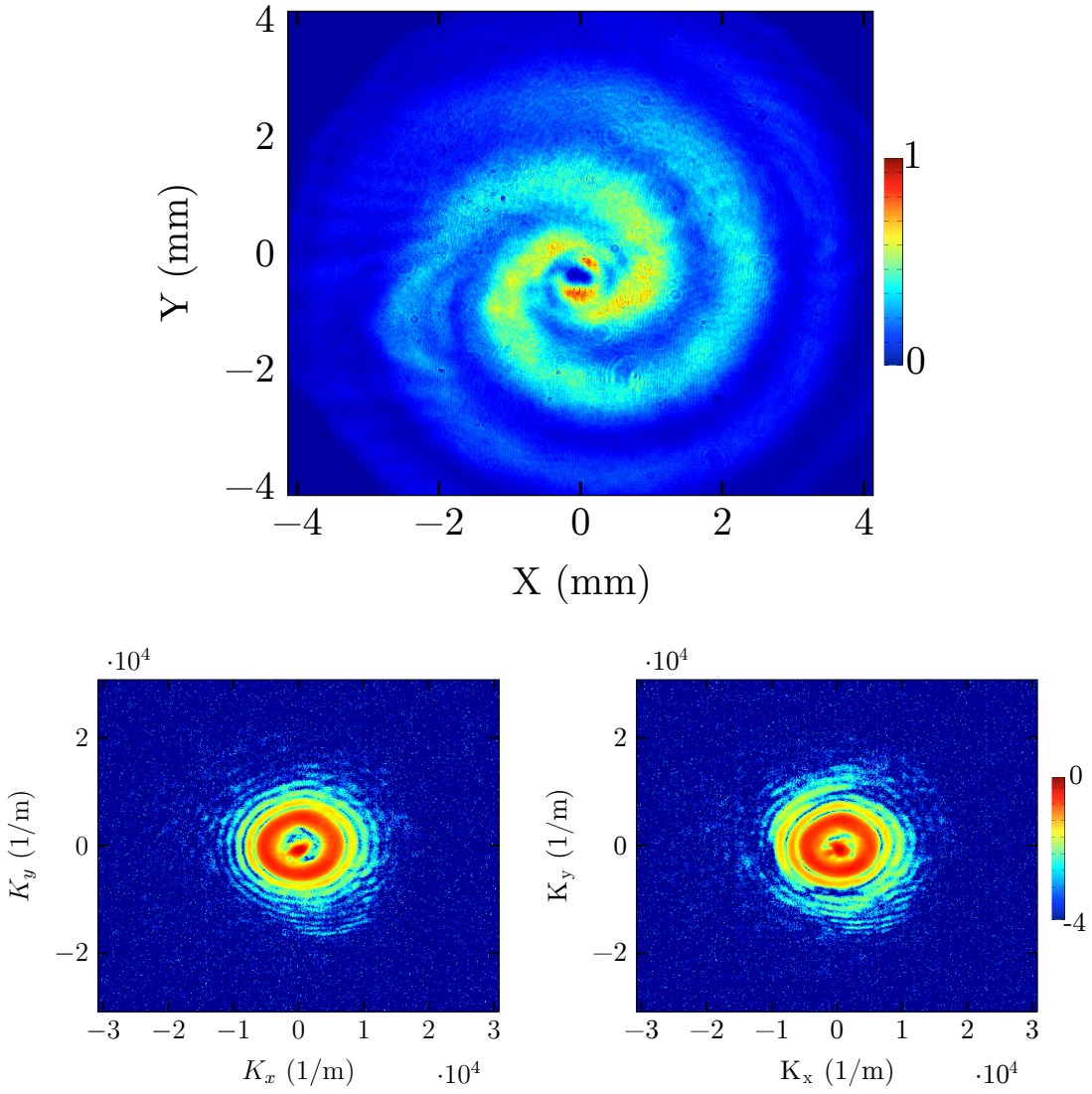

Figure 5.13: Top: Nearfield image of the pump beam with phase creating a black hole according to Eq. (5.3.1) with m=2, $r_0 = 0.5$ mm and co-propagating plane wave probe beam at $t = 300$ ms. $I_{pump}/I_{probe} \sim 10$. The color code shows the relative intensity normalised to $I = 2$ W/cm^2. Bottom: Corresponding farfield images at $t = 0$ s (left) and $t = 300$ ms (right). The overall distribution of intensity is more spread as in the white hole case. The spiral structure of the FWM signal is also observable here, although not as clear.The color code shows the relative amplitude in $\log_{10}$-scale.

z-direction. The phase is chosen such it creates a radially outgoing flow as for white holes. The corresponding farfields after $t = 0$ s (linear propagation) and $t = 300$ ms (nonlinear propagation) are shown in Fig. 5.12b) and c). The intensity distribution at $t = 0$ s of the pump beam follows a ring that is due to the OAM and radial phase profile and the plane wave probe is a gaussian spot at the centre at $\vec{K} = (0, 0)$. After $t = 300$ ms, the farfield reveals additional features at larger K-vectors that have the spatial

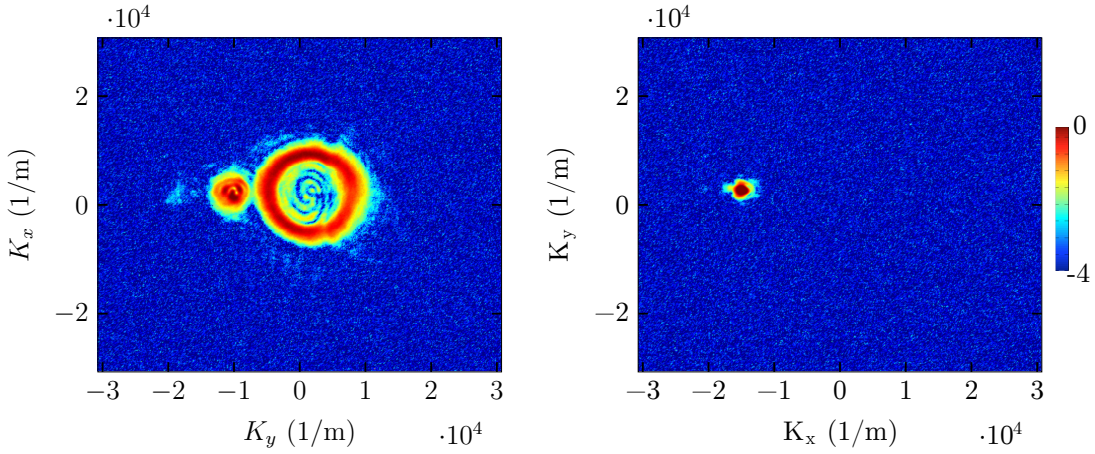

Figure 5.14: Farfield image of the pump beam with a white hole ($r_0 = 0.5$ mm, $m = 2$) and a plane wave probe beam propagating at an angle $\alpha \approx 0.06°$ with respect to the pump. (left) farfield after $t = 600$ ms with both beams and (right) with pump beam blocked. The clear broadening of the probe beam in the unblocked case is due to cross-phase modulation, while a weak idler can be identified at $K_x \approx -2 \times 10^4$ m^{-1}. The color code shows the relative amplitude in $\log_{10}$-scale.

structure of a two-armed spiral, that can be attributed to an idler beam generated by four wave mixing. The pump and probe fields are proportional to $E_0 = E_p \exp(im\theta)$ and $\epsilon = \epsilon_{pr} \exp(in\theta)$ and from the second term of Eq. (5.4.3) $E_0^2\epsilon^*$ follows that the FWM signal must carry OAM with an integer $\ell = 2m - n$. So with $m = 2$ and $n = 0$, the spiral structure can be understood as an interference between the idler carrying OAM $\ell = 4$ and the pump with OAM $m = 2$. It is different from the trivial non-FWM case where $\ell = 0$ and $m = 2$ as in this case the spiral would have opposite rotation.
The cross phase modulation is visible at larger probe angles, where the gaussian spot from the probe and the ring shaped structure for the pump are clearly separated in the farfield (Fig. 5.14). This is manifested by the broadening of the gaussian spot, which is a consequence of the accumulated phase that is proportional to $|E_0|^2\epsilon$ during propagation. The strong pump beam induces therefore a defocusing effect that disappears when the pump beam is blocked.
The experimental results have shown that both nonlinear terms in Eq. (5.4.3) are active with the used phase and beam profiles and new spatial frequencies are generated. The interesting question is what the OAM content of the newly generated field components is and for that purpose, the OAM spectrum of the total field needs to be measured and analysed in the future. In the meantime, numerical simulations with experimental parameters were performed to further to investigate the OAM spectra that is presented in the following section.

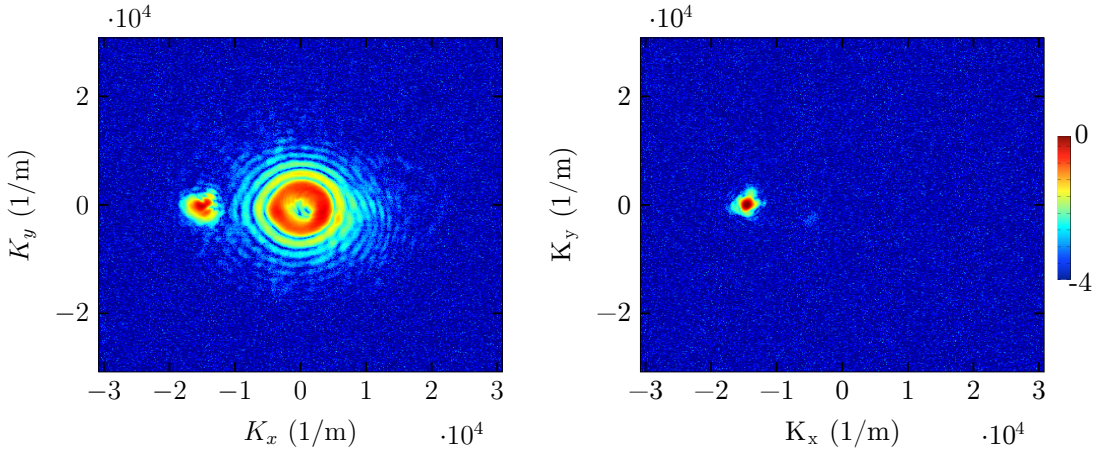

Figure 5.15: Farfield image of the pump beam with a black hole ($r_0 = 0.5$ mm, $m = 2$) and a plane wave probe beam propagating at an angle $\alpha \approx 0.06°$ with respect to the pump. (left) farfield after $t = 600$ ms with both beams and (right) with pump beam blocked. The clear broadening of the probe beam in the unblocked case is due to cross-phase modulation. The color code shows the relative amplitude in $\log_{10}$-scale.

5.4.2 Numerical simulations

The numerical technique and results presented in here were performed in close collaboration by Calum Maitland [125]. The numerical simulations were carried out by integrating the 2D NLSE in k-space by a split step technique identical to the one used in Chapter 4. As a starting point, the experiment described in the previous section was repeated in the numerics with parameters inspired by the experiment with a local nonlinearity. Nonlocality was neglected since it reduces the effective nonlinearity and dampens the FWM effects. The pump beam carries a radial and OAM phase with $r_0 = 0.5$ mm and $m = 2$ identical to the experiment that corresponds to a rotating black hole in the analogue gravity analogy, while the probe beam is a co-propagating weak plane wave. The near- and farfield of a total field intensity is shown in Fig. 5.16 after 14 cm nonlinear propagation. The two armed spiral interference pattern in the nearfield as observed in the experiment is also visible, although the modulation is not as strong due to the lower probe beam power (P_{probe}/P_{pump}=1/100). The farfield reveals also a spiral structure with opposite rotation confirming the experimental results, where the change of rotation was explained by an interference of a $m = 2$ (pump) and a $\ell = 4$ (FWM idler) beam. It is now of interest to analyze the OAM spectrum of the generated beam and measure the orbital angular momentum of the combined field E_T in the transverse plane. In analogy with quantum mechanics, the inner product is calculated between the simulated total field E_T and an orthogonal basis of fields O_m

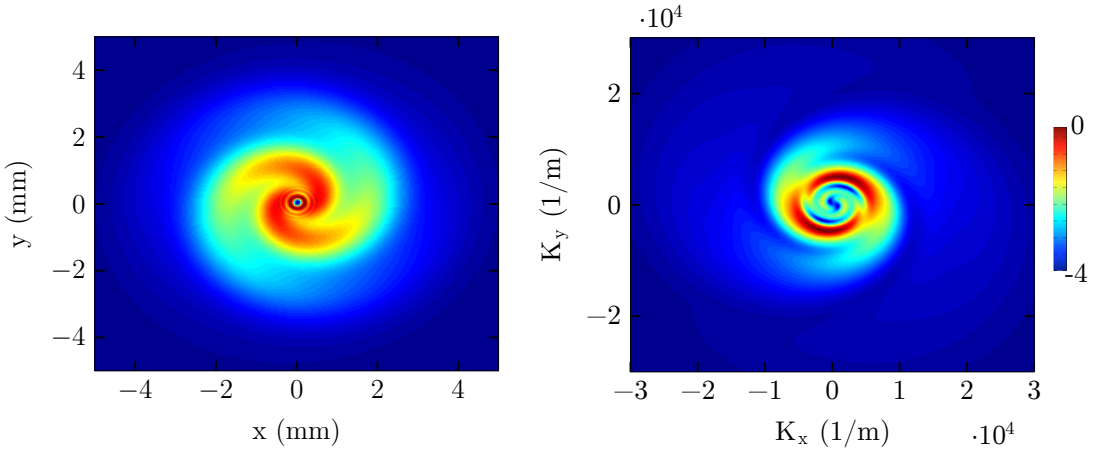

Figure 5.16: Numerics: left) Nearfield image of the pump beam with phase creating a black hole according to Eq. (5.3.1) and co-propagating plane wave probe beam at z=14 cm with experimental parameters from Fig. 5.12 obtained by integrating the full NLSE (m=2, n=0, r_0=0.5 mm, P_{Pump}=140 mW, P_{Probe}=1.4 mW, beam diameter ($1/e^2$)=7 mm). Pump and probe have the same intensity envelope. right) Corresponding farfield image, showing a spiral with opposite rotation as in the nearfield, confirming the experiment. The color code shows the relative amplitude in $\log_{10}$-scale.

each with OAM $\hbar m$, for a single integer m:

$$S_{OAM}(m) = |\langle E_T|O_m\rangle| = |\int_0^\infty \int_0^{2\pi} E_T(r,\theta)^* O_m(r,\theta) dr d\theta \tag{5.4.4}$$

Orthogonality in this context means $\langle O_n|O_m\rangle = 0$ if $n \neq m$. Laguerre-Gauss modes are such an orthogonal basis, however the intensity distribution changes between LG modes as well as the OAM integer. This is not ideal for measuring OAM, as varying the overlap with the test field's intensity will give false contributions to the spectrum. On the other hand, any collection of fields with the same amplitude A(r) and varying single-valued OAM will be orthogonal:

$$\begin{aligned} \langle O_m|O_n\rangle &= \int_0^\infty \int_0^{2\pi} A(r) e^{in\theta^*} A(r) e^{im\theta} dr d\theta & (5.4.5)\\ &= \int_0^\infty |A(r)|^2 dr \int_0^{2\pi} e^{i(m-n)\theta} & (5.4.6)\\ &= P\delta_{m,n} & (5.4.7) \end{aligned}$$

as summing the complex exponential $e^{ik\theta}$ around the unit circle gives always 0 for all $k \neq 0$. Note P is just the power, so defining the OAM basis as $O_m = \frac{1}{\sqrt{P}} A(r) e^{im\theta}$ provides an orthonormal set. In principle $A(r)$ may be any integrable radial function,

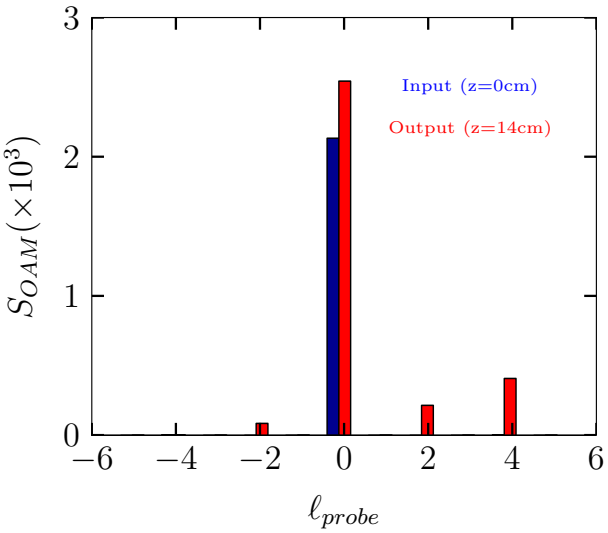

Figure 5.17: Numerics: Overlap integral showing the OAM spectrum of the pump background corrected field shown in Fig. 5.16 at the input (blue bar) and output (red bars). The initial plane wave gains orbital angular momentum due to the nonlinear interaction with the pump beam.

but for numerics purposes should go to zero as r approaches the half-width of the simulation window. It has been proven useful to split the radial integral into small intervals $r_j = j\Delta r$, to prevent numerical artefacts such as aliasing and finite simulation window [125]. With this, the overlap integral of a test field $E_T(r,\theta) = F(r)e^{in\theta}$ can be defined as:

$$S_{OAM}(m) = |\int_0^\infty F(r)^* A(r) dr \int_0^{2\pi} e^{i(m-n)\theta} d\theta| \tag{5.4.8}$$

$$\approx \sum_j^\infty |F(r_j)| A(r_j) \Delta r \delta_{n,m} \tag{5.4.9}$$

If Δr is small compared to the typical phase variation length scale of $F(r)$ and $A(r)$ then $S_{OAM}(m)$ is locally independent of the radial field and thus a good measure of the azimuthal content of E_T.

With this technique, the OAM content of the background corrected field and the output OAM spectra normalised to the input spectrum $S_{OAM}(\ell, 0)$ is shown in Fig. 5.17. For a plane wave probe incident at zero angle, the $\ell = 4$ mode is amplified after nonlinear propagation. This confirms the experimental observation of the spiral interference pattern being flipped from left to right and goes also in line with angular momentum conservation according to the phase matching condition: $\ell = 2m - n$.

Next, a more interesting situation is studied where a pump beam with $m = 10$ and

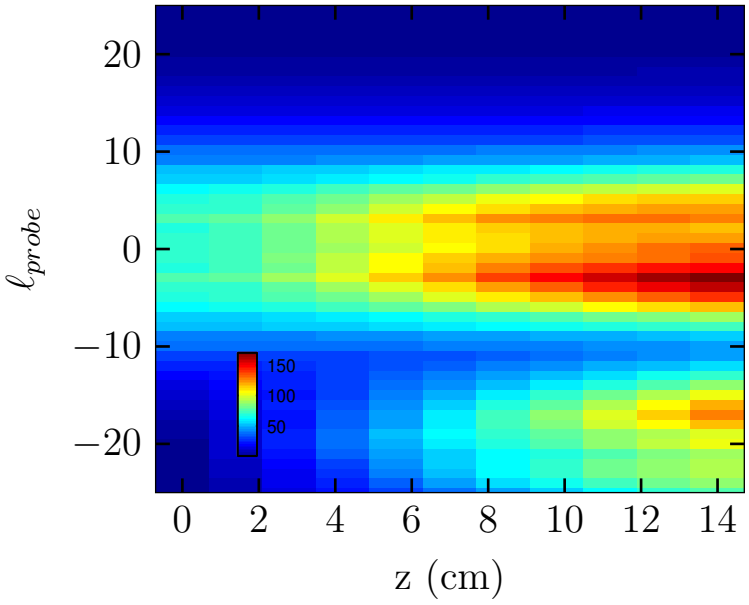

Figure 5.18: Amplification spectrum of the probe field (background corrected) as a function of z for a plane wave propagating at an angle $\alpha = 0.01°$. The angular momentum spectrum arises through the projection of the probe field onto the basis of the orthogonal OAM functions. At z=14 cm, a clear asymmetry in the OAM spectrum with respect to l=0 has developed, while co-rotating modes ($\ell > 0$) are more amplified than counter rotating modes ($\ell < 0$). Parameters: m=10, n=0, P_{Pump}=0.5 W, $P_{Probe} = 10^{-4} \times P_{Pump}$.

a probe beam propagating at an angle with respect to the k_z direction of the pump beam (propagation axis) is used, that creates an interference pattern corresponding to an ingoing wave towards the black hole horizon. The higher pump OAM corresponds to a faster rotating black hole and should in general yield a larger amplification. Note that by changing the angle one can effectively control the phonon frequency (for small angles $\Omega \propto K = k_0 \sin\alpha$) and study the OAM spectrum of the background corrected probe field as a function of frequency. In particular, the relative amplification coefficient $A(\ell, z) = (S(\ell, z) - S(\ell, 0))/S(\ell, 0)$ is studied for different probe angles. As a first proof of principle, Fig. 5.18 shows the evolution of $A(\ell, z)$ along z at a fixed angle $\alpha = 0.01°$. Even if the probe field has no OAM phase, the projection of the probe field onto the basis of the orthogonal OAM functions shows a non-zero amplitude distribution between $\ell \approx \pm 7$ at z=0. However, in total the positive and negative components cancel each other out so that the total OAM phase is $\sum_l A(\ell, z = 0)\ell = 0$. After nonlinear propagation, the overall amplitude is increasing and an additional peak appears between $\ell \approx 13 - 23$ that approximately satisfies $\ell = 2m - n$ (Note, $n \approx \pm 7$). The

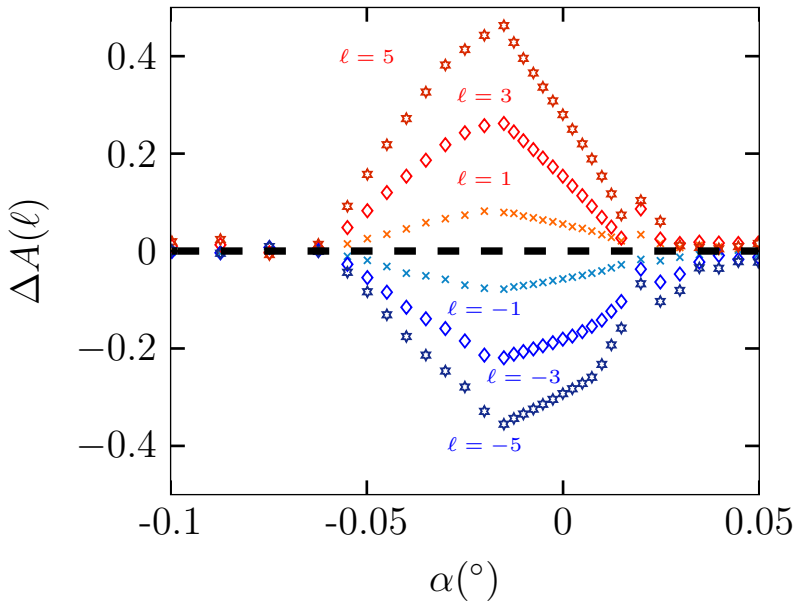

Figure 5.19: Relative amplification $\Delta A(\ell) = A(\ell, z = 14\text{ cm})$-$A(\ell = 0, z = 14\text{ cm})$ for a focusing beam carrying OAM ℓ with different focusing angles with the same parameters as in Fig 5.18. Negative angles correspond to a focusing of the beam and radially ingoing phonon waves. Positive modes $\ell > 0$ are amplified whereas negative modes $\ell < 0$ are depleted for $-0.06^\circ < \alpha < 0.03^\circ$.

overall amplification indicates an energy transfer from the pump towards the probe beam while the OAM modes around $\ell = +3$ show higher amplitudes than those around $\ell = -3$. This is a first indication that modes with a co-rotating angular momentum are stronger amplified than counter-rotating modes.

Next, instead of using a plane wave probe beam at an angle, the probe beam is now loosely focused in order to create a radially symmetric ingoing wave towards the black hole. This has the advantage that the signal to noise ratio of the amplification can be signficantly increased by summing over the azimuthal angle θ.

The amplification is studied for a scenario that corresponds to the experiment proposed by Marino et al. [77]. Accordingly, an OAM phase is added to the weak probe, and the amplification relative to the $\ell = 0$ mode ($\Delta A(\ell) = A(\ell, z = 14\text{ cm})$-$A(\ell = 0, z = 14\text{ cm})$) is shown in Fig. 5.19. Note that negative angles correspond to a focusing of the beam and radially ingoing phonon waves. At large angles (corresponding to large frequencies) no amplification is observed, while a triangular shaped amplification/depletion peaked at $\alpha \approx -0.02^\circ$ for positive/negative OAM modes is observed for angles between $-0.06^\circ < \alpha < 0.03^\circ$. This result shows that the scattering amplitudes depend on the frequencies as well as their angular momentum, a basic common feature with

superradiance. However, the latter predicts the largest amplification for the $\ell = 1$ modes that is not confirmed in the numerical simulations. The amplification seems to increase with increasing ℓ, but starts to decrease for values that exceed the pump OAM m (not shown). Furthermore, these simulations were repeated by integrating the linearised NLSE that provides the advantage of artificially switching off the $E^2\epsilon^*$ or $|E|^2\epsilon$ term. The results with both terms active gave almost identical results, but if one is neglected, the total amplification for all modes was suppressed [125]. A possible explanation may be indicating that the effect is driven by an interplay between both terms similar to what is observed for modulational instability. There, the $|E|^2\epsilon$ term provides an effective phase-matching between otherwise mismatched beams and therefore allows amplification under certain conditions [48].

5.5 Conclusion

The realisation of an analogue of a two-dimensional black and white hole in a photon fluid was shown. A major challenge was to accurately shape the beam profile, so that the phase gradient and the intensity of the beam translate into a scenario of an inhomogeneous flow creating an acoustic horizon and ergosphere. In particular, the speed of sound was measured by the transient characterisation of the thermal nonlinearity while the flow was measured by directly recording the spatial phase gradient of the beam. It proved to be vital to use the slow build up of the nonlinearity in order to control the nonlocality in the system. With this, it was possible to build a two-dimensional photon fluid which is governed by a linear dispersion for experimentally realistic wavelengths. The experimental results of the radial and azimuthal flow showed very good agreement with the expectation values, however deviations were found in the radial components close to the centre of the beam. Overall, the complex phase topology of the beam seemed robust along propagation even in the presence of nonlinearity.

Penrose superradiance was predicted to be observable in a photon fluid by shaping the topology of the pump beam such that it mimics the spacetime of a rotating black hole [77]. Here, a first experimental and numerical study was carried out by probing such an analogue black hole with plane waves provided by the intereference with an additional probe beam. Whereas in the common literature, superradiant amplification is formulated in terms of the amplitudes of asymptotic solutions, the photon fluid that is studied here only allows scenarios where the wave amplitudes may only be analyzed during the scattering event. Here, it was shown experimentally and numerically that a scattering of such waves occurs, which is considered to be a proof of concept that the underlying requirement for superradiance in this system is given. However, it is

so far not known under what condition amplification occurs that bears resemblance to Penrose superradiance. Furthermore, it was shown that the scattering leads to the generation of new spatial frequencies that may be linked to a modulational instability, that is described by $E^2\epsilon^*$ and $|E|^2\epsilon$ terms in the linearised NLSE. Both terms have shown to be active in the experiment and it was numerically shown that the presence of both terms is needed to observe the experimental results. Preliminary numerics show an amplification of modes that are co-rotating and a dampening of modes which are counter-rotating with respect to the rotation of the black hole. Nevertheless, the observations need further investigation and theoretical and experimental efforts are currently underway to establish a clear link to superradiance. The idea here is to derive a generalized Klein-Gordon equation, whose validity does not rely either on the hydrodynamic approximation, nor on the separation between amplitude and phase perturbations before linearization [126]. In optical terms, superradiance would appear as a modulational instability of OAM beams that is to our current knowledge still unknown. The experimental approach aims at investigating the OAM content of the total field at the sample output. A major challenge there is to distinguish between pump and probe light, which is necessary to accurately measure gain or loss in the amplitudes of the weak probe beam.

Summarising, the experiment and numerics present promising results that may lead to the observation of superradiant scattering from a rotating black hole in a photon fluid.

Chapter 6

Emergent geometries and nonlinear wave dynamics

In this chapter, the nonlinear wave dynamics of large amplitude waves in a (1+1)D photon fluid are investigated from two different perspectives. In particular, self-steepening and shock formation are described by analysing the full nonlinear Navier-Stokes equation, whereas the same phenomena can be explained in an analogue spacetime scheme, where the nonlinear coupling is established by a self-induced spacetime metric. The discussions are corroborated by experimental and numerical results and were published in Marino et.al "Emergent geometries and nonlinear-wave dynamics in photon fluids" [127].

6.1 Introduction

In General Relativity, the geometry of spacetime plays the key role in the description of various phenomena and allows us to understand the gravitational force as a consequence of distortions in this geometry. Analogue gravity models have opened up experimental possibilities to study kinematical problems of curved spacetimes, but usually rely on perturbative schemes, i.e. the equation of motion for elementary excitations in a condensed matter system is a linear wave equation that emerges from a pertubative linearisation of the complete nonlinear problem. Therefore, the geometry in which the waves propagate is given by the background and is not influenced by the waves themselves. In that sense, effects that are based on a gravitational backreaction are negligible.

Recently, a different perspective was introduced by Goulart et al. [128]. If the excitations or waves are strong enough, their evolution is no longer governed by a linear wave equation in a stationary metric, since the propagation will lead to nonlinear dynamics. However, the equation of motion can be interpreted, as if the wave is propagating in an effective emergent spacetime created by itself. In this way, the full nonlinear problem is encoded in the back-reaction between metric and wave and includes the entire system dynamics. Although the back-reaction represents in a way a dynamical system, it cannot be used to test dynamical problems of General Relativity (i.e. the gravitational effect of one test mass on another) since the metric-wave dynamics in the nonlinear analogue gravity models is not coupled via Einstein's equations. However, the mutual interplay is woven into a geometrical framework that could allow insights to specific dynamical features in General Relativity. Wave dynamics have been investigated long before the concept of analogue gravity was conceived. The study of nonlinear wave dynamics dates back to the early 19^{th} century with the discovery of solitons and the connection to differential geometry was established decades later by Riemann in his work on flow discontinuities [129]. Today, there exist a countless number of works that led to the mathematical understanding of numerous nonlinear wave phenomena such as shock waves [37, 130], solitons [131, 132], or rogue waves [133, 134]. These phenomena are not restricted to classical fluids or gases, but have also been investigated in optical fibres [135], Bose-Einstein condensates [136, 137] or plasmas [138]. As described in Chapter 5, these systems in the linear regime display workbenches for studies on acoustic black holes with the bulk interest in analogue Hawking radiation and superradiance. They have proven to be a useful tool for studying kinematics of event horizons, but these horizons are not a consequence of a matter distribution. However, it was shown that there exist situations, where parameters that define the fluid dynamics and

that describing a 4D black hole could be put in correspondence [139]. In the nonlinear regime, it was pointed out that the evolution of waves can still be described in an acoustic metric that is dynamically coupled to fluid parameters [140]. Therefore, analogue models could be used to investigate some dynamical aspects of black hole physics.
This chapter presents the experimental and numerical study of nonlinear acoustic waves in a photon fluid. The nonlinearity in the system leads to a characteristic wave steepening of density waves, that is understood as a backreaction of a self-induced background flow from the wave itself. This backreaction can be interpreted as an self-induced effective curved spacetime metric. The self-steepening is eventually leading to a shock, i.e. a discontinuity in density that is regularized in compressible, non viscous fluids by dispersion in the form of a train of oscillatory fronts [141]. The formation of a shock can be geometrically associated to a singularity of the emergent metric.

6.2 Self-steepening of density waves

In this study a quasi 1+1 dimensional photon fluid in a nonlocal defocusing media is considered as described in detail in Chapter 3. This is governed by the NLSE for the optical field:

$$\begin{aligned} \partial_t E &= \frac{i}{2k}\partial_x^2 E - i\frac{k}{n_0} E\Delta n \\ \text{with } \Delta n &= \gamma \int R(x-x')|E(x')|^2 dx' \end{aligned} \tag{6.2.1}$$

The hydrodynamical analogue is established by means of a Madelung transform that leads to a set of hydrodynamical Navier Stokes equations (see Ch. 3, Eq. (3.2.2) and (3.2.3)). The wave propagation of linear density waves was introduced and studied and the results obtained in there discussed density perturbations that are described by the linearised Navier-Stokes equations. In this regime, higher order perturbations are neglected and the background solutions can be separated from the small amplitude solutions and thus the waves are described by a set of linear wave equations. Therefore, nonlinear terms in the equation of motion are not present and consequently no self-action effects are incorporated. In other words, the density and phase variations caused by the wave modulations are negligible with respect to the background parameters, and thus have no influence on the latter.
If the wave amplitudes are large, the modulations will have influence on the background and therefore the linearisation is not a good assumption anymore. It is therefore necessary to consider the full nonlinear problem. As a reminder, Eq. (3.2.2) and (3.2.3) in

1+1D are inserted here where for further analysis:

$$\partial_t \rho + \partial_x(\rho v) = 0 \tag{6.2.2}$$

$$\partial_t \psi + \frac{1}{2}v^2 + \frac{c^2 n_2}{n_0^3}\rho - \frac{c^2}{2k^2 n_0^2}\frac{\partial_x^2\sqrt{\rho}}{\sqrt{\rho}} = 0 \tag{6.2.3}$$

Now, by applying the first spatial derivative to Eq. (6.2.3) and neglecting the quantum pressure term one obtains

$$\partial_t v + v\partial_x v + \frac{\partial_x P}{\rho} = 0 \tag{6.2.4}$$

with $P = \frac{c^2 n_2}{2n_0^3}\rho^2$ being the bulk pressure. In the case for small amplitude perturbations, Eq. (6.2.2)-(6.2.2) can be converted into linear wave equations for density, pressure and velocity perturbations (Chapter 3). Now, instead of looking for linearised solutions, the goal is to find the velocity of a point at a given fixed density ρ using the full nonlinear Navier Stokes equations [129, 142], i.e.

$$u = \left(\frac{\partial x}{\partial t}\right)_\rho = -\left(\frac{\partial \rho}{\partial t}\right)_x \Big/ \left(\frac{\partial \rho}{\partial x}\right)_t \tag{6.2.5}$$

To derive this, it is assumed that the velocity is a function of the density for any time and spatial coordinate only, i.e. $v = v(\rho)$. With this, Eqs. (6.2.2) and (6.2.4) can be written as:

$$\partial_t \rho + \frac{\partial(\rho v)}{\partial \rho}\partial_x \rho = 0 \tag{6.2.6}$$

$$\partial_t v + \left(v + \frac{1}{\rho}\frac{\partial P}{\partial v}\right)\partial_x v = 0 \tag{6.2.7}$$

Thus from Eq. (6.2.6) one obtains:

$$\left(\frac{\partial x}{\partial t}\right)_\rho = \frac{\partial(\rho v)}{\partial \rho} = v + \rho\frac{\partial v}{\partial \rho} \tag{6.2.8}$$

and equivantly from Eq. (6.2.7):

$$\left(\frac{\partial x}{\partial t}\right)_v = v + \frac{1}{\rho}\frac{\partial P}{\partial v} = v + \frac{1}{\rho}\frac{\partial P}{\partial \rho}\frac{\partial \rho}{\partial v} = v + \frac{c_s^2}{\rho}\frac{\partial \rho}{\partial v} \tag{6.2.9}$$

Since v is uniquely dependent on ρ, the time derivatives of x at constant velocity and density must be equal and therefore $\partial v/\partial \rho = \pm c_s/\rho$. Reinstating this into Eq. (6.2.8) one obtains $u = \partial x/\partial t = v(\rho) \pm c_s(\rho)$, and after integrating the solution for $x(t)$ is

given by [142]:

$$x(t) = (v(\rho) \pm c_s(\rho))t + \text{constant} \tag{6.2.10}$$

This is the solution of a travelling wave, every point x is propagating at a velocity $u(\rho)$ that is determined by the density. Therefore, the shape of the wave profile changes as time evolves. For example, a wave propagating along the positive x-direction travels at $u = v + c_s$. As derived above, the gradient $\partial v/\partial\rho > 0$ and the sound speed is $c_s \propto \rho$. Hence the total change of wave velocity with increasing density is positive, i.e. $\partial u/\partial\rho > 0$, and points of higher density propagate faster than points at lower density. This is the fundamental reason for wave steepenening in the hydrodynamic context.
In the photon fluid, wave breaking as observed in real fluids is avoided by the quantum pressure term (dispersion) and nonlocality for nonlocal thermal nonlinearities [41]. This can be understood by looking at the spatial Fourier spectrum of the wave. As long as the wave is of sinusoidal shape the spatial fourier spectrum is a δ-function at the given spatial frequency (momentum) of the wave. As soon as the shape approximates a sawtooth like pattern, non-zero momenta appear in the spectrum, and if these happen to lie in the dispersive (non-linear) part of the dispersion, all the spectral contributions travel at different phase speed and therefore the wave packet spreads. The nonlocality on the other hand smoothens the nonlinearity, hence the build up of self-induced density discontinuities is weakened. Only when the quantum pressure and nonlocality are weak with respect to the nonlinear term, self-steepening is clearly visible, otherwise the effect is weakened. The speed of sound is given by $c_s^2 = \partial P/\partial\rho$ and hence the nonlocal dispersion of the photon fluid (Eq. (3.3.8)) can be written as:

$$\Omega^2 = c_s^2 K^2 \left(\frac{1}{1 + \sigma^2 K^2} + \frac{\xi^2}{4\pi^2} K^2 \right) \tag{6.2.11}$$

Thus, dispersion effects are negligible if the term in brackets is constant and close to unity. This condition is met for $\sigma K \ll 1$ and $\xi K \ll 1$. Therefore, the regime where steepening is clearly observable is given by the corresponding wavelengths that must be larger than the healing length ξ and the nonlocal length σ. This is exactly the requirement for excitations to be considered as phonons in the photon fluid. Note that this argument is based on the assumption that the dispersion of the nonlinear waves considered here is the nonlocal Bogoliubov dispersion derived for small amplitude perturbations. However, it provides a rough estimate of the regime where nonlocality and quantum pressure is negligible.
The experiments to observe self-steepening were conducted in a quasi 1-D photon fluid. Similar to the experiment presented in Chapter 3, a broad CW laser beam is split into

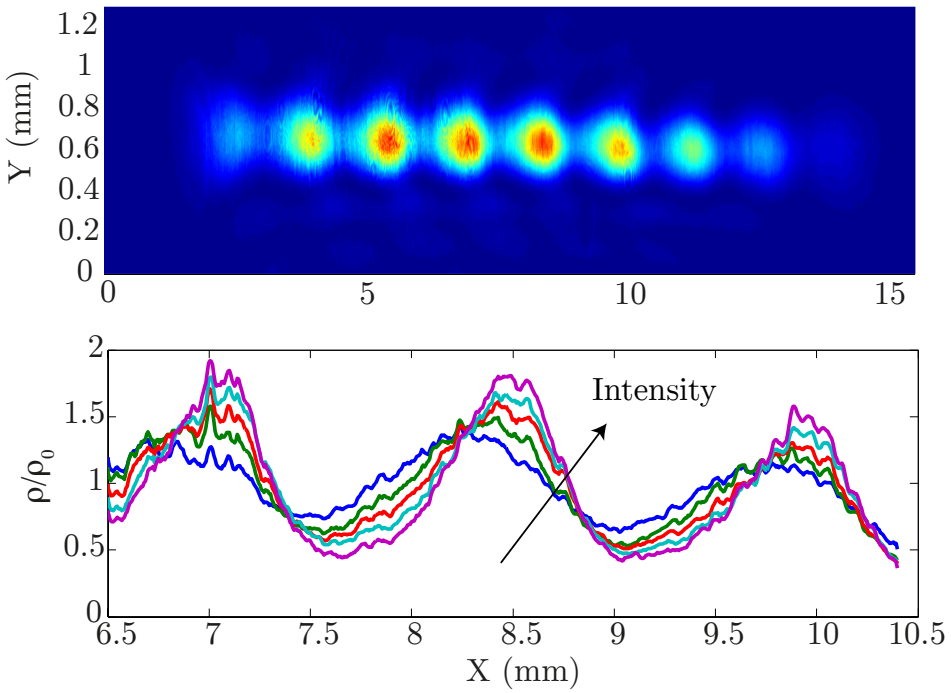

Figure 6.1: Top: Nearfield of the total beam profile at the sample output. The intensity modulation is associated to a density wave in the photon fluid. Bottom: Lineouts showing the normalized beam profile at different intensities. At low intensities, the wave possesses a sinusoidal shape (blue). For increasing nonlinearity, the wave propagates and develops a steepening of the leading edge.

a strong pump and a weaker probe component. Both beams are then loosely focused onto the sample input using a set of cylindrical lenses ($f_1 = 200$ mm and $f_2 = 50$ mm) to create an elliptical beam with a narrow minor axis waist radius $w_y = 180$ μm and a wide axis radius with $w_x = 0.7$ cm. In this way, the system can be considered as 1-dimensional. By controlling intensity and angle between pump and probe one is able to easily control the desired modulation depth (up to$\approx$ 40%) and wavelength of the resulting interference pattern, that in this context is associated to a density wave. The angle between both beams is chosen such that the propagation dynamics of the wave follows the x-axis. After the sample, the negative spatial momentum components of the probe beam are spatially filtered with a pinhole in the focus of the 4-f imaging telescope that images the sample output onto a CCD camera (see Fig. 3.6). The more intense pump beam has a peak intensity of about ~ 1 W/cm^2 inducing a nonlinearity of approx. $\Delta n \approx 10^{-5}$ (as measured in Chapter 3) and therefore the resulting healing length is of the order of $\xi \approx 70 - 80$ μm. In a quasi 1-D photon fluid, the nonlocal length is approximately given by the smallest beam dimension, therefore $\sigma < 180$ μm as was verified in Chapter 3, Fig. 3.8 and Chapter 4. The angle between pump and probe measures 0.02° resulting in a density wave of roughly $\Lambda = 1$ mm wavelength. There-

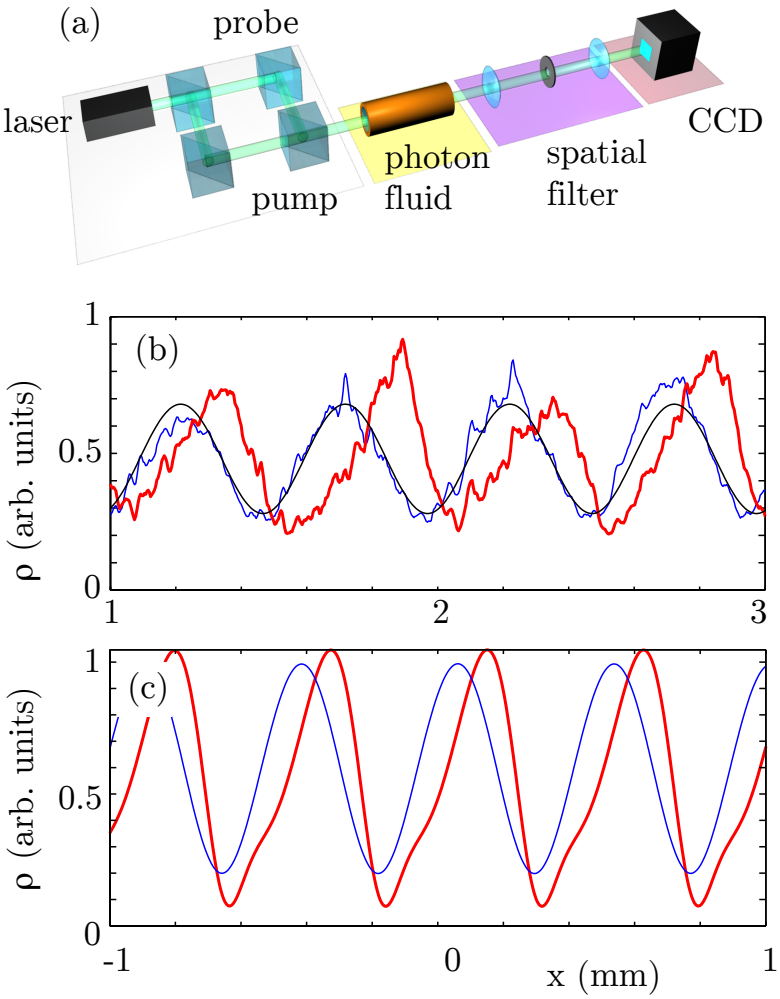

Figure 6.2: a) The experimental layout. b) Measured density wave profile after spatial filtering for low intensity ($I = 0.02$ W/cm^2, linear density wave propagation) and high intensity ($I = 1$ W/cm^2, nonlinear propagation). c) Numerical simulation under the same conditions of the experiment, including also the nonlocal medium response, with nonlocal length $\sigma = 110$ μm [126].

fore, the wavelength is larger that the healing and nonlocal length and consequently the wave is situated in the regime of self-steepening. Examples of typical profiles of density waves in the photon fluid is shown in Fig. 6.1 at different laser powers. At low power, where the nonlinearity is small enough such that the propagation can be assumed to be linear, the wave is of sinusoidal shape and this can be regarded as the initial condition. For increasing power, the wave propagates along the positive x-direction and starts to steepen at the leading edge. Since the temporal evolution in the photon fluid is given by total nonlinear propagation length (21 cm), the wave propagation and hence the maximum steepening that can be experimentally observed is limited. Another factor is certainly the nonlocality that has the effect of smoothening sharp features.

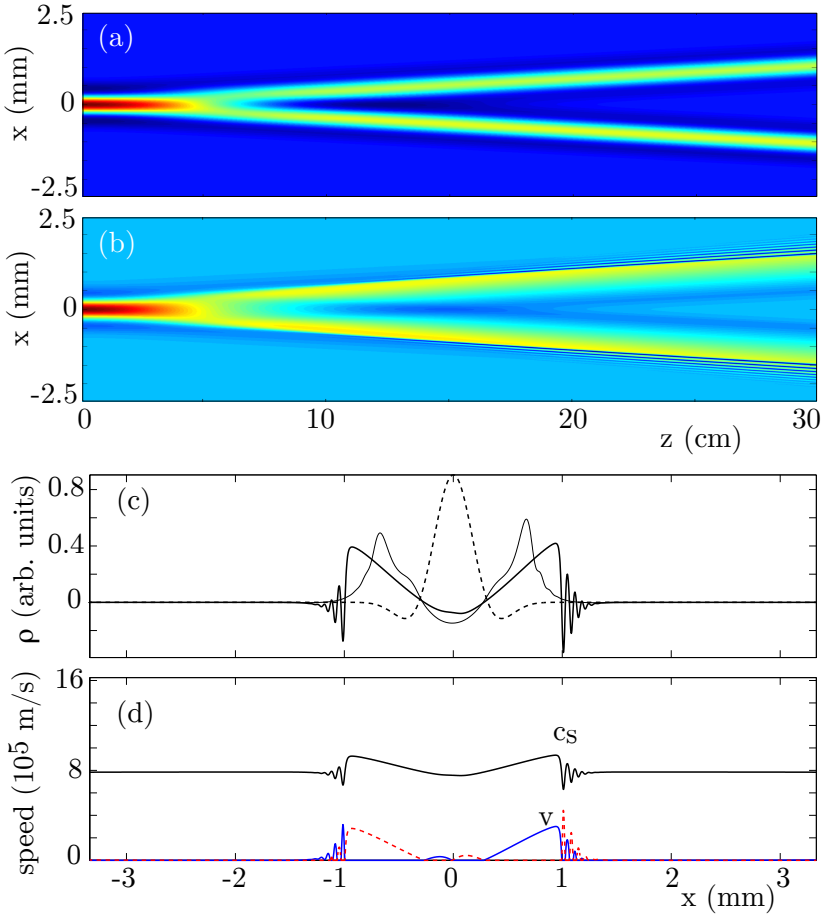

Figure 6.3: Numerical results: Evolution of probe beam in the presence of a flat pump beam. a) linear dynamics, i.e. 1% pump power, 0.02° tilt angle, $\sigma = 0$: Input wave splits into two Bogoliubov particles travelling in opposite directions. b) nonlinear dynamics, probe and pump at equal power, pulse splits and propagates nonlinearly while developing self-steepening and eventually forms dispersive shock fronts. c) Lineouts of b) at $z = 0$ cm (dashed line, input profile), at $z = 18$ cm for a nonlocal medium (thin solid line, $\sigma = 110$ μm) and $z = 18$ cm for a local medium (thick solid line, $\sigma = 0$. d) Sound speed c_s and flow velocity v as a function of space (blue line- positive x-direction; dashed red line - negative x-direction) [126].

For further analysis, numerical simulations were carried out where the technical limitations in the experiment can be easily overcome. This is done by numerically solving Eq. (6.2.1) with similar input conditions as in the experiment. With a nonlinearity of $n_2 = 8 \times 10^{-6}$ cm^2/W, beam diameter w_x =1 cm and a tilt angle between pump and probe of 0.02°, the numerical results recover well the wave steepening as observed in the experiment (Fig. 6.2). The power ratio between both beams is changed in order to compare the linear and the nonlinear wave dynamics along the propagation. As initial condition, the probe diameter is chosen such it approximately creates a modulation of one wavelength on top of the background. At small ratios, $I_{\text{probe}}/I_{\text{pump}}$ <0.1, the initial

wave splits into two parts each travelling in opposite direction while maintaining their shape (Fig. 6.3a). After separation, these can be identified as the positive and negative momentum components of the solutions to the linearised hydrodynamic equations of a quantum fluid described by the Bogoliubov theory [43] (see Chapter 3, Eq. (3.3.5)). At higher ratios, $I_{\mathrm{probe}}/I_{\mathrm{pump}}$ >0.5, the propagation dynamics enter the nonlinear regime. After separation, the wave profile steepens at the leading edge and eventually develops high frequency ripples at the front (Fig. 6.3b)). This is the above discussed onset of a dispersive shock wave. For later discussion, this effect can also be interpreted as a result of a spatially dependent sound speed. Since the wave amplitudes strongly modify the density of the fluid and hence the local sound speed: points at higher density on the wave crests (higher intensity) travel faster than points in the wave troughs (low density/intensity) resulting in a faster movement of the crests that eventually leads to steepening. Fig. 6.3c) shows the corresponding lineouts of the profile for the input condition and after 18 cm propagation for a nonlocal and local nonlinearity. As expected, the steepening and wave breaking is damped in the nonlocal case. The velocity components of the travelling pulse are plotted in Fig. 6.3d) and as can be seen, both are now dependent on the density as predicted by Eq. (6.2.10). Therefore, the background flow v is induced by the wave itself. If the flow geometry is described in the context of acoustic spacetimes, the initially flat spacetime is distorted by the wave which then has a backreaction on the shape of the wave again. In this description, the dynamical interplay between wave and effective metric can be interpreted geometrically.

6.3 Geometrical interpretation

The results from the previous section showed that the dynamics of a nonlinear wave in the photon fluid can be described as a result from a self-induced flow. Interestingly, such waves or more specifically points at a given density are propagating at a constant speed $u = v \pm c_s$ that depends on the local density. In correspondence to analogue gravity, it will be shown how such waves can be interpreted as scalar waves in a curved spacetime geometry, that is usually given by the background flow v, but with the difference, that the curvature is now induced by the wave itself.
Starting from the (1+1) dimensional Navier Stokes equations (6.2.2) and (6.2.4) neglecting the quantum pressure and taking the time derivative of the continuity equation one finally arrives at a wave equation with the form [126]:

$$\partial_t^2 \rho - \partial_x \left((v^2 + 2v\rho \frac{dv}{d\rho} + c_s^2) \partial_x \rho \right) = 0 \tag{6.3.1}$$

From previous section $dv/d\rho = \pm c_s/\rho$ and $u(\rho) = v \pm c_s$, this becomes:

$$\partial_t^2 \rho - \partial_x \left(u^2 \partial_x \rho \right) = 0 \tag{6.3.2}$$

which can be written in a more compact form by using (1+1) spacetime coordinates $x^\mu = (t, x)$:

$$\partial_\mu (f^{\mu\nu} \partial_\nu \rho) = 0 \tag{6.3.3}$$

with the matrix:

$$f^{\mu\nu} = \begin{pmatrix} 1 & 0 \\ 0 & -u^2 \end{pmatrix} \tag{6.3.4}$$

Note that since $u(\rho)$ is a function of the density, this is a nonlinear wave equation for ρ. To show the analogy to a wave equation in an acoustic metric, one has to find a matrix that satisfies $f^{\mu\nu} = \sqrt{-g} g^{\mu\nu}$ ($g = \det g_{\mu\nu}$). Unfortunately, when dealing with (1+1) dimensional systems, it is known that the description of an acoustic metric fails, since the step from $f^{\mu\nu} = \sqrt{-g} g^{\mu\nu}$ breaks down [96]. However, this is a problem of intrinsically one-dimensional systems. Therefore, one can use a higher dimensional system, i.e (2+1)D with line symmetry where the metric is well defined. The experiments were carried out in an intrinsically (2+1)D photon fluid, where the symmetry along the y-axis was exploited to create a quasi (1+1)D system. With this, the equivalence between Eq. (6.3.3): $\partial_t^2 \rho - \nabla_\perp (u^2 \nabla_\perp \rho) = 0$ in (2+1)D and the Klein-Gordon equation in a curved spacetime can be shown and the wave equation can be reformulated using

the d'Alembert operator:

$$\frac{1}{\sqrt{-g}}\partial_\mu\left(\sqrt{-g}g^{\mu\nu}\partial_\nu\rho\right) = 0 \tag{6.3.5}$$

with the metric $g_{\mu\nu}$:

$$g_{\mu\nu} = \begin{pmatrix} u^4 & 0 & 0 \\ 0 & -u^2 & 0 \\ 0 & 0 & -u^2 \end{pmatrix} \tag{6.3.6}$$

This equation has the same algebraic form as Eq. (5.2.9) for small amplitude perturbations with a different metric, where in particular the flow v is density dependent and thus affected by a wave propagating in it. An expression for $u(\rho)$ can be derived from expanding $dv/d\rho = \pm c_s/\rho$ and $u(\rho) = v \pm c_s$ using the expression for the sound speed $c_s = \sqrt{c^2 n_2 \rho/n_0^3} = b^2\sqrt{\rho}$. With this, the flow is given as $v(\rho) = \pm 2b\sqrt{\rho} + v_0$. Here, v_0 appears as the integration constant and can be associated to the background flow. It is convenient to define a density ρ_0 at which the velocity $v = 0$ for a uniform density distribution. Hence, a wave propagating on such a background induces a flow $v(\rho) = \pm 2b(\sqrt{\rho} - \sqrt{\rho_0})$, while the total propagation velocity is given by:

$$u(\rho) = v(\rho) \pm c_s(\rho) = \pm b(3\sqrt{\rho} - 2\sqrt{\rho_0}) \tag{6.3.7}$$

Note, for small amplitude pertubations of the form $\rho = \rho_0 + \rho_1$ with $\rho_1 \ll \rho_0$, u reduces to the constant speed of sound. In the nonlinear case, a point in the profile at given density ρ will propagate at speed $u(\rho)$ and therefore wave crests are travelling faster than throughs which is the fundamental reason for wave steepening. As time evolves, this will lead to a situation where the leading slope of the wave becomes infinite and forms a density discontinuity (shock front), i.e. for a wave propagating in positive x-direction: $\partial\rho/\partial x = -\infty$ or $\partial x/\partial\rho = 0$. From geometrical considerations, it is clear that this point is not and extremum of the function $x(\rho)$, but a point of inflection. Therefore, also the second derivative $\partial^2 x/\partial\rho^2$ must vanish. Such a point can be associated to a singularity in the metric, that can be calculated via the Ricci scalar $\mathcal{R}$, which is in hand waving terms, a measure of curvature in differential geometry, i.e. $\mathcal{R}$ diverges in the presence of a singularity. The calculation is quite complicated [143], therefore only the result obtained with Maple shall be presented here:

$$\mathcal{R} = -\frac{2(3u^3(\partial_x^2 u + \partial_y^2 u) + u^2((\partial_x u)^2 + (\partial_y u)^2) - 2u(\partial_t^2 u) + 3(\partial_t u)^2)}{u^6} \tag{6.3.8}$$

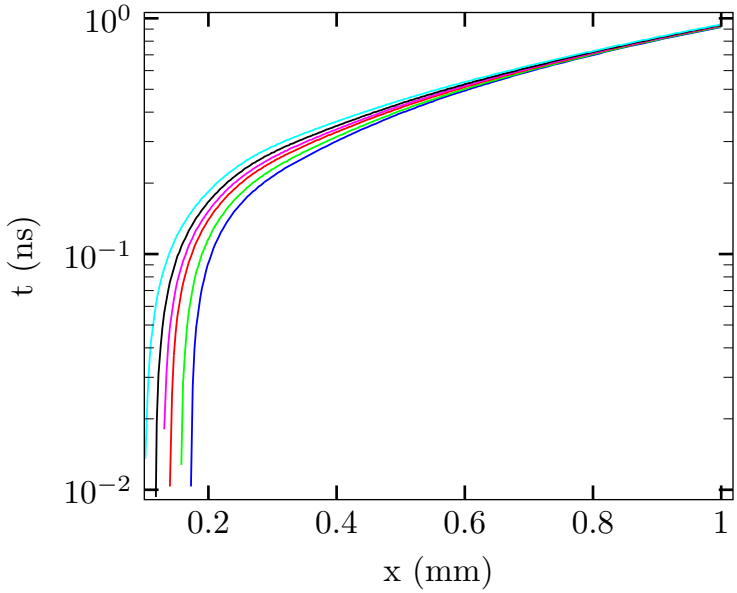

Figure 6.4: Numerical simulation of trajectories of points at constant density over time for an in positive x-direction travelling wave. Due to the self-induced spacetime curvature, they all intersect at a finite time corresponding to a singularity.

Hence, $\mathcal{R}$ diverges if $u = 0$ or if one of the summands diverges. The first case $u = 0$ is true for a critical density $\rho = 4/9\rho_0$. In this situation, points with densities lower than ρ_c travel in opposite direction to points above ρ_c and depends in the end how ρ_0 is chosen. Such a situation is not necessarily a singularity since the g_{00} in metric does not change sign beyond the horizon as is true for usual acoustic metrics where $g_{00} = c_s^2 - v^2$. The second case is given for the above conditions $\partial\rho/\partial x = -\infty$ and $\partial^2\rho/\partial x^2 = \infty$ since $u(\rho) \propto \sqrt{\rho}$. In linear analogues, such singularities are imposed by the background. Here however the singularity emerges in a finite time, starting from an initially flat spacetime. This is a consequence of the dynamic, nonlinear coupling between the wave and the self-induced metric.

Figure 6.4 shows the trajectories of points with equal density over time for the right moving wave in Fig. 6.3d), i.e. $x(\rho, t)$. From the geometrical perspective, these can be interpreted in terms of null geodesics. With Eq. (6.3.6) the line element can be written as:

$$ds^2 = g_{\mu\nu}dx^\mu dx^\nu = u^4dt^2 - u^2dx^2 - u^2dy^2 \tag{6.3.9}$$

and thus the null geodesic $ds^2 = 0$ along the positive x-direction is given by $dx = u(\rho)dt$. In linear acoustics, i.e where perturbations travel at a fixed speed solely determined by the background, geodesics are parallel in flat space and only intersect if the background

imposes a certain curvature. Here, since u is density dependent, two geodesics emanating from two spacetime points in an initially flat spacetime are no longer parallel and will intersect after a finite time.

6.4 Conclusion

The nonlinear wave dynamics in a quasi (1+1)D photon fluid have been investigated numerically and experimentally from two perspectives. While the linear propagation of pertubative waves is determined by a constant background configuration only, large amplitude waves significantly alter the background and are thus dynamically coupled to a self-induced, spatially and temporally varying background. The experimental and numerical results of propagation of these waves show self-steepening and eventually shock formation after a finite time. From a hydrodynamical viewpoint, the nonlinear dynamics can be derived from the Navier-Stokes equation where i.e. the self-steepening is understood as a consequence of a density dependent sound speed and self-induced flow for each point in the wave profile. Thus, wave crests are propagating faster than wave troughs.

A different point of view of these phenomena is derived in the perspective of analogue gravity. Usually, the analogy between fluid dynamics and acoustic spacetimes is established in the linear regime, i.e. the fluid variables and flow geometry is static and small amplitude perturbations can be described as scalar waves with a Klein-Gordon equation on a curved spacetime metric. In other words, the equation of motion for such perturbations are intrinsically linear and do not allow nonlinear phenomena such as self-steepening. However, as was shown by considering the full nonlinear problem, one can still find a wave equation that can be cast into a form of a Klein-Gordon equation on an effective metric, but now the metric will depend on the scalar wave itself. At first sight this is a bit surprising, since the mathematical form of this equation looks like a linear wave equation. The nonlinearity however is "hidden" in the metric and therefore the wave is influenced by the metric and vice versa. This describes a dynamically coupled system, where the self-steepening is understood as an increasing curvature of the spacetime induced by the wave propagating on it. As previously discussed, this self-interaction may be interpreted as a sort of gravitational influence of the wave itself. However, such a nonlinear coupling in general relativity is governed by the Einstein equations which are very different from the nonlinear equation described here. It has to be noted that, although the experiments were carried out in a thermal nonlinear medium that incorporates a finite nonlocality, the theoretical discussion is based on a local nonlinearity. This was mainly done to simplify the analysis and proof that the

nonlinear coupling of wave and metric is a valid approach to describe wave-steepening phenomena. Numerically it was found that the nonlocality indeed has an influence on the dynamics in way that smoothens the density profile and thus will have similar influence on self-induced flow and metric. Experimentally and numerically it was verified that the steepening can be observed, but is damped due to nonlocal effects.

Chapter 7

Incoherent nonlocal shock waves

So far, linear as well as nonlinear wave dynamics in nonlocal photon fluids have been presented in previous chapters. This chapter studies the stochastic dynamics of random nonlinear waves in nonlocal turbulent flows. In particular, in the presence of strong nonlinearity, a sea of random small scale waves develop a turbulent regime of dispersive shock waves. When the nonlocality is increased, the long range interactions between the random waves lead to the emergence of a collective incoherent shock wave. These results are interpreted in the context of the long range Vlasov equation, a formalism used to describe the statistical evolution of long range interacting random waves. The experimental and numerical results were published in "From coherent shocklets to giant collective incoherent shock waves in nonlocal turbulent flow", Nature Communications (2015) [144].

7.1 Introduction

The previous chapter presented the propagation dynamics of large amplitude waves that are governed by a nonlinear wave equation and as was shown, such waves develop a self-steepening that eventually leads to a shock front. In this scenario, the shock front is characterised by a train of oscillations due to dispersive regularisation and are thus coined as dispersive shock waves (DSW) [37, 39, 40, 145]. A similar effect occurs when a sea of random waves propagate in the presence of strong nonlinearity. In such a situation, each wave propagates and develops their own shocks resulting in a turbulent sea of nonlinear waves. The statistical description of turbulent flows is well understood in the weak nonlinear limit and describes various observations from classical to quantum fluids. In the case of optics, similar to a gas of weakly interacting particles, the thermalization of classical waves in a local photon fluid has been observed as a result of a self organisation process, leading to a large scale coherent structure with properties analogous to Bose Einstein condensates [42]. These observations can be understood on the basis of wave turbulence theory [146]. In the case of strong nonlinearities however, these models break down and therefore novel observations of wave turbulence in such a regime are of paramount interest. An additional level of complex phenomena occur in the presence of long range interactions between nonlinear waves that lead to different forms of self-organisation processes. Among these phenomena are the formation of incoherent solitons [35, 63] that can be studied in optics with incoherent beams in non-instantaneous nonlinear material. The random waves are created by a spatially (and temporarily) incoherent beam that has a random distribution of phase and intensity. In this situation, a soliton results from self-trapping via the nonlocal (non instantaneous) interactions and has recently been reported in highly nonlocal media [62], where the spatial smoothing of the nonlocality leads to a global nonlinear potential. In the presence of long range interactions or nonlocality, the inhomogeneous dynamics can be described by the long range Vlasov equation. This equation belongs to a family of kinetic equations used to describe long-range incoherent nonlinear waves [147]. This chapter presents the turbulent flow of strongly interacting shock waves in the presence of nonlocality. As will be shown, if the nonlocality is increased, a novel phenomena of self-organization is observed in a global collective shock front that emerges from the random field as a whole. This phenomenon is characterised as a radial shock front that features a non-homogeneous redistribution of the small scale fluctuations. Although no general theory in the strong nonlinear limit exists, it is outlined how this behaviour may be described by a hydrodynamic-like model derived from a long range Vlasov equation. The underlying theory and numerical simulations presented in this Chapter were

developed in the group of A.Picozzi at the Université de Bourgogne, Dijon, while the experiments were conducted at Heriot Watt University. The focus of this chapter is therefore set on the experimental results. However, a simplified outline of the theoretical background is presented for context. For more information, a comprehensive review is given in [147, 148].

7.2 From coherent shocklets to giant collective incoherent shock waves

7.2.1 Local versus nonlocal regimes

The system that is studied considers a spatially incoherent optical beam that is propagating through a nonlocal nonlinear medium. The incoherent field is characterised by a random distribution of phase and amplitude fluctuations, whose length scale is determined by the spatial coherence length λ_c. The dynamics are governed by the 2D nonlinear Schrödinger Equation (NLSE) with a nonlocal nonlinearity described a nonlocal response function with width σ:

$$\frac{\partial}{\partial z}E_0(r,z) = \frac{i}{2k_0}\nabla_\perp^2 E_0(r,z) + \frac{ik_0}{n_0}E_0(r,z)\gamma\int dr' R(r-r')|E_0(r',z)|^2 \qquad (7.2.1)$$

Note, that in the here discussed defocusing regime $\gamma < 0$. This equation conserves two important quantities: the power $N = \int |E_0|^2 dr$ and the energy (Hamiltonian) $H = \mathcal{E} + \mathcal{U}$. $\mathcal{E}(z)$ is the linear contribution $\mathcal{E}(z) = 1/(2k_0)\int \nabla^2|E_0(r,z)|^2 dr$ and the nonlinear contribution is denoted as $\mathcal{U} \propto \gamma\int |E_0(r,z)|^2 R(r-r')|E_0(r',z)|^2 dr dr'$. The important factors that rule the dynamics are the nonlocal length σ, the coherence length λ_c and the healing length ξ. It is known that the formation of shock waves require strong nonlinear interactions in the sense that linear (or dispersive) effects are negligible over nonlinear dynamics. This is expressed in the condition $\mathcal{U}_0 \gg \mathcal{E}_0$, or similarly $\lambda_c \gg \xi$. The coherence length determines the size of the fluctuations while the nonlocal length rules their interaction length scale. Thus if this length scale is larger than the average distance (or size) of the fluctuations, self organization processes play a significant role. In the following, the dynamics in a quasi local ($\sigma \ll \lambda_c$) and a highly nonlocal regime are discussed ($\sigma \gg \lambda_c$). The results were obtained by numerical simulations of the NLSE, starting with an input field shown in Fig. 7.1a) propagating along the z-direction.

In the case of a quasi local nonlinearity, the coherence length is much bigger than the nonlocal length and each fluctuation evolves independently and forms of a dispersive

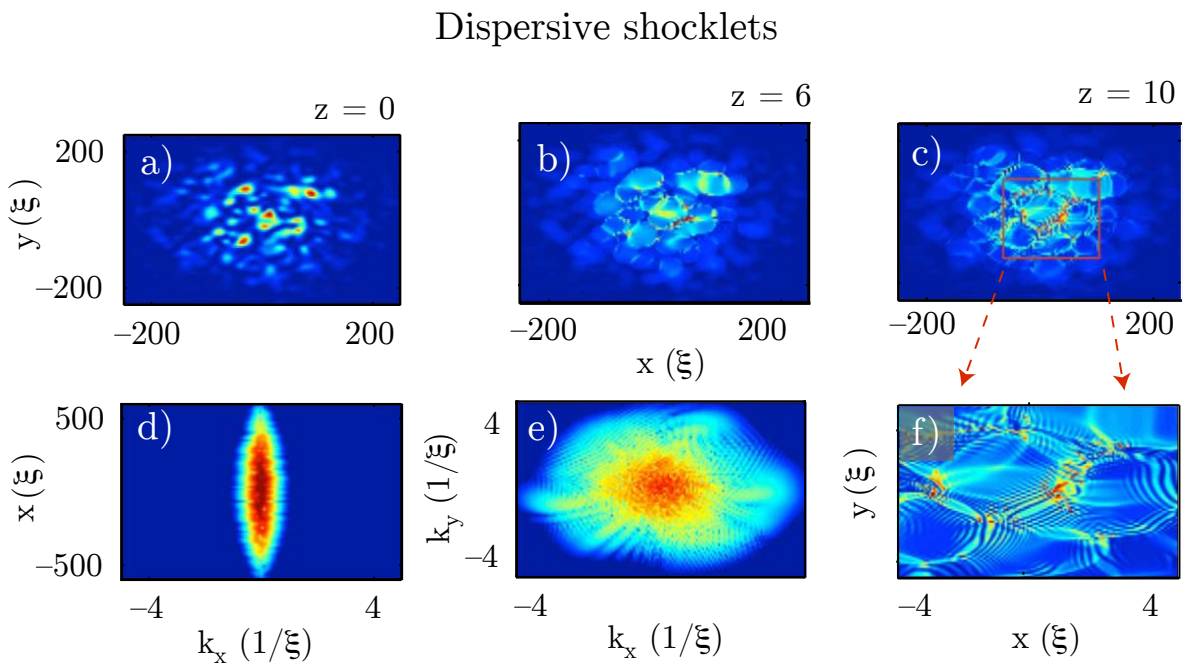

Figure 7.1: Quasi local regime, $\sigma \sim \xi \ll \lambda_c$, formation of dispersive shocklets: Numerical simulations of the NLSE with input field $|E_0|^2$ (a) and corresponding spectrogram (d). During propagation along z, each fluctuation in the incoherent field develops its own dispersive shock wave (shocklets) (b) and (c) and (f), as evidenced by a spectral broadening (e).

shock wave (Fig. 7.1). The result is a turbulent regime in which small scale coherent shock waves interact only over short distances. The sea of shock waves is manifested by a broadening of the k-space spectrum (Fig. 7.1e)), while the polygon like shape in real space is a result of the compression against each other alongside with a quasi 1D dispersive shock fronts.

These dynamics change drastically in the highly nonlocal regime. Here, the nonlocal length reaches beyond the coherence length and the dynamics are now ruled by a collective behaviour. Starting from the same initial condition, the fluctuations of the incoherent beam evolve into a giant incoherent shock front that is born at high intensity regions and develops a radial, collective shock front (Fig. 7.2). The radially oriented momentum (Fig. 7.2e)) exhibits a shock-like singularity, while the intensity develops an annular ring of small high intensity speckles. Along with the shock formation, a dramatic redistribution of fluctuations is observed. At the shock front, the speckles are pushed into a ring of even smaller sized structures, leaving a sea of much larger, low amplitude fluctuations behind in the centre of the beam. This redistribution is reflected in the spatially resolved spectrograms (Fig. 7.2g)-i)), showing a narrow spectrum at the beam centre and a significantly broadened spectrum in the shock front region.

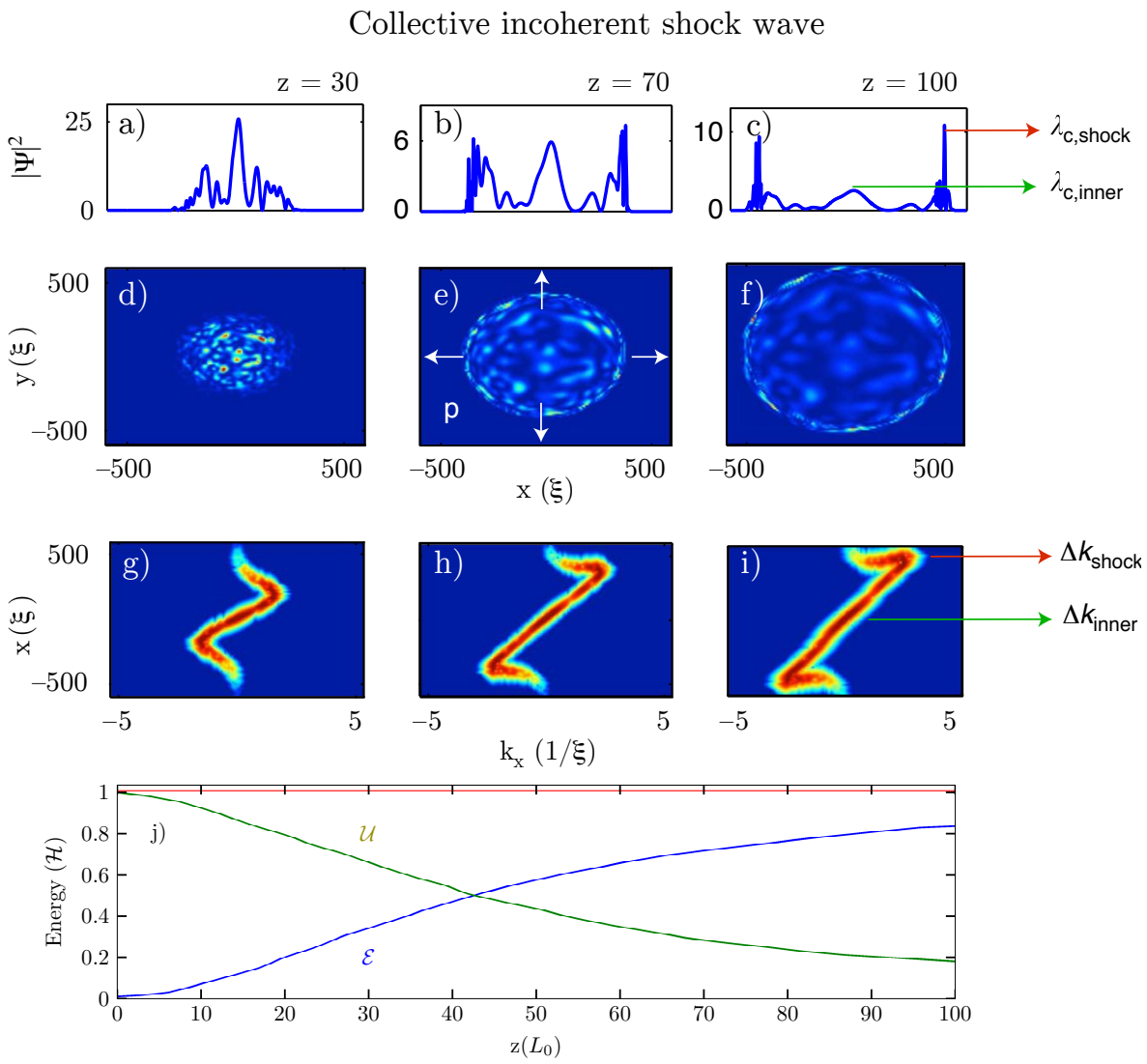

Figure 7.2: Highly nonlocal regime, $\sigma \gg \lambda_c > \xi$, emergence of collective incoherent shock wave. Starting from the same initial condition as shown in Fig. 7.1a) and d), the incoherent field develops a giant collective shock wave in the form of radially outgoing annular ring (a)-(f). The corresponding spectrograms during propagation (g)-(i) reveal a dramatic spectral redistribution (Z-shape) in the form of coherence degradation at the annular boundary ($\lambda_{c,shock} \sim 1/\Delta k_{shock}$) with a coherence enhancement in the inner region ($\lambda_{c,inner} \sim 1/\Delta k_{inner}$). The shock develops in the highly nonlinear regime ($\mathcal{U} \gg \mathcal{E}$) and is regularized by coherence degradation ($\mathcal{U} \sim \mathcal{E}$) during propagation (j). Propagation length in units of the nonlinear length $L_0 = 1/\gamma E_0^2$ [144].

The dynamics are thus featured by a coherence enhancement in central region and a degradation on the annular beam boundary. The radially outgoing, induced self-steepening is characterized by a tilt in the k_x-x spectrogram that together with the broadening at the annular boundary results in the Z-shaped pattern. This broadening

reflects the coherence degradation from $\lambda_c \gg \xi \rightarrow \lambda_c \sim \xi$ or equivalently $\mathcal{U} \gg \mathcal{E} \rightarrow \mathcal{U} \sim \mathcal{E}$ (Fig. 7.2j)). This regularization is in marked contrast to coherent dispersive shock waves where such a balancing of nonlinear and linear energies is due to the formation of regular dispersive shock wave oscillations.

7.2.2 Theoretical background

The incoherent shock phenomenon is a novel observation in the highly nonlocal and strongly nonlinear regime of turbulent flows. The wave turbulence theory describes the evolution of turbulent flows in the weakly nonlinear limit [42]. Here it is outlined how based on a generalized wave turbulence approach, the statistics of the incoherent shock can be described by a collsionless long-range Vlasov equation (LRVE) [61, 147]. In contrast to the NLSE where the nonlinear propagation of a local field is described, the Vlasov equation governs the evolution of the averaged spectrum of a random field distribution. The long-range Vlasov equation differs from the traditional Vlasov formalism used to study random wave in plasmas [149] or hydrodynamics [150], whose validity is constrained in the weak nonlinear limit for quasi-homogeneous statistics. In the highly nonlocal regime however, the LRVE provides an exact statistical description of a random inhomogeneous field and was used to model clustering of incoherent solitons [147] and is formally identical to the formalism to describe long range interacting, for example gravitational systems [151].
By comparison of numerical solutions using the NLSE and the LRVE, it is shown that the Vlasov formalism is valid beyond the weak nonlinear limit and provides a valid description of the random field in the highly nonlocal limit. In Fig. 7.2e) it was shown that in the presence of strong nonlinearity, i.e. $\mathcal{U} \gg \mathcal{E}$, the dynamics are ruled by a radially outgoing momentum of the field. It can be shown that in this case the 2D LRVE is reduced to an effective one dimensional equation [144]:

$$\partial_z n_k(r,z) + \frac{k}{2k_0}\partial_r n_k(r,z) - \partial_r V \partial_k n_k(r,z) = 0 \tag{7.2.2}$$

where $n_k(r,z)$ is the local averaged spectrum of the field at radial position r and $V(r,z) = \gamma/(2\pi)^2 \int_0^\infty \mathcal{R}(r,r')N(r',z)dr'$ with an effective radial response function $\mathcal{R}$. $N(r,z) = \int_0^\infty n_k(r,z)dk$ is the 'particle density'. Eq. (7.2.2) can be linked to a hydrodynamic-like model in the strongly nonlinear regime by means of "plane wave" solutions of the form $n_k(r,z) = N(r,z)\delta(k - K(r,z))$ with extremely narrow spectral distribution, where the particle density N and momentum K obey a set of equations

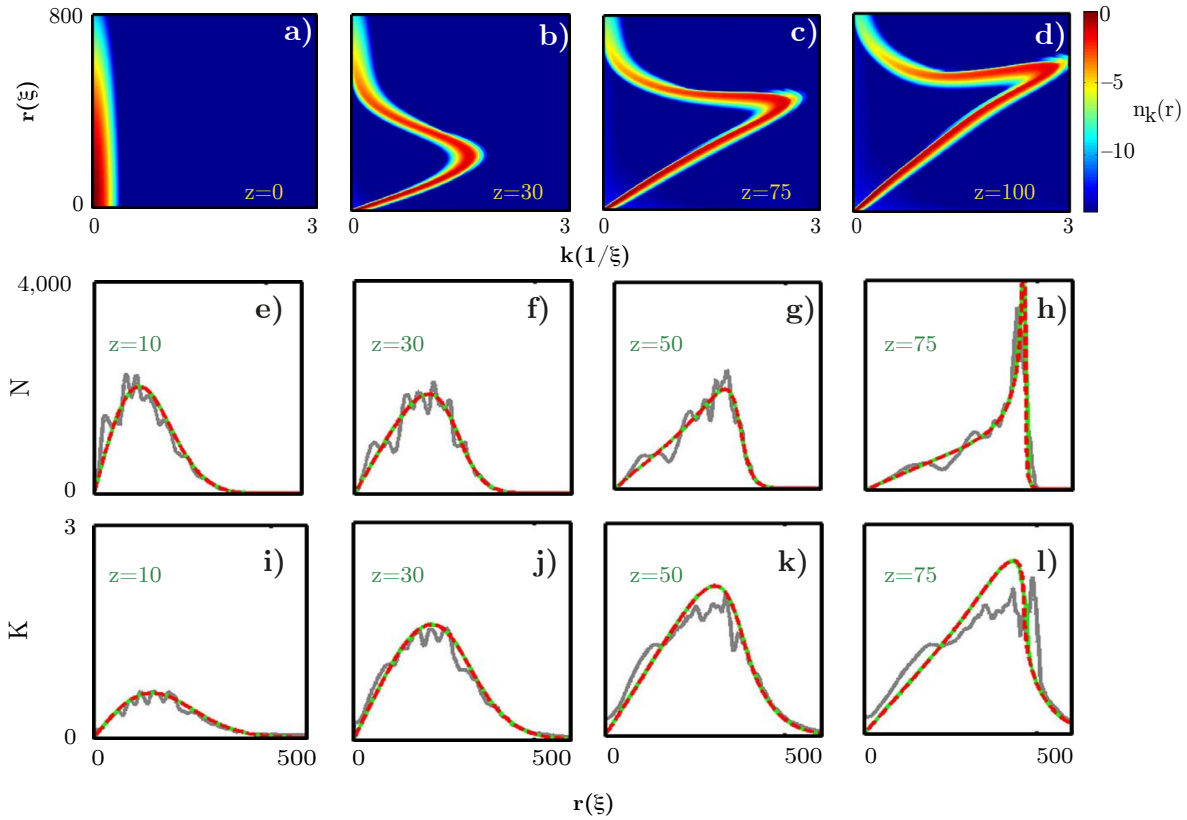

Figure 7.3: Comparison between NLSE and LRVE: (a)-(d) Numerical solution of the propagation along z of the spectrogram: $\tilde{n}_k(r,z) = n_k(r,z)/(rk)$ obtained by solving the effective 1D LRVE (Eq. (7.2.2)). Propagation of the intensity $N(r,z)$ (e)-(h), and momentum $K(r,z)$ (i)-(l) obtained by numerically solving the NLSE (grey, Eq. (7.2.1), LRVE (green, Eq. (7.2.2)) and the hydrodynamic-like model (red dashed, Eq. (7.2.3) and (7.2.4)). The propagation length z is in units of L_0. The NLSE simulation in (e)-(l) refers to the radial averaging of the results reported in Fig. 7.2.

of the same form as the Navier-Stokes equations (Eq. (6.2.2) and (6.2.4)):

$$\partial_z K + \frac{1}{2k_0} K \partial_r K + \partial_r V = 0 \tag{7.2.3}$$

$$\partial_z N + \frac{1}{2k_0} \partial_r (NK) = 0 \tag{7.2.4}$$

These so-called singular solutions are, from a broader perspective known as 'mono-kinetic' solutions, i.e. to each spatial position (r,z) corresponds a unique well-defined spectral velocity component (k,z) [152]. This particular form provides a direct correspondence to a general hydrodynamic formalism, that brought vital insights in numerous long-range interacting systems [152, 153].

In Fig. 7.3 numerical solutions of the three underlying formalisms, the NLSE, the LRVE and the hydrodynamic model are compared and show a quantitative agreement without

using any adjustable parameters. As discussed in the previous Chapter on nonlinear self-steepening, analogous effects can be observed here. Starting from $K(r, z = 0)$ and $N(r, z = 0)$, the dynamics are first driven by the nonlinear term $\propto \partial_r V$ in the first of the above equations, that acts as an effective pressure term. Then, once enough momentum (velocity) is gained, the steepening rate of the spectrum is ruled by the second term $\propto K\partial_r K$ and eventually leads to a gradient catastrophe of $K(r, z)$. Although there is no proof that the LRVE is valid in the strongly nonlinear regime, the results indicate that in this situation the long range Vlasov formalism is indeed suitable to interpret the observations. The hydrodynamic model equations provide an important insight into the formation of the collective shock phenomenon from a self-steepening perspective that is analogous to the problem studied for coherent nonlinear waves in Chapter 6. The difference in the incoherent case is that the momentum experiences a steepening and shock-like singularity, while the intensity experiences an annular collapse-like behaviour.

7.3 Experiment

The previously described phenomena of turbulent nonlinear wave dynamics in the presence of nonlocality can be studied in a photon fluid experiment consisting of a strong, spatially incoherent beam propagating through a thermal nonlinear medium. By controlling the range of nonlocality, the dispersive shocklets as well as the collective incoherent shock wave may be observed.

The experimental layout is shown in Fig. 7.4, where the incoherent field is realised by a speckle pattern that is generated by focusing the beam on a ground glass plate placed in the focal region of the first lens of a telescope. The beam does not need to satisfy gaussian statistics, as the LRVE accurately describes the dynamics in the highly nonlocal regime, thus the incoherent shock occurs regardless of the wave statistics. The beam is recollimated and sent through the nonlinear sample filled with a slightly absorptive methanol/graphene solution. Finally, the output is imaged by a 4-f imaging telescope onto the CCD camera for nearfield measurements. The spatially dependent spectrum $K_x(x)$ is measured by imaging and magnifying ($\times 2$) the sample output onto an translatable iris ($\oslash \approx 0.5$ mm) to image the farfield of selected parts of the beam. The beam has a diameter of 2.3 mm ($1/e^2$) in the absence of the ground glass plate and at the sample input. The coherence length, i.e. the size of the speckles can be controlled by changing the size of the beam on the glass plate by an iris or shift of the glass plate along the beam propagation in the focal region of the lens. The measured absorption coefficient was $\alpha = 0.013$ cm^{-1} and beam powers up to $P = 2.5$ W were

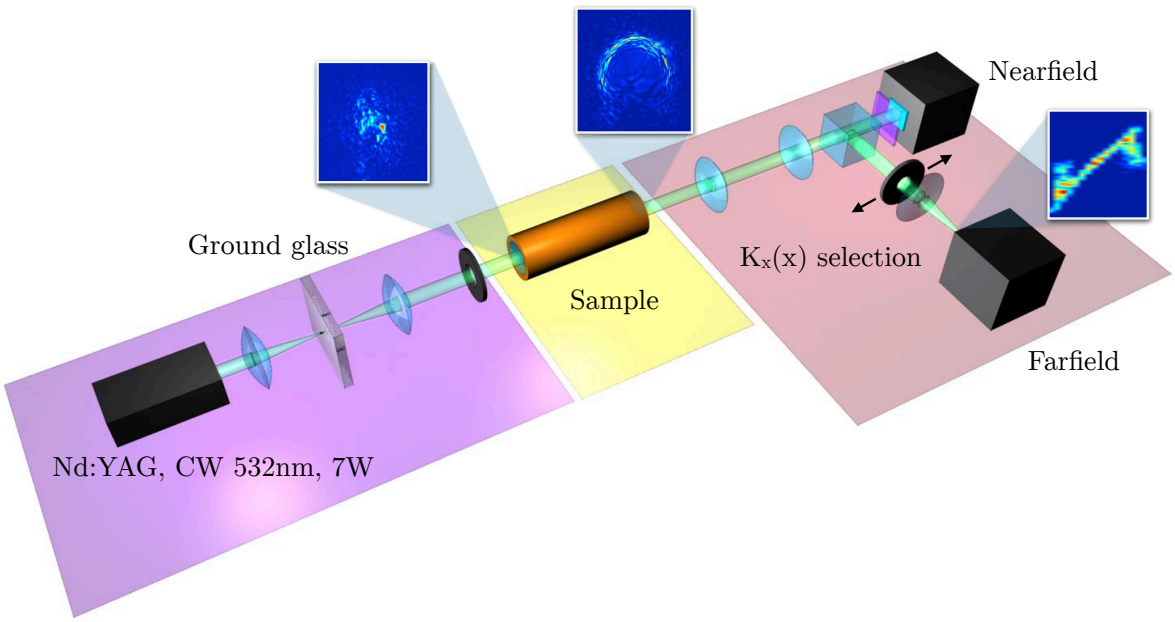

Figure 7.4: Experimental setup: The incoherent field is generated via focusing onto a ground glass plate, whose position is adjusted along the propagation direction to control the desired coherence length. The speckled beam is launched through the sample (12 cm) filled with a methanol/graphene solution providing a thermal nonlocal nonlinearity. The near- and farfield of the sample output is imaged to measure the intensity and k-space Fourier plane of the beam. The spatially resolved spectrograms are measured by translating an iris across the beam profile.

used. The coherence length of the speckle pattern can be estimated by the width of the transverse k-space spectrum, i.e. $\lambda_c \sim 1/\Delta k_\perp$. The typical coherence length and hence average speckle size was $\lambda_c \sim 200$ μm. The total power is distributed over few speckles of very high intensity ($I \sim 10-20$ W/cm^2), therefore an estimated value of the nonlinearity $\Delta n = \gamma_L(t > 10^3 s)I \approx -(2-4) \times 10^{-4}$ (γ_L taken from Fig. 5.7) leads to a healing length of $\xi < 5$ μm. The relatively low absorption does not cause longitudinal temperature gradients and hence the nonlocal length is given by the transverse sample dimensions, $\sigma \approx 10$ mm. Note, that despite absorption, the system can be regarded as Hamiltonian since the absorption length (~ 77 cm) is much larger than the nonlinear length (~ 0.04 cm) and the sample length (12 cm). With these parameters the scale separation $\sigma \gg \lambda_c > \xi$ required to be in the highly nonlocal regime to observe the incoherent shock wave is fulfilled.

Fig. 7.5d)-f) shows typically measured nearfield images of the incoherent beam at the sample output. With increasing power, the initial speckle pattern develops a ring-shaped pattern with high spatial frequency components on the annular boundary, leaving a smooth low-frequency region behind at the beam center. The corresponding

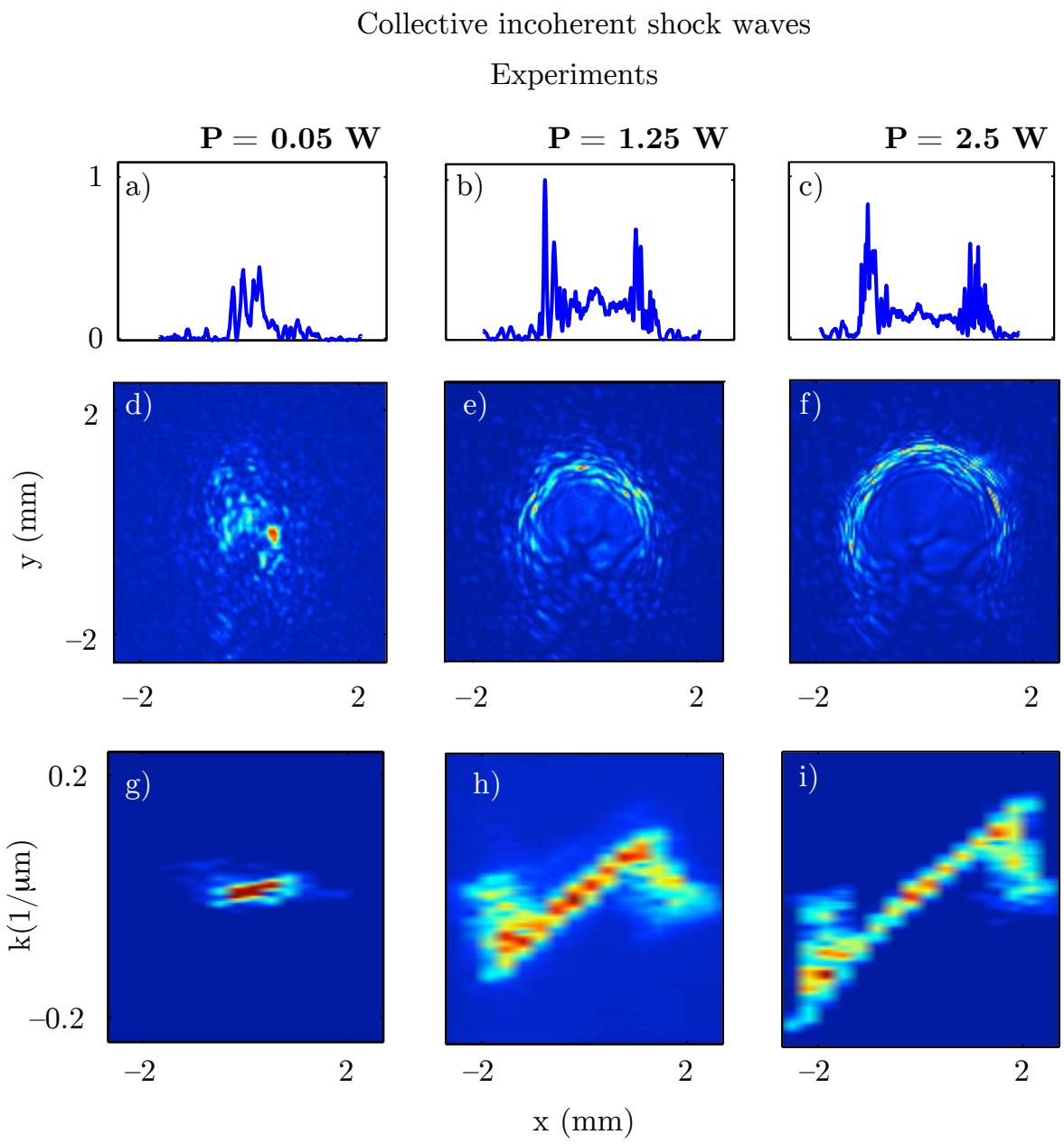

Figure 7.5: Experiments: Incoherent collective shock waves. (a)-(f) Nearfield beam profiles recorded at the sample output at various beam powers. With increasing power, the dynamics of the speckled input develop into an annular redistribution of the speckles. The up-down asymmetries are due to convection inside the sample (Lower part of the image corresponds to the upper part of the beam in the experiment). (g)-(i) Corresponding spectrograms confirm the emergence of a giant collective shock wave evidenced by the characteristic Z-shaped structure. Spectrograms measured along the x-axis (y=0).

lineouts at $y = 0$ confirm high intensity peaks at the annular boundary as predicted by the collapse behaviour and a rather flat region in the inner region. The absence of

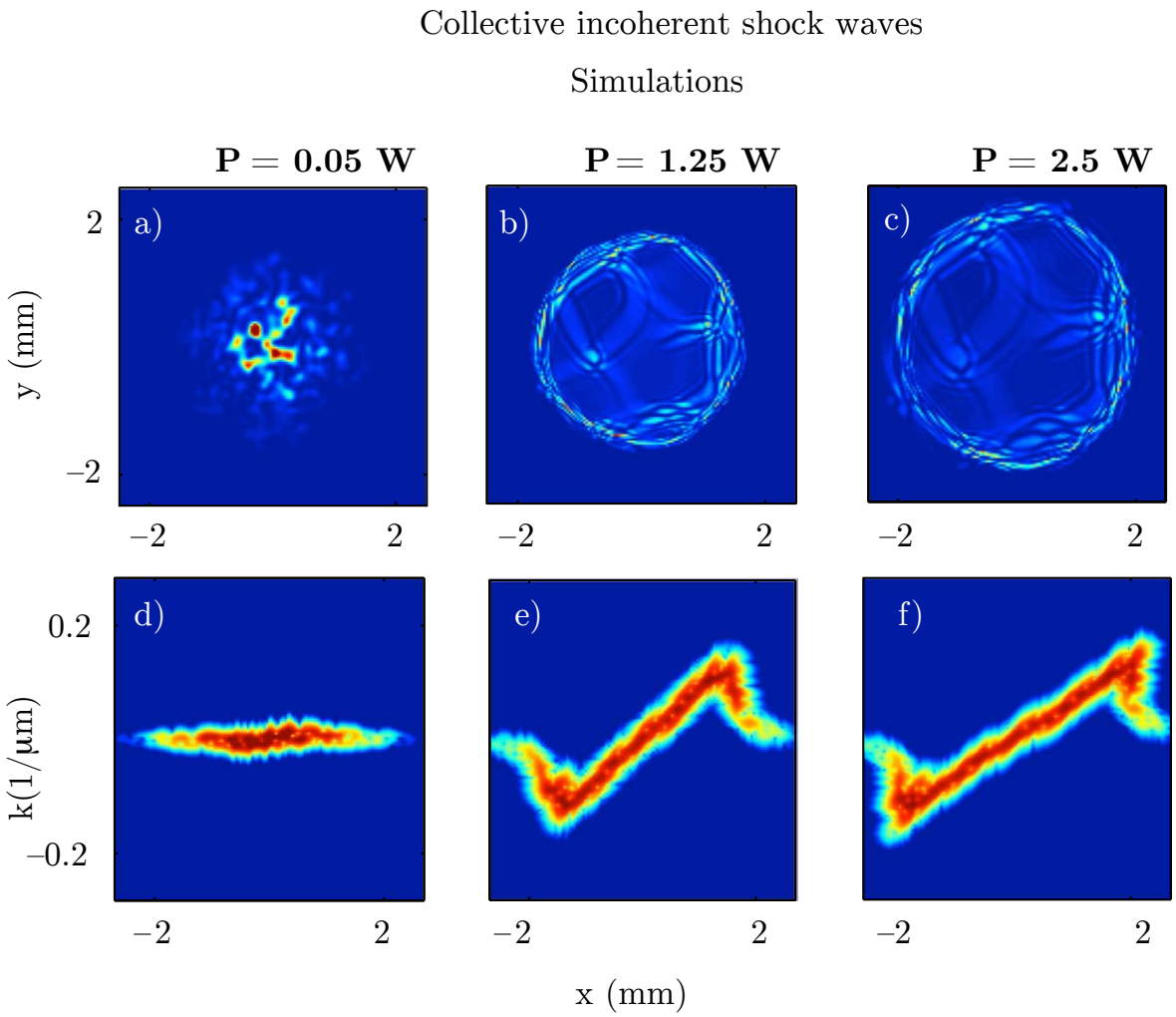

Figure 7.6: Numerics: Incoherent collective shock waves. The simulations of the NLSE were carried out with corresponding experimental parameters ($\lambda_c = 200$ μm, $\xi = 4$ μm, $\sigma = 590$ μm). The simulation are in excellent agreement to the experimental results in Fig. 7.5.

the shock in the bottom part is due to convection inside the sample, that completely distorts the beam. Note, the image is flipped due to imaging and the bottom part of the beam is actually the upper part in the experiment. The corresponding spectrograms were measured by spatially selecting parts of the beam with an iris that can be translated along the x-axis at $y = 0$. The transmitted light is focused by a cylindrical lens onto the CCD camera to record the farfield. In this way, the spatial dependence of the transverse Fourier transform k_x is recorded. The results show the characteristic Z-shaped distortion of the spectrograms as discussed earlier and confirm the coherence enhancement in the inner region and degradation at the annular boundary. For comparison, numerical simulations of the NLSE were performed with parameters matching

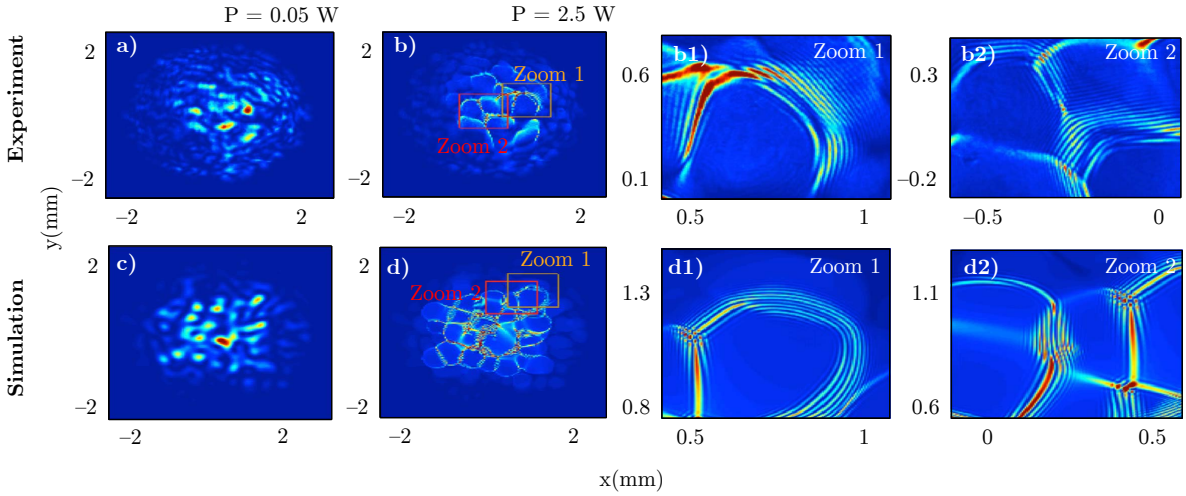

Figure 7.7: Experiment vs. numerics: Dispersive shocklets. (a)-(b) measured nearfield intensity at the sample (length: 1 cm) output for low and high power. To reduce the nonlocal length, an absorption coefficient of $\alpha \approx 1.7$ cm^{-1} was used. The zoomed in regions (b1)-(b2) show the characteristic undular patterns found for dispersive shock waves. (c)-(d2) Numerical results with experimental parameters ($\lambda_c = 250$ μm, $\xi = 3$ μm, $\sigma = 59$ μm).

those of the experiment. The nonlocal nonlinearity was modelled according to the DLM model where the nonlocal response function is described by the modified Bessel function of the second kind. Especially in this study, a nonlocal length of $400 < \sigma < 900$ μm [144] was estimated for the observation of the collective shock wave. Note, that the exact value of $\sigma \approx 10$ mm as presented in Chapter 2 was not known at the time of these studies, but this does not violate the condition $\lambda_c \ll \sigma$ to observe the collective shock wave. It is remarkable how the experimental results can be very well captured by the NLSE model with nonlocal nonlinearity. Regarding the similarity between the NLSE and LRVE in this highly nonlocal regime, this confirms that the experimental results indeed show the formation of a giant collective shock wave.

The numerical and experimental results so far demonstrated the emergence of the incoherent shock phenomenon. To validate that this is indeed a consequence of long-range interaction, the transition from the collective shock wave to dispersive shocklets is to be tested via the reduction of the nonlocal length. Although various methods to achieve this have been presented throughout this thesis, none of them is an experimentally realistic approach to reduce the nonlocal length while leaving beam size and nonlinearity untouched. In the past, several works highlighted the influence of boundary effects and strong absorption on the heat diffusion and thus on the nonlocal length [33, 40, 154]. In these studies, by considering the full 3D heat equation it was shown that temperature gradients along the beam propagation effectively reduces the transverse heat flux and

for similar arguments regarding the beam geometry (Chapter 4.3), the nonlocal length becomes a function of the absorption $\sigma \propto 1/\sqrt{\alpha}$ in the presence of strong longitudinal temperature gradients. These are relevant in short samples and this model was successfully applied to tweak the nonlocality on the study of shock waves in nonlocal media [40]. Following this approach, the nonlocality is reduced by significantly increasing the graphene concentration such that the absorption coefficient is roughly 100 times larger than before ($\alpha \approx 1.7$ cm^{-1}). Due to such strong absorption, a shorter sample (1 cm) was chosen in order to compensate for the large intensity drop during propagation. Although the shorter propagation corresponds to a 10 times reduction in the evolution in the photon fluid, the higher absorption leads to a higher nonlinearity that accelerates the dynamics by a factor ~ 10, compensating the effect.

The nonlocal length in the transverse domain can therefore be significantly reduced until the dynamics now reveal the independent formation of dispersive shock waves from individual speckles (Fig. 8.1). The experimental results are confirmed by numerical simulations that are in excellent agreement, both showing the characteristic undular structures as evidenced by the zoomed in parts of the beam. To further emphasize the importance of the ratio between the coherence and the nonlocal length that essentially define dynamics, the experiment was repeated for a reduced coherence length of $\lambda_c \sim 70$ μm (Fig. 7.8). Here, the individual speckles develop again a collective behaviour in the form of a low intensity region near the centre of the beam without developing dispersive shocklets. The dominating impact of the smaller coherence length is a slowed down dynamics of the incoherent shock, that can be qualitatively understood by the LRVE formalism. A decrease of λ_c corresponds to a broadening of the spectrum $S_0(k) = \int n_k(r, z = 0)dr$ in k-space and since the total power is conserved, this leads to a decreased amplitude n_k resulting in a slowing down of the dynamics. This is confirmed by the spectrograms shown in Fig. 7.8e)-f), where the characteristic Z-shaped structure is not fully evolved yet. In other words, the radial flux of the speckles toward the beam boundaries is evident in the tilted spectrogram, but the decoherence at the annular boundaries is not yet developed. Further decrease of the coherence length revealed, that the regular Z-shaped deformation disappeared, resulting only in a tilted spectrogram whose width Δk is independent of its position x [144, 148]. Therefore, the dynamics are slowed down where the observation of a collective shock front is completely suppressed.

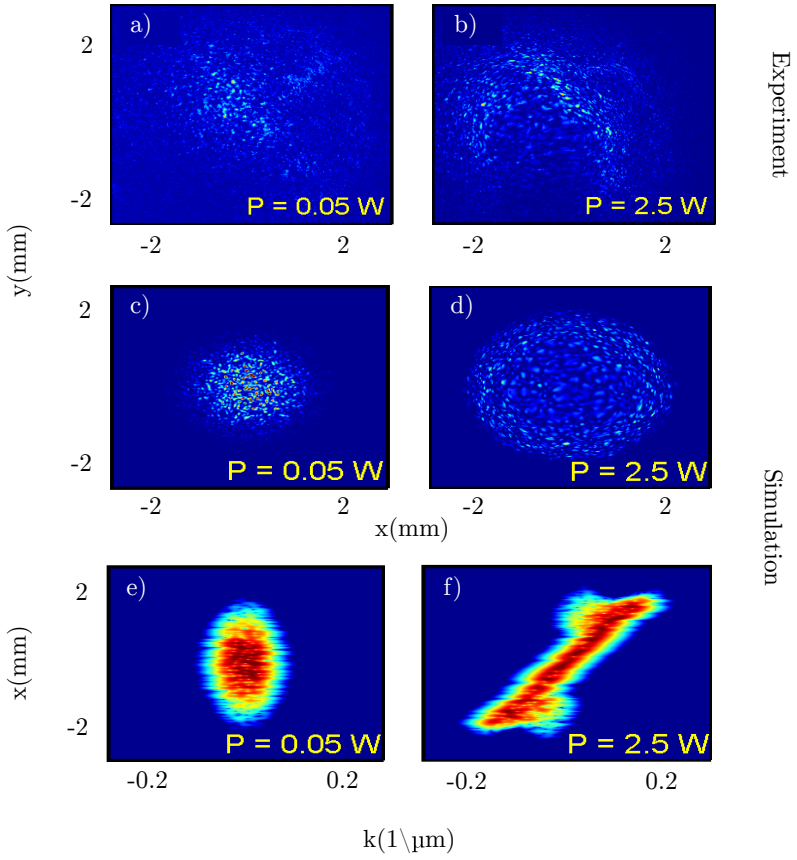

Figure 7.8: Incoherent shock regime at reduced coherence length: The experimental conditions are the same as in Fig. 7.5, except for $\lambda_c \sim 70$ μm. The nearfield intensity patterns (a) and (b) recorded at the sample output for low (0.05 W, linear regime) and high power (2.5 W, nonlinear regime). Numerical simulations performed with the same parameters are in qualitative agreement and confirm a slow down of the dynamics (c)-(f).

7.4 Conclusion

The study of turbulent flows can be realised in photon fluids by using highly incoherent speckle beams. When using a thermal nonlinearity, the inherent nonlocality leads to a long range interaction of individual speckles that in the language of photon fluids is translated into a sea of nonlinear random waves with long range interaction. Here, it was shown that in such a scenario the whole field develops a giant collective incoherent shock wave in contrast to a turbulent sea of dispersive shock waves as expected when the interactions are of short range character. The transition is ruled by the comparison of the average speckle size and the length of the long range interaction. In the photon fluid, these length scales are given by the spatial coherence length of the beam and the nonlocal length of the thermal nonlinearity. It was shown, that by controlling

these parameters the transition from a turbulent sea of dispersive shock waves to the formation of the collective shock wave can be experimentally observed and was verified by numerical simulations that are qualitatively in excellent agreement.
In the highly nonlocal regime, it was shown that the dynamics are accurately described by a long range Vlasov equation which was verified via comparison of numerical solutions to the NLSE. The radial structure of the incoherent shock allowed to apply a 1D hydrodynamic like model derived from the LRVE to provide physical insight into the shock formation.
In general, this photon fluid system displays a useful platform to study wave turbulence regime. Furthermore, the wide tunability of the nonlocality opens the possibility to access a wide range of regimes to study such turbulent, nonlinear flows. In the current experiment, the nonlocality was tuned via strongly changing the absorption in the system. Other self-organization processes mediated by long range interactions in these systems could be investigated when using a focusing thermal nonlinearity, i.e incoherent soliton turbulence [61] or gravitational systems. In the latter case, the long range nature of the focusing nonlinearity may be used to study galaxy dynamics [155], where the random distribution of stars that create their own collective potential can be modelled by a long range Vlasov formalism [156].

Chapter 8

Summary and Future Perspectives

8.1 General conclusions

A photon fluid in a propagating geometry was realised in a thermal nonlinear medium using a Nd:YAG CW laser and a methanol/graphene solution. The photon fluid is established via the optical nonlinearity in the transverse plane of the laser beam inside the nonlinear medium while spatial amplitude modulations behave as excitations in a quantum fluid. In contrast to many other studies in these systems that concentrated on nonlinear wave phenomena such as solitons or shock waves, the work presented here focussed mainly on pertubative excitations such as small amplitude waves. The dynamics are ruled by the system nonlinearity in which the diffusive nature of the thermal nonlinearity leads to a nonlocal response of the nonlinear refractive index. The nonlocal response may be understood as a long-range interaction of excitations in the photon fluid that significantly alter their dynamics.

In Chapter 2, the thermal nonlinearity of a dilute methanol/graphene solution in a cylindrical sample was characterized and was used in all experiments in this thesis. The nonlinearity is commonly described by the convolution of a response function and the intensity profile of the laser and is derived from the 2D heat diffusion equation. By adding a distributed loss term to incorporate the effect of finite boundaries, it was shown that the nonlinear response function could be analytically derived. It was shown that for the cylindrical symmetry, the width of the response function (nonlocal length) is given by the smallest sample dimensions. The model was confirmed by spatial phase interferometry experiments that measured the nonlinear change in refractive index induced by a narrow gaussian beam in the stationary and transient regime. The rather slow temporal build up of the thermal nonlinearity is confirmed by the time dependent heat equation and opens up wide tunability of the nonlocal length.

In Chapter 3, the dispersion relation for elementary excitations was measured in two different experiments. The first was inspired by oceanography, where the evolution of low amplitude noise on the laser profile was recorded along propagation and corresponds to video recording amplitudes of random ocean waves. The dispersion relation was then obtained by a Fourier transformation along the spatial and temporal coordinates. The second technique involved a pump and probe scheme, where the weak interference between two beams was used to seed a defined wave and measure its propagation speed in the photon fluid as a function of wavelength. The oceanographic technique revealed a purely parabolic dispersion relation that qualitatively agreed with the predicted Bogoliubov dispersion for superfluids, but was not able to resolve the low frequency part. However, it proved useful to detect the overall flow. The pump and probe technique overcomes the resolution problems and revealed the linear dispersion for waves that are

larger than the healing and the nonlocal length. The results agreed with the theoretical Bogoliubov dispersion relation including a nonlocal nonlinearity and it was shown that it alters the dispersion for wavelengths smaller than the nonlocal length in a way that their dynamics are governed by an effectively reduced nonlinearity. However, beyond those length scales, the waves behave as collective excitations of a superfluid. It was noted that the nonlocal length sets a new length scale for observing superfluidity. Nevertheless, the nonlocal length obtained in the dispersion relation measurements was two orders of magnitudes less than that obtained in the earlier thermal nonlinearity characterisation experiments. It was realised that the discrepancy arose due to different beam geometries and in the case of a highly elliptical beam profile, the effective nonlocal length that governs the dynamics is given by the smallest beam dimension rather than by the boundary conditions. This opened a new way of controlling the nonlocal length for re-establishing superfluidity in highly nonlocal media.

The collective excitations in the long wavelength limit are a requirement for superfluidity that can be formulated in terms of the Landau criterion for persistent currents below a critical speed. In Chapter 4, this was tested by immersing an extended obstacle into the highly elliptical photon fluid that was flowing at a relative speed around the obstacle. When the flow speed is smaller than the speed of sound in the photon fluid, the onset of superfluidity was observed by a suppression of scattering in the downstream region of the obstacle. For flow speeds larger than the sound speed, the nucleation of quantized vortices was observed confirming the superfluid character of the photon fluid.

The linear dispersion in the photon fluid allows to reformulate the equation of motion for small amplitude waves as an analogue of the Klein-Gordon equation for scalar fields in a curved spacetime. This analogy establishes the link between hydrodynamics and general relativity and allows to build artificial spacetimes for example of a black hole. In Chapter 5, this was realised by shaping the topology of the spatial phase of the beam via diffractive phase masks. The inhomogeneous flow of a rotating black hole and a white hole (time reversed black hole) was obtained by measuring the spatially resolved phase gradient. The speed of sound could be adjusted by the laser intensity such that there exists a spatially confined region where the flow speed is larger that the sound speed, creating a two dimensional acoustic horizon and ergosphere. These analogue models are promising candidates to experimentally test concepts of general relativity, i.e. Hawking radiation or superradiance. The 2D rotating black hole allows the study of the analogue of Penrose superradiance, i.e simply speaking an amplification of reflected waves off a spinning black hole. Preliminary experimental results show the scattering of waves from such a rotating spacetime that were confirmed by numerical simulations. In the simulations, an amplification could be observed for modes that carry an orbital

angular momentum that co-rotates and an absorption for modes counterrotating with the black hole. These results are promising and are a first step towards the observation of a superradiant scattering from a rotating black hole.

The analogy to general relativity was revisited in Chapter 6, where the nonlinear dynamics of photon fluid waves such as self-steepening and shock formation, was reformulated in terms of a self-induced spacetime curvature that back reacts on the wave itself. These so-called emergent geometries are different from the classical analogue gravity approach where linear perturbations propagate on a stationary background. In this perspective, it was shown that the nonlinear wave induces a gradually increasing curvature of the spacetime in the propagation direction that eventually results in a space-time singularity that is known as the shock formation in hydrodynamics. This was underlined by experimental and numerical results, that showed the nonlinear wave steepening and shock formation in a quasi (1+1)D photon fluid.

Next to coherent nonlinear wave dynamics, the turbulent behaviour of a sea of random nonlinear waves with long range interactions was studied in Chapter 7. This system is described by a stochastic mathematical formalism (long range Vlasov formalism) that is also used to describe long range interacting systems such as gravitational systems, i.e. galaxies. The experiment involved a spatially highly incoherent beam propagating in the nonlocal thermal medium, where the random pattern of intensity modulations correspond to a turbulent sea of nonlinear waves. Depending on the range of nonlocality, a transition from a turbulent sea of small scale coherent dispersive shock waves to a giant collective incoherent shock wave could be observed. This novel observation of a self-organisation process can be understood in the Vlasov formalism and can be mapped onto a hydrodynamic like model for the average speckle density and its momentum that is ruled by the interplay between the average speckle size and their range of interactions. The incoherent shock was confirmed by a spatially resolved measurement of the local spectrum, that revealed the regularization of the shock via a drastic decoherence of the field along the annular boundary along with a coherence enhancement in the beam centre.

Summarising, photon fluids are a versatile platform for exploring the rich physics of quantum fluids, from perturbative schemes that proved useful to study analogue gravity to nonlinear dynamics to study many-body physics. The nonlocal character of the nonlinearity adds another level of complexity that opens the door to the physics of long range interacting system such as gravitational systems or self-organisation of turbulent flows.

8.2 Future perspectives

So far, the scene is set to study analogue gravity in propagating photon fluids, but the more interesting question is where the journey goes from here. The outstanding feature of the analogue black hole presented in here lies certainly in its (2+1) dimensional geometry and the relatively straight forward control of sound and flow speeds. The higher dimensions allows to study rotational black holes and Penrose superradiance where already theoretical and experimental efforts are being made for its observation. This superradiant scattering is a stimulated process that does not involve spontaneous emission of quanta from the vacuum and should be therefore observable in classical fluids as well as photon fluids with a thermal nonlinearity. Quantized superradiance as well as the spontaneous Hawking emission requires a quantum description of the underlying field. In general, a temporally varying medium emits quanta from the vacuum according to quantum field theory [157]. In the case of photon fluids in a propagating geometry, theoretical works reported a quantum theory of the many-body dynamics of a paraxially propagating laser beam in a local Kerr medium, where such a quantum emission was discussed [45, 158]. It is however not clear if such a theory can be applied to system with a noninstanteneous thermal nonlinearity, where the slow response of the medium does not support measurable quantum fluctuations. Nevertheless, a gas of strongly interacting photons at the quantum level has been reported in a propagating geometry using a dressed ^{87}Rb gas in the Rydberg electromagnetically induced transparency (EIT) regime [159]. Thus, atomic gases could be used to study quantum effects in propagating photon fluids in the future.

Apart from the quantum effects, the stimulated Hawking process could still be observable in the current configuration. Similar to the experiments in water [160], the peculiar nonlocal dispersion relation provides a subluminal part that enables a wave blocking horizon for a certain range of frequencies. When the waves are blocked, energy can be converted to other branches in the dispersion and amplify modes with negative norm, which is the fundamental process of stimulated Hawking emission. This could be measured by looking for correlations of random thermal noise in the farfield spectrum.

Photon fluids are also becoming more and more attractive for studying the physics of many-body systems. Whereas exciton-polariton systems have been dominating the field, propagating geometries catching up not only for their easy implementation, but also since they are governed by a conserved Hamiltonian as opposed to driven-dissipative systems, where dynamics and the description of purely quantum features is complicated due to pumping and losses. In this regard, investigating the quantum aspects of the propagating light fluid may lead to Bose-Einstein condensation, that could be achieved

by an equivalent of evaporative cooling of the beam via a tapered waveguide [45]. Furthermore, the prospect of quantum simulation using quantum fluids has so far been mainly devoted to cold atomic systems [161]. In particular, the study of magnetic phenomena in such systems demands for alternative ways of simulating magnetism, since the atoms are neutral and are thus not affected by the Lorentz force. A possible way is to set the atom cloud under rotation, where the effective Coriolis force in the co-rotating reference frame is formally equivalent to the effect of a magnetic field.
The same problem arises in photon fluids, where no magnetic field for charge- and massless photons exist. A recent study in our group reported a theory how to make a magnetic field in a photon fluid, based on artificial gauge fields [162]. In photon fluids, the theory applies to weak excitations on a strong background field carrying orbital angular momentum and opens the door to study many-body dynamics under synthetic magnetic fields.

8.3 More analogies

8.3.1 Optical analogues of Boson stars

The testbed for gravity in optics is widely understood in terms of a fluid of light that provides a useful connection to hydrodynamics when the nonlinearity is defocusing, i.e. inherits a repulsive photon-photon interaction. Another example of the analogy between optics and gravity can be established when considering a nonlocal focusing nonlinearity, that allows to study the dynamics of the Newton-Schrödinger equation:

$$i\hbar\psi_t + \frac{\hbar^2}{2m}\nabla^2\psi + m\phi\psi = 0 \tag{8.3.1}$$

which describes the evolution of a massive particle with wave function ψ in a self-induced gravitational potential ϕ given by the poisson equation:

$$\nabla^2\phi = -4\pi G m|\psi|^2 \tag{8.3.2}$$

with the gravitational constant G. In contrast to the "general" analogue gravity approach, the gravitational field here is induced by the quantum matter itself and was proposed by Diosi [163] and Penrose [164] to investigate the collapse of the wave function in its own gravitational potential. As such, due to the coupling between gravity and quantum matter states, the Newton-Schrödinger equation (NSE) was used to describe the evolution of Bose-Einstein condensate stars or boson stars [165]. These objects are considered to be an alternative interpretation to black holes. The analogy of the NSE

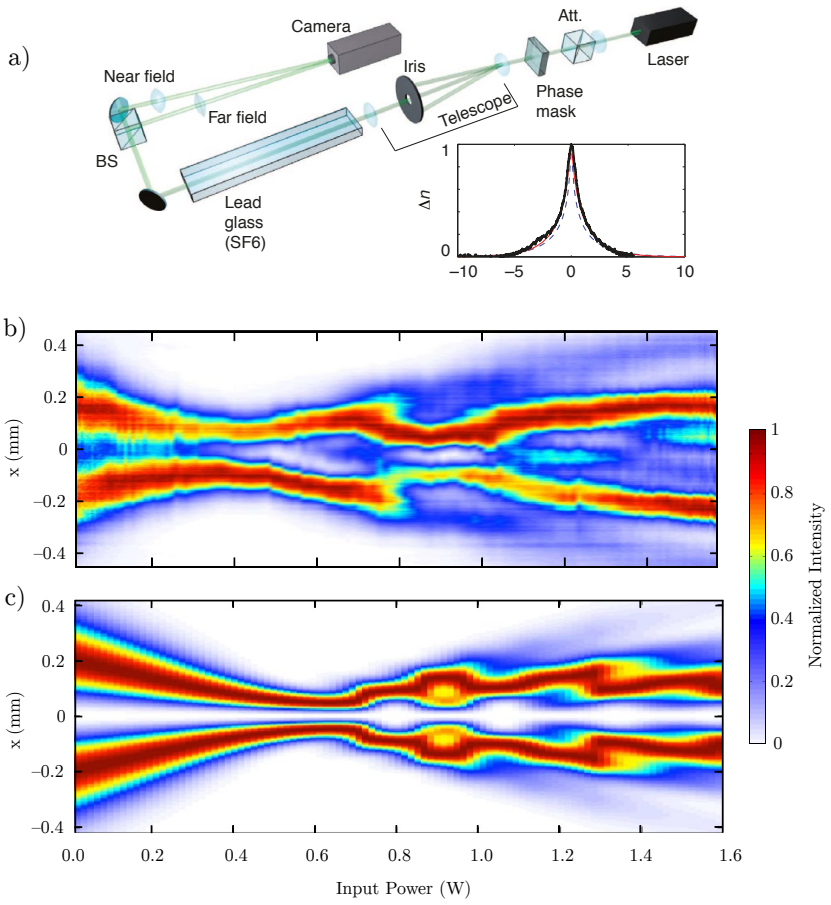

Figure 8.1: Experiments and numerical simulations studying the dynamics of a rotating boson star in a focusing thermal medium. (a) Experimental layout: A CW beam is attenuated and launched onto a diffractive phase mask to imprint an OAM phase ($\ell = 1$). The beam is demagnified and launched in a 400 mm long lead-doped glass slab, exhibiting a focusing thermal nonlinearity. The far- and nearfield is imaged at the output onto a CCD camera. Inset: Induced nonlinear refractive index in the glass (normalised to one) calculated by numerically solving the 2D heat equation (blue dashed line), by analytical solution of the DLM model (red) and measurement (black line). b) Experimental and c) numerical example of the real space intensity distribution $I(x, 0)$ as a function of laser power corresponding to the dynamics of 2D slice of a rotating boson star. Note that the increasing power leads to a faster evolution that qualitatively resembles the propagation along z. Taken from Roger et al. [123].

to nonlinear optics becomes evident when the Nonlinear Schrödinger equation (NLSE) with a focusing nonlinearity is considered:

$$i\frac{\partial E_0}{\partial z} + \frac{1}{2k}\nabla_\perp^2 E_0 + \frac{k}{n_0}\Delta n E_0 = 0 \tag{8.3.3}$$

with a thermal nonlinearity that is governed by a Poisson equation of the same form as Eq. (8.3.2):

$$\nabla_{\perp}^2(\Delta n) = -\frac{\alpha\beta}{\kappa}|E_0|^2 \tag{8.3.4}$$

Hence, the NSE provides the possibility to study a 2D slice of the full 3D gravitational system. It was shown that under appropriate experimental conditions, the nonlinear response qualitatively mimics an attractive gravitational potential in the transverse profile of the beam. In particular, this is true for beams that carry orbital angular momentum which describe in this scenario the evolution of a rotating boson star with quantized angular momentum [123]. With this, it could be shown that the star undergoes contraction cycles at low densities (i.e. beam intensities). Numerical simulations confirm the experiments, that show at higher densities that the star becomes unstable, although the phase singularity prevents complete collapse. This is understood as a result of the quantised angular momentum of the boson star.

8.3.2 Cosmological analogy

The concept of analogue spacetimes has been introduced in Chapter 5 for small amplitude perturbations and Chapter 6 for large amplitude waves. In the latter case it was shown that the nonlinear wave dynamics could be interpreted as a wave propagating in a self-induced spacetime. In a similar manner, the same effect may be used to simulate a rapidly expanding universe, i.e cosmological inflation. In general, the idea is based on a strongly defocusing gaussian beam in a defocusing nonlinear media, whose diameter is drastically increasing during propagation. The analogy is established in a rapidly expanding photon fluid, where a scale factor for the (radial) velocities that depend on time i.e. z is introduced. Assuming this is a linear function in the transverse direction r:

$$v = H(t)r \tag{8.3.5}$$

This is known as the 'Hubble law' with the Hubble parameter $H = \frac{\dot{a}}{a}$, that is defined by the scale factor $a(t)$. By redefining the radial coordinate $\tilde{r} = r/a$, one can show that the metric for pertubations (Eq. (5.2.10)) can be expressed as

$$ds^2 = \left(\frac{\rho}{c}\right)^2 \left[-c^2dt^2 + a(t)^2(d\tilde{r}^2 + \tilde{r}^2 d\Omega^2)\right] \tag{8.3.6}$$

which is conformal to an expanding Friedmann-Lemaitre-Robertson-Walker (FLRW) spacetime. Apart from optics, these models were proposed to study i.e. particle production driven from the analogue of the expansion of the universe in an expanding BEC [96, 166, 167]. Inflation models of the early universe give an explanation for small

fluctuations in the Cosmic Microwave Background (CMB). In a nutshell, these fluctuations are linked to amplified quantum fluctuations that were frozen during the rapid expansion of the universe, and according to the current cosmological models, are the seeds for structure formation such as galaxies. Apart from the quantum effects that are experimentally not realistic in thermal media, mode freezing of thermal fluctuations may be studied in these systems.
The equation of motion of the coupled scalar field in such a FLRW spacetime is essentially a wave equation with a time dependent damping term, i.e.

$$\partial_t^2\phi + \frac{\dot{a}}{a}\partial_t\phi + \frac{c^2k^2}{a^2}\phi = 0 \tag{8.3.7}$$

If the expansion is fast enough, i.e. if the damping is changing faster than the oscillation of a wave, then such modes are effectively frozen in time. This mode freezing can also be understood in terms of a maximum co-moving spatial distance, at which events can be in causal contact, a cosmological horizon. If the wavelength of a mode is stretched beyond this horizon due to cosmic expansion, the causality is lost and the modes cannot oscillate anymore.
This effect can be simulated by a rapidly expanding beam with random small amplitude thermal noise. This noise plays the role of the fluctuations that may be frozen. In such a scenario, various expansion rates can be tweaked by controlling the defocusing of the beam, and test the effect on mode freezing with different inflation models.

8.4 Epilogue

Despite the rich and interesting physics that these analogue gravity systems provide, one must not forget that they are a lot of fun to work with. I am still amazed that I can actually build a black hole with a laser and a water pipe filled with a cloudy alcohol solution. It doesn't end with black holes, there are also (Boson) stars, expanding spacetimes and literally, there is a whole universe in a (laboratory not much bigger than a) nutshell.

Bibliography

[1] M. Brambilla, L. A. Lugiato, V. Penna, F. Prati, C. Tamm, and C. O. Weiss, "Transverse laser patterns. II. Variational principle for pattern selection, spatial multistability, and laser hydrodynamics," *Physical Review A*, vol. 43, pp. 5114–5120, 1991.

[2] K. Staliunas, "Laser Ginzburg-Landau equation and laser hydrodynamics," *Physical Review A*, vol. 48, pp. 1573–1581, 1993.

[3] F. T. Arecchi, G. Giacomelli, P. L. Ramazza, and S. Residori, "Vortices and defect statistics in two-dimensional optical chaos," *Physical Review Letters*, vol. 67, no. 27, pp. 3749–3752, 1991.

[4] M. Vaupel, K. Staliunas, and C. O. Weiss, "Hydrodynamic phenomena in laser physics: Modes with flow and vortices behind an obstacle in an optical channel," *Physical Review A*, vol. 54, pp. 880–892, 1996.

[5] J. Kasprzak, M. Richard, S. Kundermann, A. Baas, P. Jeambrun, J. M. J. Keeling, F. M. Marchetti, M. H. Szymańska, R. André, J. L. Staehli, V. Savona, P. B. Littlewood, B. Deveaud, and L. S. Dang, "Bose Einstein condensation of exciton polaritons," *Nature*, vol. 443, pp. 409–414, 2006.

[6] J. J. Baumberg, P. G. Savvidis, R. M. Stevenson, A. I. Tartakovskii, M. S. Skolnick, D. M. Whittaker, and J. S. Roberts, "Parametric oscillation in a vertical microcavity: A polariton condensate or micro-optical parametric oscillation," *Physical Review B*, vol. 62, pp. R16247–R16250, 2000.

[7] R. Balili, V. Hartwell, D. Snoke, L. Pfeiffer, and K. West, "Bose-Einstein condensation of microcavity polaritons in a trap.," *Science*, vol. 316, no. 5827, pp. 1007–10, 2007.

[8] J. Klaers, J. Schmitt, F. Vewinger, and M. Weitz, "Bose-Einstein condensation of photons in an optical microcavity.," *Nature*, vol. 468, pp. 545–548, 2010.

[9] R. Nyman and M. Szymańska, "Interactions in dye-microcavity photon condensates and the prospects for their observation," *Physical Review A*, vol. 033844, pp. 1–7, 2014.

[10] J. Keeling and N. G. Berloff, "Exciton polariton condensation," *Contemporary Physics*, vol. 52, pp. 131–151, 2011.

[11] I. Carusotto and C. Ciuti, "Probing microcavity polariton superfluidity through resonant rayleigh scattering," *Physical Review Letters*, vol. 93, no. 16, 2004.

[12] R. Chiao and J. Boyce, "Bogoliubov dispersion relation and the possibility of superfluidity for weakly interacting photons in a two-dimensional photon fluid," *Physical Review A*, vol. 60, pp. 4114–4121, 1999.

[13] A. Amo, D. Sanvitto, F. P. Laussy, D. Ballarini, E. del Valle, M. D. Martin, A. Lemaître, J. Bloch, D. N. Krizhanovskii, M. S. Skolnick, C. Tejedor, and L. Viña, "Collective fluid dynamics of a polariton condensate in a semiconductor microcavity," *Nature*, vol. 457, pp. 291–295, 2009.

[14] A. Amo, J. Lefrère, S. Pigeon, C. Adrados, C. Ciuti, I. Carusotto, R. Houdré, E. Giacobino, and A. Bramati, "Superfluidity of polaritons in semiconductor microcavities," *Nature Physics*, vol. 5, pp. 805–810, 2009.

[15] D. Sanvitto, S. Pigeon, A. Amo, D. Ballarini, M. De Giorgi, I. Carusotto, R. Hivet, F. Pisanello, V. G. Sala, P. S. S. Guimaraes, R. Houdré, E. Giacobino, C. Ciuti, A. Bramati, and G. Gigli, "All-optical control of the quantum flow of a polariton condensate," *Nature Photonics*, vol. 5, pp. 610–614, 2011.

[16] A. Amo, S. Pigeon, D. Sanvitto, V. G. Sala, R. Hivet, I. Carusotto, F. Pisanello, G. Leménager, R. Houdré, E. Giacobino, C. Ciuti, and A. Bramati, "Polariton superfluids reveal quantum hydrodynamic solitons.," *Science*, vol. 332, no. 6034, pp. 1167–1170, 2011.

[17] F. Marino, "Acoustic black holes in a two-dimensional photon fluid," *Physical Review A*, vol. 78, p. 063804, 2008.

[18] P. Grisins, H. S. Nguyen, J. Bloch, A. Amo, and I. Carusotto, "Theoretical study of stimulated and spontaneous Hawking effects from an acoustic black hole in a hydrodynamically flowing fluid of light," *Physical Review B*, vol. 94, no. 14, 2016.

[19] H. S. Nguyen, D. Gerace, I. Carusotto, D. Sanvitto, E. Galopin, A. Lemaître, I. Sagnes, J. Bloch, and A. Amo, "Acoustic black hole in a stationary hydrodynamic flow of microcavity polaritons.," *Physical Review Letters*, vol. 114, 2015.

[20] G. Swartzlander and C. Law, "Optical vortex solitons observed in Kerr nonlinear media," *Physical Review Letters*, vol. 69, no. 17, 1992.

[21] C. Josserand and S. Rica, "Coalescence and Droplets in the Subcritical Nonlinear Schrödinger Equation," *Physical Review Letters*, vol. 78, pp. 1215–1218, 1997.

[22] M. Segev, B. Crosignani, A. Yariv, and B. Fischer, "Spatial solitons in photorefractive media," *Physical Review Letters*, vol. 68, pp. 923–926, 1992.

[23] C. Conti, A. Fratalocchi, M. Peccianti, G. Ruocco, and S. Trillo, "Observation of a Gradient Catastrophe Generating Solitons," *Physical Review Letters*, vol. 102, p. 083902, 2009.

[24] D. Suter and T. Blasberg, "Stabilization of transverse solitary waves by a nonlocal response of the nonlinear medium," *Physical Review A*, vol. 48, pp. 4583–4587, 1993.

[25] D. N. Christodoulides and M. I. Carvalho, "Bright, dark, and gray spatial soliton states in photorefractive media," *Journal of the Optical Society of America B*, vol. 12, p. 1628, 1995.

[26] G. Duree, M. Morin, and G. Salamo, "Dark photorefractive spatial solitons and photorefractive vortex solitons," *Physical Review Letters*, vol. 74, no. 11, 1995.

[27] A. Mamaev, M. Saffman, and A. Zozulya, "Propagation of Dark Stripe Beams in Nonlinear Media: Snake Instability and Creation of Optical Vortices," *Physical Review Letters*, vol. 76, pp. 2262–2265, 1996.

[28] M. Taya, M. Bashaw, M. Fejer, M. Segev, and G. Valley, "Observation of dark photovoltaic spatial solitons," *Physical Review A*, vol. 52, no. 4, 1995.

[29] Y. Kivshar and B. Luther-Davies, "Dark optical solitons: physics and applications," *Physics Reports*, vol. 298, pp. 81-197, 1998.

[30] G. I. Stegeman, "Optical Spatial Solitons and Their Interactions: Universality and Diversity," *Science*, vol. 286, pp. 1518–1523, 1999.

[31] Z. Chen, "Optical spatial solitons: historical overview and recent advances," *Reports on Progress in Physics*, vol. 75, 2012.

[32] N. I. Nikolov, D. Neshev, W. Królikowski, O. Bang, J. J. Rasmussen, and P. L. Christiansen, "Attraction of nonlocal dark optical solitons.," *Optics Letters*, vol. 29, pp. 286–8, 2004.

[33] C. Rotschild, B. Alfassi, O. Cohen, and M. Segev, "Long-range interactions between optical solitons," *Nature Physics*, vol. 2, pp. 769–774, 2006.

[34] A. Dreischuh, D. Neshev, D. Petersen, O. Bang, and W. Krolikowski, "Observation of Attraction between Dark Solitons," *Physical Review Letters*, vol. 96, p. 043901, 2006.

[35] M. Mitchell and M. Segev, "Self-trapping of incoherent white light," *Nature*, vol. 387, 1997.

[36] Z. Chen, "Self-Trapping of Dark Incoherent Light Beams," *Science*, vol. 280, pp. 889–892, 1998.

[37] W. Wan, S. Jia, and J. W. Fleischer, "Dispersive, superfluid-like shock waves in nonlinear optics," *Nature Physics*, vol.3, pp. 46-51, 2007.

[38] Z. Dutton, "Observation of Quantum Shock Waves Created with Ultra- Compressed Slow Light Pulses in a Bose-Einstein Condensate," *Science*, vol. 293, pp. 663–668, 2001.

[39] A. M. Kamchatnov, A. Gammal, and R. A. Kraenkel, "Dissipationless shock waves in Bose-Einstein condensates with repulsive interaction between atoms," *Physical Review A*, vol. 69, p. 063605, 2004.

[40] N. Ghofraniha, C. Conti, G. Ruocco, and S. Trillo, "Shocks in Nonlocal Media," *Physical Review Letters*, vol. 99, p. 043903, 2007.

[41] C. Barsi, W. Wan, C. Sun, and J. W. Fleischer, "Dispersive shock waves with nonlocal nonlinearity.," *Optics Letters*, vol. 32, pp. 2930–2, 2007.

[42] C. Sun, S. Jia, C. Barsi, S. Rica, A. Picozzi, and J. W. Fleischer, "Observation of the kinetic condensation of classical waves," *Nature Physics*, vol. 8, pp. 471–475, 2012.

[43] I. Carusotto, "Superfluid light in bulk nonlinear media," *Proceedings of the Royal Society A: Mathematical, Physical and Engineering Sciences*, vol. 470, 2014.

[44] P. E. Larré and I. Carusotto, "Optomechanical signature of a frictionless flow of superfluid light," *Physical Review A*, vol. 91, p. 2, 2015.

[45] A. Chiocchetta, P. É. Larré, and I. Carusotto, "Thermalization and Bose-Einstein condensation of quantum light in bulk nonlinear media," *arXiv*, 1605.01870, 2016.

[46] M. Elazar, V. Fleurov, and S. Bar-Ad, "All-optical event horizon in an optical analog of a Laval nozzle," *Physical Review A*, vol. 86, p. 063821, 2012.

[47] S. Bar-Ad, R. Schilling, and V. Fleurov, "Nonlocality and fluctuations near the optical analog of a sonic horizon," *Physical Review A*, vol. 87, p. 013802, 2013.

[48] R. W. Boyd, *Nonlinear Optics*. Academic Press, 3rd ed., 2008.

[49] K. D. Singer, M. G. Kuzyk, and J. E. Sohn, "Second-order nonlinear-optical processes in orientationally ordered materials: relationship between molecular and macroscopic properties," *Journal of the Optical Society of America B*, vol. 4, p. 968, 1987.

[50] S. Haroche and F. Hartmann, "Theory of Saturated-Absorption Line Shapes," *Physical Review A*, vol. 6, pp. 1280–1300, 1972.

[51] P. L. Kelley, "Self-Focusing of Optical Beams," *Physical Review Letters*, vol. 15, pp. 1005–1008, 1965.

[52] J. P. Gordon, R. C. C. Leite, R. S. Moore, S. P. S. Porto, and J. R. Whinnery, "Long-Transient Effects in Lasers with Inserted Liquid Samples," *Journal of Applied Physics*, vol. 36, no. 1, p. 3, 1965.

[53] A. Minovich, D. N. Neshev, A. Dreischuh, W. Krolikowski, and Y. S. Kivshar, "Experimental reconstruction of nonlocal response of thermal nonlinear optical media.," *Optics Letters*, vol. 32, pp. 1599–601, 2007.

[54] S. Gatz and J. Herrmann, "Anisotropy, nonlocality, and space-charge field displacement in (2+ 1)-dimensional self-trapping in biased photorefractive crystals," *Optics Letters*, vol. 23, no. 15, pp. 1176–1178, 1998.

[55] D. McLaughlin, D. Muraki, and M. Shelley, "Self-focussed optical structures in a nematic liquid crystal," *Physica D*, Vol. 97, 4, pp. 471-497, 1996.

[56] S. Sarkar and a. Bhattacharyay, "Non-local interactions in a BEC: an analogue gravity perspective," *Journal of Physics A*, vol. 47, p. 092002, 2014.

[57] D. Vocke, T. Roger, F. Marino, E. M. Wright, I. Carusotto, M. Clerici, and D. Faccio, "Experimental characterization of nonlocal photon fluids," *Optica*, vol. 2, no. 5, p. 484, 2015.

[58] O. Bang, W. Krolikowski, J. Wyller, and J. Rasmussen, "Collapse arrest and soliton stabilization in nonlocal nonlinear media," *Physical Review E*, vol. 66, p. 046619, 2002.

[59] S. Skupin, O. Bang, D. Edmundson, and W. Krolikowski, "Stability of two-dimensional spatial solitons in nonlocal nonlinear media," *Physical Review E*, vol. 73, p. 066603, 2006.

[60] M. Peccianti, K. Brzdąkiewicz, and G. Assanto, "Nonlocal spatial soliton interactions in nematic liquid crystals," *Optics Letters*, vol. 27(16), pp.1460-1462, 2002.

[61] A. Picozzi and J. Garnier, "Incoherent Soliton Turbulence in Nonlocal Nonlinear Media," *Physical Review Letters*, vol. 107, p. 233901, 2011.

[62] O. Cohen, H. Buljan, T. Schwartz, J. W. Fleischer, and M. Segev, "Incoherent solitons in instantaneous nonlocal nonlinear media," *Physical Review E*, vol. 73, p. 015601, 2006.

[63] C. Rotschild, T. Schwartz, O. Cohen, and M. Segev, "Incoherent spatial solitons in effectively instantaneous nonlinear media," *Nature Photonics*, vol. 2, pp. 371–376, 2008.

[64] J. Wyller, W. Krolikowski, O. Bang, and J. Rasmussen, "Generic features of modulational instability in nonlocal Kerr media," *Physical Review E*, vol. 66, p. 066615, 2002.

[65] C. Barsi, W. Wan, and J. W. Fleischer, "Imaging through nonlinear media using digital holography," *Nature Photonics*, vol. 3, pp. 211–215, 2009.

[66] D. Briedis, D. E. Petersen, W. Krolikowski, D. Edmundson, and O. Bang, "Ring vortex solitons in nonlocal nonlinear media," *2005 European Quantum Electronics Conference, EQEC '05*, vol. 2005, no. 2, p. 46, 2005.

[67] Y. Pomeau and S. Rica, "Model of superflow with rotons," *Physical Review Letters*, vol. 71, no. 2, pp. 247–250, 1993.

[68] F. Bonaccorso, Z. Sun, T. Hasan, and A. C. Ferrari, "Graphene photonics and optoelectronics," *Nature Photonics*, vol. 4, pp. 611-622 ,2010.

[69] Schott AG, "Schott Optical Glass Datasheet, http://www.schott.com."

[70] K. Moutzouris, M. Papamichael, S. C. Betsis, I. Stavrakas, G. Hloupis, and D. Triantis, "Refractive, dispersive and thermo-optic properties of twelve organic solvents in the visible and near-infrared," *Applied Physics B*, vol. 116, pp. 617–622, 2014.

[71] K. Kinnstaetter, A. W. Lohmann, J. Schwider, and N. Streibl, "Accuracy of phase shifting interferometry.," *Applied Optics*, vol. 27, no. 24, pp. 5082–5089, 1988.

[72] J. R. Whinnery, "Laser measurement of optical absorption in liquids," *Accounts of Chemical Research*, vol. 7, pp. 225–231, 1974.

[73] S. J. Sheldon, L. V. Knight, and J. M. Thorne, "Laser-induced thermal lens effect: a new theoretical model," *Applied Optics*, vol. 21, p. 1663, 1982.

[74] I. Carusotto and C. Ciuti, "Quantum fluids of light," *Reviews of Modern Physics*, vol. 85, pp. 299–366, 2013.

[75] J. D. Jackson, "Electrodynamics," in *The Optics Encyclopedia*, Weinheim, Germany: Wiley-VCH Verlag GmbH & Co. KGaA, 2007.

[76] F. Dalfovo, S. Giorgini, L. P. Pitaevskii, and S. Stringari, "Theory of Bose-Einstein condensation in trapped gases," *Reviews of Modern Physics*, vol. 71, pp. 463–512, 1999.

[77] F. Marino, M. Ciszak, and A. Ortolan, "Acoustic superradiance from optical vortices in self-defocusing cavities," *Physical Review A*, vol. 80, p. 065802, 2009.

[78] J. Dugan, H. Suzukawa, C. Forsyth, and M. Farber, "Ocean wave dispersion surface measured with airborne IR imaging system," *IEEE Transactions on Geoscience and Remote Sensing*, vol. 34, no. 5, pp. 1282–1284, 1996.

[79] D. Stilwell, "Directional energy spectra of the sea from photographs," *Journal of Geophysical Research*, vol. 74, pp. 1974–1986, 1969.

[80] C. Bosshard, P. V. Mamyshev, and G. I. Stegeman, "All-optical steering of dark spatial soliton arrays and the beams guided by them.," *Optics Letters*, vol. 19, no. 2, p. 90, 1994.

[81] P. V. Mamyshev, C. Bosshard, and G. I. Stegeman, "Generation of a periodic array of dark spatial solitons in the regime of effective amplification," *Journal of the Optical Society of America B*, vol. 11(7), pp. 1254, 1994.

[82] J. Vogels, K. Xu, C. Raman, J. Abo-Shaeer, and W. Ketterle, "Experimental Observation of the Bogoliubov Transformation for a Bose-Einstein Condensed Gas," *Physical Review Letters*, vol. 88, p. 060402, 2002.

[83] D. Vocke, K. Wilson, F. Marino, I. Carusotto, E. M. Wright, T. Roger, B. P. Anderson, P. Öhberg, and D. Faccio, "Role of geometry in the superfluid flow of nonlocal photon fluids," *Physical Review A*, vol. 94, 2016.

[84] L. P. Pitaevskii, "Vortex Lines in an imperfect Bose Gas," *J. Exptl. Theoret. Phys. (U.S.S.R.)*, vol. 13, no. 40, pp. 646–651, 1961.

[85] E. P. Gross, "Structure of a quantized vortex in boson systems," *Il Nuovo Cimento*, vol. 20, pp. 454–477, 1961.

[86] M. Tsubota, "Quantum turbulence: from superfluid helium to atomic Bose Einstein condensates," *Contemporary Physics*, vol. 50, pp. 463–475, 2009.

[87] L. Santos, G. V. Shlyapnikov, and M. Lewenstein, "Roton-Maxon Spectrum and Stability of Trapped Dipolar Bose-Einstein Condensates," *Physical Review Letters*, vol. 90, p. 250403, 2003.

[88] T. Frisch, Y. Pomeau, and S. Rica, "Transition to dissipation in a model of superflow," *Physical Review Letters*, vol. 69, pp. 1644–1647, 1992.

[89] T. Lahaye, C. Menotti, L. Santos, M. Lewenstein, and T. Pfau, "The physics of dipolar bosonic quantum gases," *Reports on Progress in Physics*, vol. 72, p. 126401, 2009.

[90] S. J. Robertson, "The theory of Hawking radiation in laboratory analogues," *Journal of Physics B: Atomic, Molecular and Optical Physics*, vol. 45, p. 163001, 2012.

[91] S. W. Hawking, "Black hole explosions?", *Nature*, vol. 248, pp. 30–31, 1974.

[92] L. Parker, "Particle creation and particle number in an expanding universe," *Journal of Physics A*, vol. 45, p. 374023, 2012.

[93] J. Bekenstein, "Black holes and Entropy," *Physical Review D*, vol. 7, no. 8, 1973.

[94] W. Unruh, "Experimental Black-Hole Evaporation?," *Physical Review Letters*, vol. 46, pp. 1351–1353, 1981.

[95] M. Visser, "Acoustic propagation in fluids: an unexpected example of Lorentzian geometry," *arXiv*, gr-qc/9311028, 1993.

[96] C. Barceló, S. Liberati, and M. Visser, "Analogue gravity," *Living Rev. Rel*, 2005.

[97] T. Jacobson, "Black Hole Evaporation and ultrashort distances," *Physical Review D*, vol. 44, no. 6, pp. 1731–1739, 1991.

[98] T. Jacobson, "Black hole radiation in the presence of a short distance cutoff," *Physical Review D*, vol. 48, no. 2, pp. 728–741, 1993.

[99] W. Unruh, "Sonic analogue of black holes and the effects of high frequencies on black hole evaporation," *Physical Review D*, vol. 51, no. 6, 1995.

[100] S. Weinfurtner, E. W. Tedford, M. C. J. Penrice, W. Unruh, and G. a. Lawrence, "Measurement of Stimulated Hawking Emission in an Analogue System," *Physical Review Letters*, vol. 106, p. 021302, 2011.

[101] L. J. Garay, J. R. Anglin, J. I. Cirac, and P. Zoller, "Sonic analog of gravitational black holes in Bose-Einstein condensates," *Physical Review Letters*, vol. 85, pp. 4643–4647, 2000.

[102] L. J. Garay, J. R. Anglin, J. I. Cirac, and P. Zoller, "Sonic black holes in dilute Bose-Einstein condensates," *Physical Review A*, vol. 63, p. 023611, 2001.

[103] O. Lahav, A. Itah, A. Blumkin, C. Gordon, S. Rinott, A. Zayats, and J. Steinhauer, "Realization of a sonic black hole analog in a Bose-Einstein condensate," *Physical Review Letters*, vol. 105, p. 240401, 2010.

[104] J. Steinhauer, "Observation of quantum Hawking radiation and its entanglement in an analogue black hole," *Nature Physics*, 12, p. 959-965, 2016.

[105] T. G. Philbin, C. Kuklewicz, S. Robertson, S. Hill, F. König, and U. Leonhardt, "Fiber-optical analog of the event horizon.," *Science*, vol. 319, pp. 1367–70, 2008.

[106] F. Belgiorno, S. L. Cacciatori, M. Clerici, V. Gorini, G. Ortenzi, L. Rizzi, E. Rubino, V. G. Sala, and D. Faccio, "Hawking Radiation from Ultrashort Laser Pulse Filaments," *Physical Review Letters*, vol. 105, p. 203901, 2010.

[107] R. Penrose and R. M. Floyd, "Extraction of Rotational Energy from a Black Hole," *Nature Physical Science*, vol. 229, no. 6, pp. 177–179, 1971.

[108] Y. B. Zel 'dovich, "Amplification of Cylindrical Electromagnetic Waves Reflected from a Rotating Body," *Zh. Eksp. Tear. Fiz*, vol. 35, no. 62, pp. 2076–2081, 1972.

[109] J. Bekenstein, "The many faces of superradiance," *Physical Review D*, vol. 11, pp. 453–457, 1998.

[110] A. Prain, *The Analogue Gravity Challenge*. PhD thesis, University of Trieste, 2012.

[111] M. Richartz, A. Prain, S. Weinfurtner, and S. Liberati, "Super-radiant scattering of dispersive fields," *Classical and Quantum Gravity*, vol. 30, p. 085009, 2013.

[112] C. W. Misner, "Interpretation of Gravitational-Wave Observations," *Physical Review Letters*, vol. 28, pp. 994–997, 1972.

[113] M. Visser and S. Weinfurtner, "Vortex analogue for the equatorial geometry of the Kerr black hole," *Classical and Quantum Gravity*, vol. 22, pp. 2493–2510, 2005.

[114] M. Richartz, A. Prain, S. Weinfurtner, and S. Liberati, "Super-radiant scattering of dispersive fields," *Classical and Quantum Gravity*, vol. 30, p. 085009, 2013.

[115] V. Cardoso, A. Coutant, M. Richartz, and S. Weinfurtner, "Rotational superradiance in fluid laboratories," *arXiv*, 1607.01378, 2016.

[116] S. Basak and P. Majumdar, "Superresonance from a rotating acoustic black hole," *Classical and Quantum Gravity*, vol. 20, pp. 3907–3913, 2003.

[117] T. R. Slatyer and C. M. Savage, "Superradiant scattering from a hydrodynamic vortex," *Classical and Quantum Gravity*, vol. 22, pp. 3833–3839, 2005.

[118] P. Painleve, "La mécanique classique et la théorie de la relativité," *C. R. Acad. Sci.*, vol. 173, pp. 677–680, 1921.

[119] A. Gullstrand, "Allgemeine Lösung des statischen Einkörperproblems in der Einsteinschen Gravitationstheorie," *Arkiv. Mat. Astron. Fys.*, vol. 16, no. 8, pp. 1–15, 1922.

[120] D. Faccio, F. Belgiorno, S. Cacciatori, V. Gorini, S. Liberati, and U. Moschella, *Analogue Gravity Phenomenology: Analogue Spacetimes and Horizons, from Theory to Experiment*, vol. 870. Springer, 2013.

[121] C. Barcelo, S. Liberati, and M. Visser, "Analogue gravity from Bose-Einstein condensates," *Classical and Quantum Gravity*, vol. 1137, 2001.

[122] M. Visser, "Acoustic black holes: horizons, ergospheres and Hawking radiation," *Classical and Quantum Gravity*, vol. 15, no. 6, pp. 1767–1791, 1998.

[123] T. Roger, C. Maitland, K. Wilson, N. Westerberg, D. Vocke, E. M. Wright, and D. Faccio, "Optical analogues of the Newton Schrödinger equation and boson star evolution," *Nature Communications*, vol. 7, p. 13492, 2016.

[124] G. Walker, A. S. Arnold, and S. Franke-Arnold, "Trans-Spectral Orbital Angular Momentum Transfer via Four-Wave Mixing in Rb Vapor," *Physical Review Letters*, vol. 108, p. 243601, 2012.

[125] C. Maitland, "Photon Fluid OAM Spectra - Numerical Measurements," tech. rep., Heriot-Watt University, Edinburgh, 2016.

[126] F. Marino, "A link between the linearized NSE and the gravitational analogy," tech. rep., CNR-Istituto Nazionale di Ottica, L.go E. Fermi 6, I-50125 Firenze, Italy, 2016.

[127] F. Marino, C. Maitland, D. Vocke, A. Ortolan, and D. Faccio, "Emergent geometries and nonlinear-wave dynamics in photon fluids.," *Scientific reports*, vol. 6, p. 23282, 2016.

[128] E. Goulart, M. Novello, F. T. Falciano, and J. D. Toniato, "Hidden geometries in nonlinear theories: a novel aspect of analogue gravity," *Classical and Quantum Gravity*, vol. 28, p. 245008, 2011.

[129] L. D. Landau and E. Lifshitz, *Fluid Mechanics, Band 6*. Elsevier, 1987.

[130] M. Conforti and S. Trillo, *Dispersive Shock Waves: From Water Waves to Nonlinear Optics*. Springer, 2016.

[131] N. J. Zabusky and C. J. Galvin, "Shallow-water waves, the Korteweg-deVries equation and solitons," *Journal of Fluid Mechanics*, vol. 47, p. 811, 1971.

[132] Z. Chen, M. Segev, and D. N. Christodoulides, "Optical spatial solitons: historical overview and recent advances.," *Reports on progress in Physics*, vol. 75, p. 086401, 2012.

[133] M. Onorato, S. Residori, U. Bortolozzo, A. Montina, and F. Arecchi, "Rogue waves and their generating mechanisms in different physical contexts," *Physics Reports*, vol. 528, no. 2, pp. 47–89, 2013.

[134] T. Roger, D. Majus, G. Tamosauskas, P. Panagiotopoulos, M. Kolesik, G. Genty, I. Gražulevičit, A. Dubietis, and D. Faccio, "Extreme events in resonant radiation from three-dimensional light bullets," *Physical Review A*, vol. 90, p. 033816, 2014.

[135] J. E. Rothenberg and D. Grischkowsky, "Observation of the Formation of an Optical Intensity Shock and Wave Breaking in the Nonlinear Propagation of Pulses in Optical Fibers," *Physical Review Letters*, vol. 62, pp. 531–534, 1989.

[136] S. Burger, K. Bongs, S. Dettmer, W. Ertmer, K. Sengstock, A. Sanpera, G. V. Shlyapnikov, and M. Lewenstein, "Dark Solitons in Bose-Einstein Condensates," *Physical Review Letters*, vol. 83, pp. 5198–5201, 1999.

[137] M. A. Hoefer, M. J. Ablowitz, I. Coddington, E. A. Cornell, P. Engels, and V. Schweikhard, "Dispersive and classical shock waves in Bose-Einstein condensates and gas dynamics," *Physical Review A*, vol. 74, p. 023623, 2006.

[138] S. Jaiswal, P. Bandyopadhyay, and A. Sen, "Experimental observation of precursor solitons in a flowing complex plasma," *Physical Review E*, vol. 93, p. 041201, 2016.

[139] M. Cadoni and S. Mignemi, "Acoustic analogues of black hole singularities," *Physical Review D*, vol. 72, no. 8, 2005.

[140] C. Cherubini and S. Filippi, "Von Mises' potential flow wave equation and nonlinear analog gravity," *Physical Review D*, vol. 84, p. 124010, 2011.

[141] W. Wan, S. Jia, and J. W. Fleischer, "Dispersive superfluid-like shock waves in nonlinear optics," *Nature Physics*, vol. 3, pp. 46–51, 2007.

[142] F. Marino, "Nonlinear waves in photon fluids and dynamics in analog gravity," tech. rep. , CNR-Istituto Nazionale di Ottica, L.go E. Fermi 6, I-50125 Firenze, Italy, 2015.

[143] S. M. Carroll, *Spacetime and Geometry: An Introduction to General Relativity*, vol. 1. 2004.

[144] G. Xu, D. Vocke, D. Faccio, J. Garnier, T. Roger, S. Trillo, and A. Picozzi, "From coherent shocklets to giant collective incoherent shock waves in nonlocal turbulent flows.," *Nature Communications*, vol. 6, p. 8131, 2015.

[145] J. Fatome, C. Finot, G. Millot, A. Armaroli, and S. Trillo, "Observation of Optical Undular Bores in Multiple Four-Wave Mixing," *Physical Review X*, vol. 4, p. 021022, 2014.

[146] A. C. Newell, S. Nazarenko, and L. Biven, "Wave turbulence and intermittency," *Physica D: Nonlinear Phenomena*, vol. 152, pp. 520–550, 2001.

[147] A. Picozzi, J. Garnier, T. Hansson, P. Suret, S. Randoux, G. Millot, and D. N. Christodoulides, "Optical wave turbulence: Towards a unified nonequilibrium thermodynamic formulation of statistical nonlinear optics," *Physics Reports*, vol. 542, no. 1, pp. 1–132, 2014.

[148] G. Xu, *Emergence of incoherent solitons and shock- like singularities in optical turbulence Thèse Docteur en Physique*. PhD thesis, Université de Bourgogne, 2016.

[149] V. Zakharov, S. Musher, and A. Rubenchik, "Hamiltonian approach to the description of non-linear plasma phenomena," *Physics Reports*, vol. 129, pp. 285–366, 1985.

[150] A. C. Newell, B. Rumpf, and V. E. Zakharov, "Spontaneous breaking of the spatial homogeneity symmetry in wave turbulence.," *Physical Review Letters*, vol. 108, p. 194502, 2012.

[151] A. Campa, T. Dauxois, and S. Ruffo, "Statistical mechanics and dynamics of solvable models with long-range interactions," *Physics Reports*, vol. 480, no. 3, pp. 57–159, 2009.

[152] A. Campa, T. Dauxois, D. Fanelli, and S. Ruffo, *Physics of Long-Range Interacting Systems*. Oxford Press, 2014.

[153] M. Vergassola, B. Dubrulle, U. Frisch, and A. Noullez, "Burgers' equation, Devil's staircases and the mass distribution for large-scale structures," *Astronomy and Astrophysics*, vol. 289, no. 2, p. 325-356, vol. 289, pp. 325–356, 1994.

[154] C. Rotschild, O. Cohen, O. Manela, M. Segev, and T. Carmon, "Solitons in Nonlinear Media with an Infinite Range of Nonlocality: First Observation of Coherent Elliptic Solitons and of Vortex-Ring Solitons," *Physical Review Letters*, vol. 95, p. 213904, 2005.

[155] A. Campa, T. Dauxois, and S. Ruffo, "Statistical mechanics and dynamics of solvable models with long-range interactions," *Physics Reports*, vol. 480, pp. 57–159, 2009.

[156] Z. Wang, Y. Guo, Z. Lin, and P. Zhang, "Unstable Galaxy Models," *ArXiv*, 1303.2988, 2013.

[157] A. Prain, S. Vezzoli, N. Westerberg, T. Roger, and D. Faccio, "Spontaneous photon production in time-dependent epsilon-near-zero materials," *ArXiv*, 1702.08228, 2017.

[158] P. É. Larré and I. Carusotto, "Propagation of a quantum fluid of light in a cavityless nonlinear optical medium: General theory and response to quantum quenches," *Physical Review A*, vol. 92, no. 4, 2015.

[159] T. Peyronel, O. Firstenberg, Q.-Y. Liang, S. Hofferberth, A. V. Gorshkov, T. Pohl, M. D. Lukin, and V. Vuletić, "Quantum nonlinear optics with single photons enabled by strongly interacting atoms," *Nature*, vol. 488, pp. 57–60, 2012.

[160] L. P. Euve, F. Michel, R. Parentani, T. G. Philbin, and G. Rousseaux, "Observation of Noise Correlated by the Hawking Effect in a Water Tank," *Physical Review Letters*, vol. 117, no. 12, pp. 1–6, 2016.

[161] I. Bloch, J. Dalibard, and S. Nascimbène, "Quantum simulations with ultracold quantum gases," *Nature Physics*, vol. 8, pp. 267–276, 2012.

[162] N. Westerberg, C. Maitland, D. Faccio, K. Wilson, P. Öhberg, and E. M. Wright, "Synthetic magnetism for photon fluids," *Physical Review A*, vol. 94, p. 023805, 2016.

[163] L. Diósi, "Gravitation and quantum-mechanical localization of macro-objects," *Physics Letters A*, vol. 105, pp. 199–202, 1984.

[164] R. Penrose, "On Gravity's role in Quantum State Reduction," *General Relativity and Gravitation*, vol. 28, pp. 581–600, 1996.

[165] R. Bekenstein, R. Schley, M. Mutzafi, C. Rotschild, and M. Segev, "Optical simulations of gravitational effects in the Newton Schrödinger system," *Nature Physics*, vol. 11, pp. 872–878, 2015.

[166] P. O. Fedichev and U. R. Fischer, "Cosmological quasiparticle production in harmonically trapped superfluid gases," *Physical Review A*, vol. 69, p. 033602, 2004.

[167] S. Weinfurtner, M. Visser, P. Jain, and C. W. Gardiner, "On the phenomenon of emergent spacetimes: An instruction guide for experimental cosmology," *arXiv* , 0804.1346, 2007.